NORTH ATLANTIC TREATY ORGANIZATION

SCIENCE AND TECHNOLOGY ORGANIZATION

AC/323(AVT-233)TP/961

www.sto.nato.int

STO TECHNICAL REPORT **TR-AVT-233**

Aeroacoustics of Engine Installation on Military Air Vehicles

(Aéroacoustique de l'installation des moteurs dans les véhicules militaires aériens)

This report contains the results of the RTG AVT-233 active in the period 2014 – 2017 and covering the establishment of validated methods to predict fundamental aspects of acoustic installation effects of engine noise for military aircraft.

Published October 2021

NORTH ATLANTIC TREATY ORGANIZATION

SCIENCE AND TECHNOLOGY ORGANIZATION

AC/323(AVT-233)TP/961

www.sto.nato.int

STO TECHNICAL REPORT **TR-AVT-233**

Aeroacoustics of Engine Installation on Military Air Vehicles

(Aéroacoustique de l'installation des moteurs dans les véhicules militaires aériens)

This report contains the results of the RTG AVT-233 active in the period 2014 – 2017 and covering the establishment of validated methods to predict fundamental aspects of acoustic installation effects of engine noise for military aircraft.

The NATO Science and Technology Organization

Science & Technology (S&T) in the NATO context is defined as the selective and rigorous generation and application of state-of-the-art, validated knowledge for defence and security purposes. S&T activities embrace scientific research, technology development, transition, application and field-testing, experimentation and a range of related scientific activities that include systems engineering, operational research and analysis, synthesis, integration and validation of knowledge derived through the scientific method.

In NATO, S&T is addressed using different business models, namely a collaborative business model where NATO provides a forum where NATO Nations and partner Nations elect to use their national resources to define, conduct and promote cooperative research and information exchange, and secondly an in-house delivery business model where S&T activities are conducted in a NATO dedicated executive body, having its own personnel, capabilities and infrastructure.

The mission of the NATO Science & Technology Organization (STO) is to help position the Nations' and NATO's S&T investments as a strategic enabler of the knowledge and technology advantage for the defence and security posture of NATO Nations and partner Nations, by conducting and promoting S&T activities that augment and leverage the capabilities and programmes of the Alliance, of the NATO Nations and the partner Nations, in support of NATO's objectives, and contributing to NATO's ability to enable and influence security and defence related capability development and threat mitigation in NATO Nations and partner Nations, in accordance with NATO policies.

The total spectrum of this collaborative effort is addressed by six Technical Panels who manage a wide range of scientific research activities, a Group specialising in modelling and simulation, plus a Committee dedicated to supporting the information management needs of the organization.

- AVT Applied Vehicle Technology Panel
- HFM Human Factors and Medicine Panel
- IST Information Systems Technology Panel
- NMSG NATO Modelling and Simulation Group
- SAS System Analysis and Studies Panel
- SCI Systems Concepts and Integration Panel
- SET Sensors and Electronics Technology Panel

These Panels and Group are the power-house of the collaborative model and are made up of national representatives as well as recognised world-class scientists, engineers and information specialists. In addition to providing critical technical oversight, they also provide a communication link to military users and other NATO bodies.

The scientific and technological work is carried out by Technical Teams, created under one or more of these eight bodies, for specific research activities which have a defined duration. These research activities can take a variety of forms, including Task Groups, Workshops, Symposia, Specialists' Meetings, Lecture Series and Technical Courses.

The content of this publication has been reproduced directly from material supplied by STO or the authors.

Published October 2021

ISBN 978-92-837-2282-3

Table of Contents

List of Figures

List of Tables

Acknowledgements

The authors would like to acknowledge the indispensable help of the following persons:

DLR Sections:

Michael Pott-Pollenske;

Roland Ewert;

Jan Täger;

Danica Knoblich;

Jorge Gomez; and

Colleagues of DNW-NWB.

ONERA Sections:

J. Bulté;

L. Coste;

P. Lebigot;

F. Desmerger;

E. Manoha;

C. Mincu; and

R. Davy.

NASA Sections:

Daniel Stead; and

Stuart Pope.

AVT-233 Membership List

CO-CHAIRS

Prof. Dr.-Ing. Jan Werner DELFS
DLR –Institute of Aerodynamics and Flow
GERMANY
Email: jan.delfs@dlr.de

Dr. Russell H. THOMAS
NASA Langley Research Center
UNITED STATES
Email: russell.h.thomas@nasa.gov

MEMBERS

Dr. Luca BENASSI
Airbus Defence and Space
GERMANY
Email: luca.benassi@airbus.com

Dr. Harry BROUWER
NLR
The NETHERLANDS
Email: Harry.Brouwer@nlr.nl

Dr. Oliver DARBYSHIRE
BAE Systems
UNITED KINGDOM
Email: oliver.darbyshire@baesystems.com

Dr. Denis GELY
ONERA Département Aéroacoustique – DAAC
FRANCE
Email: denis.gely@ONERA.fr

Prof. Umberto IEMMA
Universita' Roma Tre
ITALY
Email: umberto.iemma@uniroma3.it

Prof. S. LELE
Stanford University
UNITED STATES
Email: lele@stanford.edu

Prof. Philip J. MORRIS
Penn State University
UNITED STATES
Email: PJMAER@engr.psu.edu

Dr. Nathan E. MURRAY
The University of Mississippi
UNITED STATES
Email: nmurray@olemiss.edu

Mr. Dave PATIENCE
BAE Systems
UNITED KINGDOM
Email: david.patience@baesystems.com

Dr. Christian PETTERSON
FMV – Swedish Defence Materiel Administration
SWEDEN
Email: kristian.petterson@fmv.se

Dr. Robert H. SCHLINKER
United Technologies Research Center
UNITED STATES
Email: unavailable

Dr. Charlotte WHITFIELD*
NASA Langley Research Center
UNITED STATES
Email: unavailable

* Co-Chair (retired end 2015)

PANEL/GROUP MENTOR

Prof. Dr. Cord ROSSOW
DLR –Institute of Aerodynamics and Flow
GERMANY
Email: Cord.Rossow@dlr.de

Aeroacoustics of Engine Installation on Military Air Vehicles

(STO-TR-AVT-233)

Executive Summary

Noise is not only a problem with civil aviation but in the military sector as well. Jet propelled agile (unmanned) air vehicles generate particularly intense noise during operation. This is a problem in peace times due to annoyance of the community during necessary training/test flights, and in wartimes because of the risk of an early acoustic detection of the aircraft by the enemy. The particular details of engine integration on such vehicles can easily result in either a noisy or a quiet aircraft. However, today, noise is not part of the design process, but comes as a somewhat problematic by-product when the configuration has been fixed. The potential for an acoustically designed engine integration and corresponding beneficial acoustic installation effects is not exploited. The problem here is that – as opposed to more classical design disciplines – noise prediction is less developed. The applicability of acoustic prediction methods for low noise vehicle design is unclear, and so is their status of validation.

The purpose of AVT-233 was to help identify and then validate appropriate acoustic prediction methods as a basis for low noise military aircraft design with a focus on acoustic shielding of engine noise. This group of world experts in aeroacoustic prediction and testing from industry, research organizations and academia took this challenge and developed a structured approach toward progress in this area of concern.

In order to establish a fundamental aeroacoustic shielding database for validation of acoustic prediction codes of partners, a set of related aeroacoustic shielding tests was planned and executed in four different wind tunnels for three different geometries of increasing complexity to cover all relevant prediction scenarios. An exceptional aeroacoustic database of shielding problems has thus been established in AVT-233. Generic 2D diffraction (NACA0012), diffraction by a convex, sharp edged (SACCON) and a generally convex-concave shaped, sharp and round edged (HWB) configuration were all measured successfully. In preparation of these campaigns two aeroacoustic pulse test sources were developed and successfully used in the shielding experiments, one of which is nonintrusive and therefore neither disturbing the flow field nor the sound field. The repeatability of the source events turned out to be very good. The laser-based pulse source was successfully used in all four wind tunnels (open and closed section). A cross validation of the measurements over the AWB, F2 and QFF showed an excellent reproducibility of test results, slightly better than expected (deviations of about 1 dB). The various simulation approaches were validated against the measured data; simulation results were also successfully compared mutually from code to code. The use of high-fidelity numerical simulations helped to assess the step by step neglect of physical effects such as shear layer refraction, potential flow gradients and the flow itself. The overall outcome of these studies showed that for the majority of problems at low speed a uniform flow assumption or even complete neglect of the flow is acceptable. This study opened the door for justifying the use of some low- to mid-fidelity prediction approaches to the full scale aircraft shielding problem.

In conclusion, all main objectives of AVT-233 were accomplished. Validated tools have been established with which to take the next logical step toward full simulation of actual low noise design modifications on realistic NATO military air vehicles.

Aéroacoustique de l'installation des moteurs dans les véhicules militaires aériens

(STO-TR-AVT-233)

Synthèse

Le bruit n'est pas seulement un problème dans l'aviation civile, mais également dans le domaine militaire. Les véhicules aériens à réaction et agiles (sans pilote) produisent un bruit particulièrement intense en fonctionnement. Cela représente un problème en temps de paix, à cause des nuisances pour la population pendant les vols nécessaires à l'entraînement et aux essais, et en temps de guerre, en raison du risque de détection acoustique précoce de l'aéronef par l'ennemi. Les détails particuliers d'intégration du moteur dans ces véhicules peuvent facilement aboutir soit à un aéronef bruyant soit à un aéronef silencieux. Cependant, le bruit n'est actuellement pas pris en compte dans le processus de conception, mais constitue un sous-produit quelque peu problématique une fois la configuration établie. Le potentiel d'intégration d'un moteur conçu sur le plan acoustique et des effets bénéfiques de son installation n'est pas exploité. En l'occurrence, le problème est que la prédiction du bruit est moins développée que d'autres disciplines classiques de la conception. L'applicabilité des méthodes de prédiction acoustique à la conception de véhicules peu bruyants est floue, tout comme leur état de validation.

L'objet de l'AVT-233 était d'aider à identifier, puis valider, des méthodes de prédiction acoustique appropriées, afin de concevoir des aéronefs militaires peu bruyants en se concentrant sur la mise en place d'une protection acoustique atténuant le bruit du moteur. Ce groupe d'experts mondiaux en prédiction et essais aéroacoustiques, issus de l'industrie, d'organismes de recherche et du monde universitaire, a relevé le défi et élaboré une démarche structurée de progression dans ce domaine.

Afin d'établir une base de données fondamentales de la protection aéroacoustique servant à valider les codes de prédiction acoustique des partenaires, un ensemble correspondant d'essais de protection aéroacoustique a été planifié et exécuté dans quatre souffleries pour trois géométries d'une complexité croissante, dans le but de couvrir tous les scénarios de prédiction pertinents. Une base de données aéroacoustiques exceptionnelle des problèmes de protection a ainsi été créée par l'AVT-233. La diffraction générale en deux dimensions (NACA0012), la diffraction par un objet convexe à bords acérés (SACCON) et une configuration d'objet de forme généralement convexe-concave, à bords acérés et arrondis (HWB), ont toutes été mesurées avec succès. En préparation de ces campagnes, deux sources d'essai d'impulsions aéroacoustiques ont été mises au point et utilisées avec succès pendant les expériences de protection, l'une d'entre elles étant non intrusive et donc n'induisant aucune perturbation du champ d'écoulement ou du champ sonore. La répétabilité des événements avec les sources s'est révélée très bonne. La source d'impulsions laser a été utilisée avec succès dans les quatre souffleries (section ouverte et fermée). Une contre-validation des mesures dans les installations AWB, F2 et QFF a démontré une excellente reproductibilité des résultats d'essai, légèrement meilleure qu'espérée (écarts d'environ 1 dB). Les diverses démarches de simulation ont été validées au regard des données mesurées ; les résultats de simulation ont également été comparés entre eux, de code à code. L'utilisation de simulations numériques très fidèles a aidé à évaluer la négligence des effets physiques étape par étape, tels que la réfraction dans la zone de cisaillement, les gradients d'écoulement potentiels et l'écoulement lui-même. Dans l'ensemble, ces études ont montré que pour la majorité des problèmes à faible vitesse, il était admissible de partir d'une hypothèse d'écoulement uniforme, voire de négliger complètement l'écoulement. Cette étude a permis de justifier l'utilisation de quelques démarches, faiblement ou moyennement fidèles, de prédiction du problème de protection de l'aéronef en vraie grandeur.

En conclusion, tous les objectifs principaux de l'AVT-233 ont été atteints. Des outils validés ont été établis, qui permettent de passer à l'étape logique suivante, en vue de la simulation complète des modifications réelles apportées à la conception à faible bruit de véhicules militaires aériens et réalistes de l'OTAN.

Chapter 1 – INTRODUCTION TO AVT-233

Jan W. Delfs
DLR – Institute of Aerodynamics and Flow
GERMANY

Russell H. Thomas
Langley Research Center, NASA
UNITED STATES

ABSTRACT

In the AVT-233 Task Group a comprehensive research program was executed to identify and validate appropriate acoustic prediction methods as a basis for low noise military aircraft design with a focus on acoustic shielding of engine noise. A set of related aeroacoustic shielding tests was carried out in four different wind tunnels for three different geometries of increasing complexity to establish a fundamental aeroacoustic shielding database for the validation of acoustic prediction codes of partners. Generic 2D diffraction (NACA0012), diffraction at a convex, sharp edged (SACCON) and a generally convex-concave shaped, sharp- and round edged (HWB) configuration were all measured successfully. For this purpose, two aeroacoustic pulse test sources were developed successfully. A cross validation of the measurements over three wind tunnels showed excellent reproducibility of test results, even better than expected. The various simulation approaches were validated against measured data. The overall outcome showed that for the majority of problems the use of some fast low- to mid-fidelity prediction approaches to the aircraft shielding problem is justified. Validated tools have been established with which to take the next logical step toward full simulation based low noise design modifications of realistic NATO military air vehicles.

1.1 BACKGROUND

Military air vehicles cover a broad range of size and function, from large transports to small UAVs to the turbojets of high-powered fighters. Aeroacoustics – the science of sound generation by airflows, whether in isolation as in a jet plume, or as a result of interaction with a surface or an edge, or through excitation of an open cavity – plays a role in all of these. In the civilian world, much attention has been given to community noise exposure resulting from aircraft operations and to passenger comfort with regard to interior noise. The state of the art of aircraft noise prediction and reduction is aligned with transport aircraft. AVT-132 "Noise issues arising from the operation of gas turbine powered military air vehicles" and the specialists meeting AVT-158 addressed the noise from high-powered aircraft such as fighters, both in the community and on a carrier deck, but this is not the sole military aeroacoustic problem. Exploratory Team AVT-ET-130 "Aeroacoustics of Military Air Vehicles" was formed in 2012 to investigate the state of the art of aeroacoustics with respect to NATO military air vehicles, including:

- Prediction of source noise (in the near and far field);
- Prediction of received noise; effects of cavity (e.g., weapons bay) design;
- Effects of propulsion system installation and other aeroacoustic phenomena, and
- Suggestions for specific future technical activities.

AVT-233 built on the work conducted under AVT-ET-130 to report on the aeroacoustic effects of **propulsion airframe integration**. Understanding these effects and how to utilize that understanding in air vehicle design is of importance to all classes of vehicles, from transport aircraft to UCAVs and will become more important as new generations are developed.

1.2 TOPICS OF AVT-233

Installation of the propulsion with the airframe affects both the source (e.g., distorted inflow to a fan, modifications to jet exhaust flow via chevrons or other devices) and the sound propagation (e.g., shielding by a body, diffraction/refraction by a boundary layer [1]. These aeroacoustic integration effects are found on all types of air vehicles and are becoming of increasing importance as noise generated by propulsion systems and airframes in isolation is being reduced. The proposed research task was generic in nature and applicable to all classes of air vehicle, both civilian and military. In order to lay a foundation for any future inclusion of the acoustic aspects for military aircraft design, AVT-233 had to be set up mainly to establish validated prediction approaches to aeroacoustic installation effects. The Task Group was to focus on demonstrating (on generic configurations) the availability and reliability of tools capable of predicting the effects of propulsion system installation on received sound. The configurations finally chosen are the SACCON (F17) UAV configuration (see Figure 1-1), studied intensively in the former RTG on aerodynamics, stability and control, and a Hybrid Wing Body (HWB) geometry (see Figure 1-1), provided by NASA. The research activity in AVT-233 not only implied code-to-code comparisons but the need for dedicated 3D aeroacoustic validation experiments, which were conducted in the DNW-NWB. With its 3m rectangular jet, the NWB represented a large enough acoustic wind tunnel for this purpose.

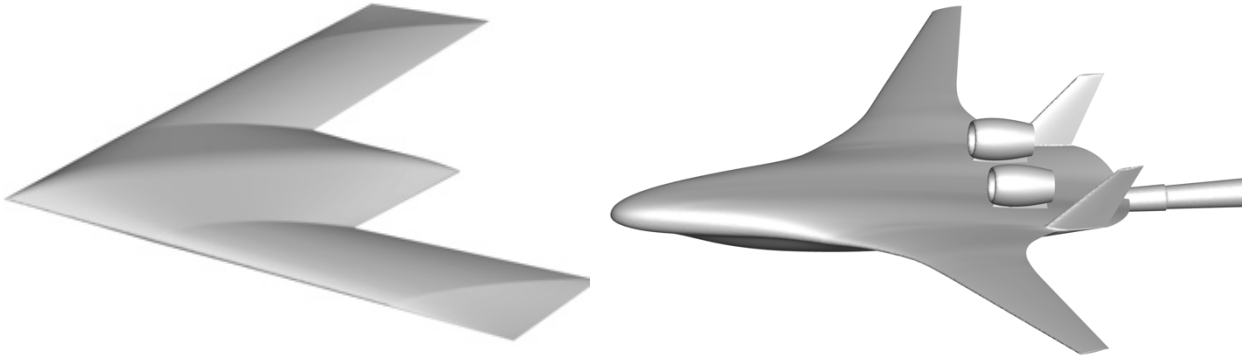

Figure 1-1: Aircraft Configurations Studied in AVT-233. Left: SACCON (F17E), Right: HWB, (not to scale).

In view of the complexity of the problems addressed partners felt that even very basic acoustic diffraction studies of a 2D airfoil [2] were necessary before stepping to the level of analysing acoustically an actual 3D aircraft model geometry. Much effort was invested in AVT-233 to qualify and describe theoretically a generic, but reliable reference acoustic source, applicable not only at zero flow conditions but as well under conditions of flow [3]. These “preliminary” studies were considered very important, because only the comparatively simple 2D geometry setup in combination with the simple point source, allowed for better capturing the complex physics of the diffraction problem including flow effects. The generic 2D airfoil shielding tests were deliberately done in the different wind tunnels with the purpose of estimating the facility related scatter in acoustic shielding results on a nominally identical model and source combination. Here, test campaigns were run in DLR’s Acoustic Wind tunnel Braunschweig (AWB), NASA’s Quiet Flow Facility (QFF), and ONERA’s F2 tunnel.

1.3 OBJECTIVES OF AVT-233

The Task Group’s objectives were:

- Demonstration of the availability and reliability of tools capable of predicting the effects of propulsion system installation for generic configurations on received sound as a basis for future acoustic design studies on military aircraft.

- Prediction of acoustic installation effects with various approaches and codes as well as code-to-code comparisons among partners.
- Performing dedicated aeroacoustic experiments for the purpose of validating the prediction codes for acoustic installation effects.

1.4 WORK PLAN

According to the defined contents of AVT-233, a work breakdown structure was set up. Three main technical work packages were established, plus a reporting phase as a concluding package. The contents of the mentioned technical work packages were defined as follows:

WP 1 Basic Studies on Acoustic Diffraction

This work package was devoted to basic studies on diffraction with and without flow influence on a 2D airfoil at zero sweep. Although highly generic, an airfoil features important geometric elements as far as diffraction (and its description in various different computational approaches) is concerned, namely a sharp (trailing) edge and a rounded (leading) edge. The group agreed to use a well-known airfoil, whose aerodynamic behaviour is documented and finally opted for the NACA0012. The task then was to measure and compute the acoustic attenuation $\gamma_p = SPL_{airfoil} - SPL_{isolated}$ dB on lines parallel to the flow on the shadow side in the symmetry plane of the airfoil as a function of the source position. A highly localized pulse source was to be considered with linear radiation characteristics (no shock signals). An idealized (monopole-like) source was chosen because the main objective of AVT-233 was not to study the source, but to study the installation effects of the aerodynamic body on its sound field. In that sense, it was useful to revert to a source, whose characteristics are so simple, that it could be described analytically to facilitate the excitation side in the computations. The generation of the pulse source and its description took place in work package 2, since in the context of AVT-233, the only task of the source was to generate “a test signal” for an appropriate way of measuring the acoustic shielding properties of the shapes. One important task in work package 1 was to design and build suitable wind tunnel models according to the special requirements of acoustic shielding tests.

WP 2 Aeroacoustic Testing Techniques

Apart from an anechoic aeroacoustic test environment, the seemingly simple basic setup for the measurement of acoustic shielding properties of (aircraft) shapes requires i) a well-defined source and ii) suitable sensor (and sensor arrangements). A localized acoustic pulse source with mostly linear behaviour (no shock generation to avoid unnecessary complexity) had to be developed and qualified for the shielding tests (i). Moreover, the source needed to be useable in different wind tunnel environments such as open test section acoustic tunnels of different sizes and closed test section wind tunnels. Since shielding typically needs to be studied using complete (aircraft) geometries, wind tunnel models for shielding tests are naturally small (highly downscaled with respect to an original aircraft size), say on the order of 1:20. This means, that sensors (ii) need to be identified and tested for very high acoustic frequencies, in fact up to ultrasonic conditions, ranging from 5kHz to about 80kHz. Reliable acoustic measurements in this range are nonstandard and therefore difficult.

WP 3 Aeroacoustic Shielding of Aircraft Configurations

This work package contained the experimental and numerical simulation of acoustic shielding of actual 3D model aircraft. The acoustic testing equipment developed in work package 2 and the numerical tools tested in work package 1 had to be applied in this complex situation. Two aircraft shapes were to be tested each with a different focus, as far as diffraction phenomena are concerned. The SACCON (F17E) configuration is of U(C)AV type and features mostly sharp edge diffraction and convex shapes while a version of the HWB of NASA, which could potentially represent a large tanker or military transport, also

contains very rounded edges and concave surface sections. As far as the wind tunnel tests were concerned, the DNW-NWB at DLR in Braunschweig turned out to be the most suitable choice for the 3D tests. While the AVT-233 took advantage of the existence and availability of a SACCON model from previous RTGs, however, the support hardware had to be adapted. Moreover, the task of designing and making a new model of the HWB to fit the dimensions of the NWB test section had to be solved. In addition, an appropriate microphone support had to be made for the NWB.

The structure of AVT-233 with these work packages and a timeline of the planned activities is shown in Figure 1-2. This figure also contains the various wind tunnel entries actually accomplished. Originally, a potential, highly interesting shielding test in UTRC's acoustic wind tunnel was planned with the objective to extrapolate the results obtained in the low speed tunnels to higher subsonic Mach numbers (of M = 0.6 or so). Unfortunately, these resources did not become available.

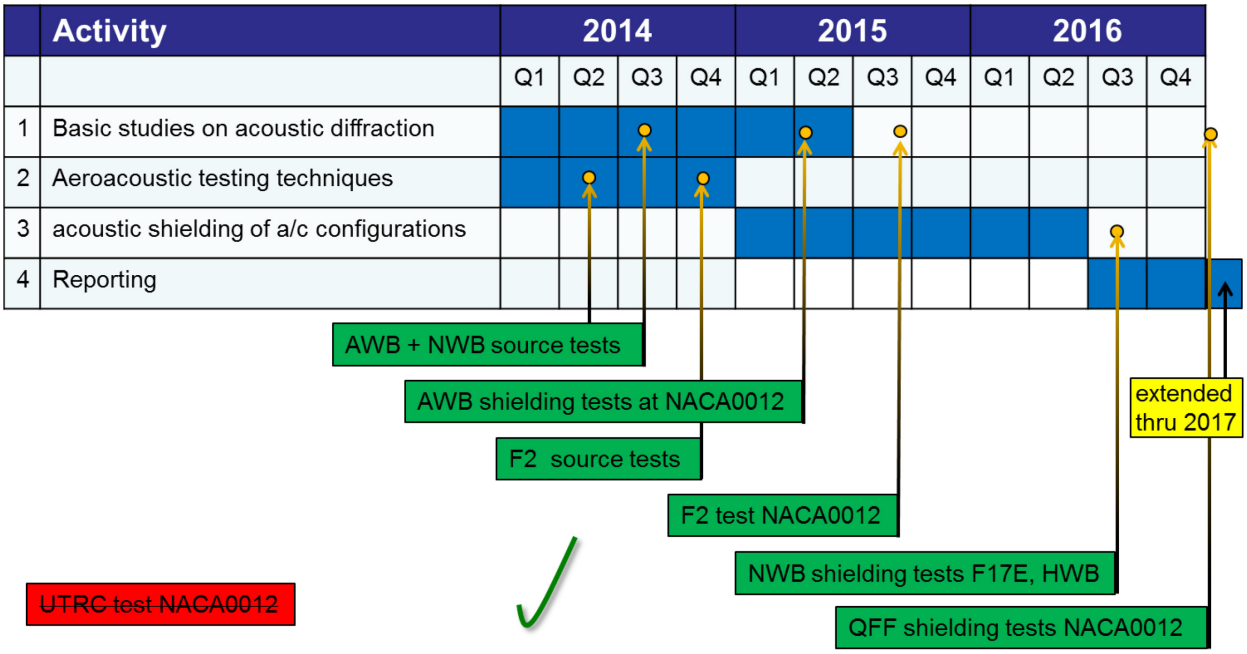

Figure 1-2: Main Work Packages of AVT-233 and Listing of Acoustic Wind Tunnel Campaigns (Green = Accomplished, Red = Not Accomplished), QFF Tests Occurred 03-05/2017.

1.5 OPERATION OF AVT-233

The RTG was initially led by Dr. Charlotte Whitfield, NASA, in cooperation with Dr. Jan Delfs, DLR. For about two years the mode of operation of collaboration was first of all based on monthly scheduled teleconferences. The group met regularly during the PBM meeting weeks at various places to discuss any issues/progress of ongoing work in more details, agree on refocusing of topics, make major decisions regarding the workflow, and on necessary next steps. Main decisions taken were to:

1) Put more emphasis on the development and analytical description of a generic pulse point-like acoustic test source, because this source would form the basis for all 2D and 3D test cases;
2) Put more emphasis on generic 2D studies to better support the understanding of complex flow-influenced diffraction as a very important preparational step to the 3D cases;
3) Use NACA0012 for the generic 2D studies;

4) As a result of (1), restrict the range of methods and number of cases in the 3D simulation tasks to a few only; and
5) Apply for a one year extension of the activity through 2017, because of delays due to unexpected complexities and temporal unavailability of scientific and technical personnel to accomplish the planned tasks, especially the completion of the experimental validation database.

Some fluctuation in the group membership occurred along its active period. Most notably, the acting co-chair from NASA retired in 2015 and had to be replaced. Moreover, in 2015, UTRC dropped out, because of retirement. The University of Mississippi left the group at the end of 2014 due to other obligations. In 2015 Uni Roma Tre, Italy joined the group, as well as Airbus Defence and Space, Germany/Spain in 2016. Finally, due to expressed interest, Dassault Aviation, France was invited to join the group, but ultimately did not participate.

Chapter 2 – AEROACOUSTIC TESTING TECHNIQUES

Jan W. Delfs
DLR – Institute of Aerodynamics and Flow
GERMANY

Karl-Stéphane Rossignol
DLR – Institute of Aerodynamics and Flow
GERMANY

Denis Gély
ONERA Département Aéroacoustique – DAAC
FRANCE

Russell H. Thomas
Langley Research Center, NASA
UNITED STATES

Florence Hutcheson
Langley Research Center, NASA
UNITED STATES

Christopher Bahr
Langley Research Center, NASA
UNITED STATES

Acoustic shielding tests in acoustic wind tunnels pose various challenges. First, it is necessary to use complete aircraft model geometries, which – due to space limitations in wind tunnels – leads to small scale models and thus measurements at very high frequencies. Special sensors have to be used and measuring out-of-flow may be difficult because of wind tunnel shear layer refraction and scattering of the sound signals. In-flow microphones are affected by self noise and will most likely be located in the geometric near field of the aircraft when the desired result is the far field sound shielding. Appropriate test sound sources are needed to provide reliable and well repeatable signals. The dimensions of the source should be as small as possible in order not to disturb the flow and/or the sound field itself, while simultaneously delivering a strong enough signal to be well above the background noise level. All of these issues need to be addressed and will be in the following sections on aeroacoustic testing techniques for shielding experiments.

2.1 AEROACOUSTIC TEST SOURCE

The appropriate test noise source is a key element to successful experimental shielding analysis. Two test source concepts were developed, implemented and employed in the acoustic shielding tests carried out in the frame of AVT-233. One source relies on the focusing of a laser beam by an appropriate lens system onto a focus in which a very short light pulse ignites a plasma and thus an acoustic pressure pulse. This concept is non-intrusive by nature and was developed by DLR and used in all four acoustic wind tunnel tests of the activity. The second source is based on an electric discharge between two electrodes, developed by ONERA is intrusive, but bears the advantage of providing a very strong signal so that decent signal-to-noise ratios may be achieved.

2.1.1 Laser Induced Acoustic Pulse

For the investigation of noise shielding properties of generic bodies or aircraft configurations it is necessary to utilize a reference sound source with known characteristics, i.e., directivity and spectral content. Such a source can be realized using a conventional loudspeaker or, as in Ref. [4], using customized pipe arrangements and pressurized air. The physical dimensions of these sources make their use in aeroacoustic investigations difficult because they interfere directly with the flow field and/or the acoustic field, thus adding perturbation to any acoustic measurement.

A laser-based (non-intrusive) pulsed sound source circumvents all of these inconveniences while providing a reference acoustic pressure wave of nearly uniform directivity and broadband spectral content. Because of its very short pulse duration, the generated sound wave also has the advantage of being easily separated from unwanted reflection. Furthermore, its characteristics can be derived directly from the solution of the acoustic wave equations, making its implementation in numerical simulation codes straightforward [2], [3], [5], [6], [7], [8], [9], [10].

2.1.1.1 Technical Concept and Realization of Acoustic Laser Source

By focusing a high energy laser beam to a point, i.e., an effective air volume, it is possible to initiate the formation of a small plasma which rapidly expands [11], [12] thus forming a pressure wave about its boundary which propagates through the surrounding medium (for illustration see Figure 2-1). From the convected wave (Equation (2-14)) for the pressure perturbation p' in a medium moving at uniform speed with a Mach number $M < 1$ and uniform mean density, the above phenomenon can be described in the following way:

$$p'(\boldsymbol{x},t) = \frac{(\gamma-1)(1-\mathrm{M}^2)}{4\pi a_\infty^2\left(\sqrt{(M\cdot r_0)^2+(1-M^2)r_0^2}\ -\boldsymbol{M}\cdot\boldsymbol{r}_0\right)}\frac{\partial\vartheta_p}{\partial\tau} \tag{2-1}$$

where all variables are to be evaluated at the retarded time τ which is related to the observer time t by:

$$t = \tau + \frac{1}{a_\infty(1-M^2)}\left\{-r_0\cdot M + \sqrt{(r_0\cdot M)^2+(1-M^2)r_0^2}\right\}. \tag{2-2}$$

In Equations (2-1) and (2-2), the distance $r_0(\tau)$ is the magnitude of the vector from source $\xi_0(\tau)$ to observer at $\boldsymbol{x}$, i.e., $r_0 := x - \xi_0$ at emission time τ. a_∞ represents the speed of sound, γ is the isentropic exponent and ϑ_p is the time history of the actual heat release at the (moving) source position. Equation (2-1) emphasizes the importance of the temporal heat input $(\partial\vartheta_p/\partial\tau)$ in generating a high amplitude pressure wave. Moreover, such a pressure wave does not exhibit any directionality for a medium at rest while featuring convective amplification in the direction of convection.

Figure 2-1: Laser Pulse Source Optical Arrangement and Optically Observed Pulse Position at DLR, (Left), Installation of Laser in AWB, (Centre), Preparation of Laser Source at NASA (Right).

To achieve plasma formation, a minimum amount of laser power or irradiance I in $\mathrm{W/cm^2}$ has to be provided into the medium to reach the breakdown threshold (I_t) for the initiation of plasma formation. Once I_t is reached, the plasma starts building up, and its temperature and density increase greatly while absorbing a large portion of the input laser beam energy [13], [14]. A theoretical description of the phenomenon is provided by the multiphoton ionization and cascaded ionization mechanisms [15]. In its early stage, the expanding plasma generates a pear-shaped pressure front with initial supersonic propagation speed which becomes an almost omnidirectional pressure wave in the far field [15], [16]. The initial shock wave slows down to the isentropic speed of sound after approximately $20\mu s$, at which point it propagates as an isentropic acoustic wave. Consequently, the small plasma generated can be seen as a breathing sphere with 10 mm radius [7]. The value of I_t is about$3.5\times10^{12}\mathrm{W/cm^2}$ for an irradiation of wavelength $\lambda = 532$ nm in air and at standard atmospheric pressure [17]. The breakdown threshold power is dependent on the type of gas, its pressure, the radiation wavelength, the duration of the laser pulse and its focusing conditions [15]. Most relevant for the current practical application, are the last two parameters.

The shape and volume of the plasma spot are strongly dependent on the angle with which the laser beam is focused. For a given input beam diameter, the longer the focal length, the longer the plasma spot will be along the beam axis. The same is also true for the minimum beam diameter achievable at the focal point. A formal description of these observations is given by the theory of Gaussian beams [18]. Even if the output beam profile of a Nd:YAG laser is not perfectly Gaussian, due to its multi-mode structure, a Gaussian beam approximation is still a good representation.

The parameters of a Gaussian beam in the waist region are given in Figure 2-2 (see also Ref. [18]).

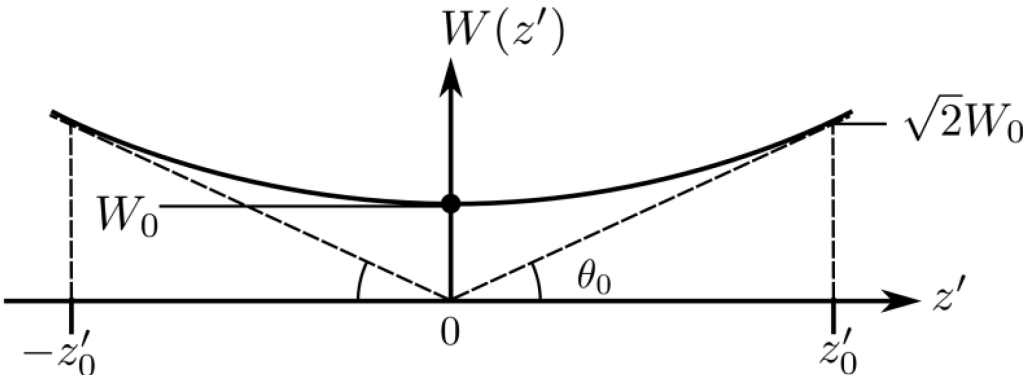

Figure 2-2: Gaussian Beam Parameters in the Waist Region. $W(z')$ is the Beam radius (where the intensity has dropped to $1/e^2$ of its on-axis value, i.e., 86% of the beam peak energy) vs. position z' along the beam axis. The minimum beam radius at $z' = 0$ is W_0. $W(z')$ increases linearly for large values of z' [16]}.

For an ideal Gaussian beam, the beam divergence is given by:

$$\theta_0 = \frac{2}{\pi}\frac{\lambda}{2W_0}. \tag{2-3}$$

The laser used in the present experiment has a nominal full-angle beam divergence of $2\theta_0 < 1$ mrad. Therefore, its beam waist radius is:

$$W_0 = \frac{2}{\pi}\frac{\lambda}{2\theta_0} = \frac{2}{\pi}\frac{532\times10^{-9}}{2(0.5\times10^{-3})} = 3.4\times10^{-4}\text{m}. \tag{2-4}$$

For a convex lens placed at the collimated beam waist, the resulting focused beam waist is:

$$W_0' \approx \frac{\lambda}{\pi W_0} f_L = \theta_0 f_L\,, \tag{2-5}$$

where $D = 2W_0$ and f_L is the lens focal length and

$$2\mathrm{W}_0' \approx \frac{4\lambda}{\pi}\mathrm{F}_{\#} \approx \frac{4\lambda}{\pi}\frac{\mathrm{f_L}}{\mathrm{D}}. \tag{2-6}$$

The depth of focus is given by:

$$2\,\mathrm{z}_0' = \frac{2\pi\,\mathrm{W}_0'^2}{\lambda} \tag{2-7}$$

with z_0' the Rayleigh length. From Equation (2-5), to ensure the highest possible energy densities, one needs to minimize $2W_0'$ by minimizing the ratio f_L/D. This can be achieved through a shorter f_L, by expanding the input beam, D, or a combination of both to effectively increase the focusing angle of the input beam.

In the present situation, a conventional Gemini double-cavity PIV laser from New Wave Research is used. This laser is capable of producing a stable maximum mean output power of 120 mJ with a pulse width of 3 – 5 ns at a repetition rate of up to 15 Hz. The laser is coupled to the appropriate optical components ensuring a maximum concentration of light energy into the focal point at the focal distance of interest. From the discussion above, this implies that the output beam of the laser has to be enlarged prior to focusing.

2.1.1.2 Transfer of Source from Small Scale Wind Tunnel to Large Scale Wind Tunnel

For the experiments in the DNW-NWB, larger focal lengths are required compared to those used in the AWB, i.e., $f_L = 500$ to 900 mm. A focal length of $f_L = 2000$ mm will allow the source to be positioned on the tunnel axis while keeping the optical components outside of the tunnel shear layer and therefore free of flow-induced disturbances. The practical implementation of an optical system with $f_L = 2000$ mm requires the use of large diameter optical components.

Using Equation (2-5), with I_t and $f_L = 2000$ mm, one finds that the breakdown threshold for plasma formation can be reached using a lens of aperture ≈ 50 mm placed in a collimated beam of equivalent diameter. In practice this result was found to be too optimistic. The formation of a plasma spot could, however, be observed but a consistent and repeatable spark could not be produced. Two aspects need consideration here; first according to the energy calculation above, the threshold for plasma formation is barely reached, and therefore, a stable plasma spot will only form when enough energy is provided in the laser output. Statistical variability of the laser output energy will inherently prevent a repeatable plasma build up. Furthermore, the beam focusing angle θ_0 will be small and the Rayleigh length z_0 correspondingly large, thus resulting in a spreading of the input beam energy over an increased volume. As a consequence, the actual location where the plasma spot forms will be unstable along the beam axis. Second, increasing the focusing lens diameter also increases the impact of lens aberrations, leading to a spreading, along the beam axis, of the focal volume and a consequent smearing of the available laser energy. This effect lowers the attainable power density in the focal region. To avoid these difficulties and make the realization of the laser-generated sound source for medium scale wind tunnels (in the range of the DNW-NWB) possible, a custom optical design was made.

The starting point is the preliminary optical design, where the fundamental properties, like working distance and lens diameters are used to set up a first layout of the optical system. This step is based on the Gaussian ray-tracing formulas described in this section. This calculation is based on the small angle approximation and is thus only valid for rays, which have a small angle with respect to the optical axis. In contrast, lens systems that incorporate more divergent ray cones do not apply to this approximation and thus have to deal with aberrations. These aberrations blur the spot formed by the optical system and degrade its performance. The most prominent are the third order monochromatic aberrations, called spherical aberration, coma, astigmatism and field curvature. For an on-axis collimated ray bundle, as it is the case in this setup, there is only spherical aberration present [19]. To evaluate aberrations of an optical system the software package Zemax is used [20]. With this software, one can perform a ray-tracing simulation and analyse the aberrations through various parameters. The optical designer can than judge the quality of a lens system. In addition to the ray-tracing mode, which does not take diffraction effects into account, there is also a physical optics mode. This mode will be used to evaluate the system in a later design stage [19].

In the preceding section, it is already described in Equation (2-6) that the size of the focused Gaussian beam is inversely proportional to the diameter of the focusing element. The waist of the $1/e^2$-diameter at the focusing lens can be calculated using Equation (2-6) with the properties of the laser and the threshold power density I_t needed to create a plasma spot.

$$2w_{spot} = \sqrt{\frac{4E_{laser}}{\pi t_{puls} I_t}} = \sqrt{\left(\frac{4 \cdot 120\text{mJ}}{\pi \cdot 5ns \cdot 3.5 \times 10^{12}\text{W/cm}^2}\right)} \tag{2-8}$$

$$D_{lens} = 2 \cdot w_{lens} = \frac{4 \cdot 532\text{nm}}{\pi} \cdot \frac{2000mm}{2 \cdot w_{spot}} \tag{2-9}$$

As the $1/e^2$-diameter covers 86% of the energy in the Gaussian beam, one needs to add a margin to avoid truncation, and it is common practice to add a factor of 1.5. By doing so only 1% of the beam energy will be truncated [21]. Also, a safety factor of 2 was chosen, in order to create a smaller spot and thus to generate a higher power density. The additional factors result in a focusing lens having a clear aperture of 140 mm.

To match the diameter of the collimated laser beam to the diameter of the focusing lens, the beam is spread by a negative lens. The whole setup is essentially a telescope where the second lens is slightly shifted to focus the beam. Figure 2-4 depicts the preliminary design consisting of two paraxial lenses, the first being negative followed by the positive focusing lens. The marginal ray represents the $1/e^2$-height at the laser output and has a $1/e^2$ waist diameter of 5 mm. As shown in Figure 2-3 this ray hits the focusing lens at the calculated diameter of 90 mm. The density of the rays is according to a Gaussian distribution. To avoid clipping of the beam, the negative lens is chosen to have a standard diameter of 25 mm. The focal length f_1 of the negative lens can be calculated using the intercept theorem with the following formula:

$$-f_1 = \frac{2 \cdot w_{laseroutput} \cdot d_1}{2 \cdot D_{1/e^2,\text{focusing lens}}} = \frac{2 \cdot 2.5\text{mm} \cdot 80\text{mm}}{90\text{mm}} \approx -50\text{mm}. \tag{2-10}$$

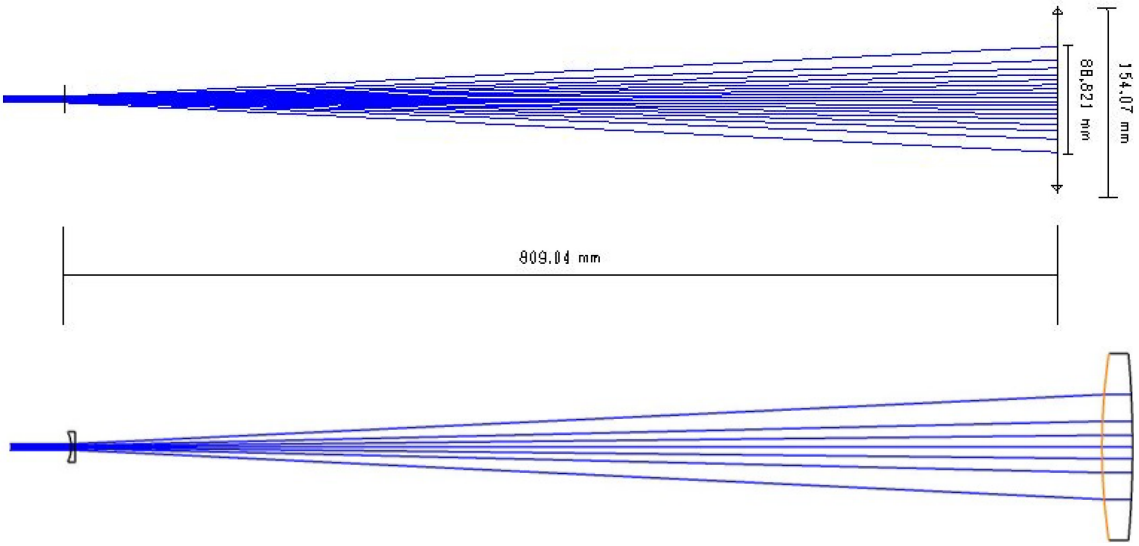

Figure 2-3: Optical Layout with Ray Paths. Above, ideal (thin lenses approximation) optimized setup. Below, actual setup, with one spherical component and one aspherical component.

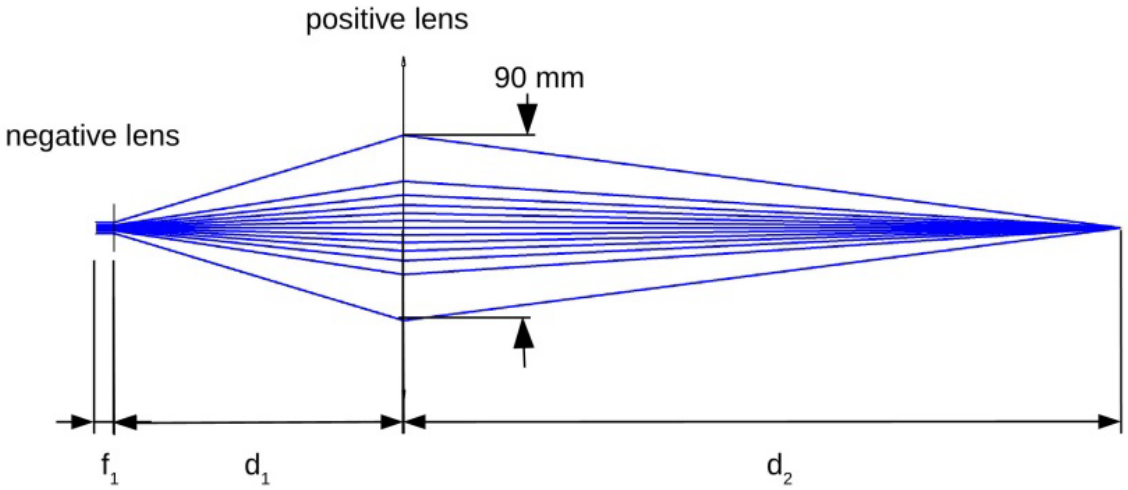

Figure 2-4: Paraxial Layout of the Optical System and Ray Paths (Not to Scale).

The distance d_1 between the two lenses was chosen 800 mm, so that it results in a focal length of $f = -50\text{mm}$. It is also possible to choose a narrower or wider distance between the lenses. In case of a smaller distance this would cause higher spherical aberration induced by the first lens due to steeper refraction angles. A wider distance might be limited by handling, alignment and available space in the wind tunnel. The focal length f_2 of the focusing lens can be calculated using the thin lens equation [22]:

$$f_2 = \left(\frac{1}{d_2} - \frac{1}{-d_1 - f_1}\right)^{-1} = \left(\frac{1}{2000\text{mm}} - \frac{1}{-800\text{mm} - 50\text{mm}}\right)^{-1} \approx 600\text{mm} \tag{2-11}$$

The next step is the design of the real lens system, where two different design approaches where chosen. For the first approach, the focusing element is considered to consist of three identical spherical lenses, while in the second approach, a single aspheric lens is used. Both systems use one single negative lens to diverge the laser beam followed by the focusing element. Going from a paraxial to a real system, the lenses where thickened and applied with a radius. Due to the high power density, the first lens is made from fused silica. With a lower power density present at the focusing element, this one is made from N-BK7. This is a standard glass, which is less expensive then fused silica. In an early stage, the design was targeted on the second approach incorporating one aspherical element. This is due to the fact that it showed a higher performance for a lower price at an early stage. An aspheric lens consists of one or two surfaces which are rotation symmetric but whose form differs from a sphere. An aspherical surface definition is already implemented in the optical design software as a standard surface and described by the following equation:

$$z(r) = \frac{cr^2}{1 + \sqrt{1 - (1 + k)c^2\, r^2}} + \sum_{i=1}^{8} \alpha_i r^{2 \cdot i}, \tag{2-12}$$

where r is the radial height, z is the sag measured from the vertex of the lens, c is the initial curvature at the vertex and k is the conical constant. Aspherical lenses are used to fully correct spherical aberrations and therefore increase the performance of a system dramatically using only one lens.

Figure 2-3 also shows the final simulated system with a total length of approximately 3 meters (overall dimension from the first lens to the focal point). The aspheric surface is depicted in orange. It was found during the design that the diffraction limited solution could be achieved while omitting the aspheric terms in Equation (2-12), using only the conic constant c as a variable. This makes the production of the aspheric lens again less costly.

As already mentioned, a pure tracing of rays does not include diffraction nor represent a real Gaussian beam. Therefore, the software is capable of performing a physical analysis of the optical system. The simulated power throughput is 99.5% yielding a power density of $8.6 \times 10^{12} \mathrm{W/cm^2}$ within the $1/e^2$-diameter of dimension $18\,\mu$m. This is more than twice the breakdown threshold power density I_t needed. This simulation does not take the reflection losses at the lenses into account, which would be around 16% in total for an uncoated system. Therefore, an AR coating is applied to the lenses after manufacturing. With this AR coating, the losses are minimized to 2% in total for the whole system.

The typical time trace of the laser-generated pressure waves, one meter away from the sound source, is shown in Figure 2-5(a). In Figure 2-5(b), the corresponding spectra are plotted. Although a focal length more than twice that of previous experiments is used, the quality of the optical setup is confirmed through an excellent repeatability of the generated pressure pulses (Figure 2-5a). In Figure 2-5a, a total count of 252 pulses is plotted along with a histogram of the maximum pulse amplitude, i.e., number of pulses vs. amplitude in Pascals. Similarly, in Figure 2-5(b), 252 spectra are shown along with the histogram of their respective Overall Sound Pressure Levels (OASPL). As in previous reports on laser-generated sound, [2], [3], [5] a high quality sound source can be obtained using the optical design described above.

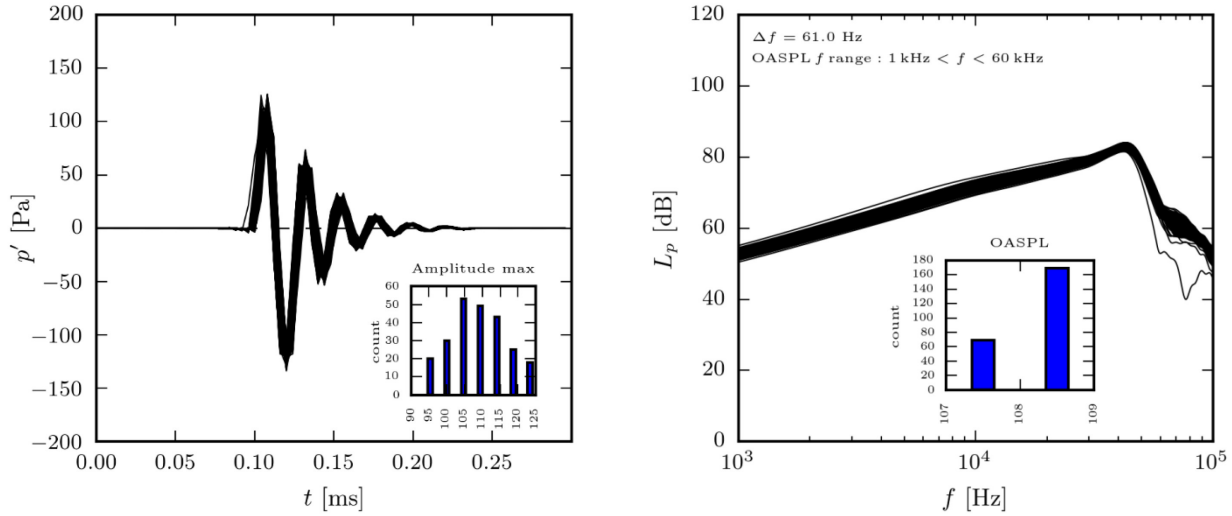

(a) Individual Time Traces. **(b) Individual Spectra.**

Figure 2-5: Repeatability of the Laser-Generated Pressure Waves.

2.1.1.3 Theoretical Description of Acoustic Laser Source

The laser sound source is modeled by a simple point heat source. The following physical picture of the source is drawn. By means of the laser light, electromagnetic power is concentrated on a tiny volume for a duration on the order of nanoseconds during which the ionization of the molecules starts. The subsequent highly nonlinear and rapidly transient complex chemical reactions of the air lead to the generation of heat in the zone where ionization took place, leading to rapid compressions and dilatations of the local air. The actual resulting pressure signal, in the far field, has a duration of about 0.1ms. The actual sound is considered to be generated by a heat release process in a very small air volume. This heat release being mechanical in nature takes orders of magnitude longer than the original application of the electromagnetic power.

In what follows the description of the laser pulse source is subdivided into three parts. In the first part, the overall analytical description of the pulse generated pressure field in a uniformly moving medium is developed. The purpose of the analytical description is to provide a simple means to use it as a source in the computation codes. However, no matter whether a time domain or a frequency domain code is used, it

may not be so simple to implement a moving pulse source. Therefore, in the second part (2.1.1.3.2) the moving source is represented as a Taylor series of point sources at a fixed position. In this representation, the higher order terms correct for the difference between a fixed and a moving point heat source, and consequently, all of these terms are proportional to powers of the flow speed. This, in turn, means that for vanishing speed the Taylor series collapses to only the zeroth order term ("monopole part"). This representation of the moving point heat source by a series of fixed point sources then easily allows for a representation in the frequency domain (in the third part (2.1.1.3.3)). This is of some importance since otherwise the implementation of a moving source would not be so simple in the frequency domain codes such as the fast multipole code used in Chapter 4.

2.1.1.3.1 Approach

Since the sound generation process takes place in a moving volume of air, one is actually dealing with a source originating from a heat release $\dot{\vartheta}'$ per unit volume in a small zone moving along with the flow. Modeled as being concentrated at a moving point, the specific heat release may be expressed as:

$$\dot{\vartheta}' = \delta(\xi - \xi_0(\tau))\vartheta_p(\tau), \tag{2-13}$$

where δ denotes the 3D delta function, ϑ_p the time history of the actual heat release and $\xi_0(\tau)$ the current position of the moving point, while ξ denotes the spatial dependence of the source. Since the observer is supposed to be attached to a fixed reference frame (not moving with the flow) the pressure field $p'(x,t)$ is governed by the convective wave equation for an ideal gas with a moving point heat release source:

$$\frac{1}{a_\infty^2}\frac{D_\infty^2 p'}{Dt^2} - \Delta p' = \frac{D_\infty \dot{\theta}'}{Dt}, \text{ with } \frac{D_\infty}{Dt} := \frac{\partial}{\partial t} + U_\infty \cdot \nabla \tag{2-14}$$

with the shorthand notation $\dot{\theta}' = \frac{\gamma-1}{a_\infty^2}\dot{\vartheta}'$ for the heat source, a_∞ representing the speed of sound, and γ the isentropic exponent. The solution of Equation (2-14) is (see, e.g., in Ref. [2])

$$p'(x,t) = \frac{(\gamma-1)(1-M^2)}{4\pi a_\infty^2\left(\sqrt{(\boldsymbol{M}\cdot r_0)^2 + (1-M^2)r_0^2} - \boldsymbol{M}\cdot r_0\right)}\frac{\partial \vartheta_p}{\partial \tau} = \frac{\gamma-1}{4\pi a_\infty^2 r_0^+}\frac{\partial \vartheta_p}{\partial \tau} \tag{2-15}$$

where all variables are to be evaluated at the retarded time τ, which is related to the observer time t by:

$$t = \tau + \frac{1}{a_\infty(1-M^2)}\left\{-r_0\cdot\boldsymbol{M} + \sqrt{(r_0\cdot\boldsymbol{M})^2 + (1-M^2)r_0}\right\}. \tag{2-16}$$

In Equations (2-15) and (2-16), the distance $r_0(\tau)$ is the magnitude of the vector from source $\xi_0(\tau)$ to observer $r_0 := x - \xi_0$ at emission time τ, see also Figure 2-6. $M = |M|$ with $M = U_\infty/a_\infty$ is the acoustic Mach number. The right hand side of Equation (2-15) expresses the solution in terms of $r^+ = r^+(r_0)$ which according to Equation (2-16) is the actual distance traveled by the signal with respect to the medium at the moment of reception. Expressed with this distance, the solution assumes the form of a simple monopole in a non-moving medium. Indeed, the right hand side of Equation (2-15) is nothing but the solution of a simple monopole convected along with the medium. Therefore, measured in r^+ (or a co-moving observer respectively) the pressure field Equation (2-15) does not contain any near field term which a fixed point source in a flow would. This conclusion is directly supported by the experimental evidence (see Ref. [3]).

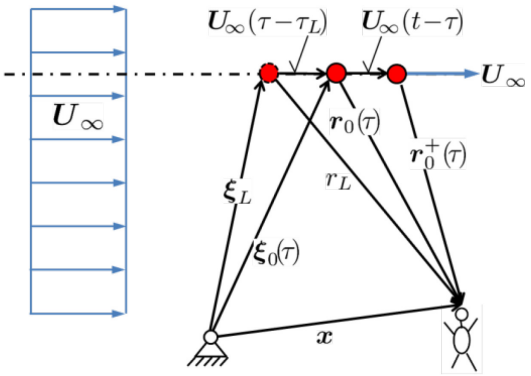

Figure 2-6: Sketch of a Convecting Point Source in a Medium Moving at U_∞; r_0 is the Distance of the Sound Source to the Observer at Emission Time τ.

Since the source is assumed to move with constant speed U_∞, one may describe the distance vector more explicitly. The position at which the laser applies its energy into the source point is denoted ξ_L (see Figure 2-6), which is independent of time. The corresponding moment of laser ignition is defined to be $\tau = \tau_L$. Then one may express the time history of the source point $\xi_0(\tau) = \xi_L + U_\infty(\tau - \tau_L)$. Now the distance vector $r_L = x - \xi_L$ pointing from laser ignition point to observer position is introduced, which represents the actual wind tunnel situation, where the microphone positions are also measured with respect to the laser ignition point ξ_L. Then the instantaneous distance vector r_0 relates as $r_0 = r_L - U_\infty(\tau - \tau_L)$. Figure 2-6 suggests the vector triangle:

$$r_0^+ = r_0 - U_\infty(t - \tau) \tag{2-17}$$

while $r_0^+ = a_\infty(t - \tau)$, which may be combined to eliminate r_0^+ and finally yield the dependence of the emission time τ on the observer time t:

$$\tau = t - \left|\frac{\boldsymbol{r_L}}{a_\infty} - \boldsymbol{M}(t - \tau_L)\right|, \tag{2-18}$$

(note $\boldsymbol{r\_L}$ and $\boldsymbol{M}$ are vectors). Clearly, compared to a source at rest, the pressure field (Equation (2-15)) shows a convection factor:

$$C := \frac{(1 - M^2)r_0}{\sqrt{(M \cdot r_0)^2 + (1 - M^2)r_0^2} - M \cdot r_0}, \tag{2-19}$$

suggesting an amplification for downstream microphones and damping for upstream microphones. In particular, a microphone located exactly downstream of the pulse source, such that $M \cdot r_0 = Mr_0$ yields a convective amplification of $C = 1 + M$, while for a microphone exactly upstream the position of the pulse source, where $M \cdot r_0 = -Mr_0$, one obtains an amplitude reduction of $C = 1 - M$. Turning to the frequency shift expected for a source in relative motion with respect to the observer, the frequency f, as sensed by the observer, may be determined like:

$$f = \frac{\partial p'}{\partial t}\frac{1}{p'} = \frac{d\tau}{dt}\frac{\partial p'}{\partial \tau}\frac{1}{p'} = \frac{d\tau}{dt} f_0 \tag{2-20}$$

where f_0 denotes the frequency of the source. Differentiation of Equation 2-16 or 2-18 yields the Doppler frequency shift:

$$D := \frac{f}{f_0} = \frac{d\tau}{dt} = \frac{(1-M^2)\sqrt{(\boldsymbol{M}\cdot\boldsymbol{r}_0^2)+(1-M^2)r_0^2}}{\sqrt{(\boldsymbol{M}\cdot\boldsymbol{r}_0)^2+(1-M^2)r_0^2}-\boldsymbol{M}\cdot\boldsymbol{r}_0} = 1+\frac{\boldsymbol{M}\cdot\boldsymbol{r}_L/a_\infty - M^2(t-\tau_L)}{|r_L/a_\infty - M(t-\tau_L)|} \tag{2-21}$$

which suggests that for downstream microphones, the signal appears at a higher frequency, upstream microphones instead sense a lower frequency compared to the source frequency. In particular, for a microphone located exactly downstream of the source pulse one obtains $M\cdot r_{0,L} = Mr_{0,L}$ and hence a Doppler factor of $D = 1 + M$, while for a microphone exactly upstream of the source, for which $M\cdot r_{0,L} = -Mr_{0,L}$ the Doppler factor is accordingly $D = 1 - M$.

2.1.1.3.2 Compactness of Moving Point Source / Fixed Point Source Representation

In the next step the source model may be used to determine the acoustically relevant heat release function $\vartheta_p(\tau)$ from the measured pressure fluctuation $p'(x,t)$ at some reception point x, far enough from the source point, such that any nonlinear effects are negligible. One has to recall that the received pressure signal $p'(t)$ has a duration of about $T_s = 0.1$ milliseconds. Therefore, it is reasonable to assume that the source is active for about the same period. This in turn means that during its operation the moving source volume of air has been moving downstream by about $l \approx 6\,\mathrm{mm}$, assuming a flow speed of $60\,\mathrm{m/s}$. Therefore, the actual ''length'' of the source is in this case on the same order. Sound waves with frequencies below about $f_0 \approx 28\,\mathrm{kHz}$ have a wavelength larger than about twice this source length and therefore may be considered a compact source. On the other hand, for the higher frequencies, the laser point source may be a non-compact source (depending on the flow speed).

For the consideration of the compactness of the source it is useful to think of it as of being produced by an equivalent nonmoving point source at position ξ_0^*. This is of interest also in view of its usage as a test source, sufficiently simple to describe for computational methods. The position of the fixed point source ξ_0^* is usefully chosen to lie on the trajectory of the actual point source sometime during the period of its activity T_s. For convenience we choose ξ_0^* equal to the actual (moving) source position after half of T_s, i.e.:

$$\xi_0^* = \xi_0\left(\tau = \tau_L + \frac{1}{2}T_s\right) = \xi_L + \frac{1}{2}U_\infty T_s \tag{2-22}$$

The delta function, describing the motion of the source in Equation (2-13) may now be written in terms of ξ_0^*:

$$\delta\big(\xi - \xi_0(\tau)\big) = \delta\big(\xi - \xi_0^* - U_\infty(\tau-\tau^*)\big) \text{ with } \tau^* = \tau_L + \frac{1}{2}T_s. \tag{2-23}$$

In a series representation this translates to:

$$\delta\big(\xi - \xi_0(\tau)\big) = \delta(\xi-\xi_0^*) - U_\infty\cdot(\nabla\delta)_{\tau^*}(\tau-\tau^*) + \frac{1}{2}U_\infty U_\infty : (\nabla\nabla\delta)_{\tau^*}(\tau-\tau^*)^2 - \cdots \tag{2-24}$$

Substitution in Equations (2-13) and (2-14) finally yields:

$$\frac{D_\infty}{D\tau}\left[\delta\left(\xi-\xi_0(\tau)\right)\,\theta_p\right] = \frac{D_\infty}{D\tau}\left[\delta\left(\xi-\xi_0^*\right)\theta_p\right] - \nabla\cdot\left(U_\infty\frac{\partial(\tau-\tau^*)\theta_p}{\partial\tau}\,\delta\right) + \\ +\nabla\cdot\nabla\cdot\left(\frac{1}{2}\mathrm{U}_\infty\mathrm{U}_\infty(\tau-\tau^*)^2\frac{\partial\theta_p}{\partial\tau}\delta\right)-\cdots, \tag{2-25}$$

with the abbreviation:

$$\theta_p := \frac{\gamma-1}{a_\infty^2}\vartheta_p\,. \tag{2-26}$$

For the interpretation of the terms in this Taylor expansion it is useful to introduce the following quantities for convenience:

$$\dot{\theta}' := \delta\left(\xi-\xi_0(\tau)\right)\,\theta_p, \tag{2-27}$$

$$\dot{\theta}'^* := \delta\left(\xi-\xi_0^*\right)\theta_p, \tag{2-28}$$

$$\boldsymbol{\nabla}\cdot\boldsymbol{f}'^* := \nabla\cdot\left(U_\infty\frac{\partial(\tau-\tau^*)\theta_p}{\partial\tau}\,\delta\right) - \nabla\cdot\nabla\cdot\left(\frac{1}{2}\mathrm{U}_\infty\mathrm{U}_\infty(\tau-\tau^*)^2\frac{\partial\theta_p}{\partial\tau}\delta\right)-\cdots \tag{2-29}$$

This form of the source is similar to a multipole expansion, and it shows that the moving point source may be expressed as a fixed point source with the same strength along with higher order poles correcting for the neglect of the source motion. The correction of these higher order terms depends on the period, during which the source is active. This period is on the order T_s, and if the flow Mach number is small, the characteristic length scale of the source $T_s U_\infty$ is small compared to a wavelength of the radiated sound pressure. The above equation suggests that the first correction term is a point dipole of strength $U_\infty\frac{\partial}{\partial\tau}\left[(\tau-\tau^*)\vartheta_p\right]$ colocated with the leading order monopole term and directed parallel to the flow. When used as a source in the Linearized Euler Equations, the heat release function ϑ_p itself appears in the right hand side of the pressure equation. The higher order correction terms appear as an equivalent point force density on the right hand side of the momentum equation as:

$$f'^*(\xi,\tau) = \frac{\partial}{\partial\tau}\left[(\tau-\tau^*)\theta_p\right]U_\infty\delta(\xi-\xi_0^*) - \nabla\cdot\left((\tau-\tau^*)^2\frac{\partial\theta_p}{\partial\tau}\frac{1}{2}U_\infty U_\infty\delta(\xi-\xi_0^*)\right)+\ldots\,. \tag{2-30}$$

with the virtual point force:

$$f_p(\tau) := \frac{\partial}{\partial\tau}\left[(\tau-\tau^*)\vartheta_p\right]U_\infty \tag{2-31}$$

and a virtual point stress:

$$T_p(\tau) := (\tau-\tau^*)^2\frac{\partial\theta_p}{\partial\tau}\,\frac{1}{2}U_\infty U_\infty. \tag{2-32}$$

As may be inferred from Equations (2-30) – (2-32), the point force density f'^* (including all higher order terms) points in the direction of the flow. The analytical solutions of the contribution of the point force f_p in uniform flow (dipole) and that for the point stress T_p (quadrupole) are given in Ref. [3]. An explicit expression for all the higher order terms is given in Ref. [3].

In order to illustrate the mapping of the moving point source to its fixed point source representation, a Gaussian heat release function $\vartheta_p = P \exp\left[-\ln 2\,(\tau - \tau_L - 3\tau_h)^2\,\tau_h^{-2}\right]$ is considered, where τ_h represents the half width of the Gaussian pulse and P is the power of the source. The moment of laser ignition at ξ_L is chosen to be $\tau_L = 0$. The fixed source point is chosen to be at the position ξ_0^*, where the Gaussian assumes its maximum, such that $T_s = 6\tau_h$ appears as a reasonable duration of source activity. The pressure field (Equation (2-15)) is evaluated for a certain reception time t and depicted in Figure 2-7. While Figure 2-7(a) shows the exact field (Equation (2-15) of the heat pulse, Figure 2-7(b) and Figure 2-7(c) represent the contributions of the monopole and dipole part of the fixed point source, respectively. Figure 2-7(d) finally depicts the monopole part corrected with the dipole part. As expected (and opposed to the exact solution), the field of a nonmoving point heat release source (Figure 2-7(b)) displays convective amplification against the flow direction along with a compression of the signal against the flow direction and a stretching of the signal in the flow direction. If the dipole part, Figure 2-7(c), of the fixed source point representation is added to this field, most of the exact signal is retrieved, evidenced by Figure 2-7(d). Taking into account even higher order contributions like the quadrupole, etc., would entirely reconstruct the original field of the moving point source.

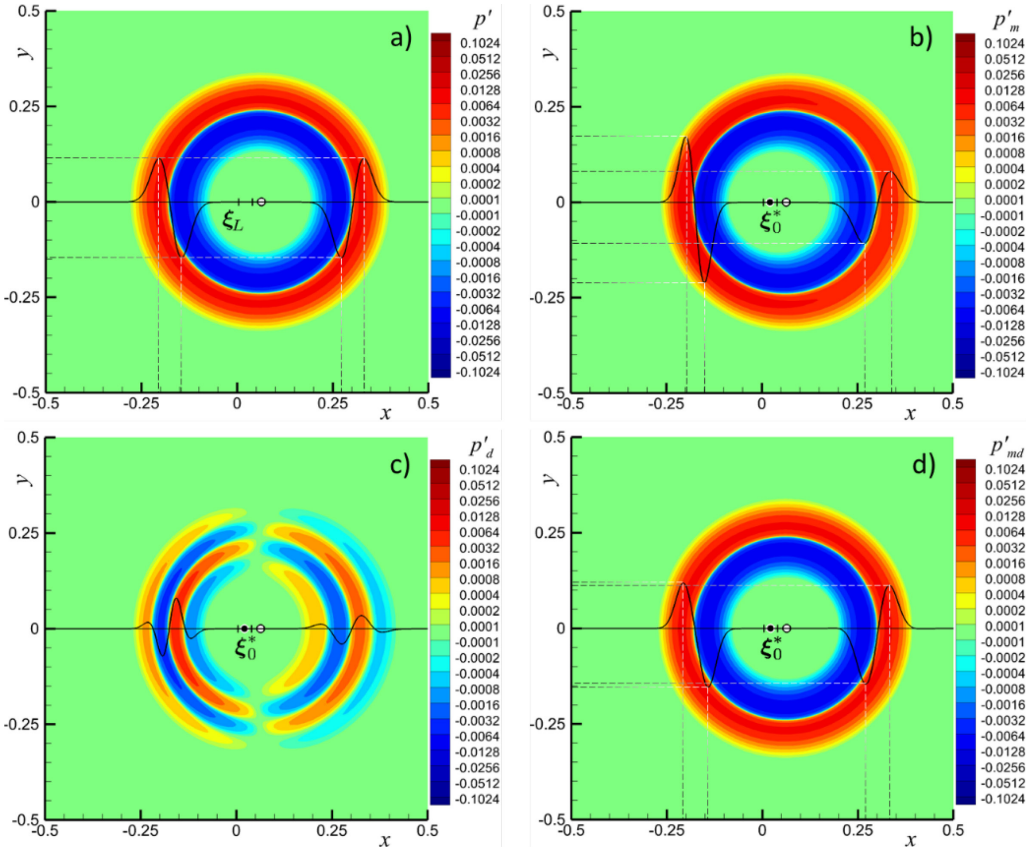

Figure 2-7: Sound Pressure Field at Reception Time $t = 10^{-3}$s for a Gaussian Heat Release Pulse with $\tau_h = 10^{-4}$s and Unit Power $P = 1$W, Generated by a Laser Pulse at $\xi_l = (0, 0, 0)$m. Speed of sound $a_\infty = 341.25$ m/s, flow $U_\infty = (60, 0, 0)$ m/s, distance in m. (a) Field of moving source according to Equation (2-15), (b) Field of monopole contribution of related source at fixed position at $\xi_0^* = (0.018, 0, 0)$ m, (c) Field of dipole contribution of related fixed source, (d) Addition of (b) and (c).

2.1.1.3.3 Frequency Domain Representation of Moving Point Source

Having expressed the moving point source in terms of an equivalent fixed point source in the preceding Section 2.1.1.3.2, it is now straight forward to describe the source in the frequency domain by simply

Fourier-transforming (Equation (2-25)). Defining the Fourier transformation of a function $h'(t)$ like $\hat{h} := \int_{-\infty}^{\infty} h' \exp(-i\omega\tau)\, d\tau$ one obtains:

$$\hat{\theta}^* := \int_{-\infty}^{\infty} \dot{\theta}'^* \exp(-i\omega\tau) d\tau = \hat{\theta}_p \delta(\xi - \xi_0^*) \tag{2-33}$$

$$\begin{aligned} \hat{f}^* &:= \int_{-\infty}^{\infty} f'^* \exp(-i\omega\tau) d\tau \\ &= -U_\infty \exp(-i\omega\tau^*)\omega \frac{\partial}{\partial\omega}\left[\exp(i\omega\tau^*)\,\hat{\theta}_p\right]\delta - \\ &\quad \nabla\cdot\left(\frac{1}{2}U_\infty U_\infty \exp(-i\omega\tau^*)\frac{\partial}{\partial\omega}\left[\exp(i\omega\tau^*)\,\omega\,\hat{\theta}_p\right]\delta\right) + \cdots, \end{aligned} \tag{2-34}$$

with the first term on the RHS of Equation (2-34) defined as $\hat{f}_p(\omega)$ and the expression in the divergence of the second term as $\hat{T}_p(\omega)$. The higher order terms of this spectral representation of the moving point heat release source are given in Ref. [3].

The frequency representation of the pressure pulse is depicted in Figure 2-8 for three different flow speeds. The center column in this figure corresponds to the parameter of the pulse shown in Figure 2-7. Figure 2-8 shows a polar plot of the frequency spectrum, i.e., the spectra radiated in the various directions. For increasing flow speed one can clearly see that (i) the spectra increasingly differ along the polar angle and (ii) the dipole correction to the representation of the source as a fixed monopole becomes more important.

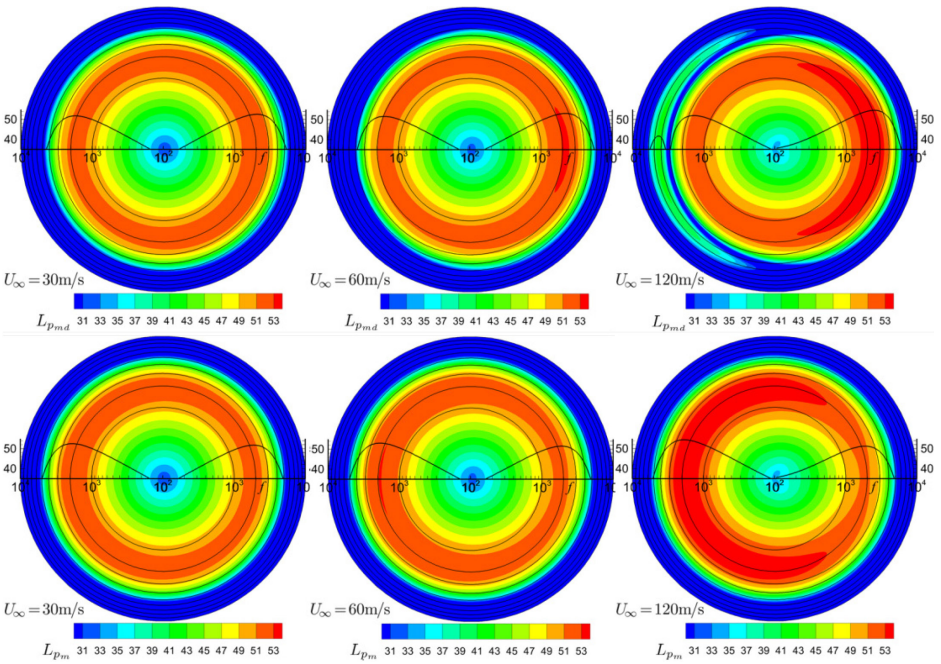

Figure 2-8: Frequency Representation of Pressure Pulse from Moving Point Heat Source at Flow Speed 30, 60, and 120 m/s (Flow from the Left). Top row: "complete" = monopole + dipole representation of source, bottom row: only monopole contribution. Parameters as in Figure 2-7 for the case 60 m/s (center column).

The complexity of this moving source represented in the frequency domain may be understood when considering a fixed frequency in Figure 2-8, as one would do in a spectral domain wave equation solver.

Evaluating the amplitude and phase along a circle in the spectral domain polar plots of this figure allows one to plot a snapshot of the wave field for this respectively selected frequency. Figure 2-9 shows this situation for a flow speed of 60 m/s, taken from the data of Figure 2-8 at two selected frequencies of 1 kHz and 3 kHz. These frequencies characterize wave field contributions on either side of the level maximum in the downstream direction as seen in Figure 2-8. Clearly, Figure 2-9 shows that these two wave fields behave qualitatively different: the low frequency component features a convective amplification in the upstream direction, while the high frequency component radiates larger amplitudes in the downstream direction. Obviously, the significance of dipole correction increases with frequency (reflecting the fact that with higher frequencies non-compactness effects occur). This shows that the spectral domain representation of the moving point source is non-trivial and care must be taken when implementing the source into a spectral domain code.

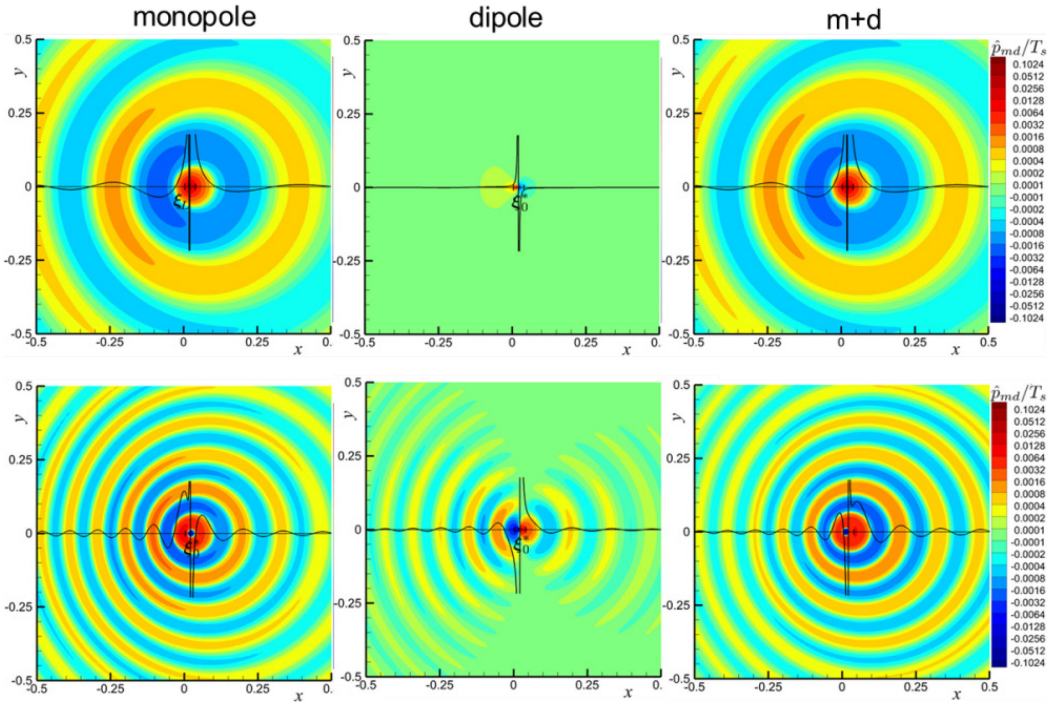

Figure 2-9: Instantaneous Wave Fields of Frequency Domain Representation of Pressure Pulse from Moving Point Heat Source at Flow Speed 60 m/s (Flow from the Left). Top row: 1 kHz, bottom row: 3 kHz. Right column = "complete" monopole + dipole contribution. Parameters as in Figure 2-7.

2.1.2 SPARC-Induced Acoustic Pulse

In 2009, ONERA started to develop an acoustic punctual source in order to provide the most powerful acoustic energy in the smallest volume [23]. The main goal is to provide very high sound pressure levels in the far field for calibration of microphones and pressure sensors during experimental tests in anechoic rooms or in wind tunnels.

2.1.2.1 Technical Concept and Realization of Acoustic Laser Source

The SPARC source (Source imPulsionnelle AeRoaCoustique) is based on electrical discharge by creating a difference of potential between two electrodes. A strong electric field is created which ionizes the air between these electrodes. The local air being ionized becomes conductive, and the local air volume conducts strong electric current that drives a significant increase in local temperature. This heating is accompanied by

a dilation of the volume of air between the two electrodes, dilatation immediately followed by a contraction. This phenomenon results in a fluctuation of the local density which leads to the emission of a high level acoustic wave in all directions. This acoustic pulse generates a famous N-wave. A prototype of the SPARC source is shown in Figure 2-10.

Figure 2-10: Prototype of SPARC.

Two major technical issues have been overcome. On the one hand, the capacity loads have to be realized rapidly (less than 100 milliseconds), and the switching for the discharge must be synchronized to reach a frequency of the order of 10 Hz. On the other hand, each discharge must be executed in a very short time (from 0.1 to 100 microseconds) for relatively high current and voltage levels. Typically, the order of magnitude is several hundred Ampere in intensity and several tens of thousands of Volts in voltage (30 kV).

Between 2010 and 2013, several modifications were made to the prototype to improve performance, to mitigate the volume of the device and to adapt the design for configuration in flow. The main evolution consists in fitting the electrodes into a fairing with a profiled support. The validation of tests in flow was mainly conducted in the ONERA anechoic wind tunnel CEPRA19 (Figure 2-11).

After these tests, several additional modifications were made to the SPARC source in order to improve its performance and to provide the most effective use for experiments in the wind tunnels:

- Integration of all the elements in a mobile bay;
- Selection of new capacitor for a maximum efficient charge;
- Improvement of the electromagnetic shielding;
- Improvement of the trigger commands;
- Optimization of the electrical connection adapted to high voltage;
- Optimization of the shape in flow;
- Improvement of the stability of the energy for each pulse; and
- Improvement of the reproducibility of the signal runs.

The SPARC source was implemented in several wind tunnels such as F1 – ONERA, Toulouse and LLF – DNW, the Netherlands (Figure 2-12) before being used in F2 – ONERA, Toulouse for the specific NATO test campaigns.

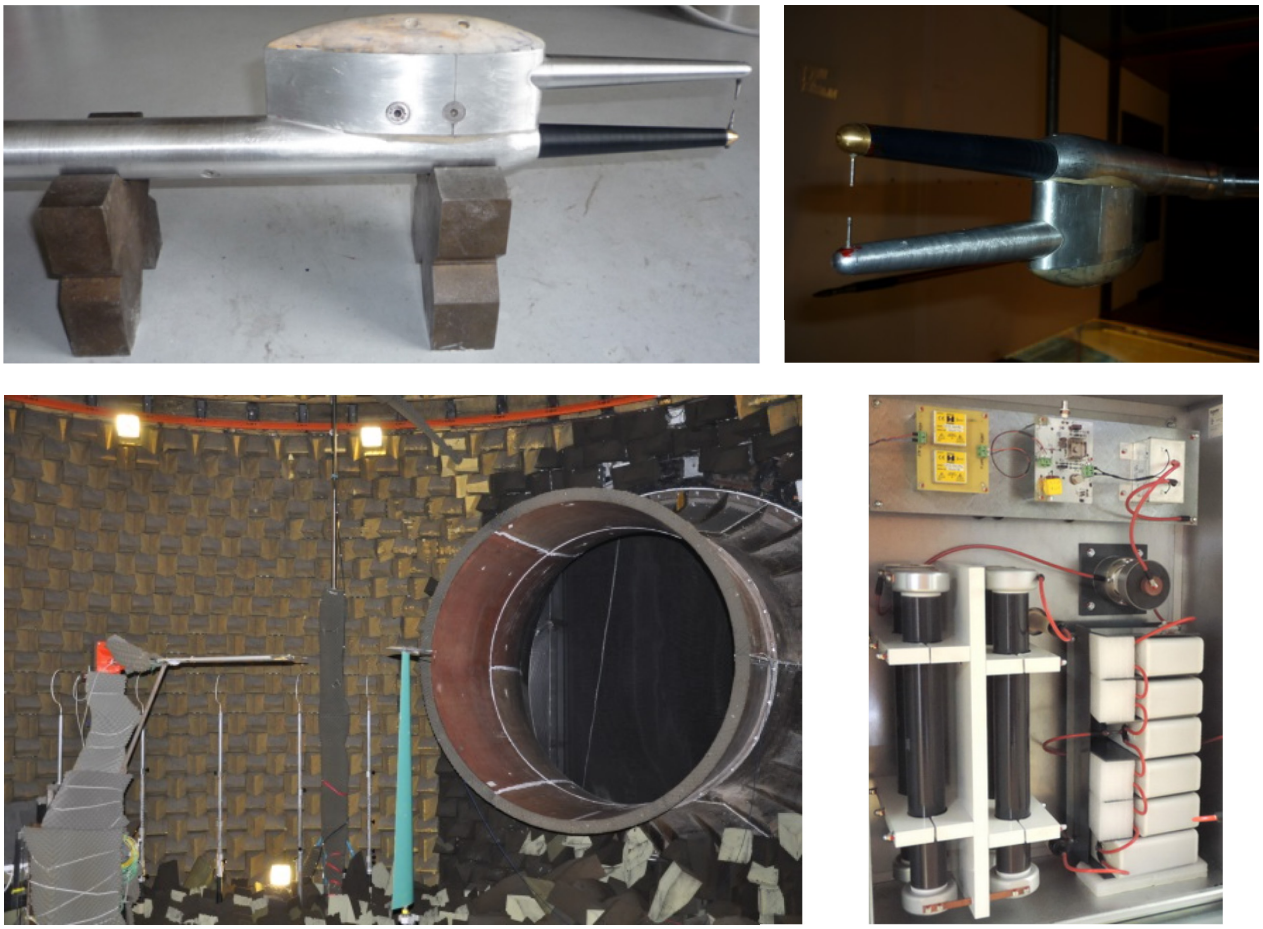

Figure 2-11: SPARC Source in CEPRA19 for Characterization Tests in Flow.

Figure 2-12: SPARC Source in F1 Aerodynamic WT and in LLF Anechoic WT.

In 2014, additional tests were carried out to test the new profiled SPARC source characteristics in static conditions and in flow as well, to provide a complete database for NATO activities.

First, the characterization was made in an anechoic chamber to verify the N-wave shape of the burst and the propagation (Figure 2-13).

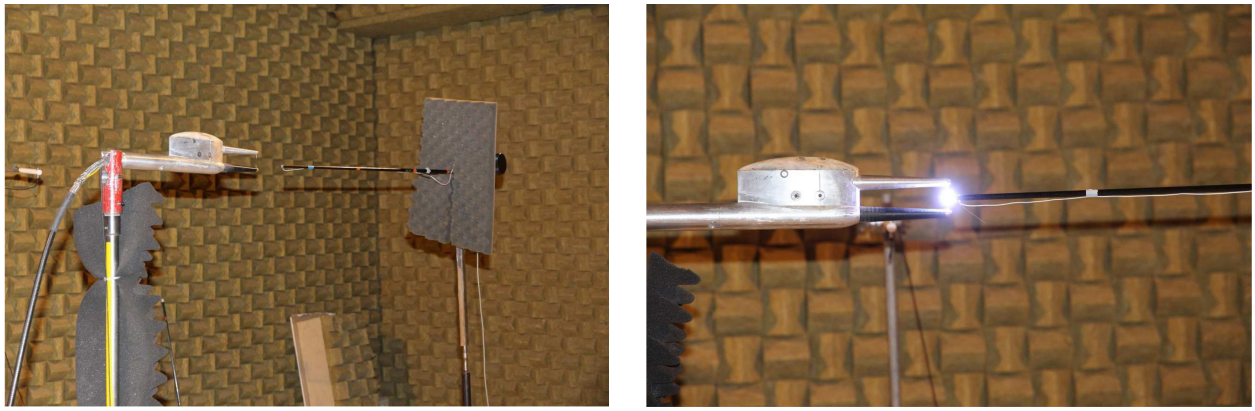

Figure 2-13: SPARC Source in Anechoic Chamber. Static Test.

Figure 2-14 shows the isolated pulse signal which is more than 500 Pa in amplitude (peak to peak), less than 100 microseconds in duration. The burst of waves is able to run more than 1 minute and produce several hundred N-waves. Generally, one makes a synchronized time-average on 300 blocks, which corresponds to 30 seconds duration signal for each run (rate of the pulse 10 Hz).

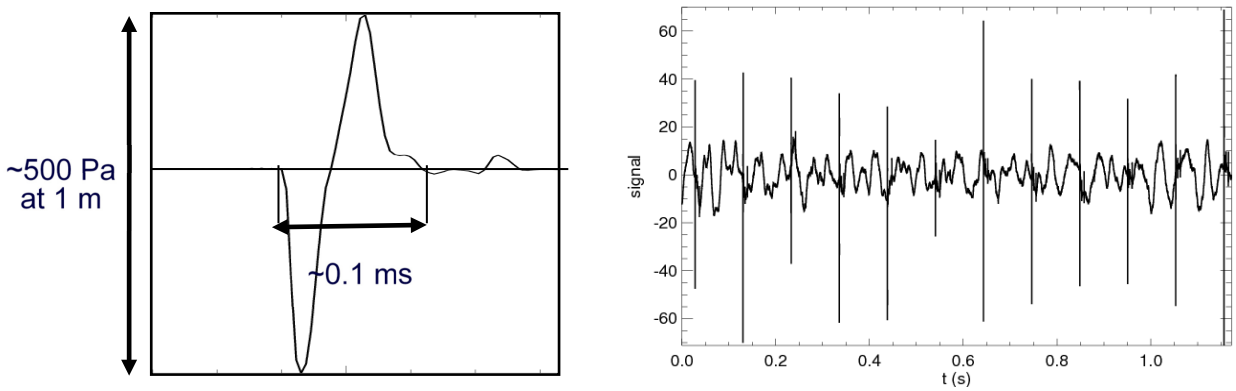

Figure 2-14: N-Wave Generated by the SPARC Source (Isolated and Burst of Waves).

In October 2014, a preliminary test campaign was carried out in F2 to implement the SPARC source and verify its behaviour in the presence of a single plate.

The signal pressure was then recorded by a microphone fitted at several distances from the SPARC source ranging from 20 mm to 200 mm in order to verify the sound pressure level available during the free field propagation. Figure 2-15 shows that one obtains very a high level of more than 160 dB at the farthest distance. Nevertheless, the closest distance between the source and the microphone one can obtain was no less than 50 mm. Close to the source the sound pressure level was so high that it induced an overload of the microphone. This is an issue for the further shielding tests in the presence of the model because one needs to fit the acoustic source as close as possible to measure accurately the shielding effects.

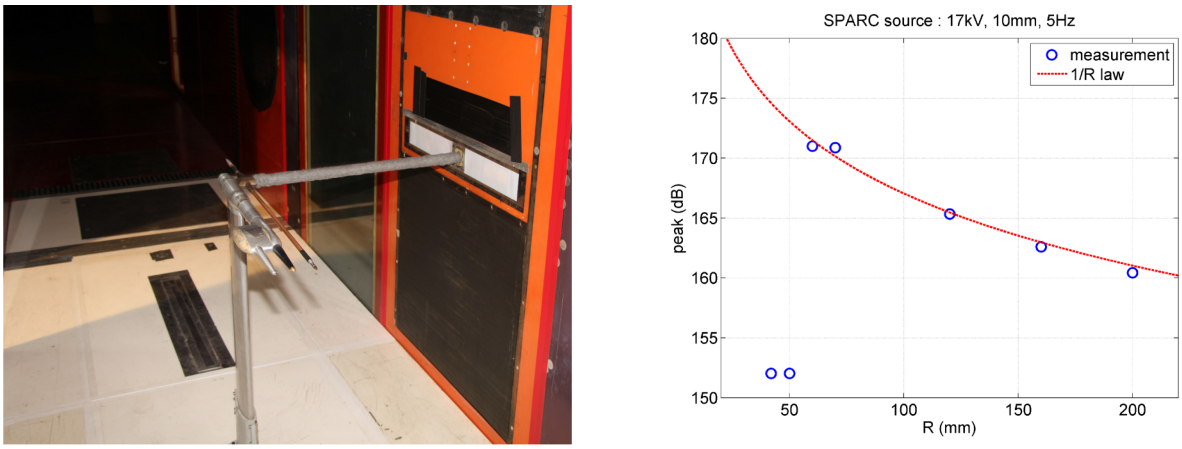

Figure 2-15: SPARC Source in F2 for Preliminary Tests.

In February 2015, a second test campaign was performed in F2. In order to avoid the microphone overload, Kulite sensors were implemented, which are less sensitive. The voltage was tested from 15 to 30 kV and the electrodes gap was adjusted from 5 mm to 15 mm. Regarding the voltage, one observed some electromagnetic perturbations on measurements and acquisition devices for the highest value 30 kV. So, the voltage was limited to 20 kV with a gap of 10 mm between the two electrodes (Figure 2-16).

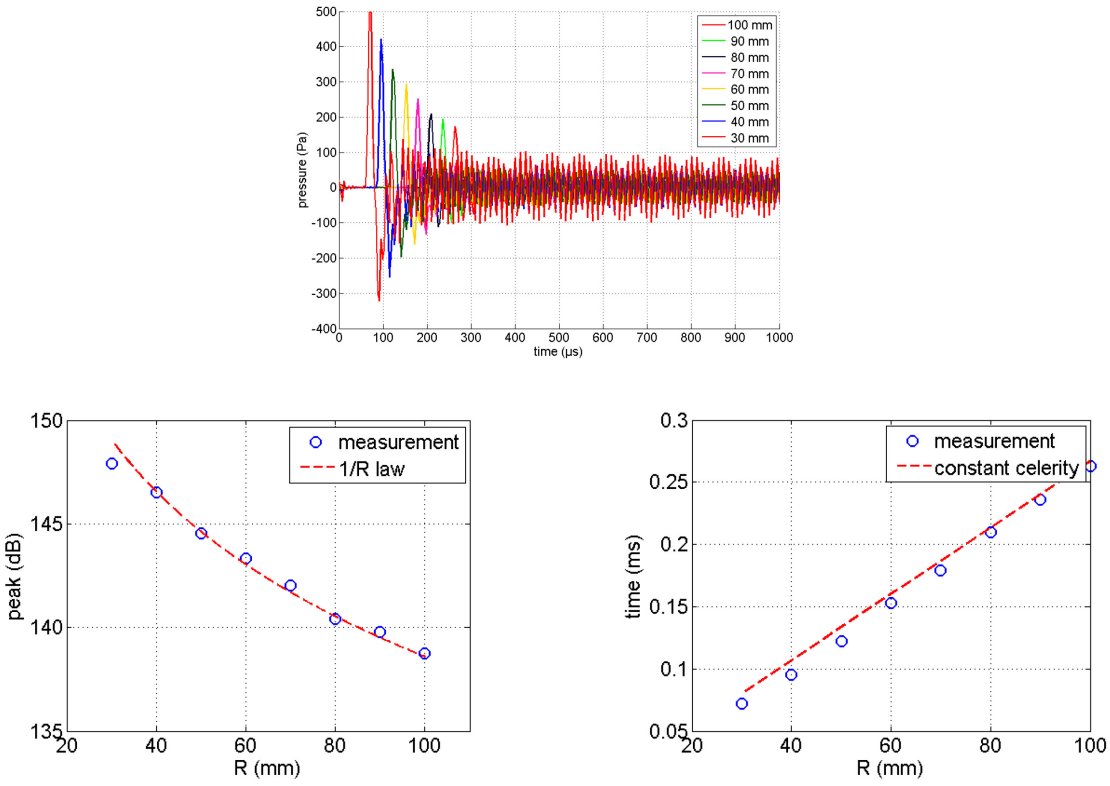

Figure 2-16: SPARC Source Free Field Characteristics.

Despite an internal resonance of the Kulite sensor due to high levels and the impulsive nature of the source, it has been demonstrated that the propagation is linear at least from a distance 30mm from the source.

Unfortunately, it was not possible to make measurements closer because the condenser discharge appears directly on the sensor and not between the electrodes. The results obtained are given on Figure 2-16. One can observe a very good agreement between the measurement and the classic 1 /R law, which confirms a linear propagation.

The directivity diagrams were obtained for several flow velocities up to Mach = 0.18 (Figure 2-17). The plotted results show a very good omnidirectional behaviour up to 2 kHz. Beyond 4 kHz, the shear layer effect induces modification of the propagation in the far field. The discrepancy between static and in-flow conditions may reach 10 dB as shown in the figure below. Meanwhile, the power spectral density is not significantly modified by the flow.

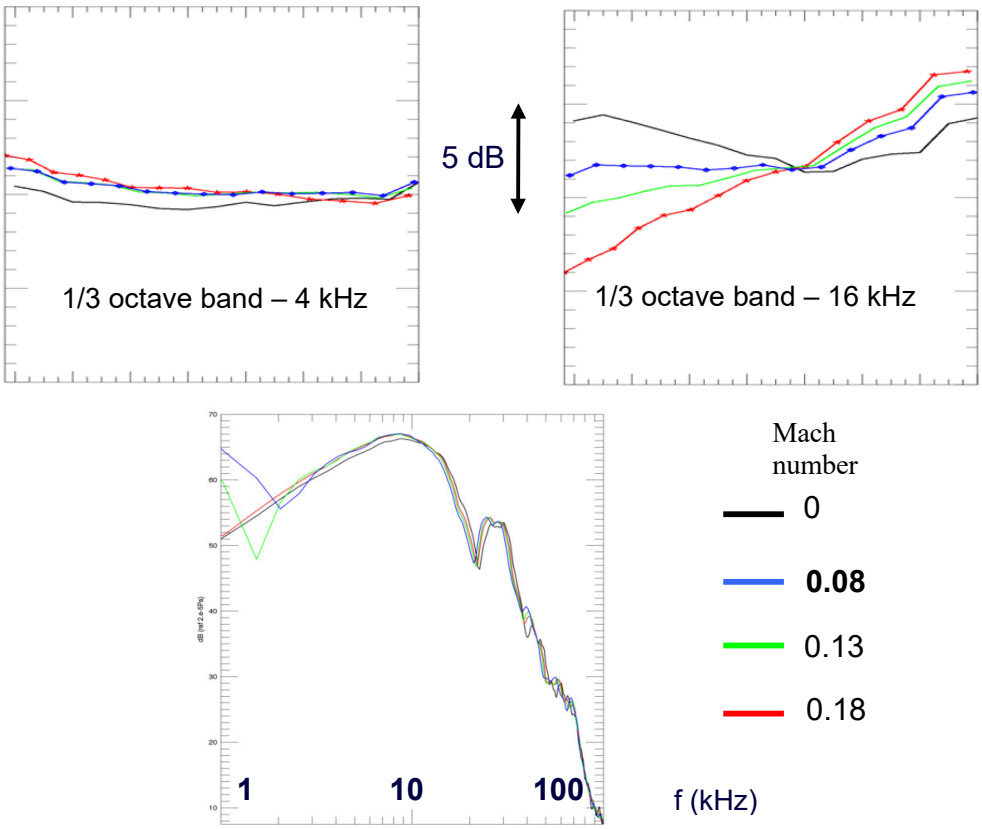

Figure 2-17: Directivity Diagrams and Spectra of the SPARC Source in Presence of Flow.

In order to check the performance of the SPARC source in the presence of a model and in flow, a few tests with a simple plane plate (Figure 2-18) were realized before the NACA0012 profile test campaign.

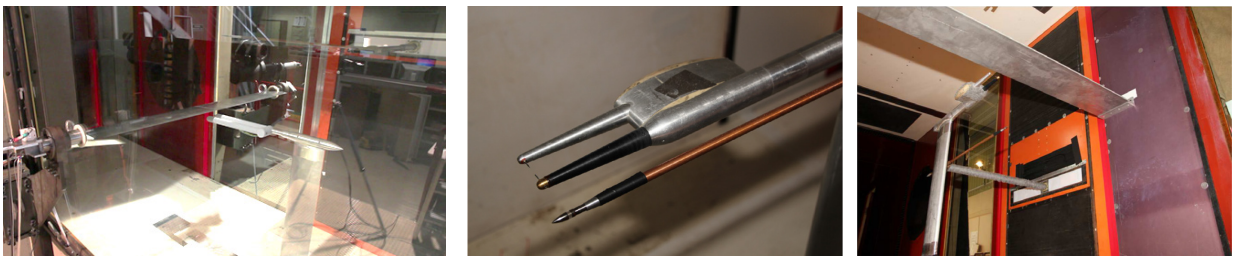

Figure 2-18: SPARC Source in F2 for Preliminary Tests with Plane Plate.

The directivity was measured at a radius of 200 mm from the plate in two planes XZ and YZ with:

- X: flow direction;
- Y: span direction of the plate; and
- Z: chord direction of the plate.

The reflections on the walls of the wind tunnel were removed using a temporal signal analysis. The results are shown on the figure ONERA 10 for a flow velocity equal to 60 m/s. The directivity diagrams are presented in RMS values (Figure 2-19).

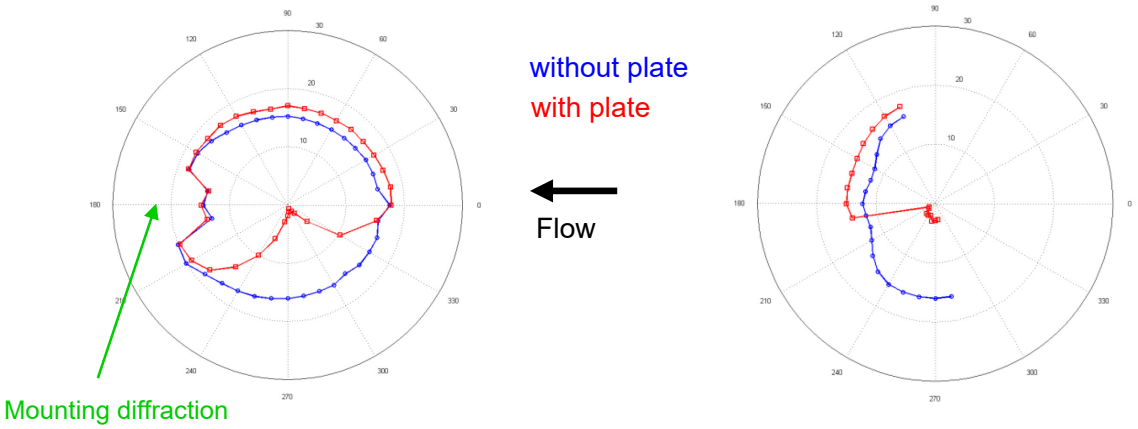

Figure 2-19: Shielding Effect with a Plane Plate.

One can observe the expected shielding effect with an increasing of the SPL on the side exposed at the source due to reflections on the plate and, on the opposite, a dramatic mitigation of the SPL in the shadow zone. The installation effect is well highlighted by this preliminary test.

One can notice in the area pointed out in green, the directivity effects due the SPARC source (support and electrode stems).

The intrusiveness of the source has been studied by numerical simulation and is detailed in the next section.

2.1.2.2 Acoustic Intrusiveness of the SPARC Source Support

In order to evaluate the acoustic intrusiveness of the SPARC source support, Boundary Element Method (BEM) simulations were performed.

The objective was to calculate the directivity of the acoustic field radiated by a monopolar source located between the electrodes of the SPARC by integrating the effects of acoustic diffraction on this support. First an approximate CAD (Computer Aided Design) of the support and device was obtained from accurate manual measurements. The BEM computations were realized with the in-house ONERA code BEMUSE. The surface of the mesh is composed of 53280 triangular elements and 260642 nodes. The spherical monopolar source is located halfway between the electrodes. The amplitude is equal to 1 Pa at a distance of 1 m. The theoretical maximum frequency available is 30 kHz, so the results with no flow are computed for 100 Hz at low frequency and then from 2 kHz to 20 kHz in steps of 2 kHz. The acoustic field is provided in three orthogonal sections (2 m x 2 m) containing 160 x 160 points that is a space interval of 12.5 mm (see Figure 2-20).

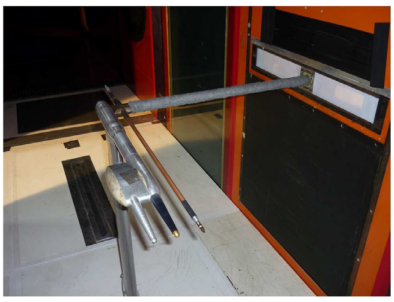

SPARC Source and Microphone in F2 WT

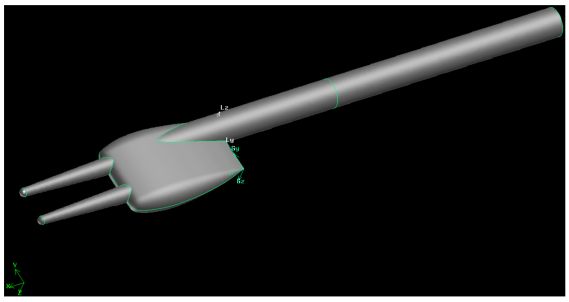

SPARC Source CAD

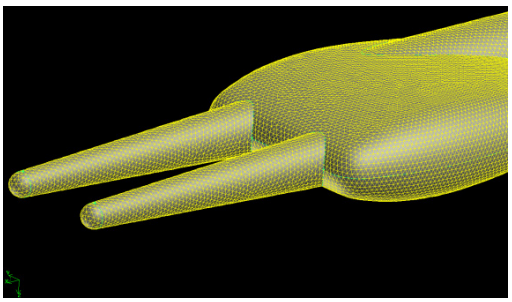

SPARC Source Triangle Mesh

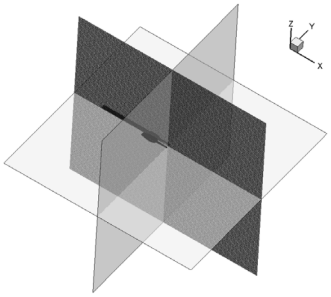

Orientation of BEM Results

Figure 2-20: Modeling of the SPARC Source for BEM Computations.

The results are presented in Figure 2-21 in 5 sections. At low frequency, less than 1 kHz, the diffraction of the monopole due to the presence of the device is not significant. The effect of the diffraction appears at 2 kHz but remains acceptable. From 4 kHz and beyond, the directivity diagrams are affected and no longer omnidirectional. Important lobes are observed at 10 kHz and 20 kHz.

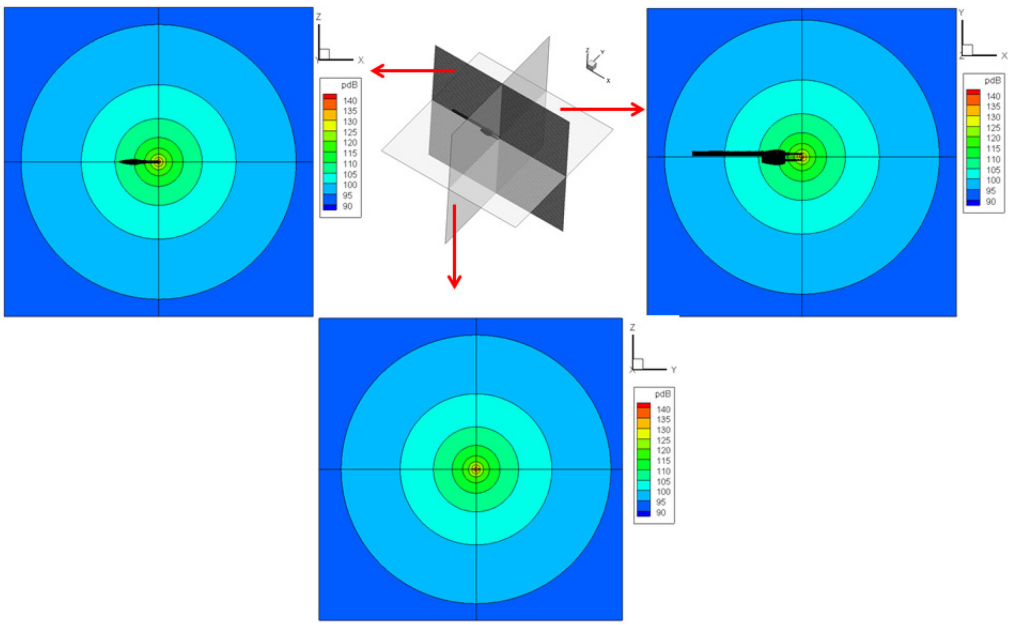

(a) 100 Hz.

Figure 2-21: Numerical Simulation of the Diffraction Effect Due to the SPARC Source. Five directivity diagrams at (a) 100 Hz, (b)2 kHz, (c)6 kHz, (d) 10 kHz, (e) 20 kHz.

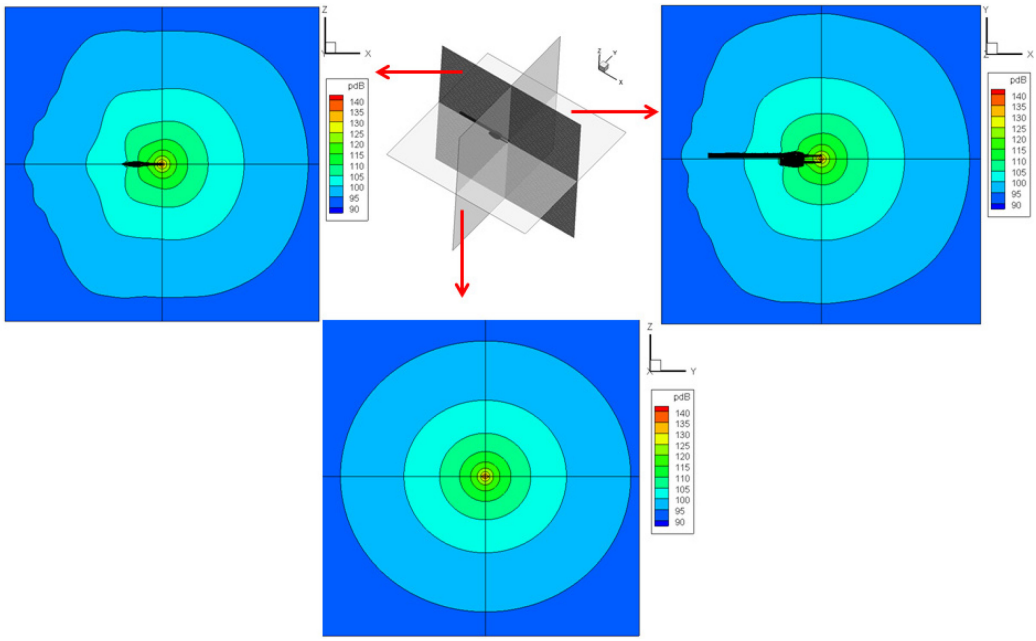

(b) 2 kHz.

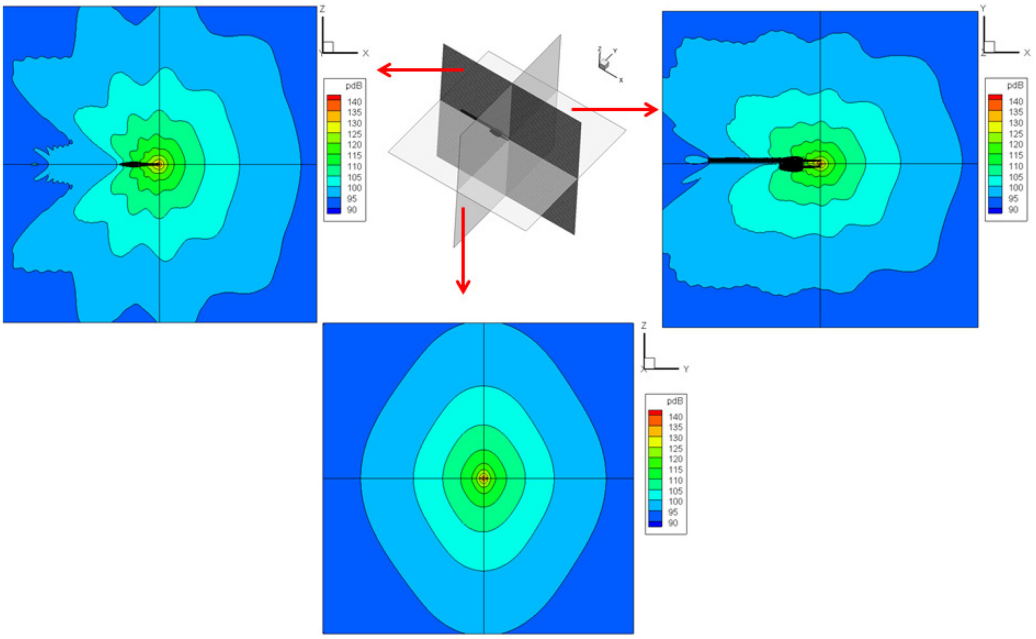

(c) 6 kHz.

Figure 2-21: (Cont'd) Numerical Simulation of the Diffraction Effect Due to the SPARC Source. Five directivity diagrams at (a) 100 Hz, (b)2 kHz, (c)6 kHz, (d) 10 kHz, (e) 20 kHz.

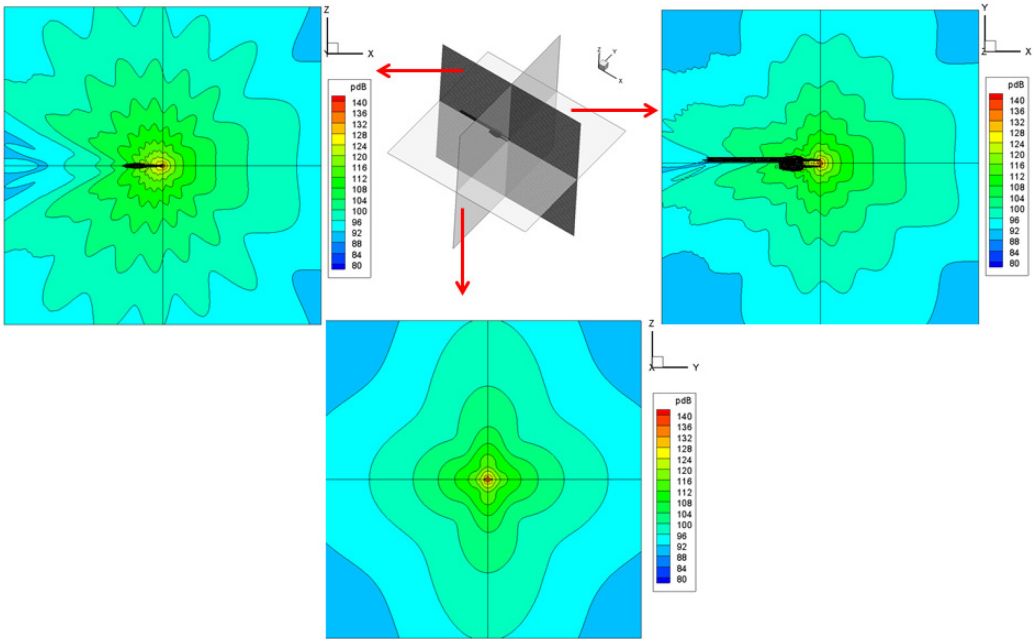

(d) 10 kHz.

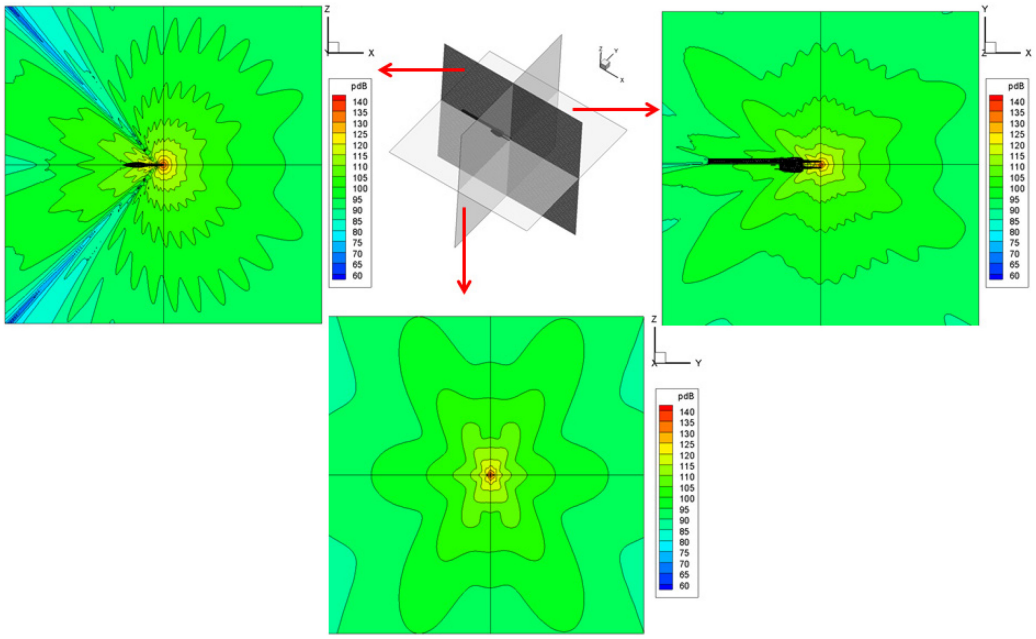

(e) 20 kHz.

Figure 2-21: (Cont'd) Numerical Simulation of the Diffraction Effect Due to the SPARC Source. Five directivity diagrams at (a) 100 Hz, (b)2 kHz, (c)6 kHz, (d) 10 kHz, (e) 20 kHz.

It is important to notice that the calculations assume a stationary harmonic point source, while the SPARC source is impulsive.

The first point to consider is that:

- With the BEM, all solid surfaces contribute to diffraction effects; and
- With experiments, the situation depends on the number of echoes that are taken into account in the analysis. However, the reflections generated by the surfaces of the support, closest to the source, are the most difficult to separate from direct propagation (these are the most energetic and the least delayed).

The second point concerns the legitimacy of the BEM calculations to validate the installation effects by an impulsive source. In experimental context, the impulse source is used to dissociate the reflections diffracted from the model and the reflections diffracted or reflected from the walls of the wind tunnel. *A priori*, the reflections diffracted on the support of the source are mixed with the first and, therefore, indissociable.

Consequently, installation or shielding effects can be simulated by BEM by the delta between

- The source in the presence of the support alone; and
- The source in the presence of the support and the model to test.

Based on the results obtained with BEM computations, ONERA started a new design of the SPARC source to make it as minimally intrusive as possible. The design and the manufacturing were done in 2015 between the test campaign in AWB wind tunnel (DLR, May 2015) and the F2 wind tunnel (ONERA, September 2015); both test campaigns carried out with the NACA0012 airfoil. Figure 2-22 presents a photo of the new SPARC source especially developed for the AVT233 applications. The mast is profiled, and the electrode stems are covered with acoustically absorbent material (foam) to avoid reflections.

Figure 2-22: New SPARC Source Especially Designed for AVT233 Tests.

2.2 CHARACTERIZATION OF WIND TUNNELS

Shielding tests were carried out in four different facilities. The basic 2D diffraction tests on the NACA0012 airfoil were done in three smaller scale facilities: a) DLR-AWB, b) ONERA F2, and c) NASA QFF. The purpose of this triplication of tests was i) to gain confidence in the shielding data and ii) to check the reproducibility of shielding data measured under nominally similar setup conditions but in three different facilities. The DNW-NWB acoustic wind tunnel was used to measure the shielding of the 3D aircraft geometries which would have been too large for the previously mentioned facilities.

2.2.1 DLR-AWB and DNW-NWB Test Environment

The Anechoic Wind tunnel Braunschweig (AWB) is DLR's small dimension high quality anechoic testing facility (see Figure 2-23, left). It is an open jet Göttingen-type wind tunnel capable of running at speeds of up

to 65 m/s, optimized for noise measurements at frequencies above 250 Hz. The AWB has been in service since the seventies and is used to conduct research on a wide range of topics, from classical airframe noise problems to propeller/rotor noise as well as jet installation noise and noise shielding problems. The AWB is equipped with most standard means for the realization of acoustic measurements as well basic aerodynamic measurements.

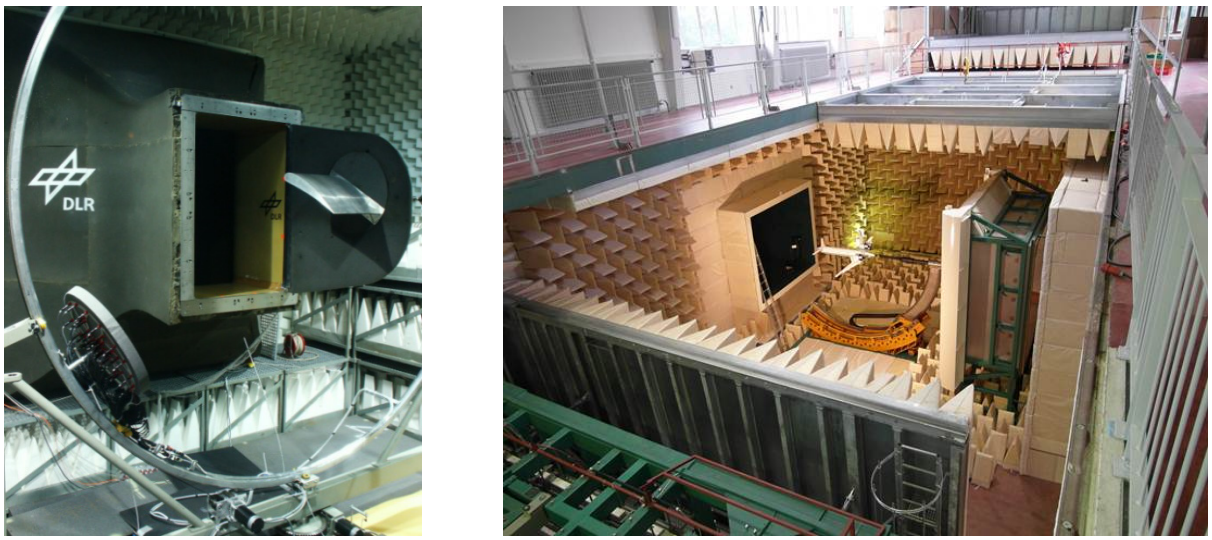

Figure 2-23: Acoustic Wind Tunnel Braunschweig, DLR-AWB (Left), DNW-NWB (Right).

The DNW-NWB (see Figure 2-23 right) in Braunschweig, Germany is an aeroacoustic wind tunnel of excellent acoustic and aerodynamic quality. It is a facility operated by the foundation Deutsch-Niederländische Windkanäle (DNW). The acoustic plenum of the DNW-NWB has a certified 99% sound wave absorption for frequencies from 100 Hz up to 40 kHz. The tunnel can operate in open or closed test section at flow velocities up to 80 m/s and 90 m/s respectively. Its nozzle has an exit area of 3.25 m by 2.80 m = 9.1 m² and a contraction ratio of 1:5.6. Like the AWB the DNW-NWB is a Göttingen-type wind tunnel.

2.2.2 ONERA F2 Test Environment

The F2 subsonic wind tunnel (see Figure 2-24) of ONERA in Mauzac, France is a low turbulence closed test section research facility with a special proficiency in layer Doppler anemometry.

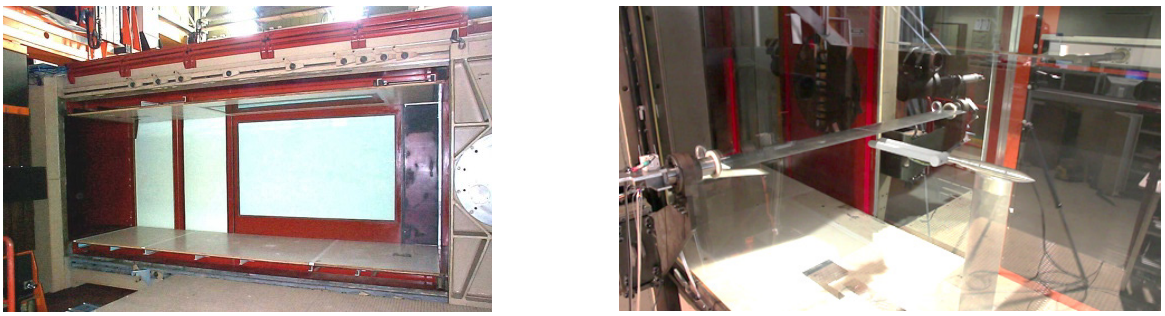

Figure 2-24: F2-Tunnel Glass Wall Test Section (Left), Test Section Equipped with 2D NACA0012 Model and SPARC Acoustic Pulse Source (Right).

Test section dimensions are length: 5 m, width: 1.4 m, height: 1.8 m. The side walls of the test section are made up of removable opaque or transparent panels which allow viewing access to be specially adapted according to the requirements of each test. The wind tunnel is equipped with a 12 bladed fan driven by a 680 kW direct current motor. The velocity can be continuously varied from 0 to l00 m/s by adjusting the motor speed. The total temperature is controlled in ± 1°C by a water cooler. The settling chamber is equipped with four screens, a honeycomb filter, and noise dampers on walls, which, in conjunction with a contraction ratio of 12, supply a flow with a very low level of turbulence in the test section (less than 0.05%).

2.2.3 NASA QFF Test Environment

The NASA laser induced noise scattering experiment was conducted in the Quiet Flow Facility of NASA Langley Research Center in Hampton, Virginia. The Quiet Flow Facility (QFF) is specifically designed for aeroacoustic testing. Its anechoic test chamber (see Figure 2-25) is equipped with a 0.61 by 0.91 m rectangular open jet nozzle. Two vertical side plates attached to the short sides of the nozzle are used to mount the test models in the test section.

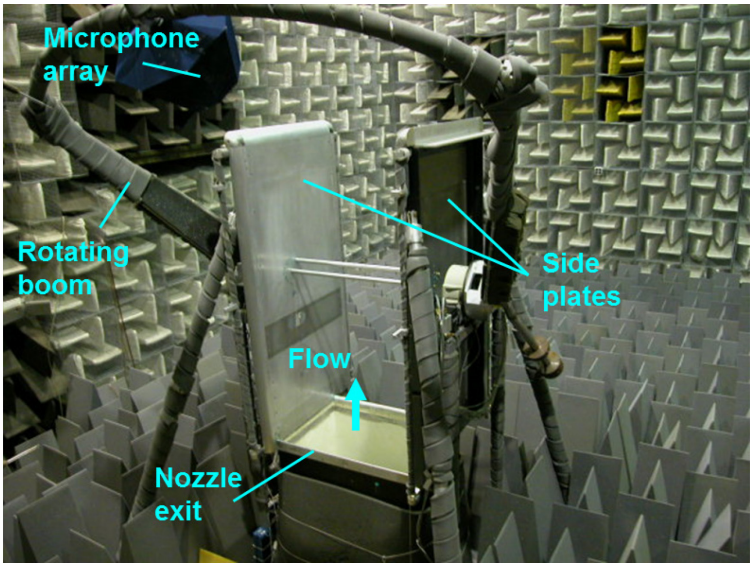

Figure 2-25: Quiet Flow Facility Test Chamber (with a Tandem Cylinder Test Model Positioned in the Test Section).

The flow circuit employs baffles, turbulence screens and turning vanes to ensure a quiet, low turbulence air flow from the open jet. Flow speeds up to Mach number of 0.17 can be obtained. The anechoic room (7.3 m wide by 9.2 m long by 6.1 m high) is lined with wedges, 91.5 cm deep, to provide an essentially reflection-free environment for acoustic measurements down to about 70 Hz. The room is constructed with a 91.5 cm air space between double walls and is mounted on springs to isolate it structurally from the remainder of the building and thus minimize the transmission of structure-borne noise arising from other parts of the building.

Chapter 3 – BASIC STUDIES ON ACOUSTIC DIFFRACTION

Jan W. Delfs
DLR – Institute of Aerodynamics and Flow
GERMANY

Karl-Stéphane Rossignol
DLR – Institute of Aerodynamics and Flow
GERMANY

Michael Mößner
DLR – Institute of Aerodynamics and Flow
GERMANY

Denis Gély
ONERA Département Aéroacoustique – DAAC
FRANCE

David Patience
BAE Systems – Military Air and Information
UNITED KINGDOM

Oliver Darbyshire
BAE Systems – Military Air and Information
UNITED KINGDOM

Russell H. Thomas
Langley Research Center, NASA
UNITED STATES

Florence Hutcheson
Langley Research Center, NASA
UNITED STATES

Christopher Bahr
Langley Research Center, NASA
UNITED STATES

Yueping Guo
Langley Research Center, NASA
UNITED STATES

Before turning to the characterization of acoustic shielding properties of actual aircraft geometries, AVT-233 decided to conduct extensive 2D diffraction studies on a well-known airfoil geometry, namely the NACA0012. The acoustic wind tunnel tests, as well as the predictions, were much less complicated, and therefore, much experience could be gained to prepare and de-risk the 3D studies considerably. One aspect of the 2D studies was to check for the importance of flow effects on shielding, which could be addressed with various computation approaches from high- to mid-fidelity. Moreover, the 2D airfoil diffraction/shielding problem was quite useful for a more comprehensive analysis than the complex 3D cases.

3.1 EXPERIMENTAL TESTS

The 2D shielding tests on the NACA0012 airfoil were conducted in DLR-AWB, in ONERA F2 and NASA QFF for nominally the same test conditions in order to learn about the measurement scatter across different facilities. In AWB and F2, both acoustic test sources were implemented and used for shielding tests, namely DLR's laser source and ONERA's electric discharge source (SPARC). One central question was, how consistent measured data would be across the two facilities given that AWB is an acoustic open section wind tunnel, while F2 is a closed section wind tunnel. Moreover, NASA's QFF served as a second acoustic wind tunnel of similar characteristics as AWB. Nominally identical airfoil models were built on both sides of the Atlantic Ocean. Formally, the same laser source as at DLR was set up at NASA.

3.1.1 NACA0012 Diffraction Tests in DLR-AWB

The experimental setup in the Acoustic Wind tunnel Braunschweig (AWB) is shown in Figure 3-1. The 2D wing with NACA0012 profile ($c = 0.2$ m) is mounted vertically in the test section with a 0.2 m shift away from the tunnel centerline (see Figure 3-2). This is done to provide enough room for the in-flow microphone, seen in Figure 3-1, to be placed in the geometric far field of the model. As can be seen in the left part of Figure 3-1, the whole laser was tilted 3° toward the model, to avoid collision of the optical components with the wing's support when moving the source. Measurements were performed for three geometrical angles of attack, $\alpha_g = 0°, \pm 10°$, corresponding to effective aerodynamic angles of attack, $\alpha = 0°, \pm 6°$. The correspondence was established through comparison of the experimental pressure distributions to those

obtained by CFD. The transition location was determined through stethoscope inspections, and found to occur at $\approx 0.8c$ for $\alpha_g = 0°$ and $\approx 0.9c$ and at $\approx 0.15c$ on the pressure and suction sides respectively for $\alpha_g = \pm 10°$. A 0.4 mm thick straight rectangular trip strip was applied at $x/c = 0.6$ on the suction side to prevent the occurrence of laminar flow separation.

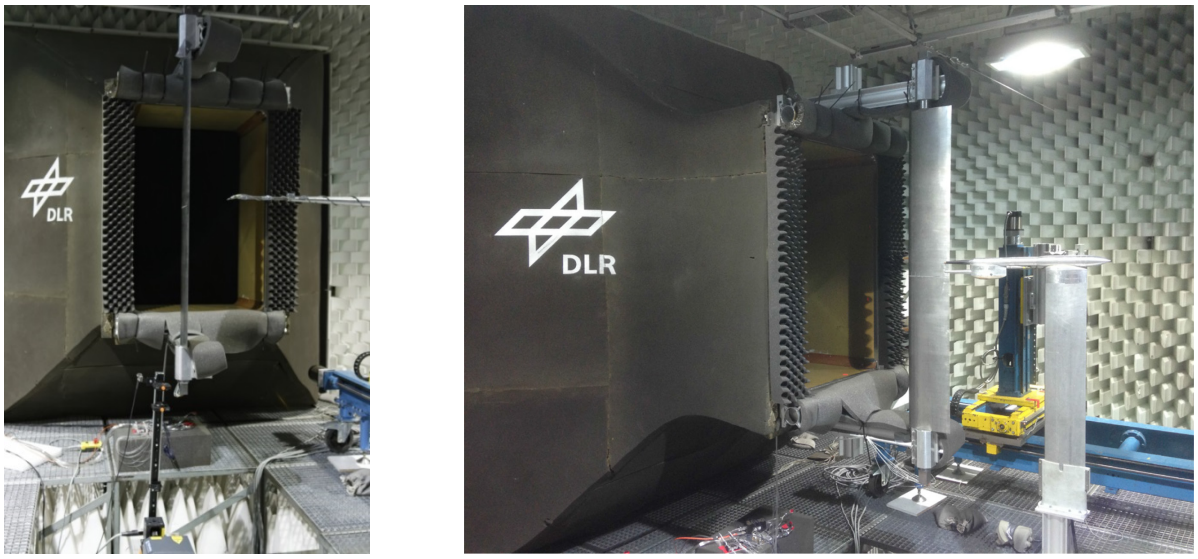

Figure 3-1: NACA Diffraction Tests in AWB. Left: DLR laser SPARC source, Right: ONERA Electric discharge SPARC source.

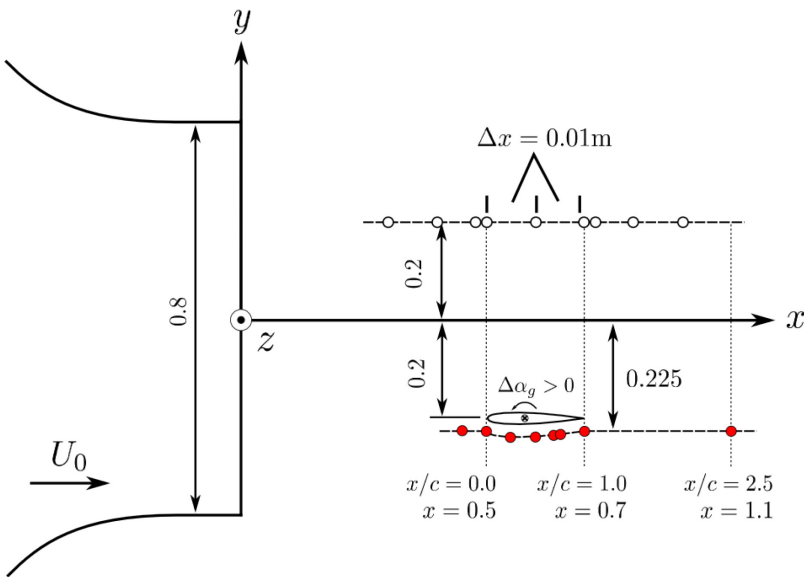

Figure 3-2: Selected Source and Microphone Positions, All Dimensions in Meters. The solid red dots represent the source positions while the empty dots represent the microphone positions.

An in-flow microphone was mounted on linear microphone traverse, 2 chords (0.4 m) away from the model chord line, on the opposite side to the sound source (Figure 3-2). The in-flow microphone was traversed in streamwise and spanwise directions; however, the focus was put on measurements along a streamwise microphone traverse. The sound source was positioned at a constant distance of 25 mm away from

the model's surface, on the opposite model side to the in-flow microphone. A rotation of the model required the source position to be adjusted to preserve a constant 25 mm distance from the surface. Also, a limited number of far field (out-of-flow) measurements were done (not presented here). Throughout the measurements, the absolute position of the microphone measurements was not changed with a change in wing's angle of attack (the microphone traverses are kept the same). The evaluation of the shielding impact of the model requires the acquisition of data once with the model installed and once in the empty test section.

The wind tunnel nozzle was covered with acoustic foam as a preventive measure to ensure that sound wave reflections did not contaminate the measurements, especially in cases where the in-flow microphone is positioned upstream of the wing's LE (Figure 3-2). Preliminary tests revealed, however, that acoustic treatment of the ground, nozzle and positioning elements was not necessary. Reflections generally do not play any important role when using the laser sound source, due to the very short duration of the generated pressure pulses ($\approx$ 0.1 s). When a shielding object is present between the sound source and a remote receiver, one has to be more careful, however, to make sure that only the meaningful part of the measured signal is kept for further processing. This is due to the longer propagation paths of the sound waves about the shielding object, requiring longer time series to be inspected in post-processing to capture all of the relevant sound intensity.

3.1.1.1 Data Acquisition and Processing

For the present experiment, a laser repetition rate of 10 Hz and an acquisition time of 10 s were chosen. This means that approximately 100 pulses are recorded per data point. Although great care was taken to ensure an optimal formation of the plasma spot, part of the recorded pulses is not valid and/or deviate too much from the statistical mean maximum amplitude values. Pulses with maximum amplitudes exceeding one standard deviation from the mean value are considered outliers and were rejected prior to the computation of average quantities. The resulting maximum deviations of the individual L_tot relative to the averaged L_tot, remain within ± 1.5 dB from the mean value in all cases. Acoustic measurements for each configuration were performed with a continuously running laser operated at full power, in order to get the maximal possible Signal to Noise Ratio (SNR). The laser output trigger signal was simultaneously recorded to facilitate data post-processing. For each configuration, all pulses were extracted from the measured time series by correlating a reference pulse signal with the raw measurements.

In cases where $U_\infty > 0$ m/s, the time signals have to be band-filtered between 3 kHz to 6 kHz and 110 kHz, at $M_0 = 0.087$ and $M_0 = 0.16$, respectively, to remove low frequency contamination of the data through flow-induced noise on the microphone body as well as from vibrations of the microphone support (see Figure 3-3). Filtering of the raw time series is necessary for a better extraction of the pulses during post-processing, especially when investigating the shielded sound field (Figure 3-3(b)), where the absolute amplitude of the sound pulses is greatly reduced. Prior to the calculation of averaged time domain data, the individual extracted pulses were superposed through peak locking of the first pressure maximum. Fourier analysis, of the individual and averaged pulses, was then performed using non-overlapping blocks zero-padded to a total length of 4096 samples for a frequency resolution of $\Delta f = 61$ Hz. This block length was kept constant throughout the post-processing even when single pulses were measured. The reasons behind this choice are twofold.

First, enough samples are needed to ensure the complete recovery of the meaningful part of the signals when measuring with the shielding object installed. Second, a constant and consistent block length has to be defined for a correct representation of the pulse's full energy content in both the shielded and free-field cases. This is necessary to get correct shielding factors. Finally, no window function is applied to the signals prior to the FFT computations as the pulses are short-time signals which tend to zero quickly toward each block's bounds.

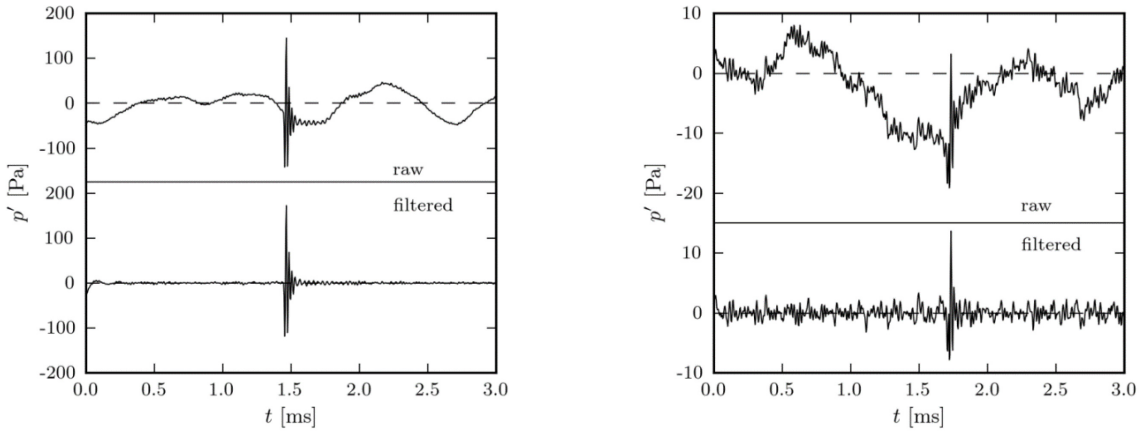

(a) Without Model Installed. **(b) With Model Installed.**

Figure 3-3: Band-Filtered Time Domain Signals.

Since one is dealing with a pulse of very short duration ($\approx$ 0.1 ms), very high sampling rates are needed. The available acquisition unit (GMB Viper, 48 channel) was therefore used at its maximum acquisition rate of 250 kHz with an anti-aliasing filter cut-off frequency fixed at 100 kHz. This setup enables a correct sampling of signals with frequencies up to approximately 100 kHz. However, in cases where $U_0 > 0$ m/s, an upper frequency of 80 kHz is considered in the analysis due to a poor SNR for frequencies above this limit. In order to measure at such frequencies, 1/8" G.R.A.S. 40DP microphones with a 140 dB dynamic range were used. These microphones are pressure field microphones, and their output needs to be corrected when they are used in a free sound field, as in the present case. Pressure field microphones are designed to measure the actual pressure in front of the sensing membrane with a flat frequency response up to very high frequencies (see Figure 3-4), and are usually used in wall-mounted situations, e.g., for surface pressure fluctuation measurements. Therefore, when used as a free-field microphone with or without protective grid, the impact of the microphone body on the sound field is not compensated by its electronics. The free-field correction is dependent on the incidence angle of the incoming sound field onto the microphone and can be as high as 10 dB at 100 kHz. Because the laser sound source has its spectral maximum at high frequencies, around 30 kHz, the free-field correction is required for a correct quantification of the source power level as well as for a correct recovery of the source time signature. This step was not accounted for in Ref. [3], when discussing the source characteristic pulse shape.

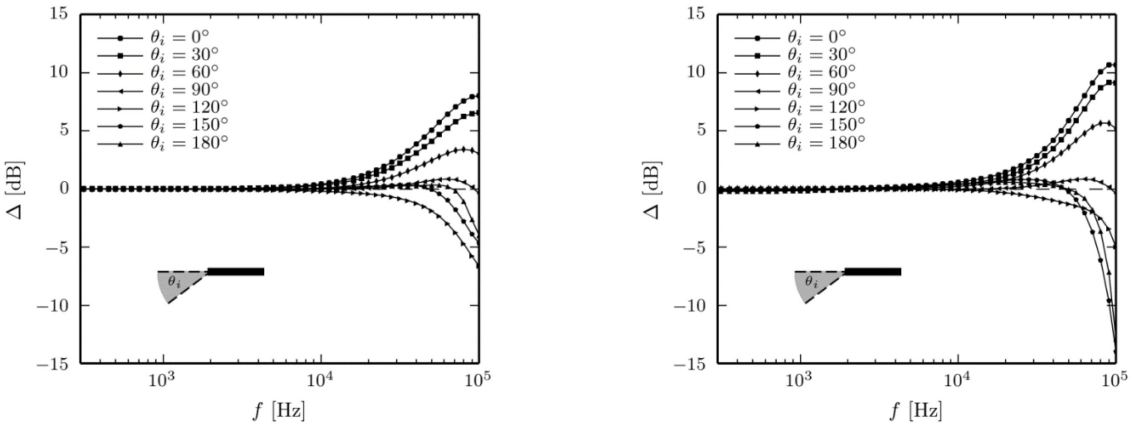

(a) Without Protective Grid **(b) With Protective Grid**

Figure 3-4: Frequency Response Curves for GRAS-40DP 1/8" Pressure Field Microphones. Courtesy of GRAS.

Because in-flow measurements are made, it is necessary to use a nose cone in front of the microphone sensing membrane. The main effect of the nose cone on the measurements is to force a shift of the spectral maximum to higher frequencies (see Ref. [3]), from $\approx$ 30 kHz to $\approx$ 50 kHz), while amplifying the high frequency spectral levels. Therefore, a supplementary and necessary correction is required to recover correct signal amplitudes and time signatures when measuring in-flow. Measurements done with a protective grid are almost not affected Ref. [3]. As a general rule of thumb, it was deduced in Ref. [3] that one should avoid measuring at small θ_i, where the corrections are most important.

The derivation of a nose cone correction can be made in-situ by running two independent set of measurements, one without nose cone and one with nose cone, at a unique set of positions. In the present case, these are the actual microphone positions of Figure 3-2. This aspect was already discussed in detail in Ref. [7] and Ref. [3] and will not be repeated here. However, the general assumption in Ref. [3] that the nose cone correction is mostly dependent on the nose cone geometry appears, based on the current experience with the source, not to be completely true. A derivation of the correction curves is necessary for each particular test case considered and is difficult to obtain and to generalize for the highest frequencies. In Figure 3-5, the source spectra for three different source positions and microphone positions for $M_0 = 0$ are plotted. The data are not corrected in any matter. Each group of lines contains three curves, one for a microphone position upstream of the source ($\theta_i > 90°$), one for a microphone directly below the source ($\theta_i = 90°$) and one downstream of the source ($\theta_i < 90°$). A striking observation is that the nose cone effectively removes any significant θ_i dependency on the measurements in the range of measurements relevant for the present experiment. This statement also holds when $M_0 > 0$, although with a slightly larger spreading (less than ± 1 dB), of the microphone output over the same range of measurements. In fact, the in-flow microphone gives the same output independently of its position relative to the source. As the source is known to radiate uniformly with monopole character Ref. [3], Ref. [7], Ref. [11], the assumption appears to be correct. Of course, if one is interested in absolute power levels, the application of the corrections discussed above still remains mandatory. This independence of θ_i of the measured data simplifies greatly the calculation of accurate shielding coefficients as the application of correction procedures can be omitted. This is particularly interesting in cases where a precise propagation direction of the radiated sound field, and therefore of its incidence on the microphone, cannot be determined precisely or at all. All the noise shielding results presented later on were not corrected prior to the computation of the shielding factors.

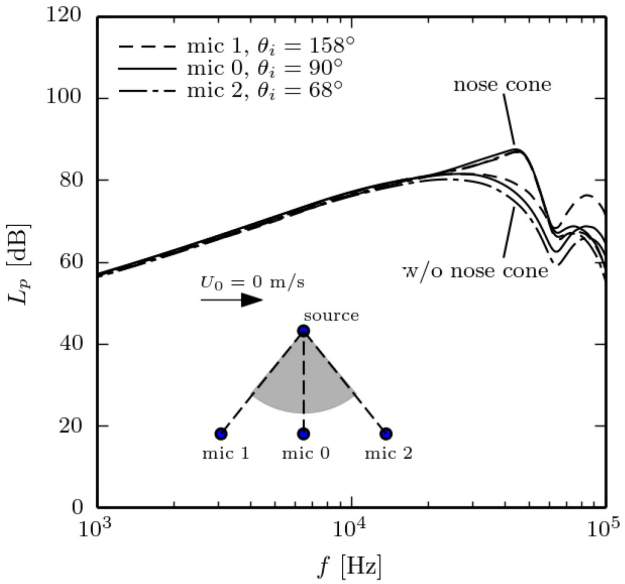

Figure 3-5: Effect of the Nose Cone on Measured Noise Spectra vs. Sound Wave Incidence.

Corrections procedures can be omitted, as discussed above, for cases where the shielding characteristics of an object are of interest. Otherwise, if one is interested in absolute quantities, corrections are still mandatory. Spectral quantities can be directly corrected in the frequency domain as the correction curves are readily available in the Fourier domain. To get corrected time signatures requires the additional step of transforming the time series to the Fourier domain before application of the correction and inverse transforming. In that case, the spectral correction is applied to the complex Fourier coefficients. Also, due to the high frequency content of the source, atmospheric attenuation also needs to be considered. An extensive discussion on this topic can be found in Ref. [2].

Finally, when performing measurements in the presence of a shielding object, care must be taken to account for sound field diffraction which leads to time delays in the reception of all incoming waves at the microphone. This delayed arrival is obviously a function of microphone position, source position, flow velocity and model setting, for instance, in the present case, the wing's angle of attack, α_g. The main quantity of interest is the acoustic attenuation or shielding factor:

$$\gamma_{\mathrm{p}} = 10 \log_{10} \left(\frac{\overline{p_s'^2}}{\overline{p_i'^2}} \right) \text{ dB} , \tag{3-1}$$

with $\overline{p_s'^2}$ being the integrated value or the root mean square acoustic pressure in the shielded field and $\overline{p_i'^2}$ the root mean square value of the incident acoustic pressure, i.e., directly emitted from the source. The computed values of the shielding factor are found to be highly sensitive to small errors in the calculated averaged time data. This is, in part, a result of a still relatively low sampling rate with which the individual pressure pulses are acquired, and also a consequence of the fluctuations in source characteristics from pulse to pulse. This is particularly relevant in cases where strong shielding occurs and in a moving medium. Therefore, great care has to be taken to ensure that the post-processing is done correctly, through thorough inspection of the data after each processing step.

3.1.1.2 Acoustic Shielding Results

Overall noise shielding results for two Mach numbers ($M_0 = 0,\ 0.16$) and three effective angles of attack ($\alpha = +6°, 0°, -6°$) and three source positions are plotted in Figure 3-6. The results for the case $\frac{x_s}{c} = 0.5$ and $\alpha = 0°$ are given in Figure 3-7. As expected, the measured shielding factor is highest when the source is deep into the shadow zone of the wing (Figure 3-6(c)). For $\alpha = 0°$, a positive γ_p is recorded (noise increase) downstream of the wing's Trailing Edge (TE). One hypothesis is that this could occur by the microphone receiving both a direct and reflected signal. A similar effect is not recorded at the Leading Edge (LE), probably due the LE's smoother geometry, resulting in the generation of a weaker secondary source. With a positive change in α, the curves for γ_p are shifted upstream while the inverse is true for a negative change in α . These variations result from a different relative position of the wing with respect to the microphone (i.e., the microphone traverse is kept the same for all three angles of attack). For $M_0 = 0.16$, and $x_s/c = 1.0$, shown in Figure 3-6(f) the results display a somewhat unusual behavior compared to the remaining data. Particularly in the deep shadow region, for about x/c < 1.0 and looking upstream the shielding factors at all three values of α are up to 3 – 4 dB less than for the no flow case. Note, that the data in Figure 3-6(e), Figure 3-6(f) almost perfectly match the data measured in the QFF test as presented in Figure 3-29. Because of the close proximity of the laser sound source to the TE, a strong interaction between the incoming source wave and the solid edge may be expected. A non-negligible secondary edge source might occur as a result of shear flow effects at the TE. Similarly, to TE noise generation by interaction of flow turbulence with the TE, an increased radiation in the upstream direction might occur. Another peculiarity of this case is that (the strongest) part of the diffracted wave from the TE, which travels upstream, parallel to the pressure surface experiences boundary layer refraction, redirecting sound into the deep shadow zone. Therefore, compared to the case without model, and without flow, the measured noise levels would be higher and, as a consequence, the shielding efficiency reduced. Note, that this effect cannot

occur when the source is at the leading edge Figure 3-6(a), Figure 3-6(b), since refraction effects are reversed here. Otherwise, the results for $M_0 = 0$ and $M_0 = 0.16$, are consistent and reveal a rather negligible impact of the flow field, in most situations, on the computed shielding factors.

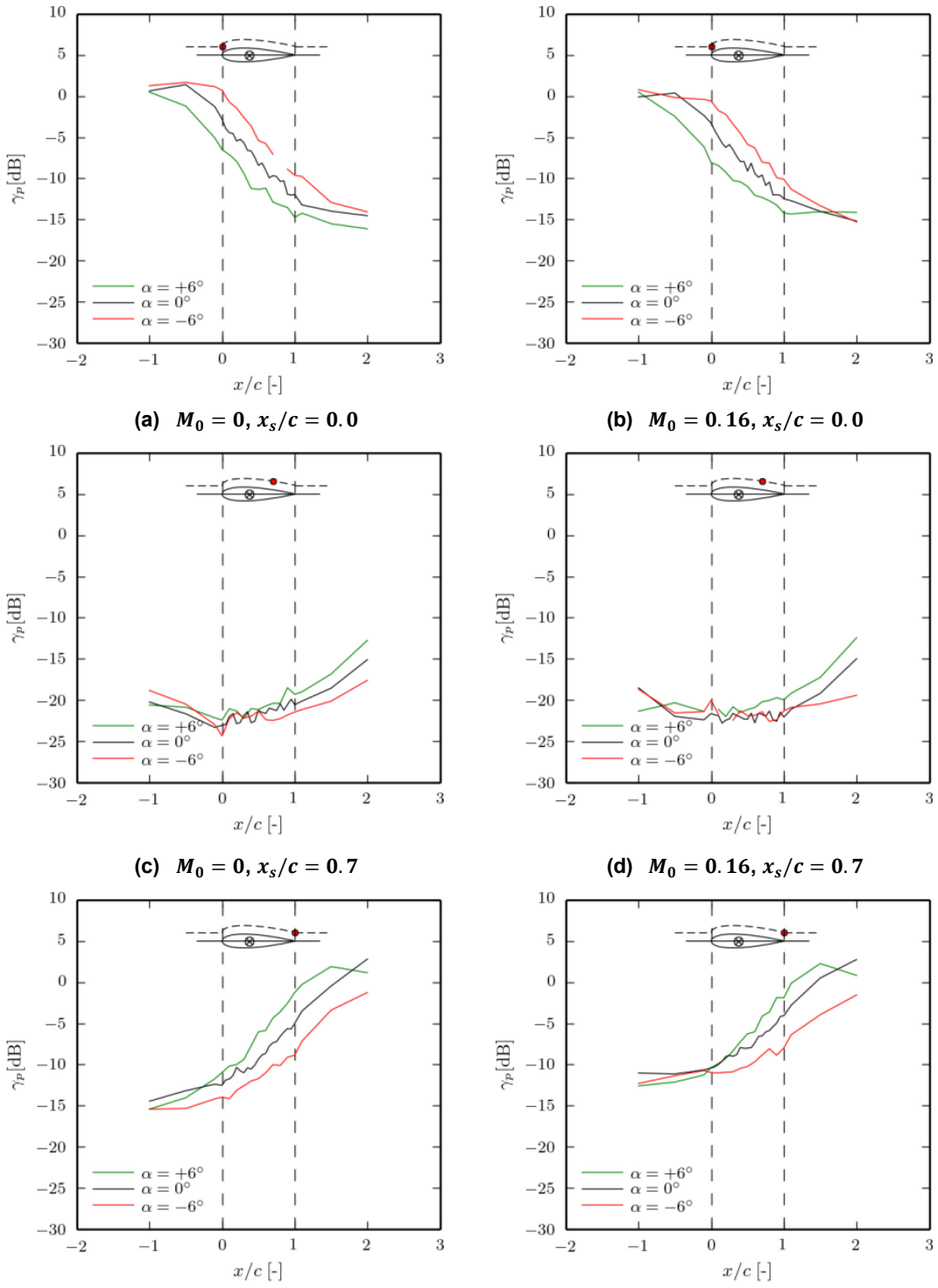

(a) $M_0 = 0, x_s/c = 0.0$ (b) $M_0 = 0.16, x_s/c = 0.0$

(c) $M_0 = 0, x_s/c = 0.7$ (d) $M_0 = 0.16, x_s/c = 0.7$

(e) $M_0 = 0, x_s/c = 1.0$ (f) $M_0 = 0.16, x_s/c = 1.0$

Figure 3-6: Effect of Aerodynamic Angle of Attack α on the Shielding Factor vs x/c (Geometric Angle of Attack $\mp 10°$).

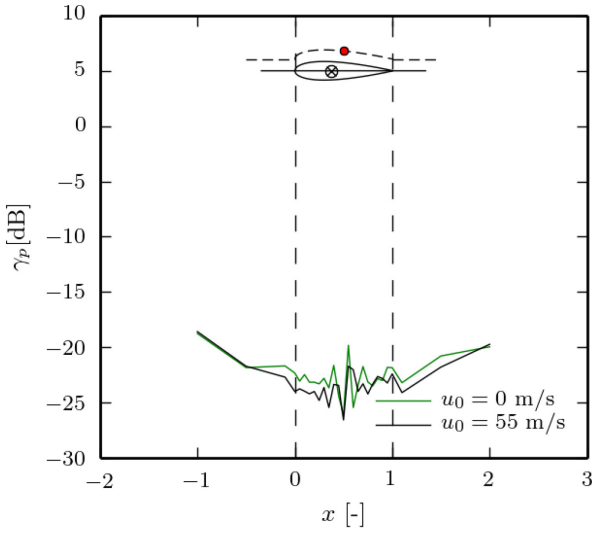

Figure 3-7: Effect of M_0 on the Shielding Factor vs x/c. $x_s/c = 0.5$, $\alpha = 0°$.

Maps of the shielded sound field (f vs. x/c) are given in Figure 3-8, Figure 3-9, and Figure 3-10 for all cases plotted in Figure 3-6. In Figure 3-9(d) and Figure 3-10(e) the black contour levels at $x/c = 0.0$ and $x/c = 0.8$, respectively, are nonphysical. Otherwise, for all cases with $M_0 = 0.16$, a tone can be identified at $f = 30$ kHz, its origin being at the arm holding the microphone. For the case $M_0 = 0.16$, data are only available between $6.0 \text{ kHz} < f < 100.0 \text{ kHz}$ because of the need to filter the time series below 6.0 kHz prior to data processing. The results of Figure 3-8, Figure 3-9, and Figure 3-10 are consistent with the trends already observed in Figure 3-6. At $M_0 = 0.0$, the results have enough resolution in the range $0.0 < x/c < 1.0$ to reveal complex interference patterns. For $M_0 = 0.16$, the patterns become less clear at the highest frequencies, while similar interference patterns are recovered for most of the spectral range. In accord with the trends of Figure 3-6, the impact of the flow is rather negligible, except for a source location x_s/c near the TE.

The ONERA test campaign in AWB wind tunnel lasted for 2 weeks with 1 week dedicated to the tests with the SPARC source. The displacement of the microphone and of the SPARC source were remote-controlled with a synchronized signal acquisition. The NACA0012 airfoil, 200 mm in chord, is vertically mounted in the test section of the wind tunnel. Eleven pressure taps are used to adjust the angle of attack from -6 to +6 degrees. The flow velocity ranges from static condition to 55 m/s. The SPARC source pulse rate is 10 Hz and the acquisition time 11 seconds in duration.

To characterize the diffraction due to the NACA0012 profile, the measurements were implemented in chord and span directions (Figure 3-11). The sampling rate is 250 kHz, and the signals are high-passed filtered at 500 Hz.

For each angle of attack, flow velocity and microphone location, two explorations were carried out:

- Longitudinal scan (red and purple dots) at mid-span (-400 mm to +200 mm in X).
- Crosswise exploration at mid-span (0 mm to + 250 mm at Y).

The acoustics measurements were performed using an in-flow 1/8'' microphone equipped with a nose cone. The laser source could be fitted at 25 mm in distance to the airfoil (green dots); on the other hand, the SPARC source could be fitted (due to mechanical and electrical interferences) at 35 mm downstream of the midchord, and 100 mm upstream of the midchord (blue dots). All measurements points made with the SPARC source have also been made with the laser source at the same positions.

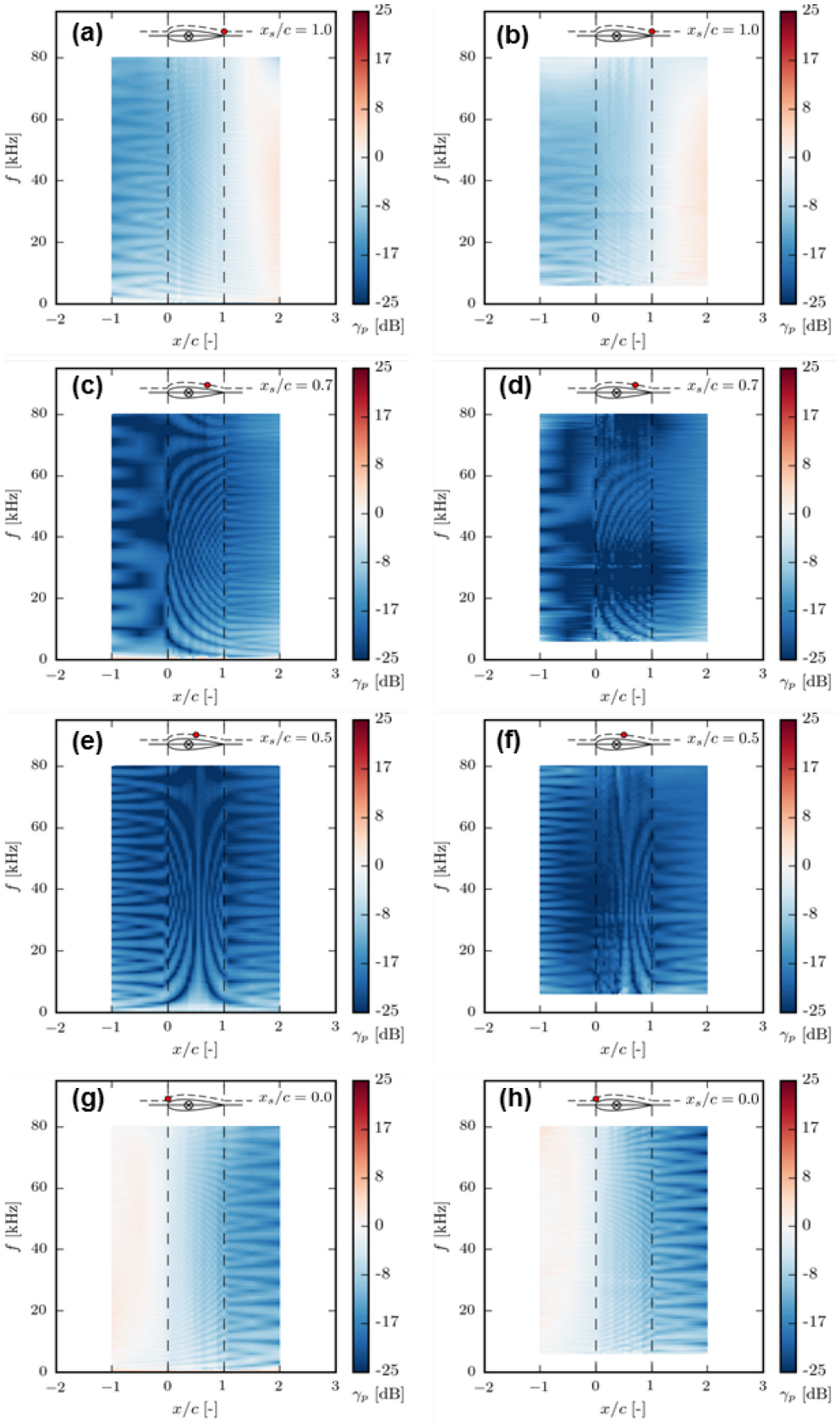

Figure 3-8: Contour Plots of the Shielding Factor at $\alpha = 0°$. Left $M_0 = 0$. Right $M_0 = 0.16$.

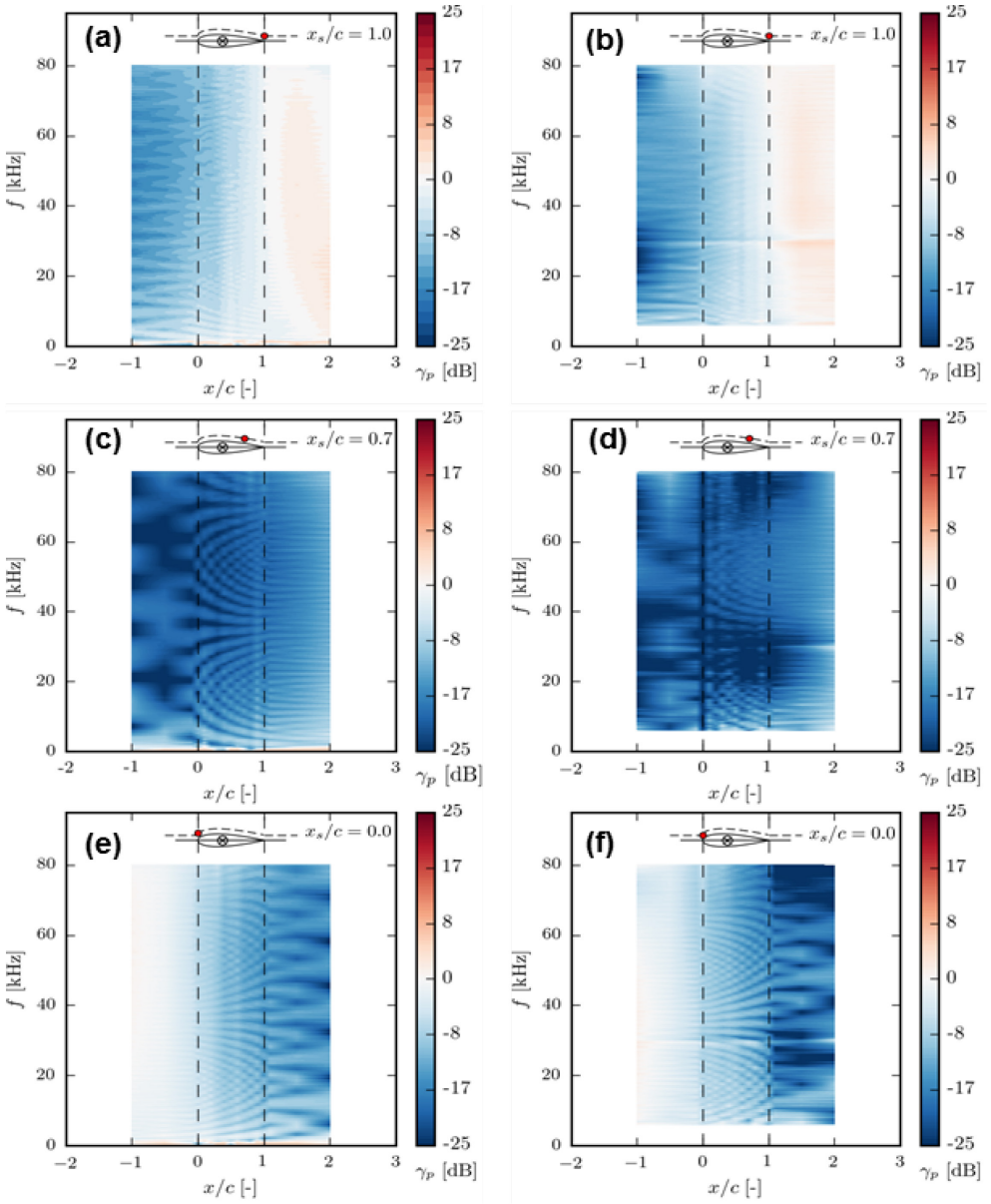

Figure 3-9: Contour Plots of the Shielding Factor at $\alpha = +6°$. Left $M_0 = 0$. Right $M_0 = 0.16$.

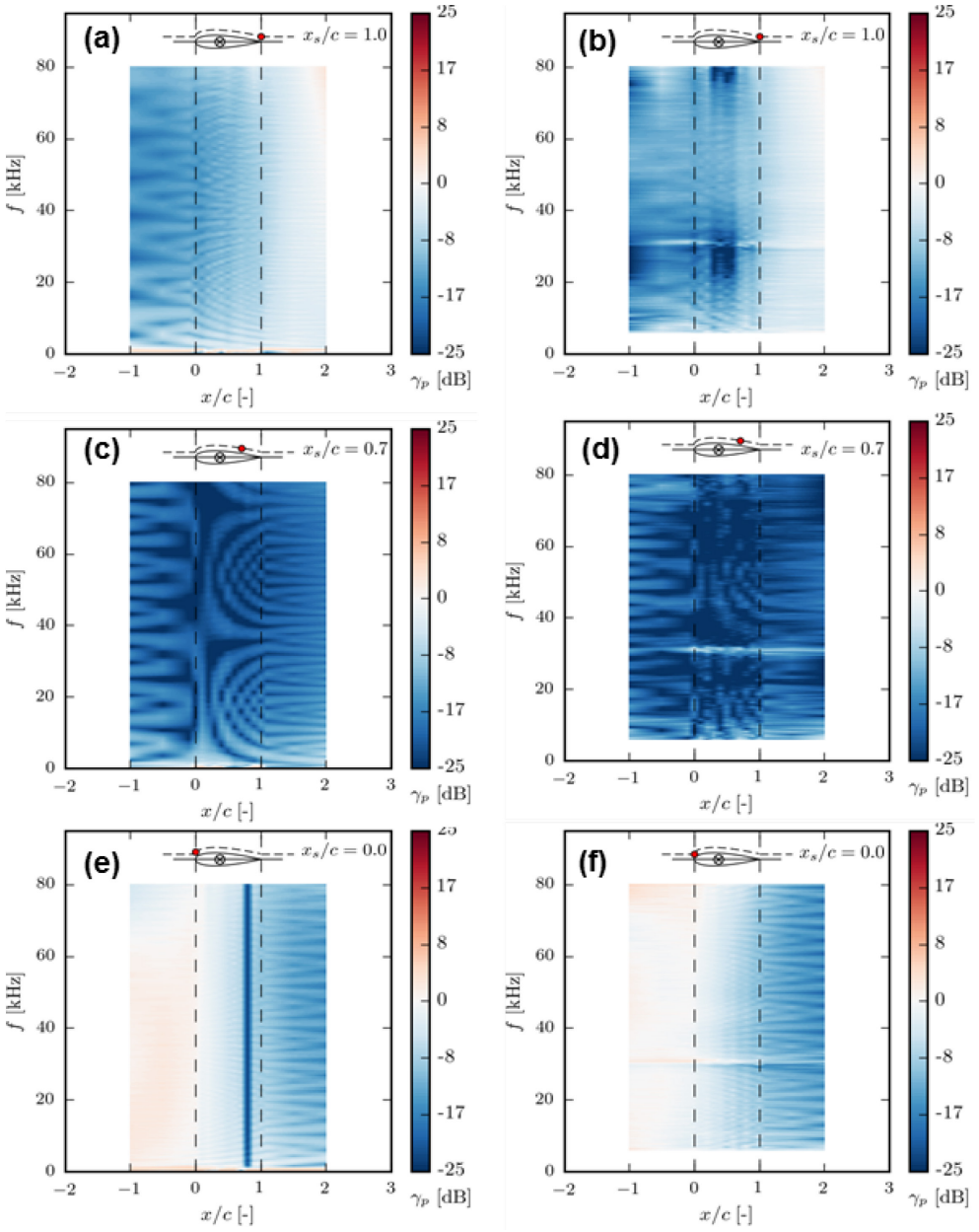

Figure 3-10: Contour Plots of the Shielding Factor at $\alpha = -6°$. Left $M_0 = 0$. Right $M_0 = 0.16$.

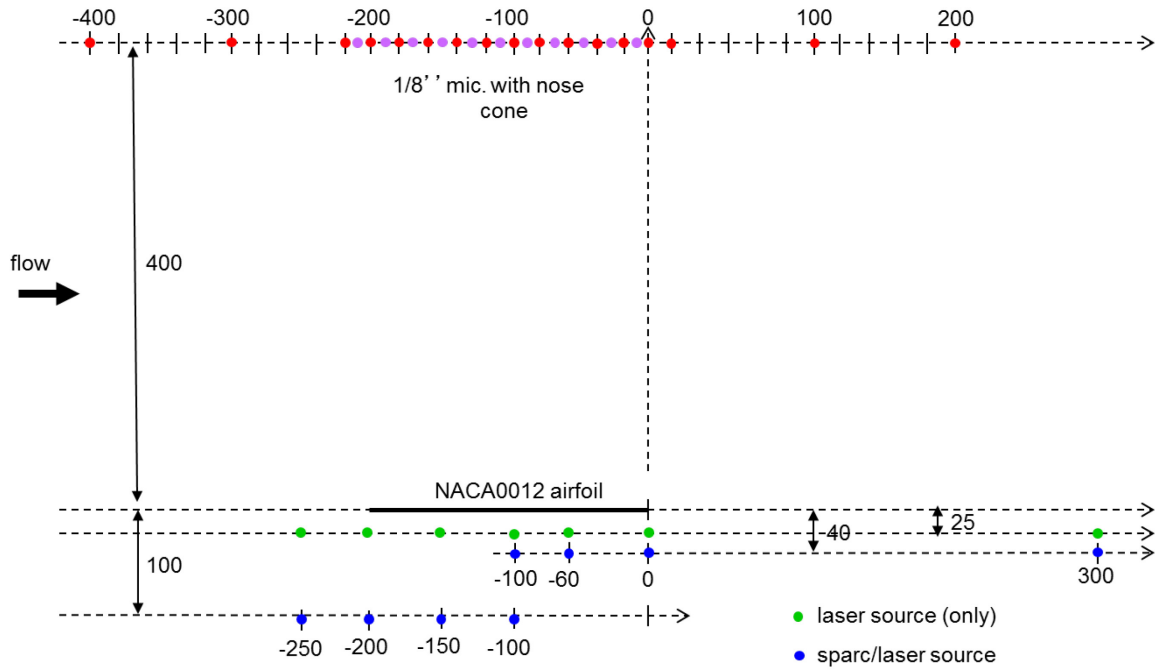

Figure 3-11: Chord and Span Explorations Around NACA Profile. Microphones and sources locations in AWB wind tunnel.

3.1.2 NACA0012 Diffraction Tests in ONERA-F2

The ONERA test campaign in F2 wind tunnel lasted only 1 week dedicated to the tests with the SPARC source (ONERA) and with the laser source (DLR). The experimental setup is presented in Figure 3-12.

The microphone and the SPARC source were moved manually, step by step. Therefore, the test matrix was reduced and limited to one angle of attack (no incidence) and only three positions for the sources (Figure 3-13). The NACA0012 airfoil, 200 mm in chord, was horizontally mounted in the test section of the wind tunnel. The ceiling and the floor of the test section were at 900 mm from the airfoil. The side walls were located 700 mm from the mid-span. The two sources were placed at the same positions (blue dots). Pressure taps were used to adjust the angle of attack at 0 degree only. The static condition (0 m/s) and a 55 m/s flow velocity were tested. The SPARC source pulse rate was 10 Hz and the acquisition time 11 seconds in duration. To characterize the diffraction due to the NACA0012 airfoil, the measurements were implemented in chord and span directions. The sampling rate was 262 kHz and the signals were high-passed filtered at 22 Hz.

For each source located at the same position (SPARC and laser source) and each microphone location, two explorations were performed in static and at 55 m/s in-flow velocity:

- Longitudinal scan (red dots) at mid-span (-200 mm to +200 mm in X).
- Crosswise exploration at mid-span (-10 mm to +250 mm at Y).

Figure 3-14 shows the comparison between the sources: SPARC forming an N-wave and laser source obtained without the airfoil mounted in the test section.

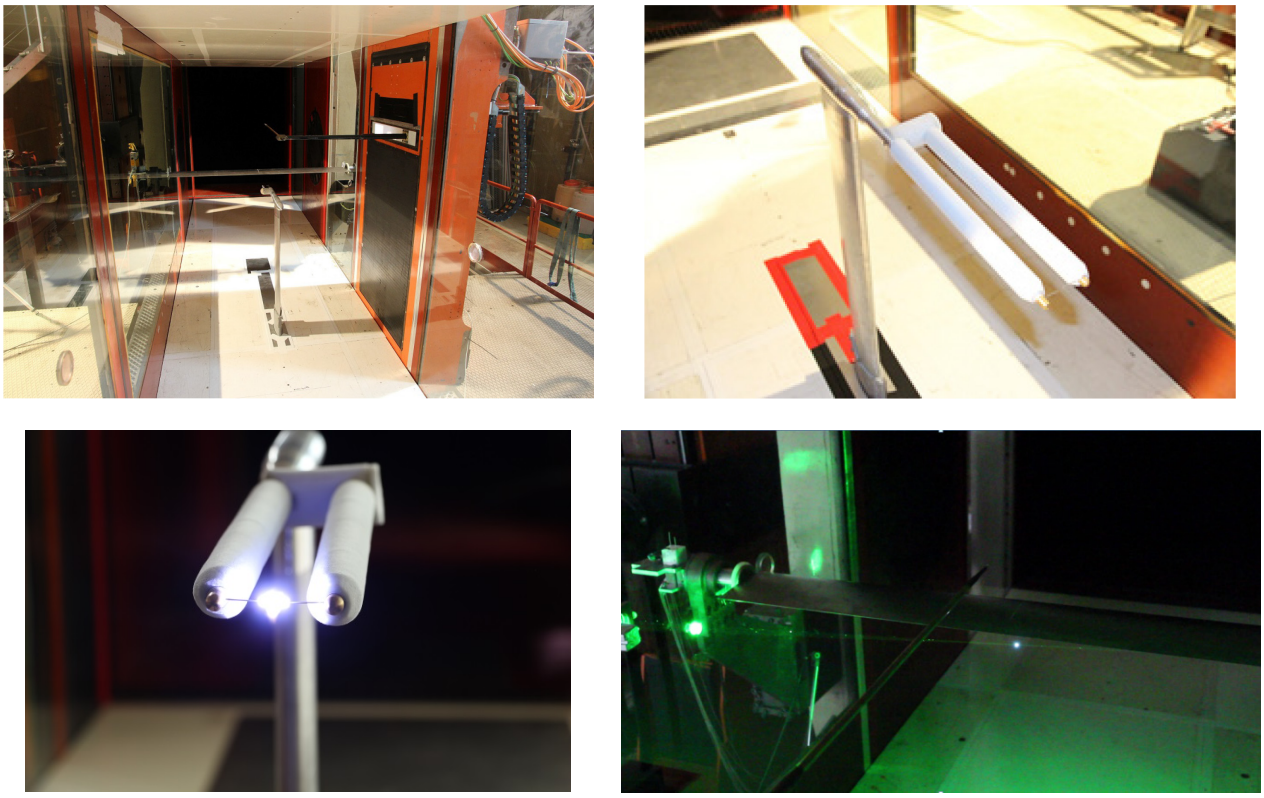

Figure 3-12: Test Setup in F2 Wind Tunnel with the New SPARC Source (Top Right and Bottom Left) and the Laser Source (Bottom Right).

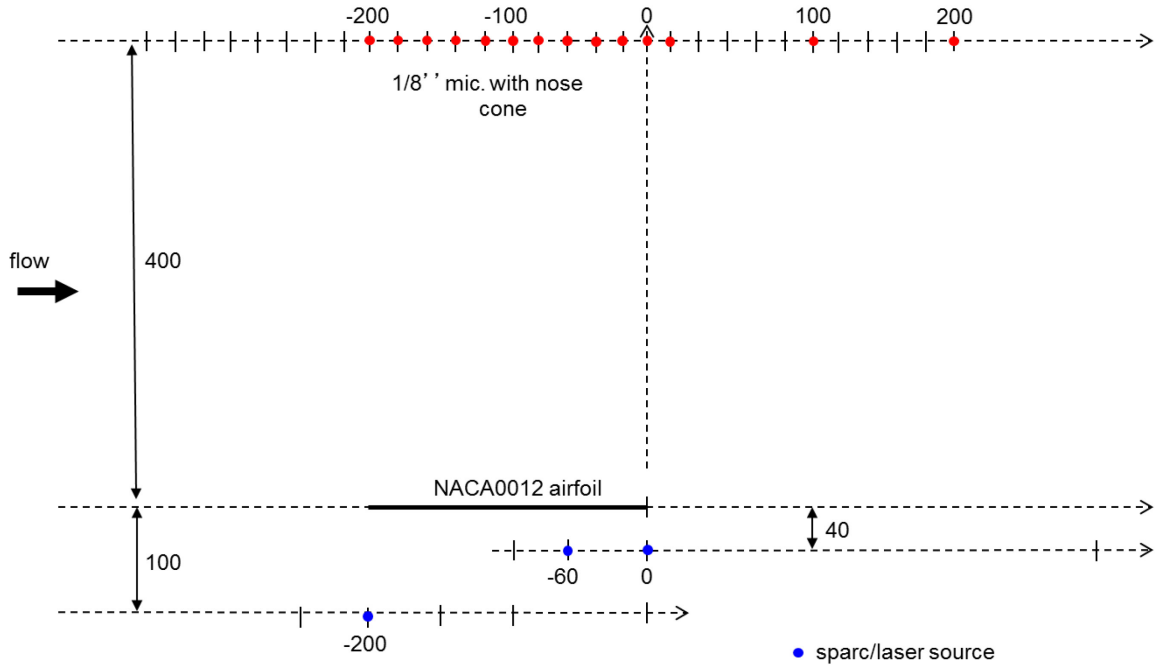

Figure 3-13: Chord and Span Explorations Around NACA Profile. Microphones (red dots) and sources locations (blue dots) in F2 wind tunnel.

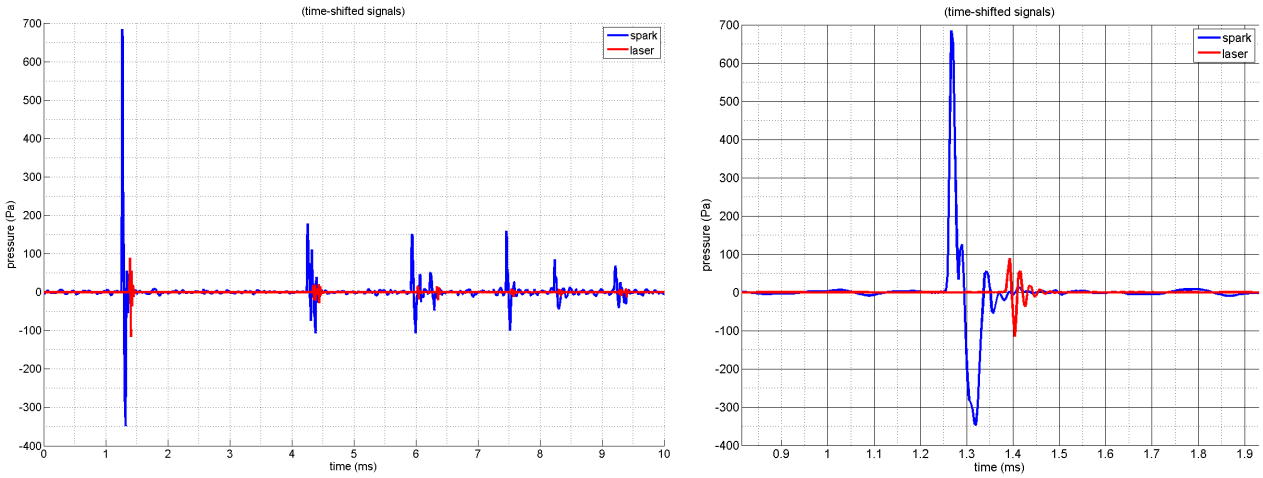

Figure 3-14: N-Wave of SPARC Source (Blue) and Laser Source (Red).

The temporal signals of the SPARC source (blue) and of the laser source (red) are recorded in the configuration without the model in the test section. In the direct wave graph (zoom, Figure 3-14, right), the signals have been deliberately shifted temporally to better bring out their shapes. For both sources, deviations from the expected shape (N-wave for SPARC) are attributed to the microphone nose cone. One can observe large differences in levels and time scales confirmed by spectral analysis shown in Figure 3-15. As expected, the SPARC source is more powerful than the laser source; nevertheless, the latter is not intrusive. In that sense, the two sources are complementary.

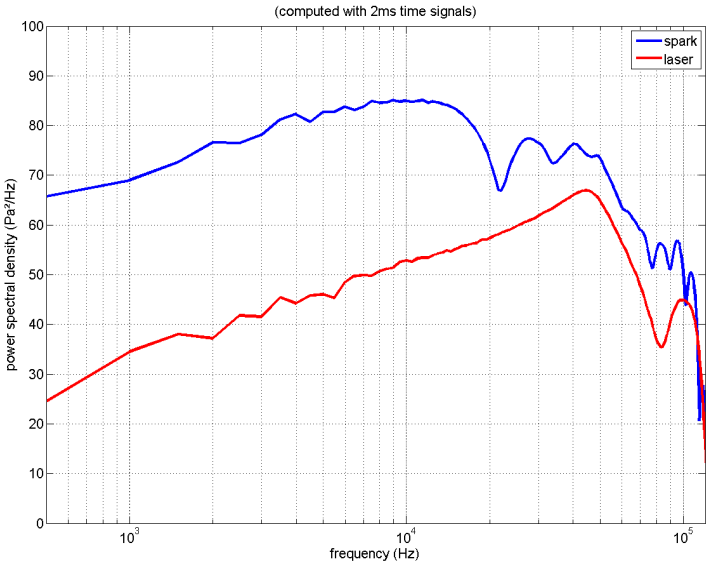

Figure 3-15: SPARC Source (Blue) and Laser Source (Red). Spectra.

The installation effects of the empty test section of the wind tunnel are clearly and identically identified (secondary peaks, reflections) by the two sources. The time delay between the main peak (direct wave) and the first secondary peak (ceiling reflection) is long enough to temporally separate the signals and to quantify the installation effects of the NACA0012 airfoil.

3.1.2.1 Diffraction Studies Based on ONERA SPARC Source

The analysis of the shielding effect due to the NACA0012 profile is firstly performed with the SPARC source located 40 mm below the profile as shown in Figure 3-16.

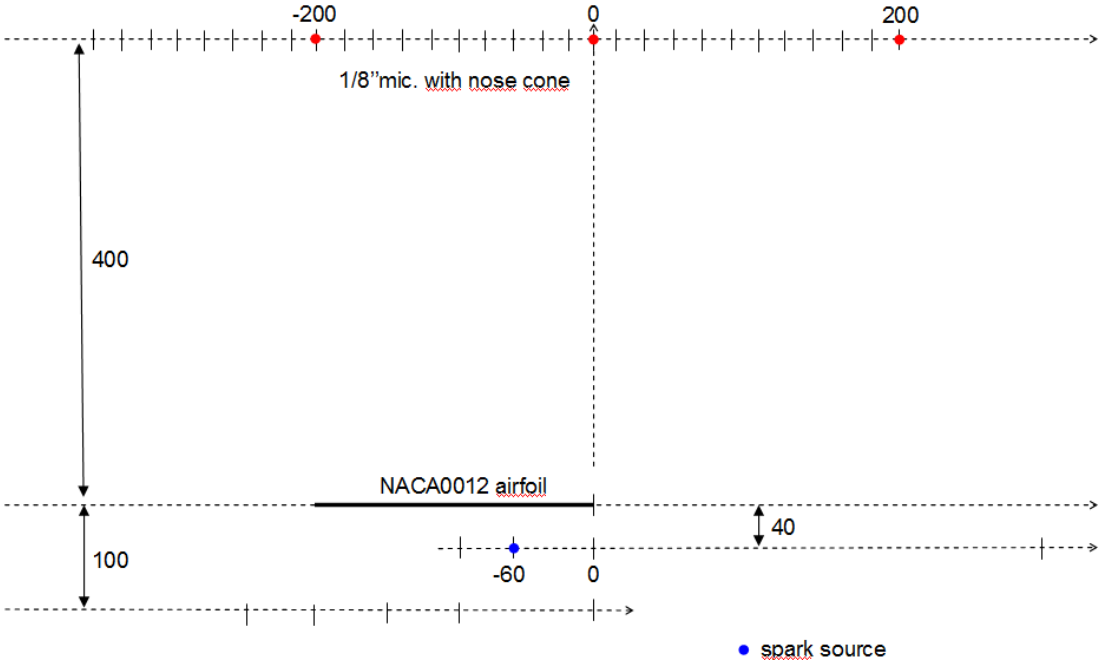

Figure 3-16: Experimental Demonstration of Shielding Effect. SPARC Source (Blue Dot) Location and Microphone Locations (Red Dots).

The time signals, truncated in time to exclude reflections from the wind tunnel walls are shown in Figure 3-17 without airfoil (blue curve) and with airfoil (red curve) for one source position and three microphone positions (referenced on Figure 3-16). For these three positions, the microphone is masked by the airfoil, which brings out the effects of installation by the NACA0012. One can notice that the diffraction is mainly due to the leading edge and the trailing edge.

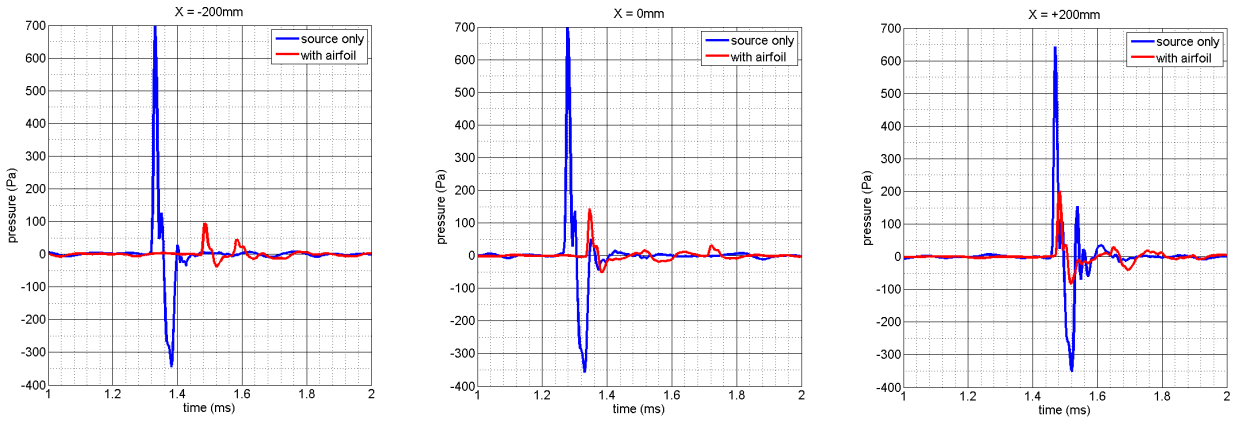

Figure 3-17: Leading Edge and Trailing Edge Effect for Three Microphone Locations. For the upstream position (X = -200 mm, left graph), the red curve clearly shows the contribution of the leading edge (left red peak) and the contribution of the trailing edge as well (right red peak). The time offset is explained by the differences in propagation time.

For the intermediate position (X = 0 mm, center graph), we observe the same tendencies. In this configuration, the contribution of the trailing edge arrives first (left red peak) then the leading edge appears (right red peak), this one being relatively low.

For the downstream position (X = + 200 mm, right graph), the contribution of the trailing edge (red curve peak) is preponderant and slightly delayed compared to the direct field (blue curve peak). This delay is due to the direction of the propagation "source-trailing edge-microphone" which are almost aligned.

In the next section, the sound pressure levels in RMS of the signals are presented which are limited in time to avoid reflections coming from the wind tunnel walls. The results concern the longitudinal and cross-span explorations with and without the NACA0012 installed in the test section (Figure 3-18).

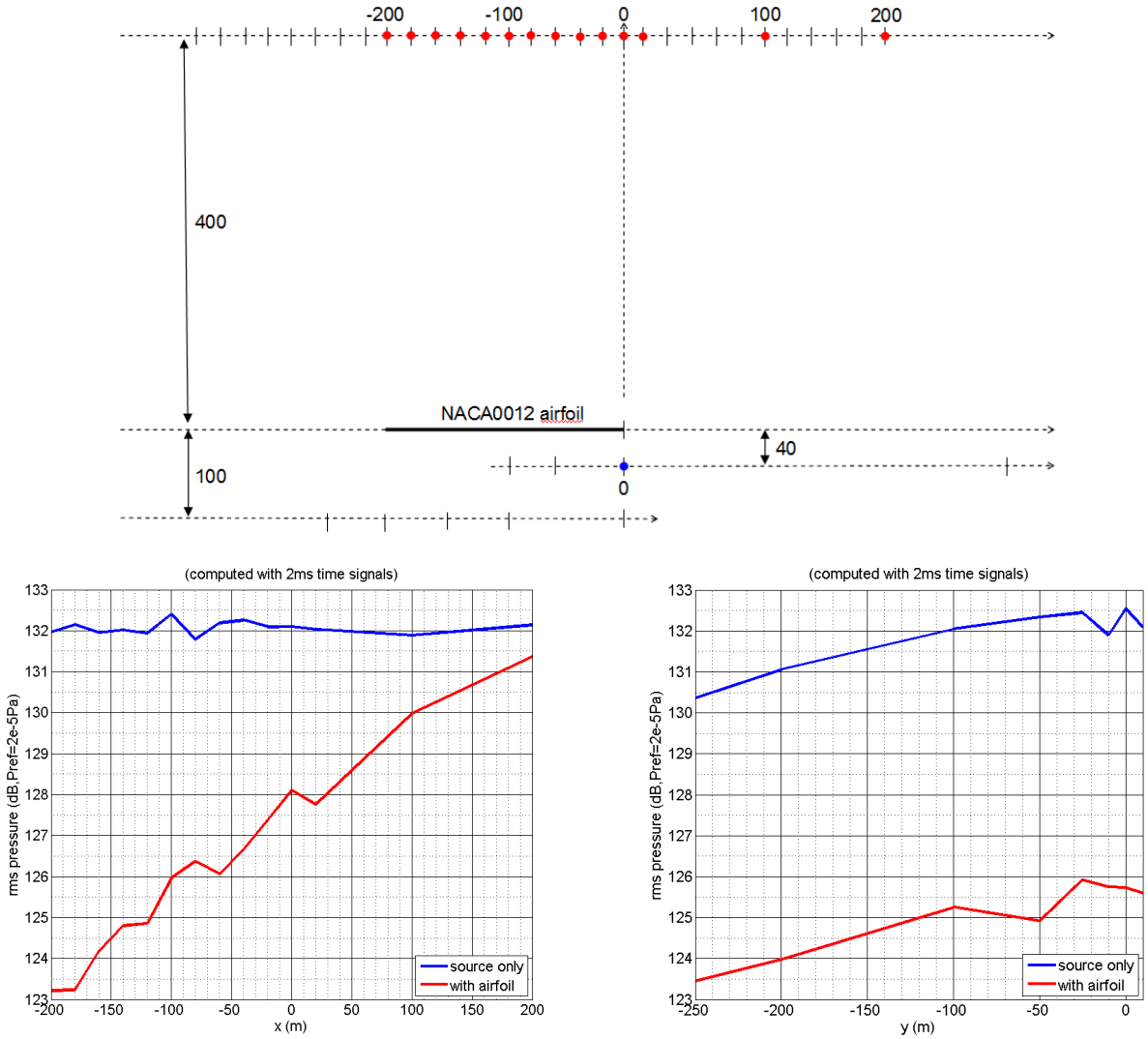

Figure 3-18: Leading Edge and Trailing Edge Effects.

As expected, these results show important installation effects due to the shielding and the diffraction phenomena.

A large database has been collected during the AWB and F2 test campaigns. In a future step, a deeper analysis can provide experimental directivity patterns, frequency by frequency, to be compared with numerical simulations.

3.1.2.2 Diffraction Studies Based on DLR Laser Pulse Source

The realization of DLR's laser-based sound source in the F2 tunnel was done using the same lens and laser setup that was used during the AWB measurement campaign. The complete assembly was mounted on a two-axis displacement system to allow precise positioning of the source about the model surface. Compared to the AWB test conditions, i.e., open test section, the F2 tunnel has transparent Plexiglas walls of 20 mm thickness. Therefore, the laser beam had to go through this wall while being focused near the wing. This, however, proved to be straightforward, and a source of equivalent quality could be produced in both wind tunnels.

As was done in the AWB, acoustic signals were acquired by a GRAS 40DP 1/8" pressure field microphone (provided by DLR) mounted "in-flow" on a traversing arm in the tunnel test section. The signal was acquired using a 262 kHz sampling rate over 11 s sampling duration and was high-pass filtered at 500 Hz. The microphone position relative to the model was set to replicate exactly the AWB experiment. For the comparison of shielding results the source was located at x/c=0.7 and 40 mm above the surface instead of 25 mm. This larger distance from the surface had to be picked to allow for a comparison between DLR's and ONERA's sound sources.

The shielding efficiency of the airfoil was computed using measurements with the airfoil installed in the test section and measurements in the empty test section, as mentioned above.

In Figure 3-19, a comparison is presented between results obtained in the AWB and in the F2 tunnel using DLR's laser-based sound source. Figure 3-19(a) shows the measured attenuation at zero flow condition, while Figure 3-19(b) depicts the respective data for the case of a M = 0.16 flow, both at zero angle of attack. The correspondence between the data taken in AWB and F2 is remarkable. Deviations of at most 1 dB or so in the case with flow are observed between the two entirely different measurement environments. For nonmoving medium the results are practically collapsing into one curve. This result not only shows that the two test setups had been prepared properly, but that the source operated in the AWB was reproduced quantitatively in F2, although a glass wall was between the laser and the source point, while in the AWB there was a (turbulent) free wind tunnel shear layer instead.

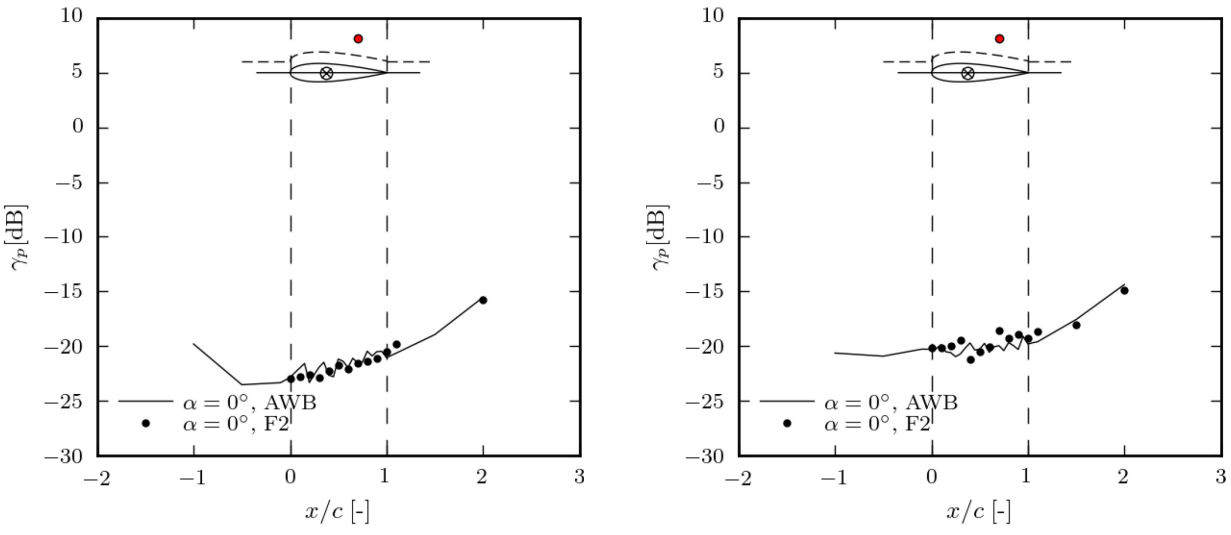

(a) $M_0 = 0$ (b) $M_0 = 0.16$

Figure 3-19: Comparison of Shielding Factors Obtained in AWB vs. F2, Using the Laser Sound Source.

3.1.3 NACA0012 Diffraction Tests in NASA QFF

Test setup: The experimental setup for the NACA 0012 scattering test conducted in the QFF is shown in Figure 3-20(a) and Figure 3-20(b). An NACA 0012 airfoil of 0.91 m span and 0.2 m chord was positioned at the center of the test section. It was supported vertically above the nozzle by the two test section side walls. Each end of the airfoil was mounted to a rotating plate to allow for angle of attack changes. A 1/8" (0.3175 cm) 4138 B&K microphone equipped with a B&K UA 0355 nose cone was used to acquire the acoustic measurements inside the test section. It was mounted on a linear traverse attached to the two test section side walls, while the laser and optic assembly was positioned behind one of the test section walls which was modified to incorporate a 0.95 cm thick tempered glass window.

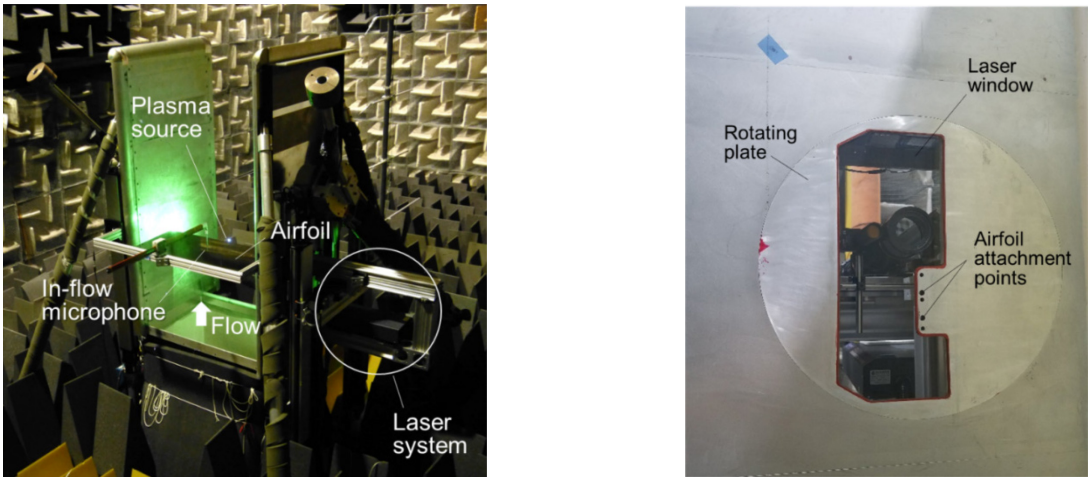

(a) (b)

Figure 3-20: (a) NASA QFF Experimental Setup; (b) Test Section Wall.

The sound source was generated by a high energy, focusing, laser beam. The laser system used was a Nd:YAG, Gemini PIV laser, with an energy pulse of 120 mJ, a wavelength of 532 nm and a pulse width of 3 to 5 ns. As depicted in Figure 3-21, a set of 7.62 cm diameter achromatic, expansion, collimating and focusing lenses was used to focus the laser beam at the test section mid-span to produce a small plasma which rapidly expands to generate a nearly omnidirectional pressure wave that propagates as an isentropic acoustic wave in the far field.

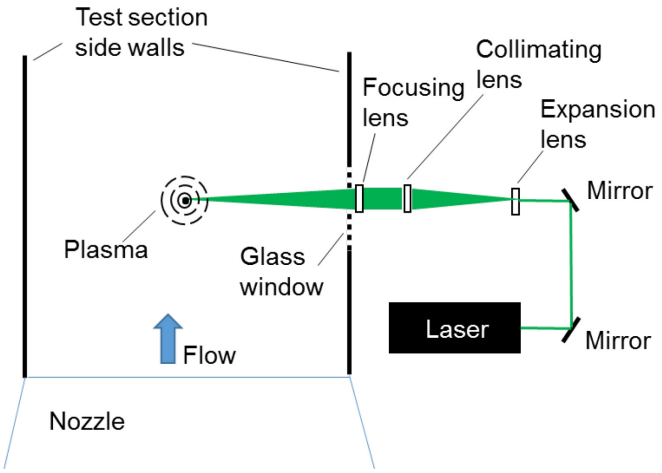

Figure 3-21: Sketch of Laser and Optical Lens Setup.

To minimize laser reflections, the path of the laser beam from the laser head to the test section wall window was encased by installing tubes between optical lenses, and between the focusing lens and the test section wall window (see Figure 3-22). A photodetector was also positioned near the laser window to record the laser-induced plasma (sound source) occurrences.

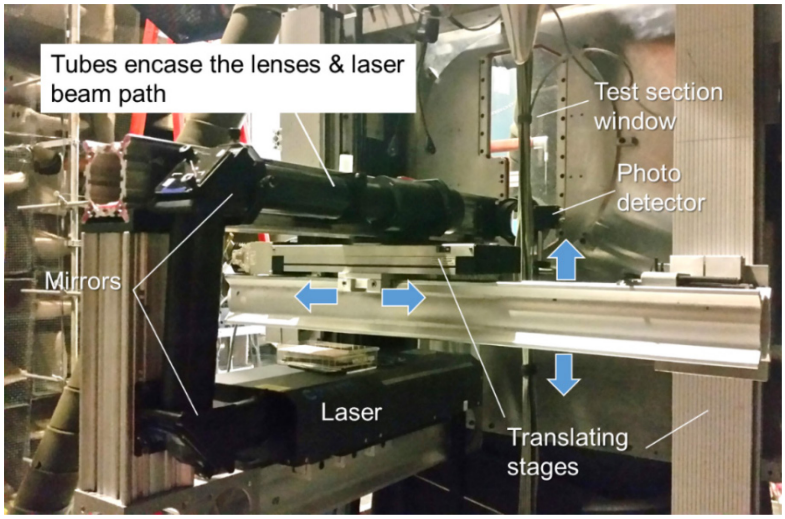

Figure 3-22: Laser and Optical Lens Assembly.

The traverse system used to position the in-flow microphone and the laser/optic assembly is shown in Figure 3-23. It was designed to be compact and rigid in order to minimize flow-induced vibrations. It was used to traverse the in-flow survey microphone in the streamwise direction, and the laser system assembly in both streamwise and crosswise directions to position the sound source at chosen locations.

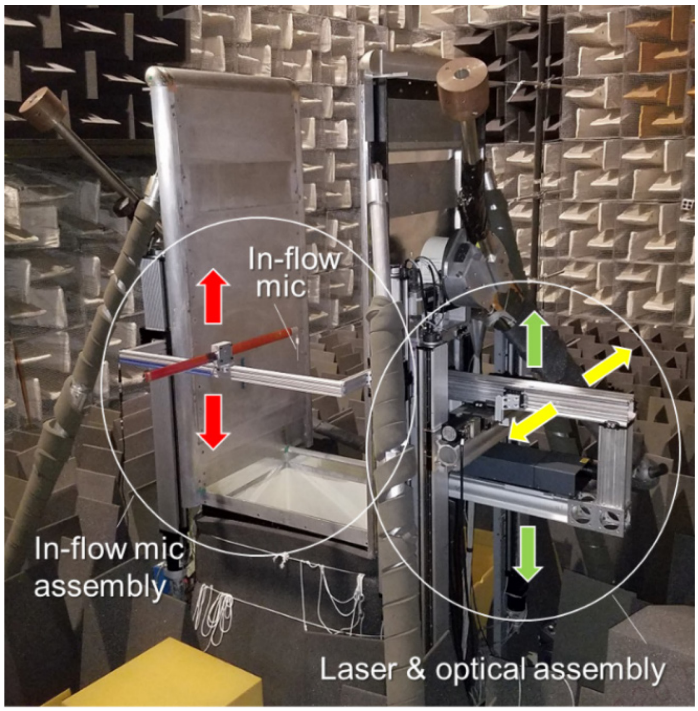

Figure 3-23: Traverse Assembly for the In-Flow Microphone and Laser System.

Test matrix: The test matrix for the NASA QFF scattering test duplicated the DLR test matrix as much as possible. Unlike in the DLR and ONERA experiments, microphone surveys performed two chords (0.4 m) away from the model chord line placed the microphone outside of the test section. Therefore, microphone surveys were performed at this location only without flow, while additional measurements were performed one chord (0.2 m) away from the airfoil chord line, both with and without flow. The survey microphone was traversed in the streamwise direction, up to 200 mm upstream and 400 mm downstream of the airfoil leading edge. The sound source locations and microphone survey locations are depicted in Figure 3-24. The sound source was positioned at a constant distance of 25 mm from the airfoil surface (or from the chord line plane when upstream or downstream of the airfoil). When the source was positioned at 70% chord, additional measurements were acquired with the source at a distance of 40 mm from the airfoil surface. The microphone surveys were performed for three flow speeds (Mach numbers 0, 0.087 and 0.16) and three angles of attack (0° and +/-6°). While the microphone survey locations remained unchanged with changes in airfoil angle of attack, the constant distance of 25 mm (or 40 mm at 70 % chord) between the sound source and the airfoil surface was maintained.

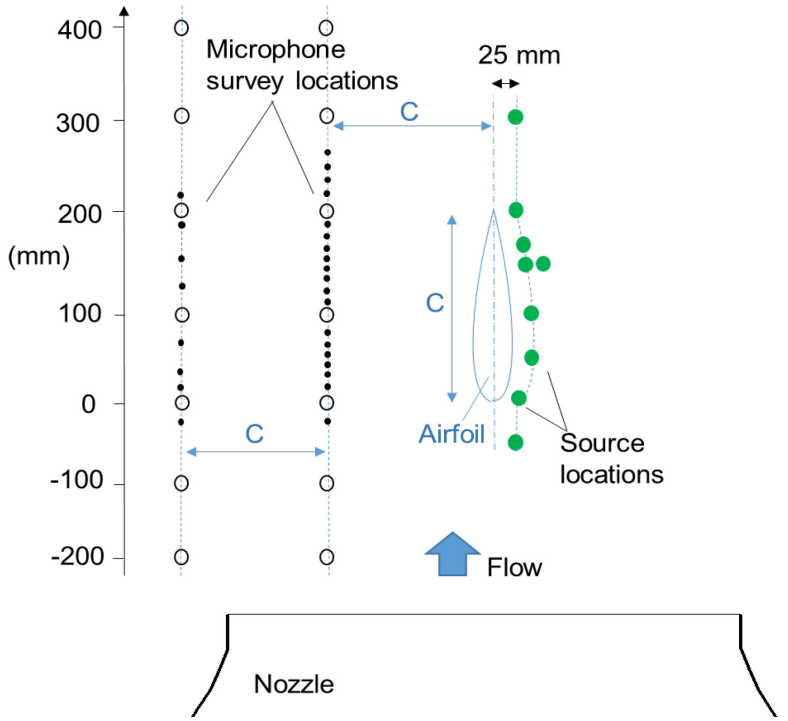

Figure 3-24: Microphone Survey and Noise Source Locations.

Data acquisition and processing: The laser-induced sound source was generated with a repetition rate of 5 Hz, and the survey microphone response was recorded for 20 s, creating time records of 100 acoustic pulses per data point. The Q-switch (laser trigger) and the photodetector signals were also recorded. The survey microphone data were acquired simultaneously with two different sampling rates, 250 kHz (as in the DLR experiment) and 10 MHz (The acoustic datasets acquired at 10 MHz are used for the sample preliminary results presented in Figure 3-30). The low-pass and high-pass filters were set at 100 kHz and 150 Hz, respectively. For the processing of each data point acquired, the acoustic pulses are extracted from the time signals, superposed and averaged. The laser Q-switch and photodetector signals are used in this process to properly extract and superpose the acoustic pulses. Spectra are then calculated for the averaged (or individual) pulses using data blocks that are zero-padded to the number of samples needed to obtain a frequency resolution of 61 Hz.

Analysis and results: The repeatability of the acoustic pulse generated by the laser-induced sound source was monitored and verified throughout the test by repeating the acquisition of a reference data point at different stages of the test. The averaged waveforms produced by the sound source for the data points acquired near the beginning, midportion and end of the test are shown in Figure 3-25. The signal waveforms recorded by the microphone are seen to be nearly identical, demonstrating the repeatability of the sound source produced by the laser system. For these sound source repeatability checks, as depicted in Figure 3-25, the airfoil is positioned at 0° angle of attack, the flow Mach number is 0, the sound source is positioned 120 mm downstream of the airfoil trailing edge (and 25 mm from the chord line plane), while the microphone is positioned 1 chord away from the airfoil and 100 mm downstream of the airfoil trailing edge.

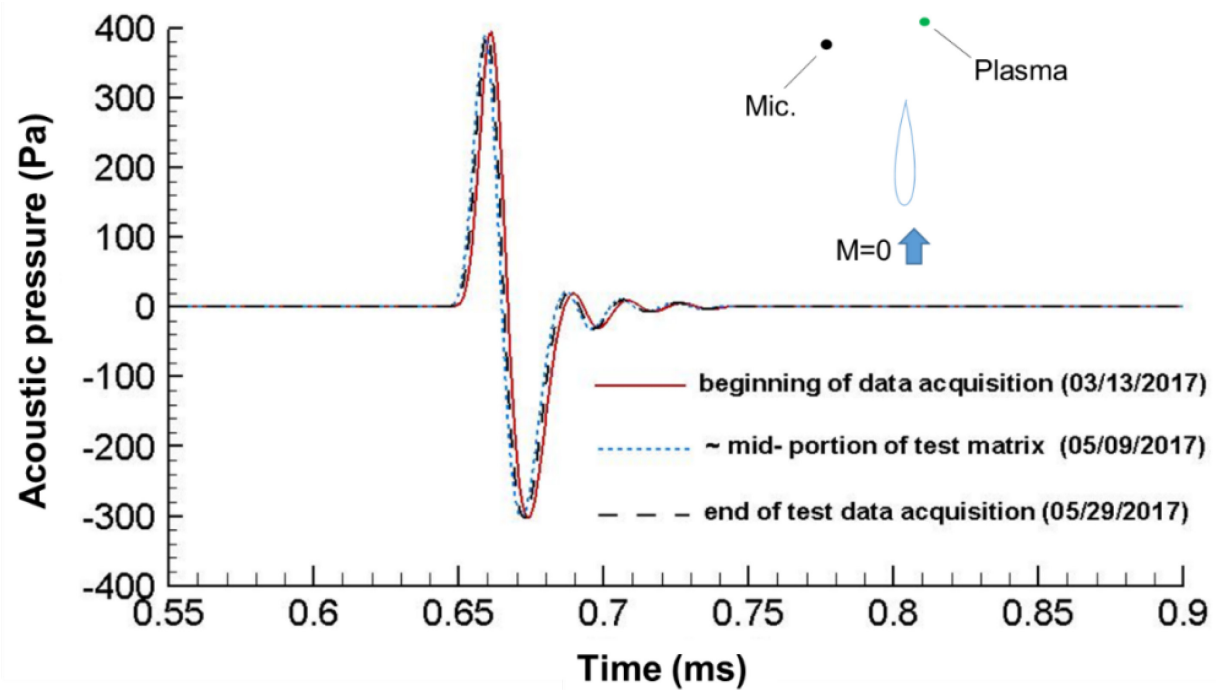

Figure 3-25: Laser-Induced Sound Source Waveform Repeatability.

The directivity of the sound source was also characterized. This was done from the acoustic measurements of the unshielded sound source performed over a broad range of microphone locations at Mach 0. The raw and free-field corrected spectra obtained from these acoustic measurements are presented in Figure 3-26. The sound pressure levels shown are adjusted to a distance of 0.2 m, and no atmospheric correction is applied. The collapse of the free-field corrected spectra seen in this figure is consistent with the expected omnidirectional ("monopole-like") character of the sound source. Note that the spectra corresponding to the 143° and 150° directivity angles (shown as red curves in Figure 3-26) were obtained from measurements acquired with the microphone positioned the farthest away from the sound source. Applying atmospheric corrections to these datasets would improve the collapse of these two spectra with the rest of the data.

Examination of the microphone time signals acquired with the wind tunnel flow turned on revealed the presence of low frequency noise contamination. An example of a contaminated microphone signal is displayed in Figure 3-27. For this test case, the flow Mach number is 0.16; the airfoil angle of attack is 0°; the sound source is aligned with the airfoil trailing edge; and the microphone is positioned 100 mm downstream of the airfoil leading edge (and one chord away from the airfoil). This sample signal also shows the occurrence of what appears to be flow-induced "ringing" which shows up as a small bump in the spectra near 30 kHz (as seen in Figure 3-28). The cause of this "ringing" remains under investigation, while the low frequency noise contamination was eliminated by applying a 2 kHz high-pass digital filter to the data.

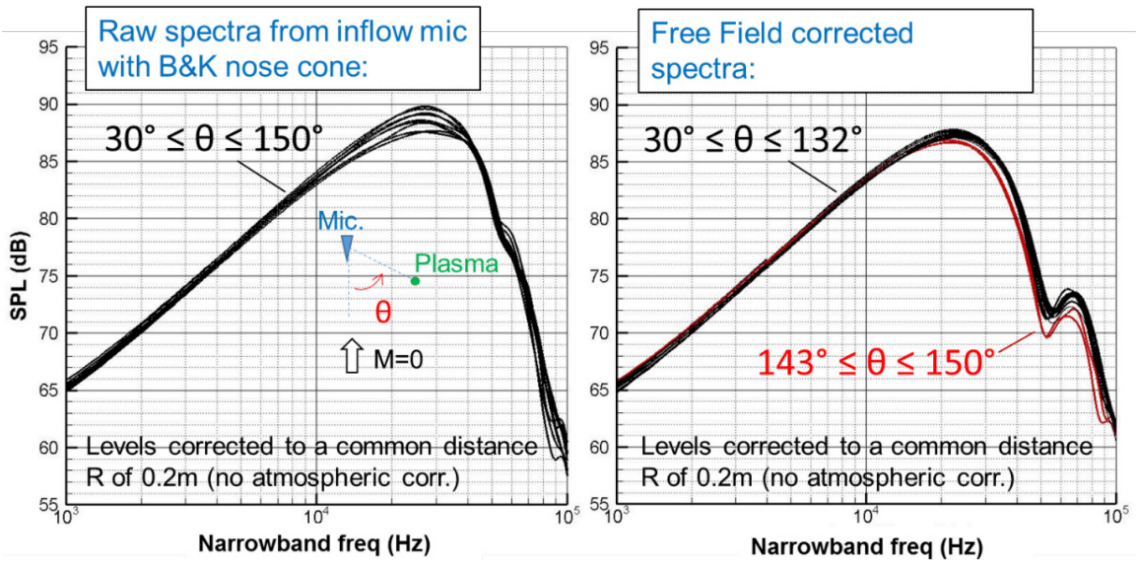

Figure 3-26: Sound Source Directivity.

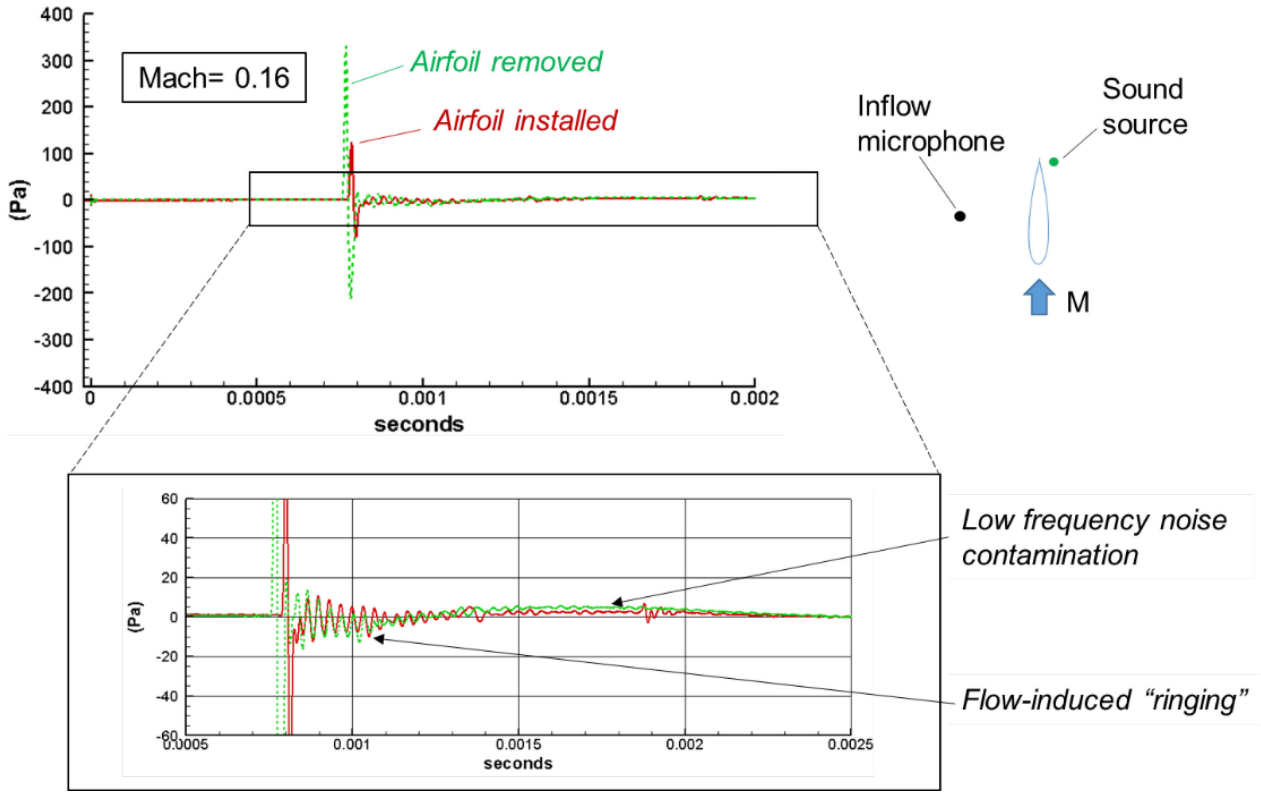

Figure 3-27: Flow-Induced Noise Contamination.

The impact of the low frequency noise contamination on the spectra and shielding levels obtained with and without the application of the 2 kHz high-pass digital filter is shown in Figure 3-28 for the same test case as in Figure 3-27.

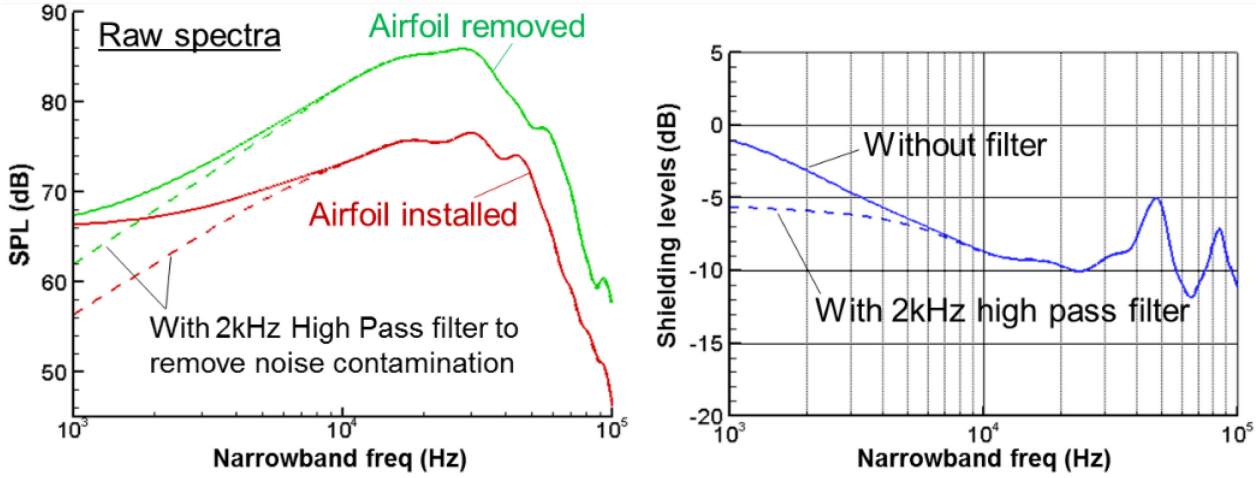

Figure 3-28: Effect of Low Frequency Noise Contamination on Spectra and Shielding Levels (Flow Mach Number of 0.16).

Finally, the last main step in the post-processing of the acquired test data is the calculation of the integrated shielding levels (shielding factors), which were defined in Equation (3-1). The integrated shielding levels calculated with and without flow for the test case where the sound source is aligned with the airfoil trailing edge are shown in Figure 3-29. It is seen in this figure that the presence of the flow leads to a small decrease in shielding levels. This finding is in agreement with that reported by DLR for the same test configuration. It is noted that the shielding factors for zero angle of attack from Figure 3-6(e), Figure 3-6(f) correspond quantitatively strikingly well with those in Figure 3-29.

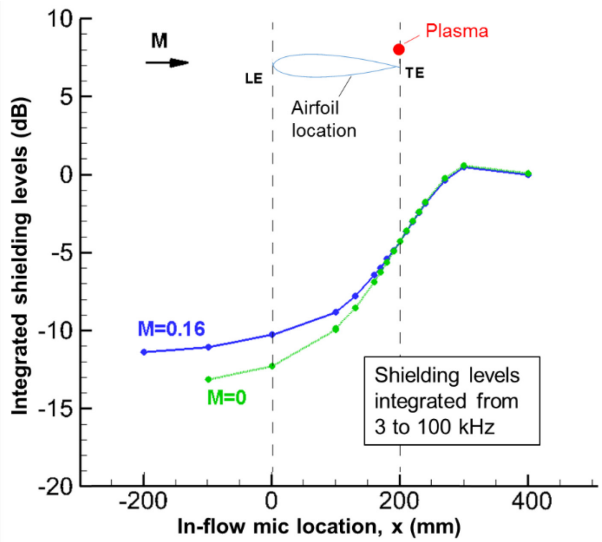

Figure 3-29: Integrated Shielding Levels, Source at 25 mm Above the Surface (Survey Microphone Positioned 1 Chord Away from the Airfoil Chord Line).

Plot for NASA/DLR/ONERA data comparison: A key objective of this AVT group was facility-to-facility comparison for the NACA 0012 scattering experiment. Figure 3-30 shows a comparison among the DLR-AWB facility and the NASA QFF facility. The distribution of the QFF shielding factor values along the chordwise direction corresponds well with the reported data from AWB to within 1 – 2 dB. Earlier, Figure 3-19 showed the comparison between the AWB and the F2 results. Therefore, overall, this is considered as excellent facility-to-facility comparison for the three experiments.

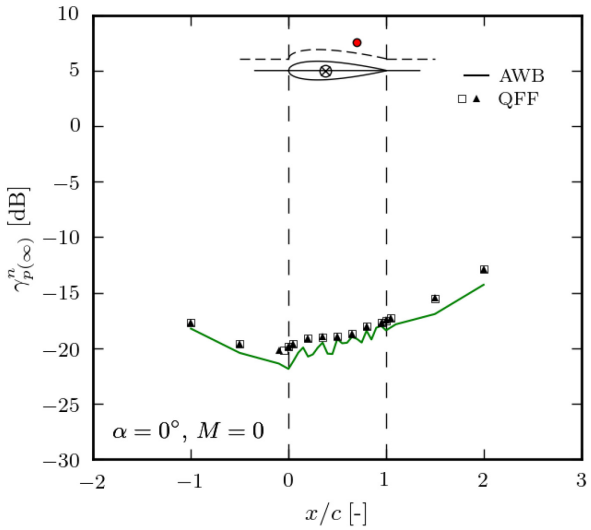

Figure 3-30: Integrated Shielded Levels as Measured in QFF and AWB. Sound source at 70% chord and 40 mm above the airfoil surface, survey microphone 2 chords away from airfoil, M = 0. QFF microphone data sampled at 10 MHz and 2 kHz high-pass digital filter applied, shielding level integration 5-80 kHz.

3.2 COMPUTATION OF 2D DIFFRACTION

The prediction of the 2D diffraction / shielding of the NACA0012 airfoil was chosen as a valuable test case because it is simple enough to resolve all propagation effects, which may be relevant (turbulent scattering excluded). The various simplifications made starting from the Linearized Euler Equations (LEE) to Acoustic Perturbation Equations (APE) (or ray-theory) to BEM on the one hand and simplified flow representations from RANS to Euler to uniform flow to eventually compute the 3D aircraft geometries may be introduced step by step. Consequences of these simplifications become visible more easily on the relatively simple shape of a 2D airfoil. In that sense, Section 3.2 is devoted to preparing simplifications used later on in Chapter 4.

3.2.1 Computations with Aeroacoustic Prediction Concepts of DLR

The shielding predictions which will be investigated here are all based on a high-fidelity volume resolved method. While volume resolved methods are very expensive regarding computation time, they are the only way to consider arbitrary mean flow fields. This allows resolving refraction phenomena in boundary layers or wakes.

Hence, the major goal of the DLR volume resolved computations is to investigate the importance of mean flow fields. This can especially give support to cheaper methods as long as it turns out that the mean flow effects are of minor importance.

For the sake of completeness it should be mentioned that also volume resolved computations suffer from difficulties, the biggest to mention is the problem of boundary conditions in the far field. A perfect simulation would consist of a very large computation domain such that the boundary effects are negligible.

However, since large domains are way too expensive to compute, they must be restricted to a very small domain. As a result, it must be ensured that the outer boundaries do not affect the inner computation domain. In other words, reflections at the boundaries must be very small.

3.2.1.1 Numerical Approach

The transport of acoustical waves is computed by discretizing the Linearized Euler Equations (LEE) or the Acoustic Perturbation Equations (APE) in time and space. The utilized solver PIANO [24] solves the equations on curvilinear block-structured meshes with a 4th order Dispersion Relation Preserving (DRP) scheme for space discretization and integrates in time with a 4th order Runge-Kutta scheme.

The outer boundaries of the computation domain are defined as a radiation condition [25]. This leads to negligible reflections for the given setup of a point source over an airfoil. The airfoil walls are defined as slip wall conditions where wall normal fluctuations are set to zero.

The background mean flow is computed with the flow solver DLR-TAU-Code which solves the RANS equations. In the present computations, turbulence was simulated by applying two-equation a k-omega turbulence model. The far field conditions are Ma = 0.16, Re = 800,000 (based on the chord length). The angle of attack is set to zero.

The sound source is setup in a way to simulate the laser pulse as described in Chapter 2. It is approximated as a point source which very locally adds heat to the acoustic computational domain. The time dependent heat flux is approximated with a temporal Gaussian distribution as shown in Figure 3-31. The heat point source is added in such a way that it follows the mean flow as time passes by.

In order to determine the shielding value, additional simulations were performed for a reference case without the airfoil being present. The reference case uses a constant mean flow which coincides with the far field conditions of the airfoil simulations.

The computational meshes contain about 5 million grid points and are constructed such that it resolves frequencies up to 80 kHz. Figure 3-32 shows the blocks of the computation mesh. The time dependent pressure signal of a LEE computation is shown in Figure 3-33.

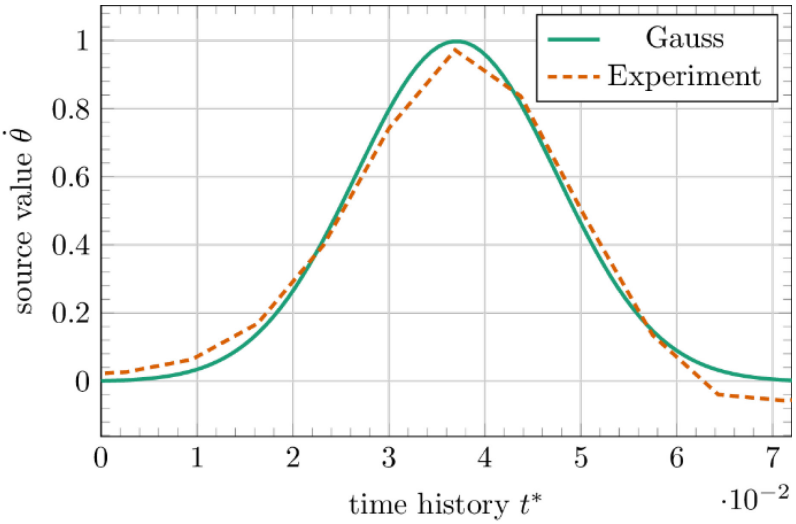

Figure 3-31: Time Dependent Heat Flux Used as Source Term for Acoustical Simulations. Instead of using the original experiment, a smooth fit of a Gaussian distribution is used.

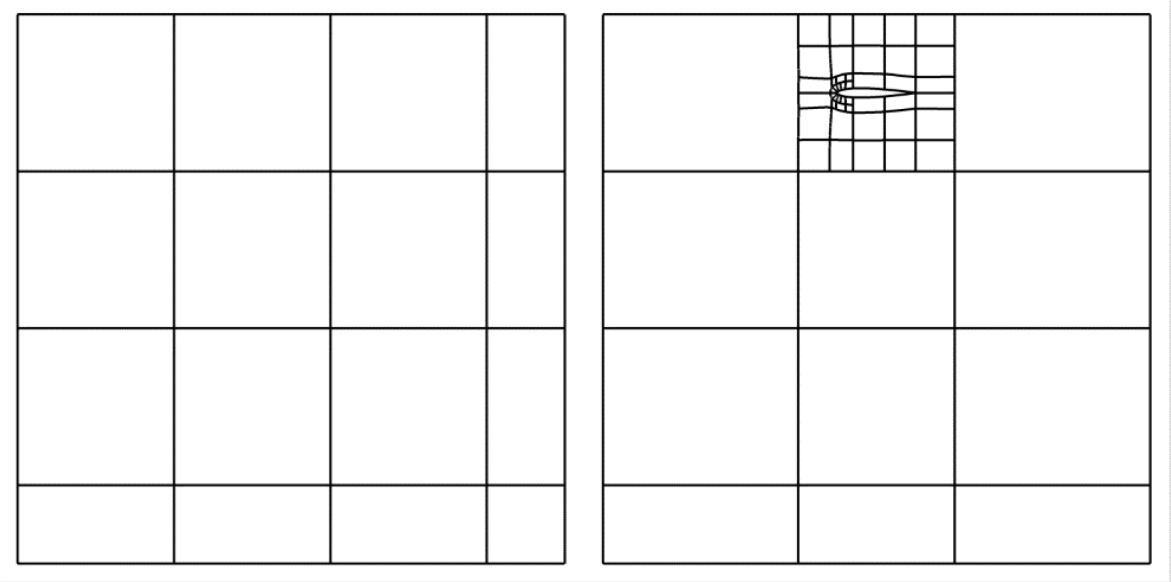

Figure 3-32: Blocks of Computation Meshes for the Reference Case Without Airfoil (Left Hand Side) and the Case with Airfoil (Right Hand Side).

Figure 3-33: Numerical Simulation of Propagation of Pressure Signal Induced by Laser Pulse Source, DLR CAA Code PIANO.

In this respect, it is interesting to observe that plotting in the density perturbation instead of the pressure perturbation, the solution shows an additional contribution. As expected, when a heat source is applied, not only a pressure pulse, but also a density spot is initiated, the latter of which gets convected downstream. One concern here is that the acceleration along the airfoil contour and/or the interaction of this (pressureless, i.e., entropy related) density spot at the airfoil's trailing edge could generate sound. Figure 3-34 shows the density perturbation of the heat pulse in the form of the entropy and acoustic part as it evolves in time. Indeed, no significant sound generation may be seen.

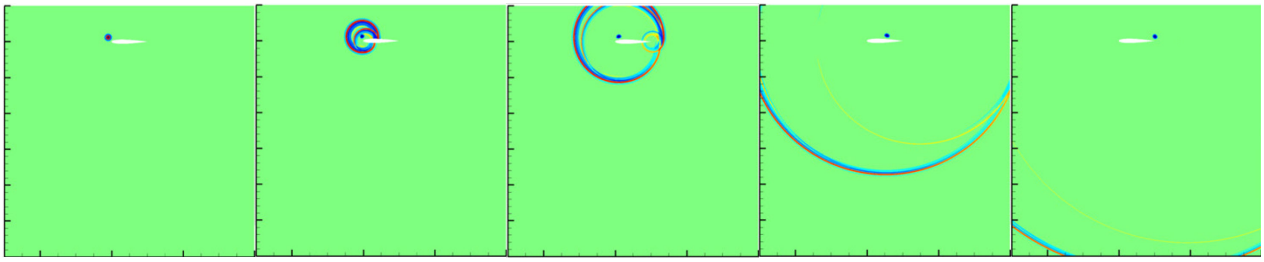

Figure 3-34: LEE Based Numerical Simulation of Propagation of Density Signal Induced by Laser Pulse Source, DLR Code PIANO. (Simulation by Oliver Günther, Student at TU Braunschweig).

3.2.1.2 Data Processing, Representation in Spectral Domain

The shielding value as used in the following is defined as the ratio between the root mean square of the pressure at an observer point for a simulation with airfoil and the root mean square of the pressure at the same observer point for a simulation without airfoil. The shielding level γ as it will be used in the following is the defined as ten times the logarithm of the shielding value.

In order to generalize the results, the pressure fluctuations will be transformed into the frequency space. This allows computing the shielding level for specified frequencies. Note, that by evaluating only specific frequencies, the results become almost independent of the temporal variation of the source variation itself. Thus, changing the source variation as shown in Figure 3-31 would not change the frequency dependent shielding levels.

3.2.1.3 Computational Results

The present section will devote itself to the different phenomena of shielding in respect to both the numerical setup and mean flow effects. It will be shown that using the APE is valid for airfoil shielding and how strongly the mean flow affects the shielding value. The microphone positions for the directivity plots are always placed in a circle around the source pulse (see, e.g., Figure 3-35).

Figure 3-36 shows the shielding results for a pressure pulse directly over the airfoil using LEE and APE. The results are very similar. Differences can hardly be recognized. Hence, all further computations are accomplished with the APE which show a more robust behavior than the LEE. However, note that for completely different setups where high mean flow density gradients are present, re-evaluation of the situation may be required.

One may observe certain characteristics of the attenuation, $\gamma_p = 10\log_{10}\left(\frac{p_s}{p_i}\right)$, evaluated frequency-wise. At low frequency, i.e., when the wavelength of the sound is large compared to the curvature radius of the edges, a symmetric shielding lobe pattern is obtained. As the wavelength increases (10 kHz) the (now multi-lobed) pattern becomes non-symmetric. Finally, at 60 kHz the wavelength is on the order of the leading edge curvature radius, and clearly, an even globally non-symmetric lobe pattern occurs. On average the attenuation to the left is about 5dB lower than to the right. The diffraction loss around the rounded leading edge is obviously smaller than around the sharp trailing edge. This difference is of interest for ray-based computation approaches, which may require the consideration of creeping rays in this case.

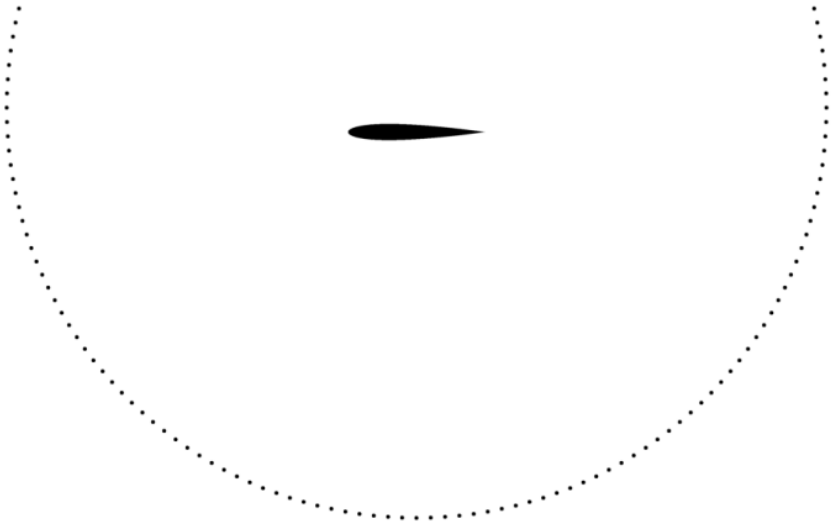

Figure 3-35: Position of Microphones Around the Airfoil for Creating Directivity Plots for a Pressure Pulse Directly Over the Airfoil (Every Fifth Microphone is Plotted).

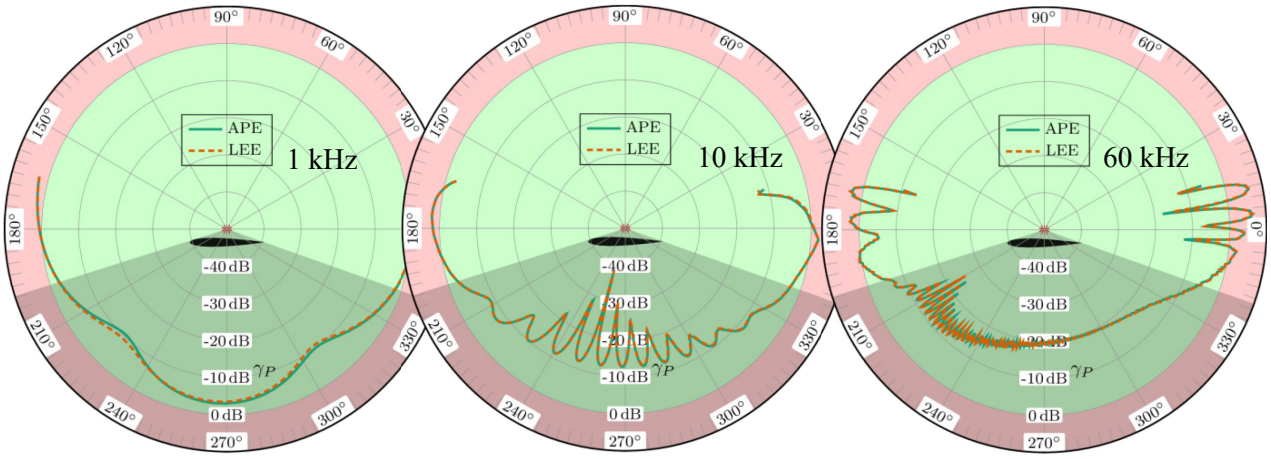

Figure 3-36: Shielding for Different Frequencies for a Pressure Pulse Directly Over the Airfoil for APE and LEE.

Next the significance of the mean flow is evaluated in Figure 3-37, Figure 3-38, and Figure 3-39. Figure 3-38 shows the solutions for several mean flow settings of a source position behind the airfoil. Four different cases are compared:

1) Viscous flow: Here the mean flow is computed with the RANS equations, no-slip walls and a k omega turbulence model. This is the only case where a boundary layer develops.
2) Slip walls: Due to the missing slip condition no boundary layer develops over the airfoil and hence turbulence is also ignored.
3) Constant mean flow: In this case a spatially constant mean flow (Ma = 0.16) is applied.
4) No mean flow: The mean flow is set to zero everywhere.

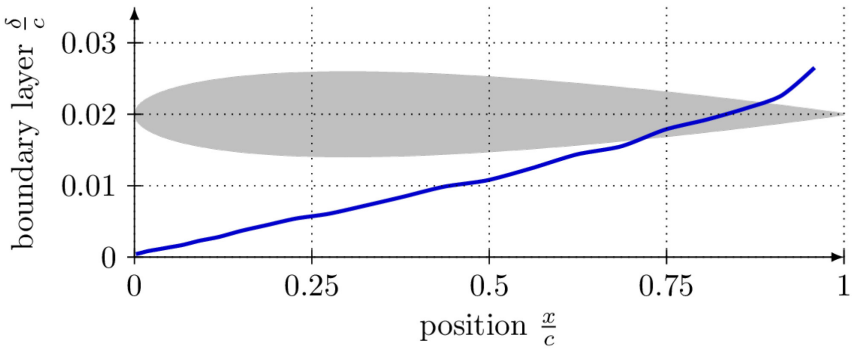

Figure 3-37: Boundary Thickness Divided by the Chord Length at Different Airfoil Positions.

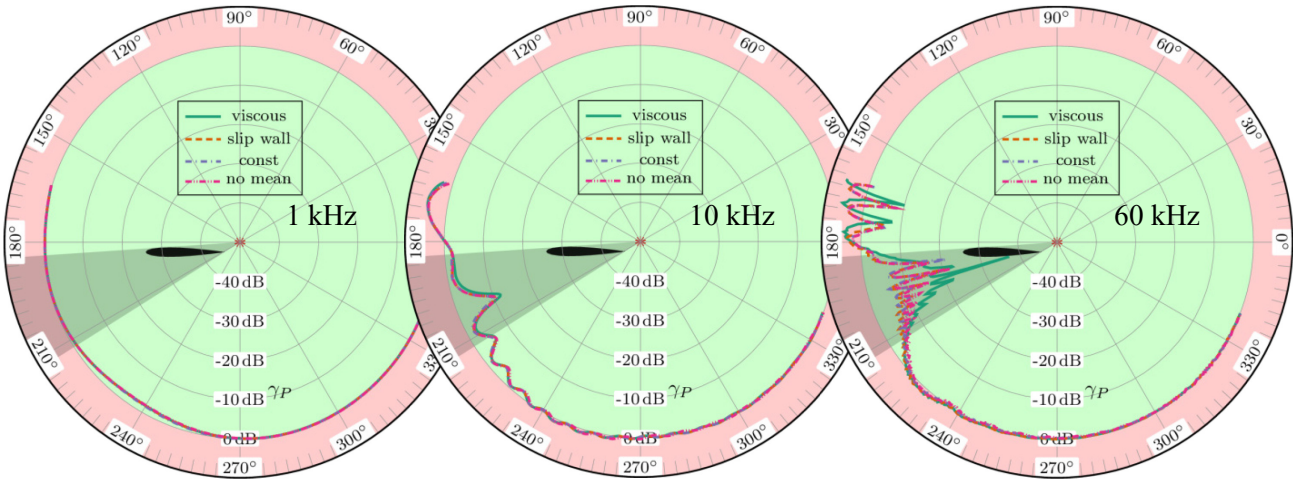

Figure 3-38: Frequency Dependence of Directivity of Acoustic Attenuation Due to Laser Pulse Initiated Downstream of Trailing Edge for Various Flow Field Simplifications (Numerical Solution of APE About RANS Background Flow).

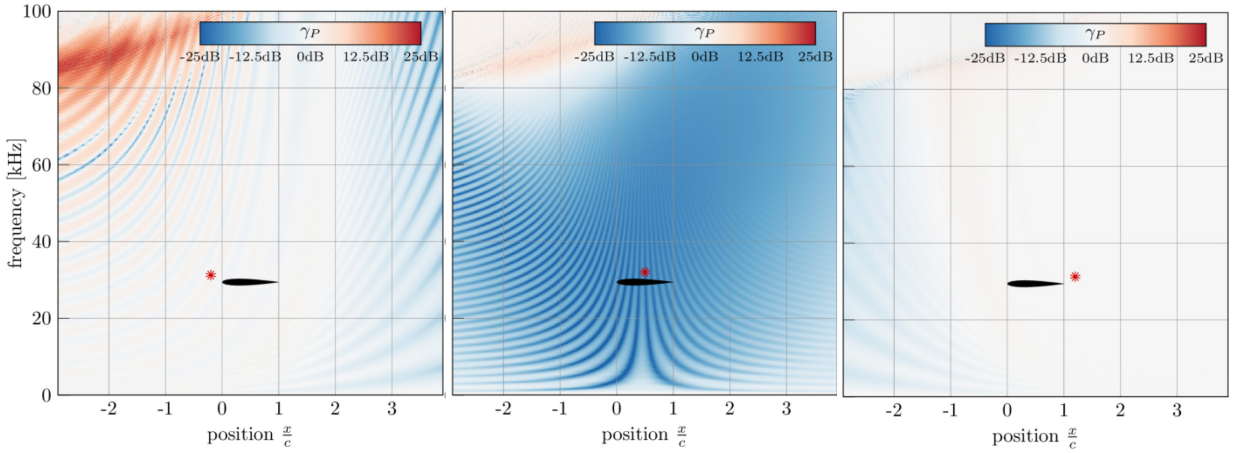

Figure 3-39: Shielding Overview for Different Frequencies and Positions Under the Airfoil. The microphones for these plots are located two chord lengths below the airfoil. The laser pulse position is shown in the picture as a red star.

For the relatively small frequency of 1 kHz (corresponding wavelength is about λ/c = 1.7) and hence a wavelength longer than the airfoil, the shielding is hardly influenced by the mean flow. A slight decrease of noise that can be recognized for all cases at 240° is accounted to destructive interference phenomena between the direct source and the diffraction related secondary source at the trailing edge. As the wavelength shortens to smaller values (10 kHz, λ/c = 0.17), shielding effects become visible. While they are all similar for the different mean flows, the case with viscous mean flow starts to show small differences. At 60 kHz (λ/c = 0.028) the wavelength is in the range of the boundary layer thickness (see Figure 3-37 for the boundary layer thickness along the airfoil). Refraction phenomena start to play a role as can be seen by the fact that the interference patterns of the viscous case differ clearly from the other cases. Even though the plot cannot provide accurate comparisons, it is assured that in the directly shielded zone, the viscous case shows stronger shielding levels, up to about 10dB higher. This is credited to refraction of waves in the boundary layer, which let the airfoil appear thicker than geometrically. Consequently, also the reflection lobes in the upper forward direction rotate to smaller polar angles, which can only barely be seen for the 10 kHz case. In contrast, the slip wall and constant mean flow cases are very similar at all available microphone positions. The no mean flow case is similar to the other non-viscous cases everywhere but in the direct shielding zone where it shows a different interference pattern. This accounted to the fact that the source itself is not moving in the no-mean flow case.

The outcome of comparing different mean flows is that viscous mean flows will only become necessary if high frequencies are considered (wavelengths on the order of the boundary layer thickness). Using no-slip mean flows hardly provide any advantage over constant mean flows. In most cases even zero mean flow is sufficient. Hence, in the current setup, computationally cheaper methods which cannot consider arbitrary mean flows are expected to show very good results. However, for high frequency sources, high-Mach number cases or more complex geometries, re-evaluation of the situation may be necessary.

In the last section, increased focus is laid on the interference phenomena at different frequencies. Therefore, the case with viscous mean flow is selected and evaluated for three different source positions. Observer points are positioned along a line two chord lengths below the airfoil. The results are shown in contour plots in Figure 3-39. The interference patterns which were quickly addressed in the previous section become nicely visible. The structures become finer as the frequency increases. Frequencies above 80 kHz cannot be resolved anymore by the grid. When looking at the central source position, one may directly compare with Figure 3-36. Clearly, the mentioned symmetry pattern as observed for low frequencies, gradually disappears as the frequency increases. Note that for the source positions left of the leading edge and right of the trailing edge, even some relevant level increase may occur on the source-ward side due to constructive interference of the direct with the diffraction source at the edge. At the leading edge this effect is clearly stronger due to its finite thickness and it increases with frequency.

3.2.1.4 Conclusions

The high-fidelity volume resolved computations help to evaluate the influence of the mean flow on the shielding levels. In the present 2D setup the mean flow effects are rather low which gives support for cheaper methods which only account for constant mean flows.

The next challenge is to extend the investigations into 3D-space. The main difficulty here is that the computational domain must be restricted to a much smaller domain in order to keep the computational cost at a feasible level. However, this will strongly increase the influence of the far field boundaries, and ways must be found to keep them low enough that it will not spoil the shielding results.

3.2.2 Computations with Aeroacoustic Prediction Concepts of BAE Systems

BAE Systems evaluated two types of computations for the 2D NACA0012 airfoil. The first technique is a ray-tracing approach utilizing a barrier prediction method for the shielding calculations. The second

technique is with the BAES Altus time domain Discontinuous Galerkin solver which is used to solve the LEE with and without mean flow. For the with flow cases the mean flow field is calculated using a RANS solution using the ANSYS CFX code. Descriptions of the computational techniques and the results for the 2D airfoil are presented with and without the presence of flow and comparisons made with wind tunnel test data and CFD/CAA based results in the following subsections.

3.2.2.1 Ray-Tracing Prediction Approach

In this section a ray-tracing prediction method using a barrier shielding method and a geometry reduced to its simplest form is described. The method was implemented as the basis of a prediction method for the shielding of a 2D airfoil in the presence of flow.

A representation of the acoustic paths around a NACA0012 airfoil is presented in the left hand diagram in Figure 3-40. As may be observed, there are two paths for an acoustic wave from the acoustic source to the receiver, one shown in green around the curved leading edge of the airfoil and the other shown in blue around the sharp trailing edge of the airfoil. This source-receiver path geometry may be simplified to that represented in the right hand diagram in Figure 3-40 where the airfoil is replaced with a thin flat plate shown in red. The main difference between these two geometrical representations is that there is a small path length difference around the leading edge path. This path length difference will result in an error in the computed attenuation values at high frequencies when the wavelength becomes a significant proportion of the path length difference.

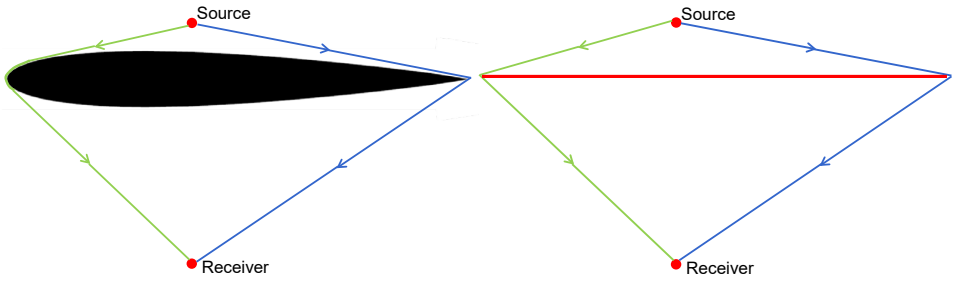

Figure 3-40: Concept of Acoustic Barrier Shielding Model.

The source-receiver path around the flat plate shown in the in the right hand diagram in Figure 3-40 may be considered analogous to acoustic path over a simple barrier. Thus, it is possible to use a barrier prediction method to calculate the attenuation of the acoustic waves passing around the leading edge (green) and trailing edge (blue). Using this simplified model, the amplitude of the acoustic wave at the receiver location can be calculated for the leading edge and trailing edge paths. As the path length is also known, the phase difference between the two paths may also be calculated based on the frequency/wavelength of the acoustic wave. Hence the acoustic level at the receiver location may be calculated from the amplitude and phase of the leading edge and trailing edge paths.

The effect of flow speed on the predicted effect of shielding is implemented using an effective propagation path as presented in Figure 3-41. For example, for the path from the source to the leading edge shown in green in Figure 3-41, the effective propagation path is defined as the path such that in the time taken for an acoustic wave to propagate from the source to a point ahead of the leading edge, the flow would propagate the acoustic wave downstream by a distance d. Thus, the distance d is equal to the flow velocity v multiplied the time t taken for the acoustic wave to propagate from the source to a point ahead of the leading edge. The path described above is a simplified geometric representation of the actual propagation path from the source to the leading edge, which in the presence of flow has a curved trajectory. Similarly, the paths from the source to the trailing edge and the paths from the leading and trailing edges to the receiver are implemented as effective paths in the presence of flow.

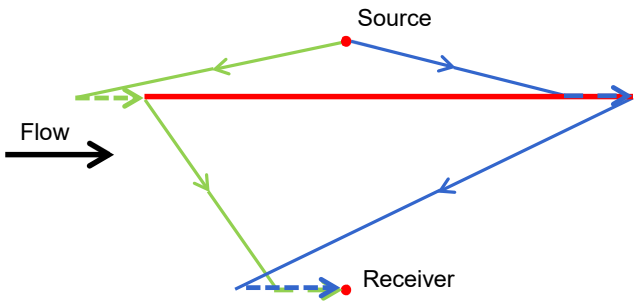

Figure 3-41: Effective Propagation Paths.

The barrier shielding method utilized in the calculations is that of ESDU 79011 [26]. The method assumes that the geometry is an infinitely long barrier, i.e., paths around the end of the barrier, the airfoil in our case, are not included in the prediction. The solution is based on Fresnel functions which have been derived from Fresnel integrals.

The attenuation values calculated from ESDU 79011 [26] can result is high attenuation values at high frequencies. In practice, there is a limit to the maximum achievable barrier attenuation, which limited to approximately 24 dB as documented in page 177, Figure 7.8 of reference [27]. Additional references to a practical limit on barrier attenuation may be found on page 149 of reference [28] which quotes 20 dB for a single diffraction barrier (i.e., a thin barrier) and 25dB for a double diffraction barrier (i.e., a thick barrier). Reference [29], Slide 11 quotes a maximum attenuation of 24 dB, and reference page 5 of Ref. [30] quotes 20 dB for thin-walled barriers and 23 dB for berms. Based on these references, an attenuation limit of 24 dB was implemented in the ray-tracing prediction method.

Note that Doppler effects have not been included in the simplified model. Doppler effects will result in a change in frequency and phase of the leading edge and trailing edge paths, which will be dependent on the flow speed and the wavelength of the acoustic wave. Furthermore, as the each of the paths consists of an upstream and a downstream component, the resultant at the receiver location will also be dependent on the source-receiver geometry. In general, the error will be lowest for low speed flows and low frequency acoustic sources and will increase with flow speed and source frequency. However, there is also a source-receiver geometry aspect, and there will be certain source-receiver geometry, flow speed and source acoustic frequency combinations where the frequency and phase differences between the leading edge path and trailing edge path will result in a low error even for high flow speeds and high source frequencies.

The sources used in the ray-tracing method predictions are located 25 mm above the upper surface of the NACA0012 airfoil as presented in Figure 3-42.

For the ray-tracing method predictions, the receiver locations are along a line in the x or chord-wise direction below the airfoil from -3 chord lengths, -600 mm, to +4 chord lengths, +800 mm from the leading edge, x = 0, of the airfoil. The linear receiver calculation points are located at 2 chord lengths, 400 mm, below the airfoil centerline and at 5 chord lengths, 1000 mm, below the airfoil centerline.

The majority of the results from the ray-tracing prediction method are presented in this report as spectral attenuation values in the form of a ratio of the receiver noise level divided by the source noise level in decibels. As such, the source noise spectral levels are arbitrary. However, where the overall attenuation is calculated the source spectra would have an effect of the value obtained. Therefore, a user specified source noise spectrum may be input such that the spectral noise levels at the receiver location may be output with the correct overall attenuation. This would permit comparison of measured test data and calculated spectra for a particular test microphone location if desired.

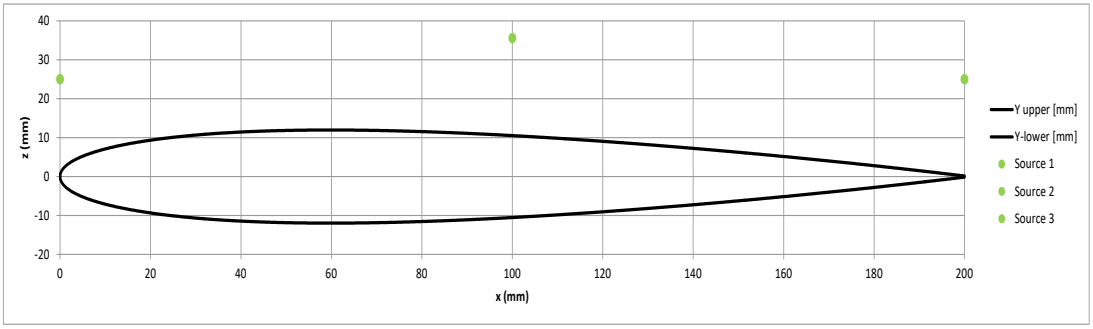

Figure 3-42: Prediction Geometry.

In 2014, DLR conducted a test to quantify the laser pulse noise characteristics. Results of these tests were presented in a telecom held on 11th December 2014 [31]. Approximate spectral levels were obtained from this laser source noise measurements presentation for the 270° angle and are presented in Figure 3-43.

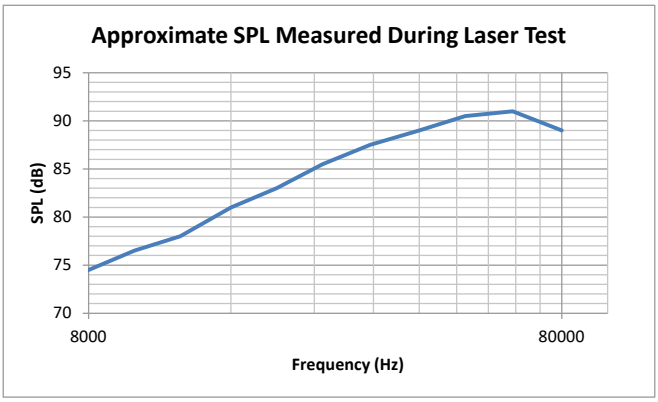

Figure 3-43: Approximate Test SPL.

The noise source was implemented in the ray-tracing prediction method with a 20 mm source diameter. The spectrum defined in Figure 3-43 was corrected to that of a 20 mm source diameter using spherical spreading resulting in a maximum third octave band level of 125dB at 63 kHz. In order to define lower frequencies, levels below 8 kHz have been extrapolated. The spectrum level input to the ray-tracing prediction method is defined in Figure 3-44.

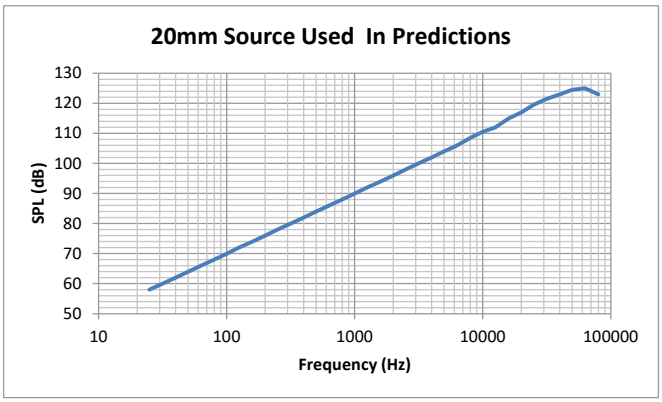

Figure 3-44: Approximate 20 mm Source SPL.

3.2.2.2 CAA Prediction Approach

The BAE Systems Altus Discontinuous Galerkin solver is used as the basis of a prediction method for the shielding of a 2D airfoil in the presence of flow. Prediction results are presented with and without the presence of flow and comparisons made with wind tunnel test data and simplified methods. Figure 3-45 shows the geometry of the airfoil using in the shielding predictions and the three source locations. Shielding predictions have been made on a line two chord lengths below the airfoil as shown in Figure 3-46. Comparison of these predictions with experiment for 0 and 55 m/s at three different source locations: Leading edge, Midchord, Trailing edge are discussed in Sections 3.2.2.4 and 3.3.2.

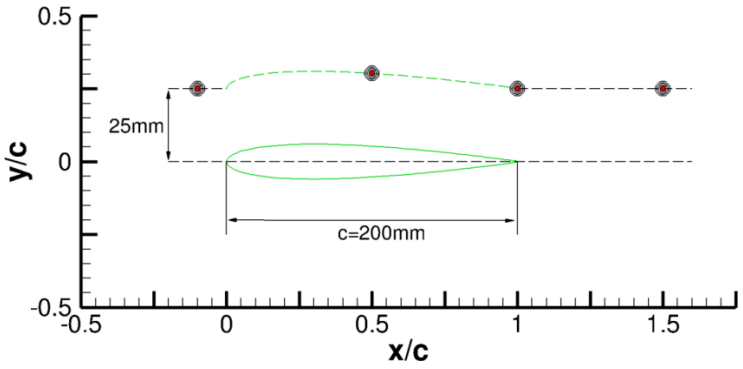

Figure 3-45: Prediction Source Geometry.

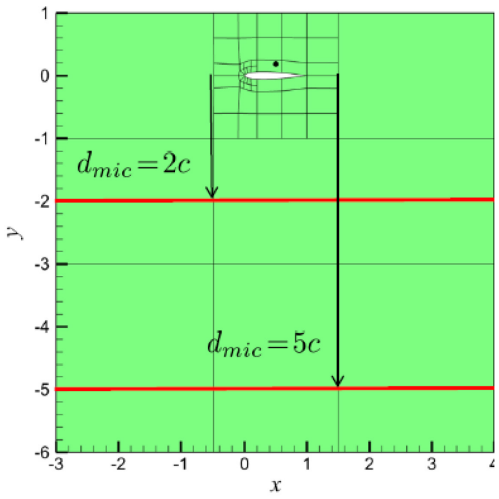

Figure 3-46: Prediction Receiver Geometry.

Numerical predictions of the 2D shielding problem were made using BAE Systems DG code Altus. Altus can solve any set of equations which can be cast in the form:

$$\frac{\partial U}{\partial t}+\frac{\partial F_j}{\partial x_j}+\frac{\partial}{\partial x_j}A_{ij}\frac{\partial U}{\partial x_i}=S \tag{3-2}$$

using a quadrature-free Discontinuous Galerkin approach [32]. In terms of aeroacoustics the Linearized Euler or APE4 equations [33] are most commonly solved. Both ADER and various Runge-Kutta time advancement schemes are available in Altus. Further details on Altus can be found in Ref. [34].

In this case, the Linearized Euler Equations (LEE) are solved using a four step Runge-Kutta time advancement scheme on a quasi-two-dimensional grid in order to propagate the source pulse around the airfoil. The method employed to predict the shielding level simply involves performing two simulations: one with the airfoil geometry and one without then subtracting one from the other to obtain the shielding level. In both cases the domains are meshed using a layer of one cell thick prismatic elements with a total of approximately 162,000 cells. The average edge length of the cells is 4 mm, and this combined with 6th order polynomial basis functions gives approximately 6 solution points per wavelength at 80 kHz. The detail of the mesh around the airfoil is shown in Figure 3-47.

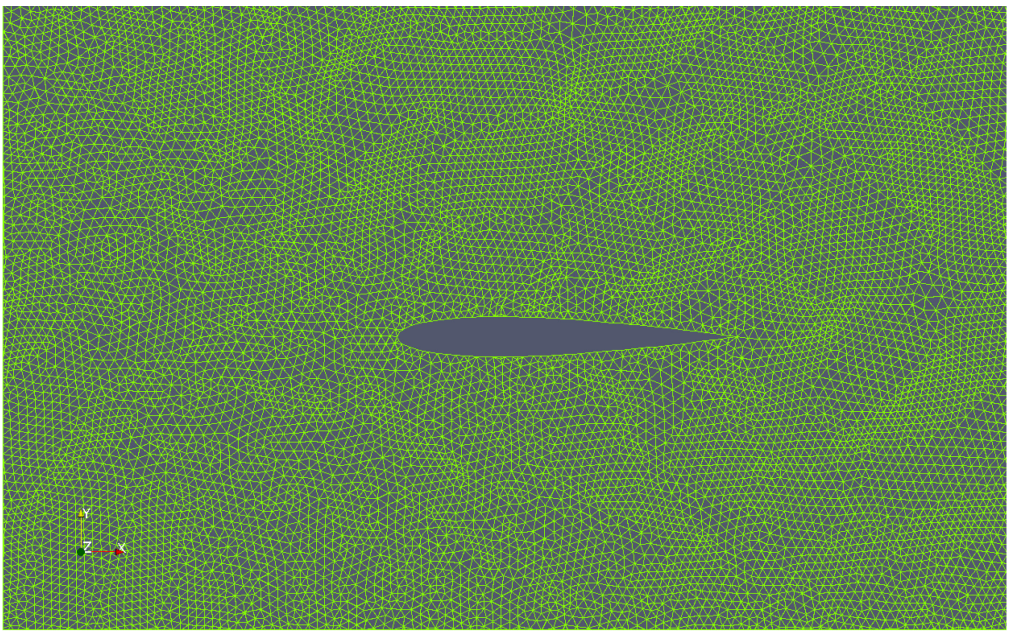

Figure 3-47: Detail of the Mesh Around the NACA 0012 Airfoil.

The laser source from the DLR experiment is represented in the simulation as a simple Gaussian pulse of pressure which appears as a source term on the acoustic pressure equation. The amplitude and width of the pulse has been tuned to recover the microphone signal, or as close to it as possible, observed in the wind tunnel experiments. The result of this tuning process can be seen in Figure 3-48.

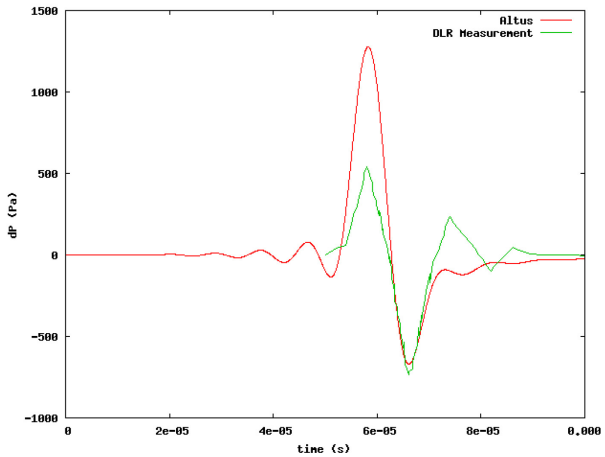

Figure 3-48: Comparison of Pulse Generated in Altus with DLR Experiment.

Figure 3-49 shows the propagation of the pressure wave created by the pulse as it travels around the airfoil geometry and also as it propagates in free space in the reference simulation.

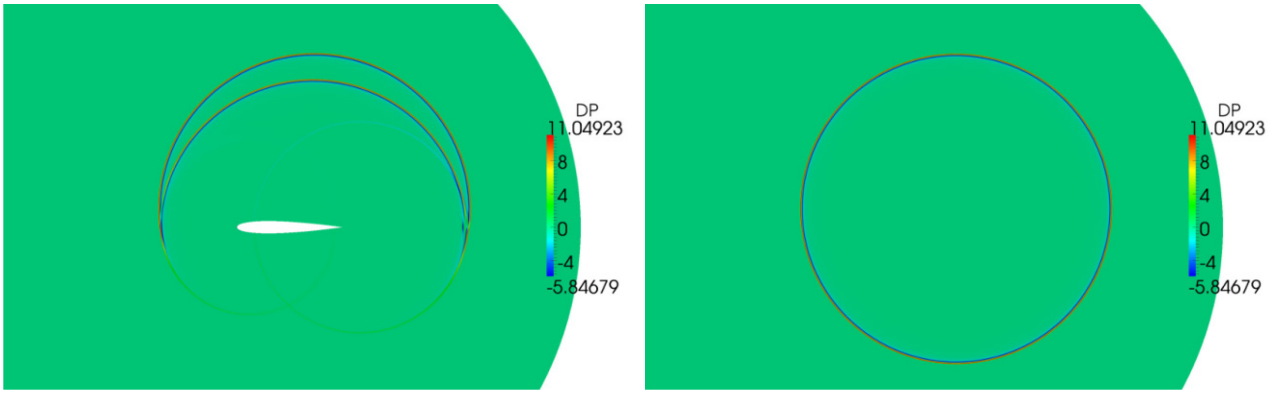

Figure 3-49: Four Solutions with and Without Airfoil.

When there is a mean flow present in the wind tunnel experiments, the laser source pulse convects downstream as it is fired. This effect is accounted for in the simulations by moving the source pulse across the solution points with a prescribed velocity vector. For the simulations with non-zero mean flow, a steady RANS CFD simulation is used to provide both this velocity vector and the required mean flow information. These simulations were carried out using the commercially available code Ansys CFX v16. A structured C-grid of hexahedral cells was built around the airfoil geometry using Ansys ICEM CFD. The grid consisted of approximately 63,000 cells and had a maximum normalized first cell height away from the wall of less than one. The grid can be seen in Figure 3-50. The simulations were run until the residuals converged below $1x10^{-5}$ and the forces on the airfoil became constant. An example of the CFD results for the turbulent kinetic energy at 55 m/s mean flow speed can be seen in Figure 3-51.

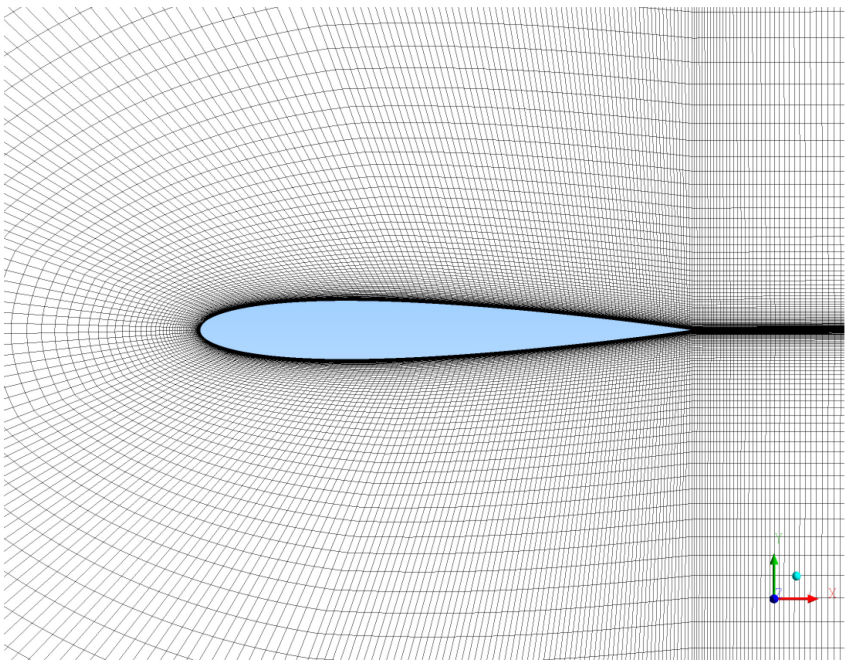

Figure 3-50: CFD Grid Around the NACA 0012.

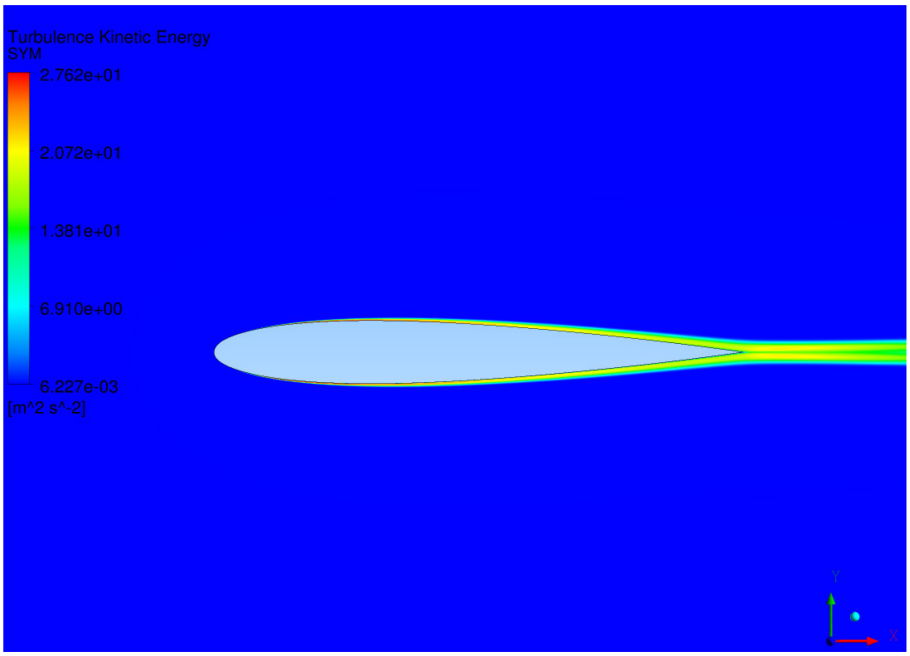

Figure 3-51: CFD Simulation Result – Turbulence Kinetic Energy at 55 m/s and Zero Degree Angle of Attack.

3.2.2.3 Ray-Tracing Prediction Results

In this section, the prediction results are presented with and without the presence of flow and comparisons made with wind tunnel test data and CFD/CAA based results.

Predictions with the source in the midchord location, the receiver along lines at Y = 2 chord lengths and Y = 5 chords lengths below the airfoil and with no flow are presented in Figure 3-52. The interference patterns between upstream and downstream paths which may be observed are due to the change in path lengths resulting in in-phase and out-of-phase addition of the leading and trailing edge paths. The interference patterns are symmetric about the midchord position (X = 0.5) in line with expectations. The broadening of the interference fringes for the Y = 5 chords case is due to a smaller change in the path length difference between the leading edge and trailing edge paths than occurs in the Y = 2 chords case.

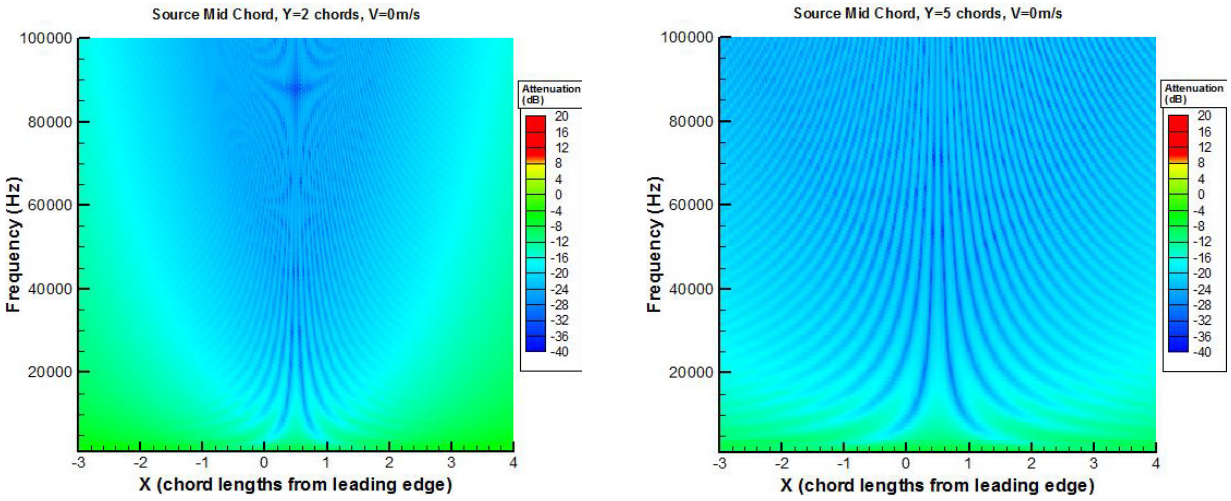

Figure 3-52: Midchord Source, 0 m/s.

The Y = 5 chords case has been plotted with the same effective x-axis range in Figure 3-53; the x-axis range is 5/2 times larger in the Y = 5 chord case than the Y = 2 chord case. It may be observed that the two plots show visually similar cancellation fringe patterns. However, there are small differences in the attenuation values due to near field acoustic effects resulting from the fixed length of the source to leading edge and source to trailing edge parts of the overall paths. The prediction method does not include the effects of atmospheric attenuation. Over significantly longer distances, the atmospheric attenuation will become significant and must be included in the prediction of overall attenuation, which will modify the attenuation values particularly at the higher frequencies.

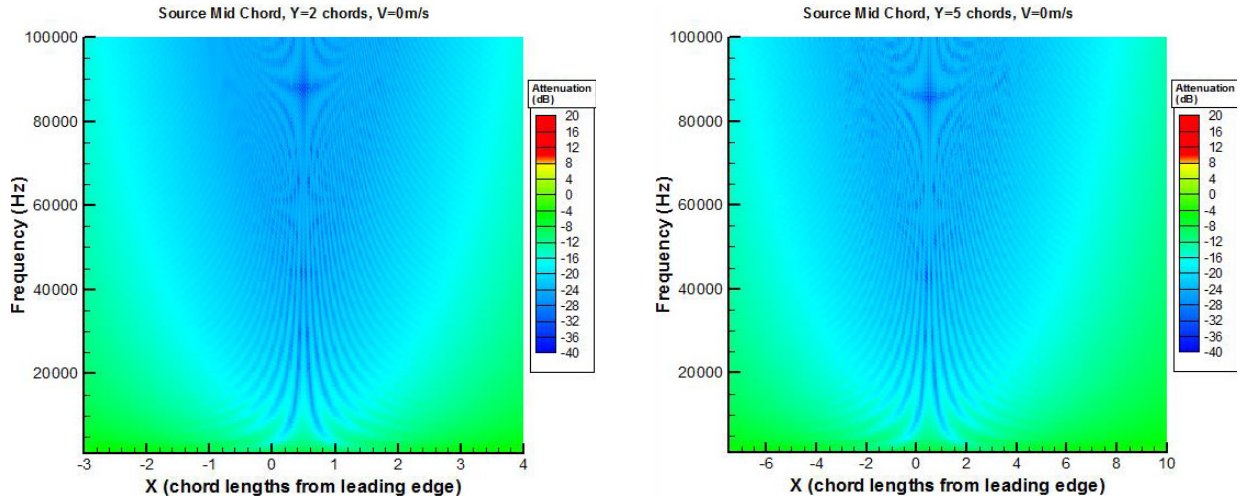

Figure 3-53: Midchord Source, 0 m/s.

Predictions with the source above the leading edge, the receiver along lines at Y = 2 chord lengths and Y = 5 chords lengths below the airfoil, with no flow, are presented in Figure 3-54. It may be observed that no shielding occurs forward of leading edge due to a direct path between the source and receiver locations. Aft of the leading edge, interference patterns between upstream and downstream paths may be observed. Note that the Y = 5 chords case has been plotted with the x-axis range scaled by 5/2, resulting in visually the same interference patterns. Once again, there are small differences in the attenuation values due to near field acoustic effects.

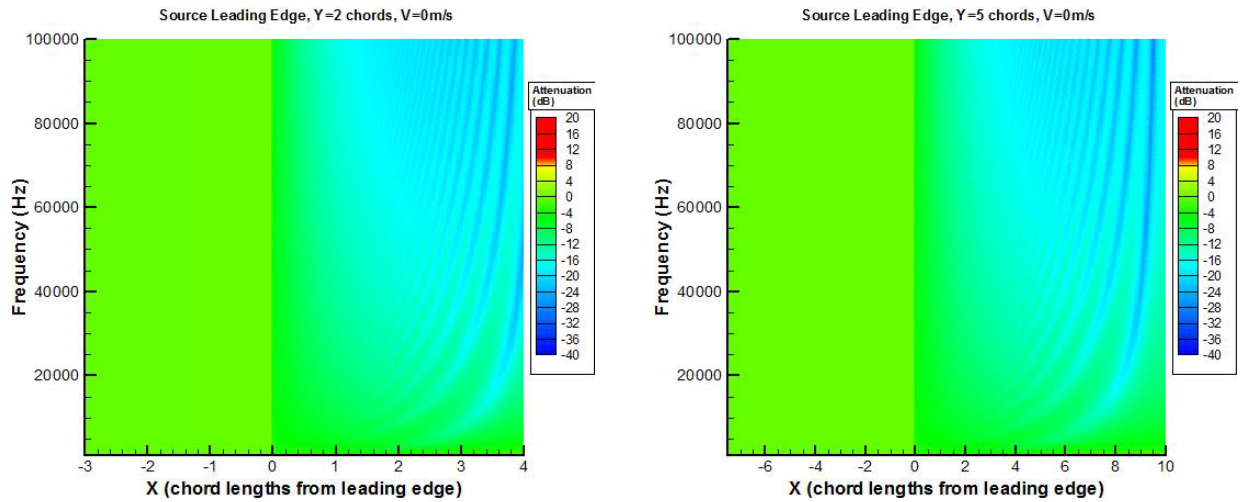

Figure 3-54: Leading Edge Source, 0 m/s.

Predictions with the source above the trailing edge, the receiver along lines at Y = 2 chord lengths and Y = 5 chords lengths below the airfoil, with no flow, are presented in Figure 3-55. It may be observed that no shielding occurs aft of trailing edge at X = 1 due to a direct path between the source and receiver locations. Forward of the trailing edge, interference patterns between upstream and downstream paths may be observed. Note that the Y = 5 chords case has been plotted with the x-axis range scaled by 5/2, resulting in visually the same interference patterns. Once again, there are small differences in the attenuation values due to near field acoustic effects.

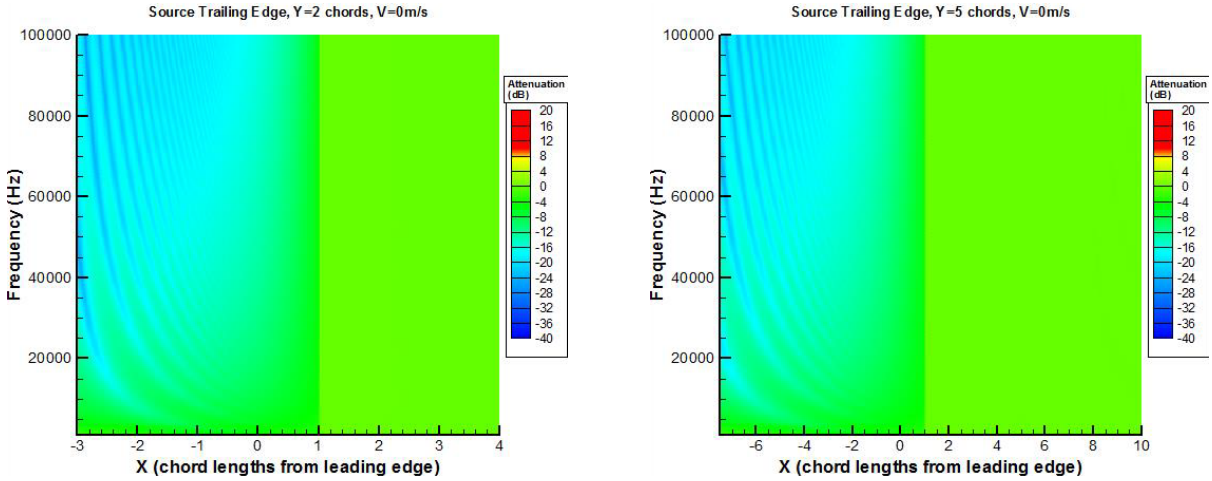

Figure 3-55: Trailing Edge Source, 0 m/s.

Predictions with variations in the source location from the leading edge to the trailing edge in 0.25 chord steps, the receiver along a line at Y = 2 chord lengths below the airfoil, with no flow, are presented in Figure 3-56.

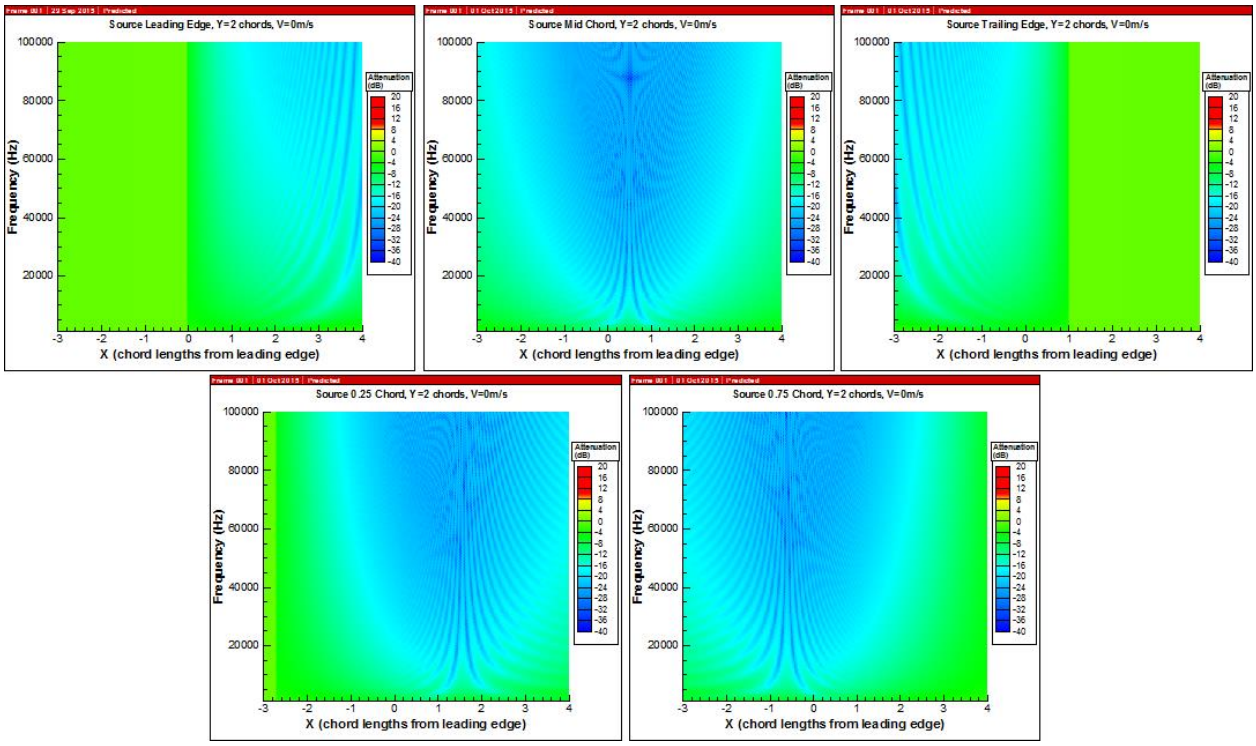

Figure 3-56: Varying Source Location, Y = 2 Chords, 0 m/s.

Predictions with variations in the source location from the leading edge to the trailing edge in 0.25 chord steps, the receiver along a line at Y = 2 chord lengths below the airfoil with 55 m/s flow are presented in Figure 3-57. Comparison between Figure 3-56 at 0 m/s and Figure 3-57 at 55 m/s reveals that the effect of shielding is subtle between 0 m/s and 55 m/s. The difference in attenuation level between no flow and 55 m/s is small.

Predictions with variations in the source location from the leading edge to the trailing edge in 0.25 chord steps, the receiver along a line at Y = 2 chord lengths below the airfoil with 204 m/s (Mach 0.6) flow are presented in Figure 3-58. Comparison between Figure 3-56 at 0 m/s and Figure 3-58 at 204 m/s reveals that the effect of shielding is more pronounced between 0 m/s and 204 m/s but difficult to quantify using these figures.

Predictions with variations in the source location from the leading edge to the trailing edge in 0.25 chord steps, the receiver along a line at Y = 2 chord lengths below the airfoil with flow speeds of 0 m/s, 55 m/s and 204 m/s (Mach 0.6) are presented in Figure 3-59. At positions forward of the source location, an increase in the attenuation is predicted with increasing flow speed. At positions aft of the source location, a decrease in the attenuation is predicted with increasing flow speed. The predicted difference in attenuation between 0 m/s and 55 m/s is small. Based on the small magnitude of the predicted difference between 0 m/s and 5 5 m/s, the difference may be difficult to observe in the test data from the wind tunnel tests.

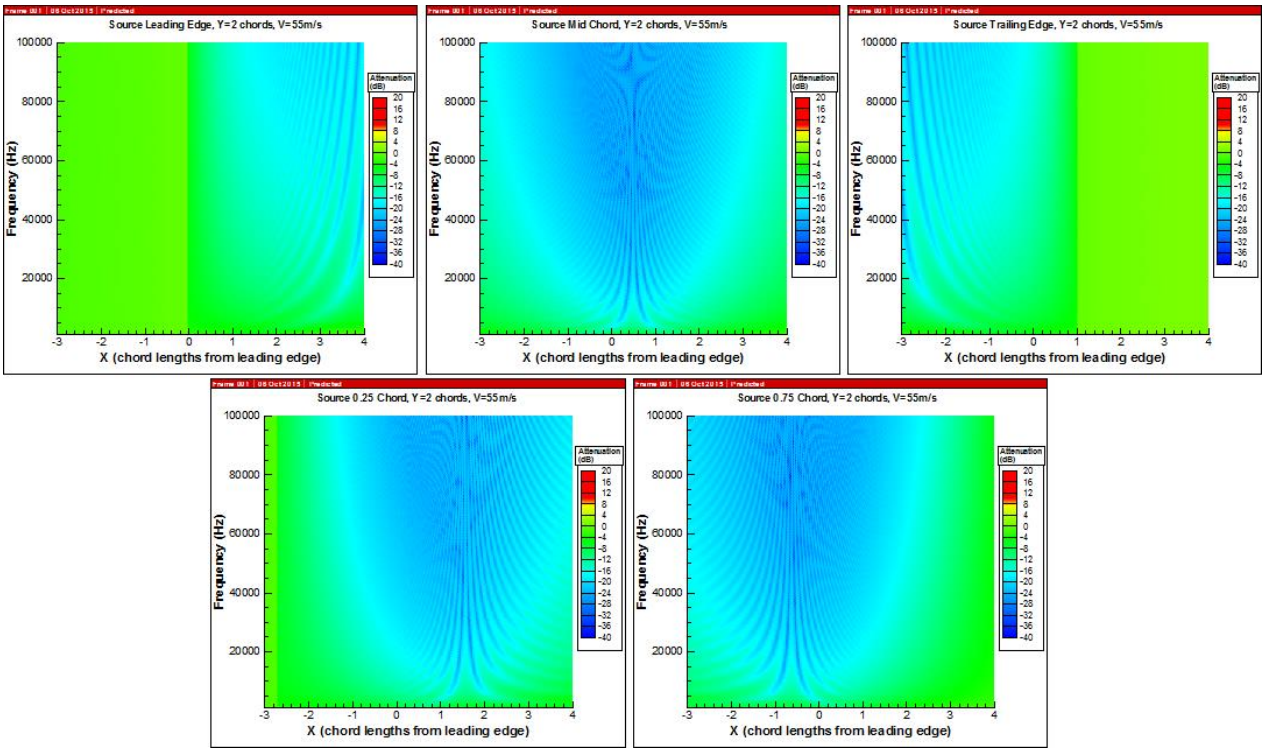

Figure 3-57: Varying Source Location, Y = 2 Chords, 55 m/s.

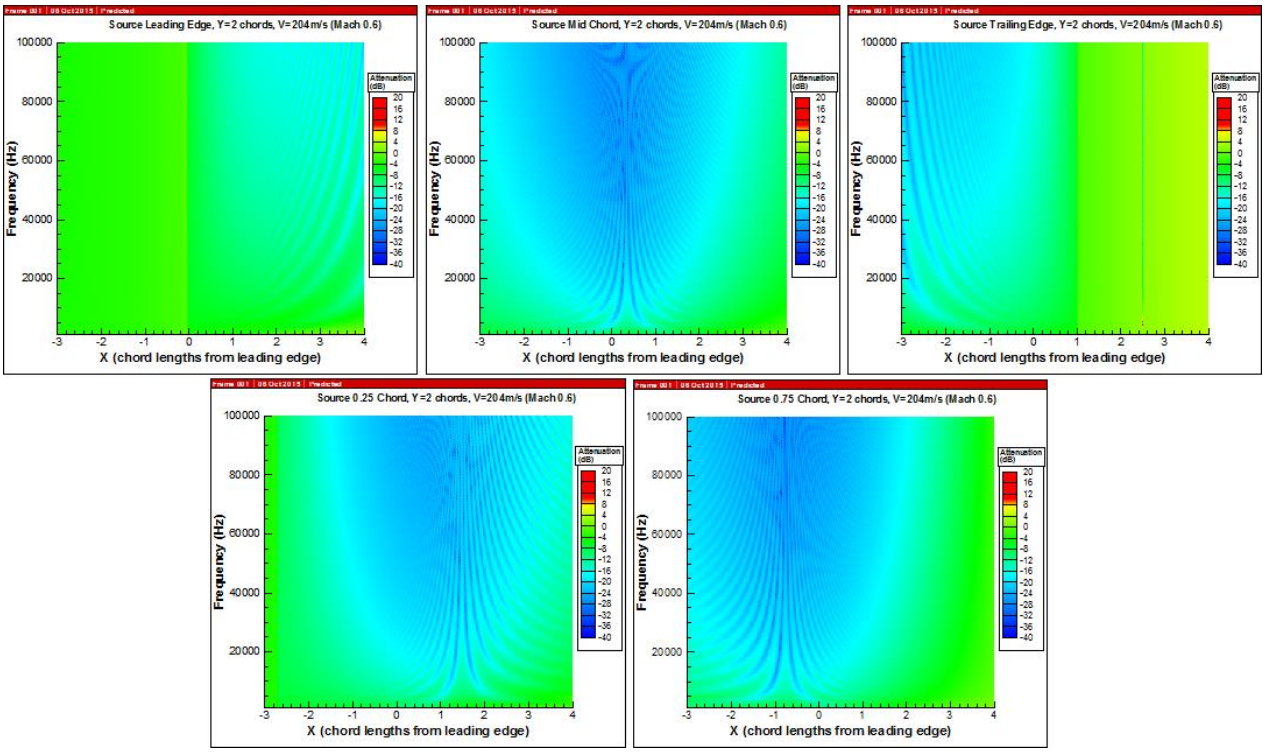

Figure 3-58: Varying Source Location, Y = 2 Chords, 204 m/s (Mach 0.6).

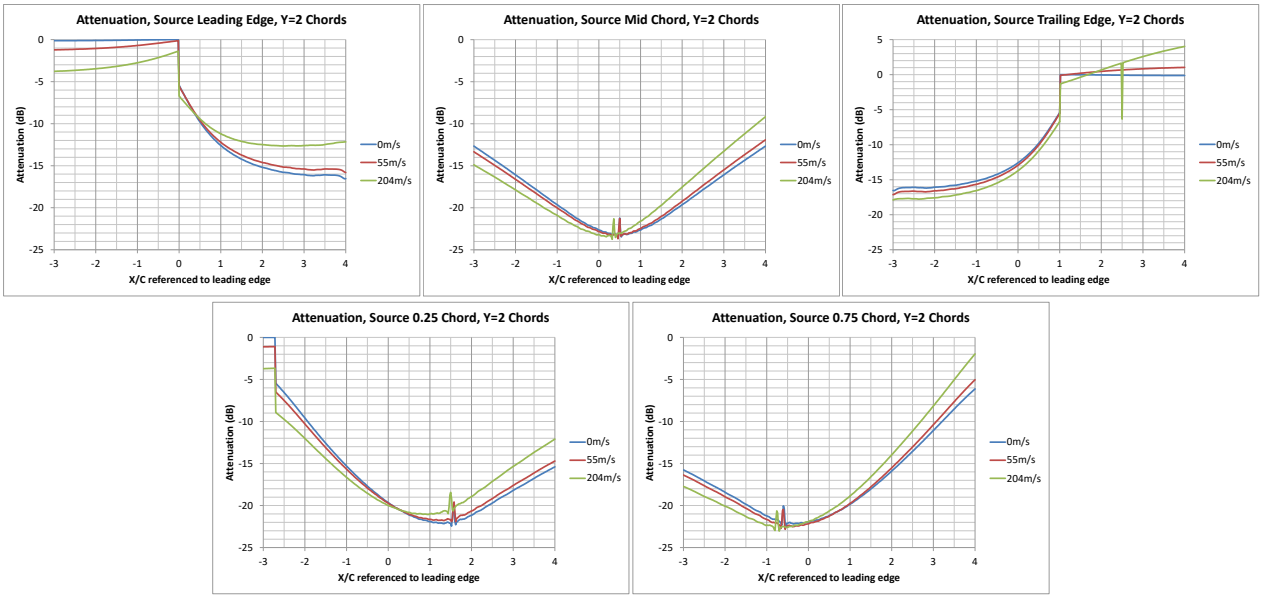

Figure 3-59: Attenuation, Varying Source Location, Y = 2 Chords.

Predictions with variations in the source location from the leading edge to the trailing edge in 0.25 chord steps, the receiver along a line at Y = 5 chord lengths below the airfoil with flow speeds of 0 m/s, 55 m/s and 204 m/s (Mach 0.6) are presented in Figure 3-60. Similar trends are obtained as the Y = 2 chord case in Figure 3-59 but occur over a longer X chord length distance, which has been factored by 5/2 in Figure 3-59.

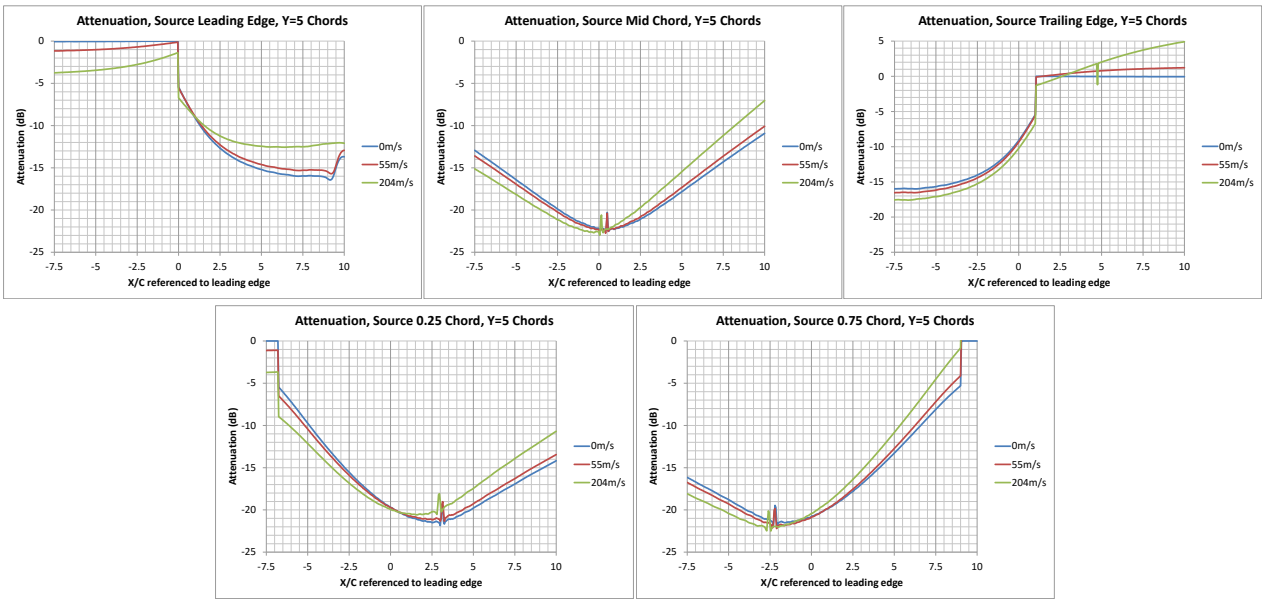

Figure 3-60: Attenuation, Varying Source Location, Y = 5 Chords.

The predicted spectra for variations in the source location from the leading edge to the trailing edge in 0.25 chord steps are presented in Figure 3-61. In Figure 3-61 the receiver locations are located along a line at Y = 2 chord lengths below the airfoil at the leading edge, midchord and trailing edge. Interference patterns, that is the peaks and dips in the spectra, resulting from the in- and out-of-phase addition of the leading and trailing edge paths may be observed in spectra. For the source at the leading edge case, the peaks and dips are present in the data for the midchord and trailing edge receiver locations, but the magnitudes are small and difficult to observe in the figure. Similarly, for the source at the trailing edge case, the peaks and dips are present in the data for the midchord and leading edge receiver locations, but the magnitudes are small and difficult to observe in the figure.

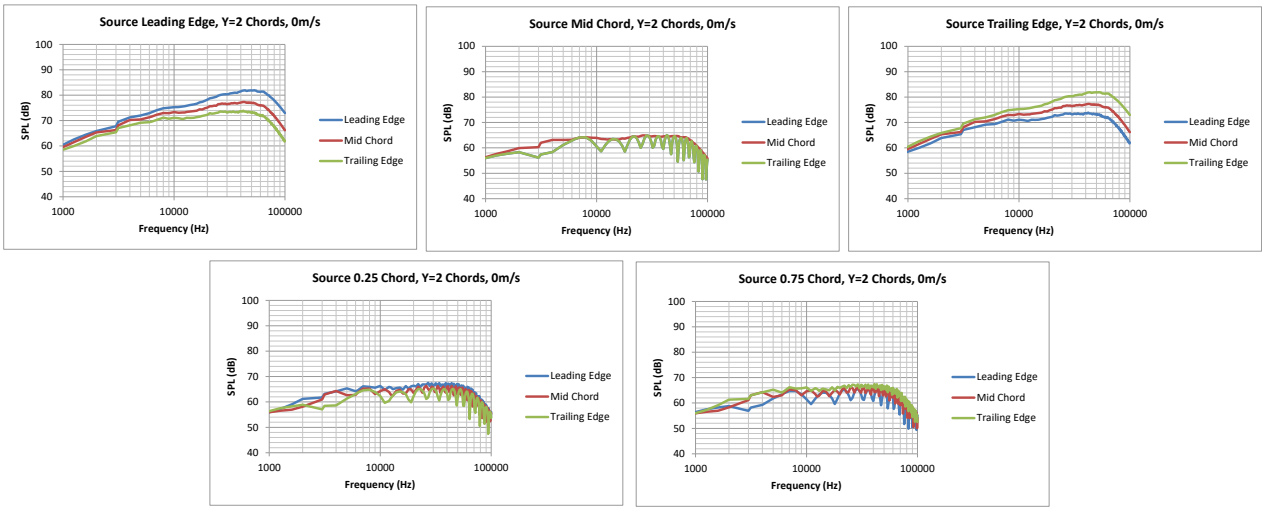

Figure 3-61: Spectra, Varying Source Location, Y = 2 Chords, 0 m/s.

3.2.2.4 CAA Prediction Results

Shielding results are shown below for the three source locations: leading edge, midchord and trailing edge at two mean flow speeds of zero and 55 m/s, as well as maps of the shielding level with frequency. Figure 3-62, Figure 3-63 and Figure 3-64 show the shielding levels two chord lengths below the airfoil both with and without a 55 m/s mean flow, as well as a map of the level at different frequencies for the zero mean flow case for the three source locations defined in Figure 3-45. With the source at the leading edge of the airfoil (Figure 3-62) there is no shielding ahead of the airfoil until approximately half a chord length ahead of the leading edge, the shielding level then increases until 2.5 chord lengths downstream of the airfoil, the point at which data are no longer available. The difference between the zero and 55 m/s mean flow cases appears minimal. In the frequency map, distinct interference patterns are visible in the shielded region from 0 to 2.5 chord lengths downstream of the airfoil.

Figure 3-63 shows the shielding level and frequency map for the simulation with the source located at the airfoil midchord for both zero and 55 m/s mean flow. For this case, there are experimental data from the DLR wind tunnel to compare with. The predicted attenuation values are close to the measured data at the X =-1 and X = 2 chord lengths. However, as the location gets closer to the midchord position at X = 0.5 chord lengths, the BAES Altus code under predicts the measured attenuation. A reduction in the shielding level appears as a spike in the graph close to 0.5 chord lengths downstream of the leading edge at the measurement location; this is due to interference when the pressure wave which has been diffracted around the leading and trailing edge meets again. This is due to the almost symmetrical nature of this setup, something which is further evident in the symmetry exhibited by the frequency map. The location of this spike predicted in the simulations is slightly ahead of the airfoil midchord yet in the experiment it is slightly behind. The influence of the 55 m/s mean flow is more clearly visible in this case with the shielding level reduced ahead of the airfoil and increased behind it. This is opposite to that of the ray-tracing predictions where a reduction was predicted forward of the airfoil and an increase to the aft.

The final set of results in this section is for the source located at the trailing edge of the airfoil. Figure 3-64 shows both the shielding level and frequency map for these simulations. From 1.5 chord lengths downstream of the airfoil there is no shielding, upstream of this location the shielding level increases. As before, interference fringes are visible in the frequency map.

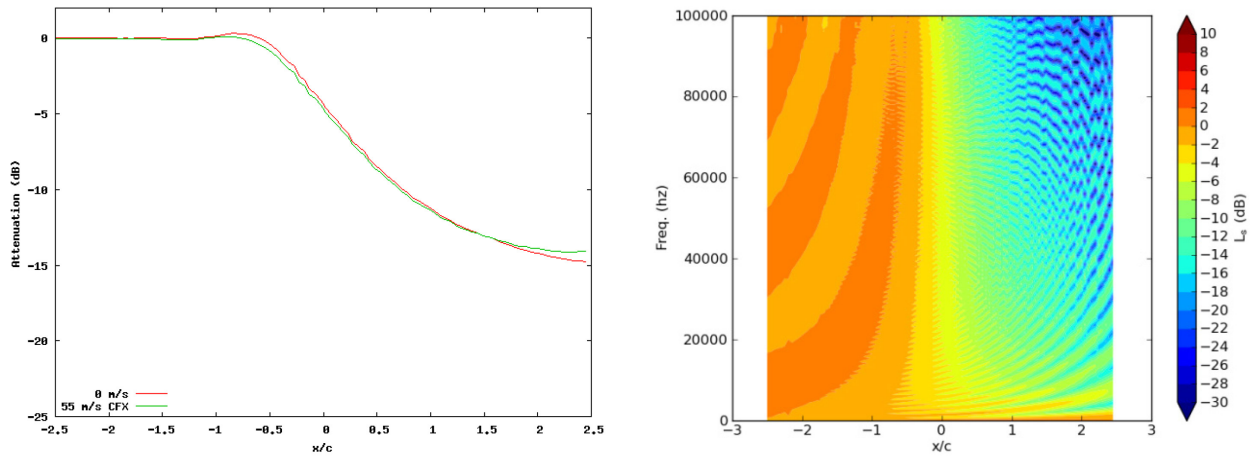

Figure 3-62: Shielding Level a Zero Degrees Angle of Attack and Zero and 55 m/s Mean Flow with Frequency Map for the Laser Source at the Leading Edge Location.

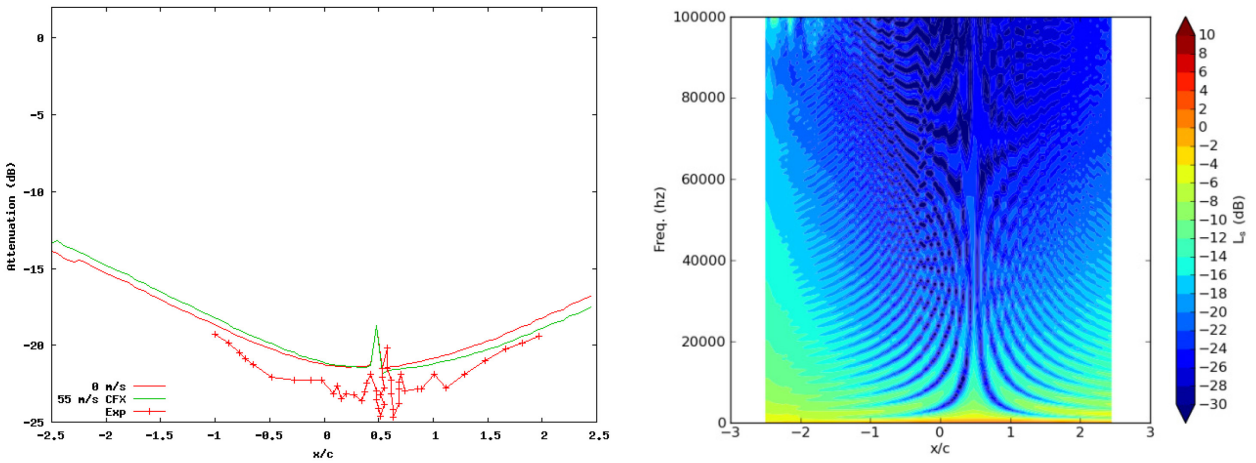

Figure 3-63: Shielding Level at Zero Degrees Angle of Attack and Zero and 55 m/s Mean Flow with Frequency Map for the Laser Source at the Midchord Location.

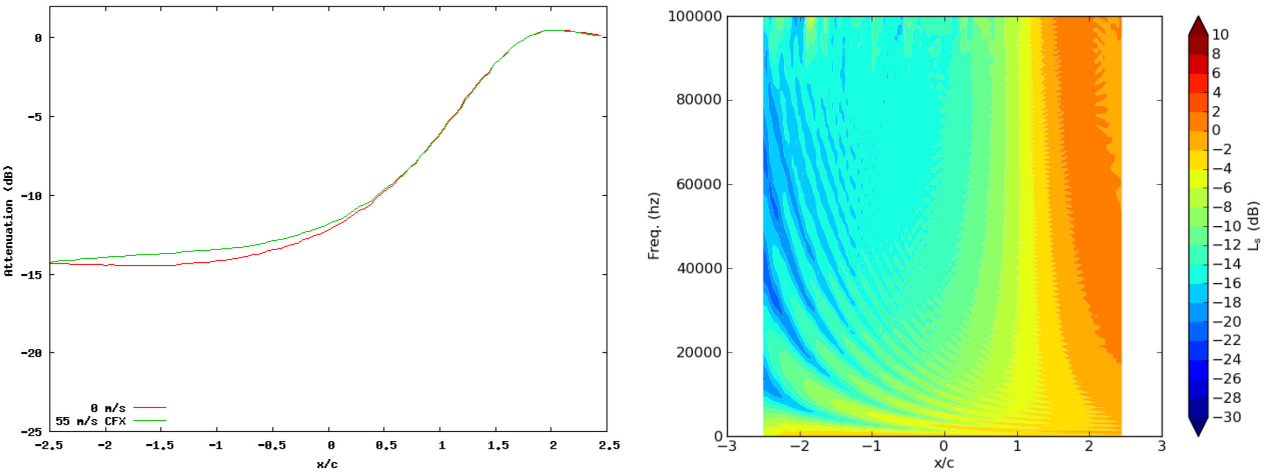

Figure 3-64: Shielding Level at Zero Degrees Angle of Attack and Zero and 55 m/s Mean Flow with Frequency Map for the Laser Source at the Trailing Edge Location.

A suite of simulations to study the shielding level dependence on angle of attack was carried out at -6, 0 and 6 degrees with a 55 m/s mean flow. The results of this study are shown in Figure 3-65. With the source located 10 mm ahead of the leading edge, the shielding level is increased in the region downstream of the airfoil with increasing angle of attack. With the source located at the airfoil midchord, increasing the angle of attack increases the shielding level ahead of the airfoil and decreases it downstream; the interference peak is also shifted. With the source located at the trailing edge, the angle of attack dependence is less pronounced, there is only a small increase in the shielding level with increasing angle of attack.

It may also be observed that the interference peak in the center of the data moves location with the change in angle of attack. With the source in the midchord location, the peak moves forward with +6° angle of attack relative to that of 0° angle of attack. The peak moves aft with -6° angle of attack relative to that of 0° angle of attack and also moves a greater distance than that of the +6° angle of attack relative to the 0° angle of attack peak. As has previously been observed, the peak in the center of the experimental data is located slightly aft of the midchord location which is located at X = 0.5 chord lengths. Based on the predicted trends of the angle of attack dependency, a possible explanation of the offset of the peak in the experimental data may be due to a small misalignment in the test geometries.

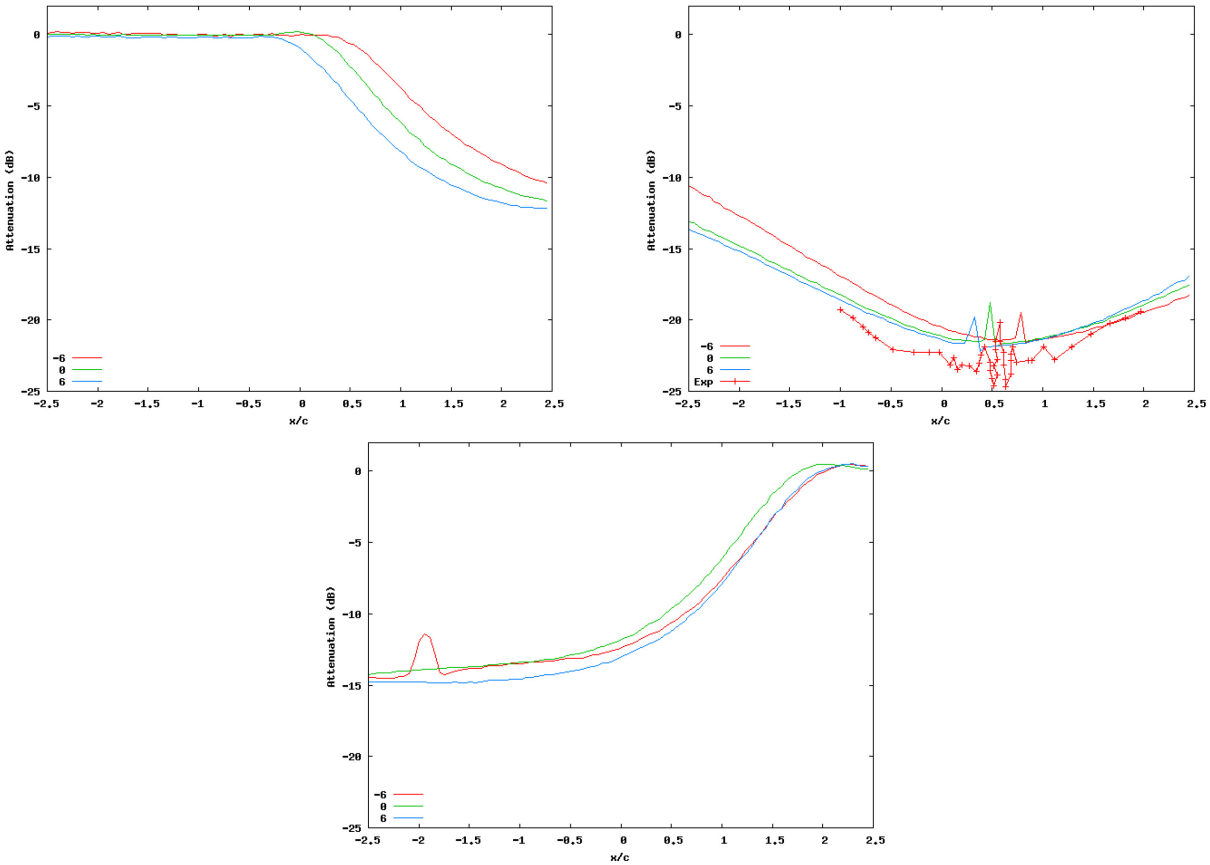

Figure 3-65: Shielding Level Dependence on Angle of Attack. Clockwise from top left: leading edge source location, midchord and trailing edge.

It was noted that the angle of attack results was sensitive to the source location. Figure 3-66 shows the shielding levels predicted with the source located in line with the leading edge and 10 mm ahead of the leading edge. There is a pronounced difference in the predicted levels due to the effect of the source convecting with the mean flow.

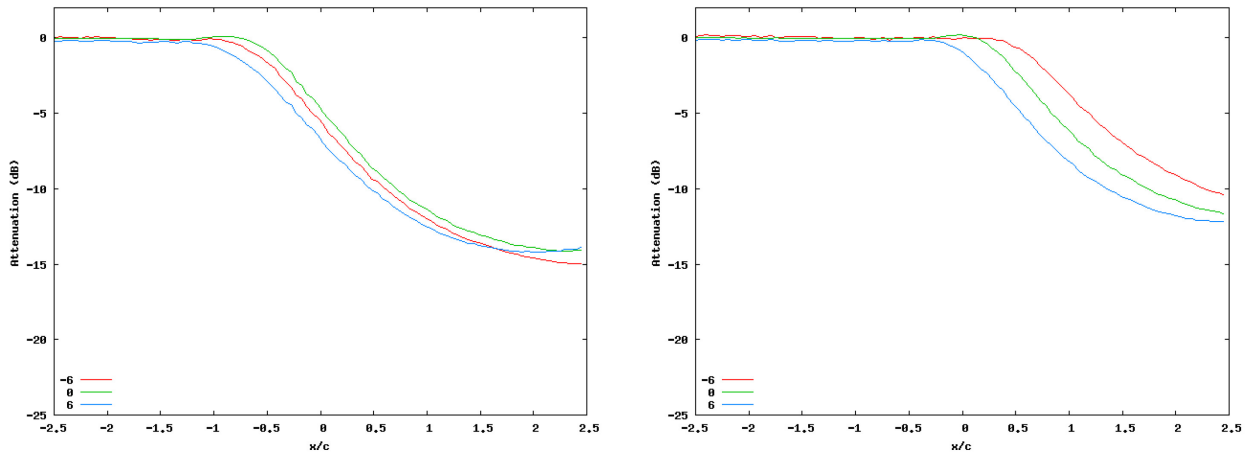

Source in Line with Leading Edge. **Source 10 mm Ahead of Leading Edge.**

Figure 3-66: Sensitivity to Source Location.

3.2.3 NASA Prediction of Shielding of the NACA 0012 Airfoil

For the objective of the prediction of acoustic scattering from airframes, there has been considerable investigation of methods that cover the entire range in accuracy, numerical efficiency, applicability, and user friendliness, and each of them has its own advantages and drawbacks. It is also clear that a tool for noise shielding calculation that is applicable to realistic aircraft configurations and is compatible to the aircraft system noise methodologies of the NASA Aircraft Noise Prediction Program (ANOPP within the ANOPP2 framework) is a key challenge. This is because aircraft system noise studies impose very practical and stringent requirements on the prediction tools, such as the capability to predict complex aircraft configurations, realistic noise sources, frequencies in the range between 50 and 10000 Hz for aircraft noise certification, and to do so with a relatively short turnaround time. Furthermore, though noise shielding is usually perceived as a problem of sound propagation in the presence of scattering bodies, and thus, treatable by solving the wave equation with suitable boundary conditions, there are many features in aircraft noise shielding, which none of these methods can handle completely for practical applications, either because of model limitations or computational intractability. Examples include the effects of nonuniform mean flow around the aircraft and the effects of the turbulent wake behind the aircraft, both of which are inevitable results of the lift requirements on the aircraft. Another example is the complexity of aircraft noise sources, which are directional and usually neither completely coherent nor completely incoherent, in contrast to what is necessarily assumed to be the case for solving the wave equation by existing numerical methods.

To address the need for a noise shielding prediction tool compatible with ANOPP, a physics-based approach can be followed, similar to many of the prediction methods implemented in ANOPP for aircraft component noise modeling and prediction. In this approach, shielding predictions rely on models, which individually capture the dominant physical features in the shielding process with the total prediction as an integration of these individual models. This approach does not solve the complete wave equation. Instead, it aims at modeling and calculating individual components of the total solution that predominantly control the shielding process. In this way, requirements imposed by full scale, full-configuration aircraft applications can be met, while maintaining accuracy compatible with other component predictions in ANOPP and acceptable to aircraft system noise studies.

One important feature to include in aircraft noise shielding is the diffraction of sound waves by the edges of the aircraft wings for conventional aircraft and by the edges of the aircraft body for unconventional aircraft such as the Hybrid Wing Body (HWB) aircraft. Depending on the frequency of the sound waves, two kinds of diffraction can occur, as illustrated in Figure 3-67, one being sharp edge diffraction typically at trailing edges of airfoil-shaped bodies where the local radius of curvature is small compared with the acoustic wavelength, and the other being creeping wave diffraction usually occurring at leading edges where the local radius of curvature is relatively large.

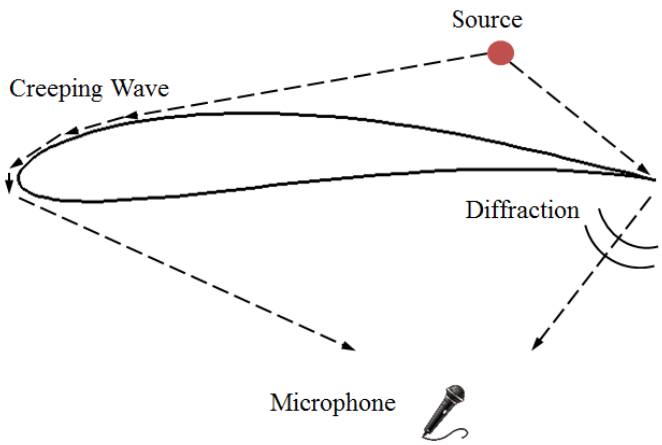

Figure 3-67: Illustration of Two Types of Diffraction.

An approach based on the Kirchhoff Integral Method (KIM) has been implemented for the prediction of these two kinds of diffraction for general geometries. This method follows the general approach of high frequency asymptotes, which is justifiable for the application of aircraft noise shielding because the sound propagation is in open spaces and all the dimensions of the aircraft, except for the local edges, are large compared with the acoustic wavelengths. The classic theories of high frequency acoustics have been studied for many years and are well documented [35], [36], [37], [38].

The acoustic pressure received at a microphone location consists of three components in the general form of:

$$p = p_I + p_R + p_D \tag{3-3}$$

where p is the total acoustic pressure with p_I, p_R, and p_D being the three components conventionally representing the incident, the reflected and the diffracted fields, respectively. At any fixed spatial location, some of the three components may not contribute to the total. The shadow region below the airfoil in Figure 3-67 is an example where only the diffracted waves can reach the microphone. The KIM deals with the diffracted field and calculates the contributions to the total acoustic pressure through an integration over a diffraction contour, expressed by:

$$p_D = \int_C W(s)ds \tag{3-4}$$

where the integration contour C is determined by the principle of line of sight from the source locations to the diffraction body and is represented by the curvilinear coordinate s along the contour. The integrand function W depends on the type of diffraction and has the general expression:

$$W = p_I(\mathbf{x}_e)S(\mathbf{x}_e)\frac{e^{ik_0|\mathbf{x}-\mathbf{x}_e|}}{|\mathbf{x}-\mathbf{x}_e|}. \tag{3-5}$$

For simplicity and illustration, the result above is given for the case without mean flow; the result can easily include convective effects due to mean flow. Here, as illustrated in Figure 3-68, the measurement location is denoted by its coordinate vector $\mathbf{x}$ and the edge coordinate by $\mathbf{x}_e$, which is a function of the contour curvilinear coordinate s, and hence, represents the integration variable in (Equation 3-4). The source is located at $\mathbf{x}_s$, as illustrated in Figure 3-68, and is characterized by its direct radiation to the edge $p_I(\mathbf{x}_e)$. The acoustic wavenumber is represented by $k_0 = \omega/c_0$ with ω being the angular frequency and c_0 the constant sound speed.

The quantity S in the result (Equation 3-5) contains the effects of the diffraction, and hence, depends on the type of diffraction. For sharp edge diffraction, it is given by:

$$S = \frac{\sin(\pi/n)}{2n\pi}\frac{1}{\cos(n\pi/4)-\cos(n\mu/2)}, \tag{3-6}$$

where n is an angle index defined by the wedge angle θ_w

$$n = (2\pi - \theta_w)/\pi \tag{3-7}$$

and the quantity μ contains the relations between various coordinate vectors, defined by:

$$\mu = \arccos\left(\frac{|\mathbf{x}_e-\mathbf{x}_s||\mathbf{x}-\mathbf{x}_e| + (\mathbf{x}_e-\mathbf{x}_s)\cdot(\mathbf{x}-\mathbf{x}_e)}{[(\mathbf{x}_e-\mathbf{x}_s)\times(\mathbf{x}-\mathbf{x}_e)]\cdot\mathbf{s}}\right) \tag{3-8}$$

with **s** being the unit vector of the contour curvilinear coordinate *s*.

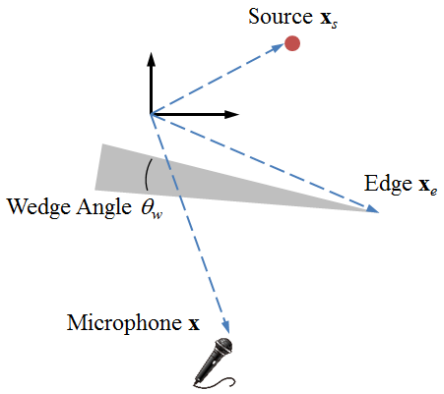

Figure 3-68: Geometry for Sharp Edge Diffraction.

For creeping wave diffraction, the local geometry and various coordinate vectors are shown in Figure 3-69, and the quantity *S* in the integrand function (Equation 3-5) is given by:

$$S = \frac{e^{i\pi/6}(k_0 a)^{1/3}}{\pi 2^{4/3}} \frac{1}{[Ai(-1)]^2} e^{-\alpha_0 t} \tag{3-9}$$

where a is the local radius of curvature at the edge, Ai is the Airy function, and α_0 is the dissipation coefficient of the creeping waves resulting from the loss of energy due to the radiation back into the acoustic medium as the creeping waves propagate along the surface. It is defined by:

$$\alpha_0 = \frac{1}{a}\left(\frac{k_0 a}{2}\right)^{1/3} e^{i\pi/6}. \tag{3-10}$$

The total propagation length of the creeping waves from the launching point $\mathbf{x}_e$ to the radiation point is denoted by t.

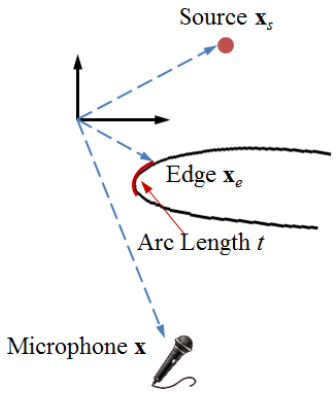

Figure 3-69: Geometry for Creeping Wave Diffraction.

The NASA implementation of this KIM prediction method has been well validated with analytical solutions and published test data for scattering from the shapes of a sphere, a cylinder, and a flat plate [39].

For the prediction of the scattering of the laser spark pulse from the NACA 0012 airfoil, the KIM is used with two implementation features to represent the experiment. The first feature is that the line integral is taken only on the leading and trailing edges of the airfoil and not on the side edges. The second feature is to accurately model the spark source with a variable amplitude spectrum similar to the experimentally measured unshielded spectrum from the QFF experiment. Experimentally, the spark has been shown to be omnidirectional, and this characteristic is also modeled in the prediction.

3.3 COMPARISON OF RESULTS

Three groups provide predictions of the shielding at the NACA0012 geometry. BAE Systems adopted a barrier shielding method and its LEE solver Altus, while DLR used its LEE/APE solver PIANO for their predictions. NASA provided predictions to the 2D airfoil shielding problem on the basis of the advanced diffraction integral approach KIM.

3.3.1 Simulation Data vs Acoustic Wind Tunnel Data

Predictions with the source above the midchord and the receiver along a line Y = 2 chord lengths below the airfoil are presented in Figure 3-70. The plot on the left of Figure 3-70 shows the spectral attenuation for the source at the midchord and with a 55 m/s flow speed**.** It is difficult to observe a difference when compared to the ray-tracing plot in Figure 3-74, which is at 0 m/s, as was stated in section 3.2.2.2 that the difference between 0 m/s and 55 m/s is small. The plot on the right of Figure 3-70 shows the ray-tracing predicted overall attenuation at 0 m/s, 55 m/s and 204 m/s (Mach 0.6) compared with the DLR-AWB wind tunnel test data at 55 m/s. Excellent agreement between the test data and the ray-tracing predicted overall attenuation is obtained.

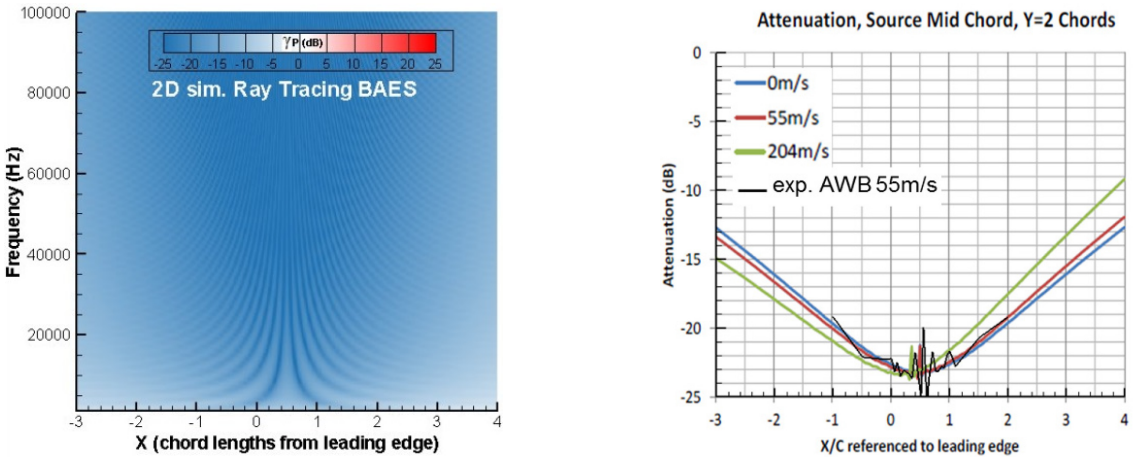

Figure 3-70: Results from Ray-tracing Prediction and AWB Test. Left: spectral attenuation at 55 m/s, right: overall attenuation for different flow speeds and comparison with AWB results.

Predictions with the source above the midchord and the receiver along a line Y = 2 chord lengths below the airfoil are presented in Figure 3-71. The plot on the left of Figure 3-71 shows the ray-tracing predicted spectral attenuation for the source at the midchord with no flow**.** The plot on the right of Figure 3-71 shows the spectral attenuation for the AWB test data source at the midchord with no flow. Due to the spatial resolution of the discrete microphone locations the interference fringes due to the addition of the leading and trailing edge paths are not well resolved above approximately 20 kHz. Below 20 kHz there is a good agreement in the spectral attenuation features, as can be seen in the vertical features centered on X = 0.5 chord lengths.

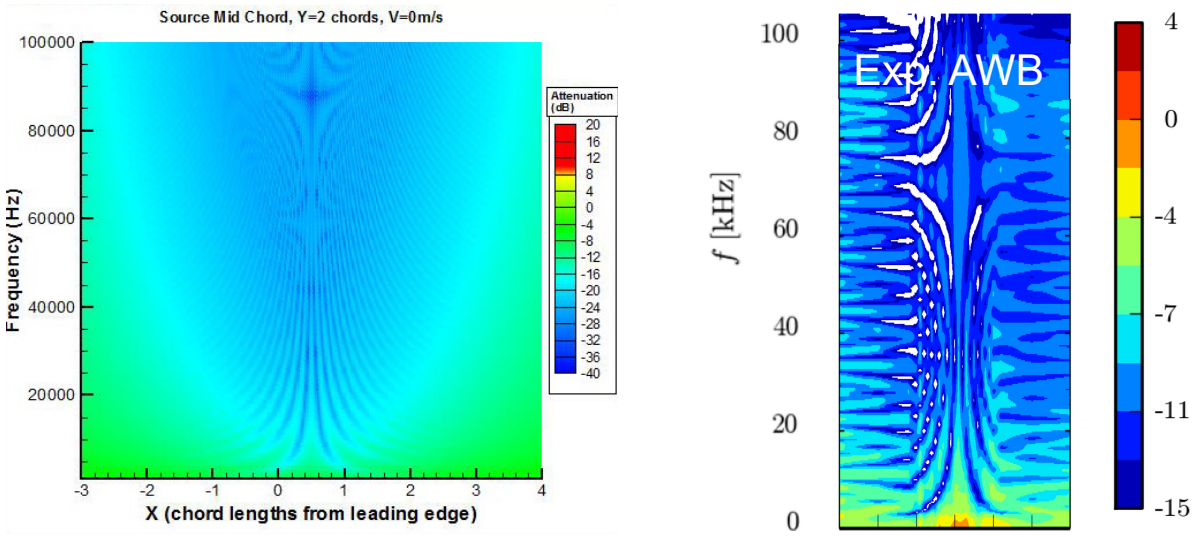

Figure 3-71: Ray-Tracing Comparison with AWB Data, Y = 2 Chords, 0 m/s.

Figure 3-72 shows the comparison of the KIM prediction with the reported data from DLR (Figure 15(e)) from Ref. [40] for the case of M = 0 and with the spark source at the trailing edge (red dot). At airfoil angle of attack, $\alpha = 0°$, the comparison shows a consistent overprediction of the noise reduction from shielding; that is, KIM predicts more shielding by only 1 – 2 dB in the shadow region where shielding noise reduction varies from 5 to 15 dB.

The KIM prediction is also shown for the α variation of +6° and –6° with a predicted trend that is expected, less noise reduction from shielding for positive α and more noise reduction for negative α. This prediction has not yet been compared with data.

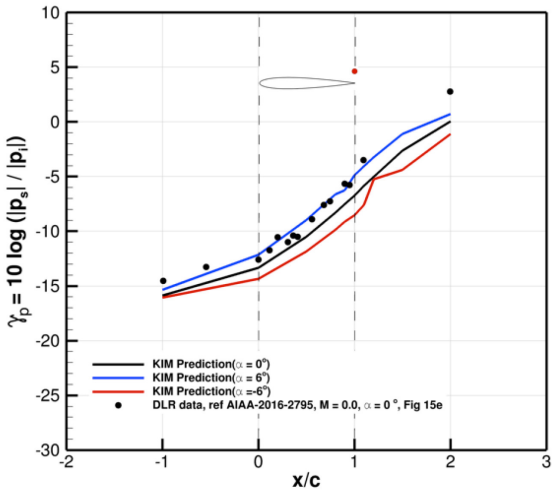

Figure 3-72: NASA KIM Prediction as Compared with DLR Data (Figure 3-6(e)), M = 0, Laser Pulse Source 25 mm Above the Surface and, Microphone Locations on a Line Two Airfoil Chords from the Airfoil Centerline.

Figure 3-73 shows the KIM prediction as compared with the NASA data from the Quiet Flow Facility (QFF), also for the case of the spark source at the trailing edge and with M = 0 and α = 0°. The initial observation is that the KIM prediction follows the data very well until the forward part of the shadow region (x/c = 0.5 and forward) where the difference can be as much as 4 dB. Nevertheless, over the whole range of x/c, the prediction is still within 1 to 4 dB, an encouraging result given the rapid computational speed of the KIM method. Another observation is that there are different features to the data (DLR and NASA) and the KIM prediction for both cases. For example, in the insonified region (x/c > 1), the QFF data stays close to a shielding factor, γ_p, of zero whereas the DLR data shows a value of 3 for x/c = 2. Also, the KIM prediction itself has a different trend in the insonified region. Most likely, at least some of these differences are related to the distance between the source with airfoil and the microphones (1c for the NASA QFF data and 2c for the DLR data). A criterion for near/far field is probably related to both frequency as well as characteristic dimensions of the source and body.

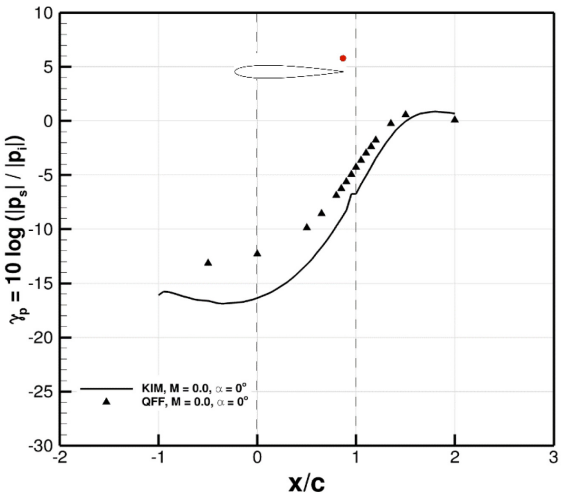

Figure 3-73: NASA KIM Prediction as Compared with NASA QFF Data (from Section 3.1.3), M = 0, Spark Source 25 mm Above the Surface and, Microphone Locations One Airfoil Chord Away from the Centerline of the Airfoil.

At this point, only an initial comparison is shown, and in-depth analysis will be necessary to begin to identify the scattering effects.

3.3.2 Code-to-Code Comparison of Simulation Results

Predictions with the source above the midchord and the receiver along a line Y = 2 chord lengths below the airfoil are presented in Figure 3-74. The predictions with the three codes show very good agreement in the spectral attenuation. The differences that may be observed at the high frequencies may be attributed to aliasing in the plotting of the results due to a different spatial sampling at the receiver locations along the line at Y = 2 chord lengths below the airfoil. Note that the barrier shielding result shows a perfectly symmetric shielding diagram.

Predictions with BAES Altus code compared with a DLR code for the angle of attack dependence of the spectral overall attenuation for the source above the leading edge and the receiver along a line Y = 2 chord lengths below the airfoil are presented in Figure 3-75. With the source located at the leading edge, the greatest difference occurs at +6° angle of attack relative to 0° angle of attack, with this trend being predicted by both the BAES and DLR codes. The change in spectral attenuation is small between 0° angle of attack and -6° angle of attack, with this trend being predicted by both the BAES and DLR codes.

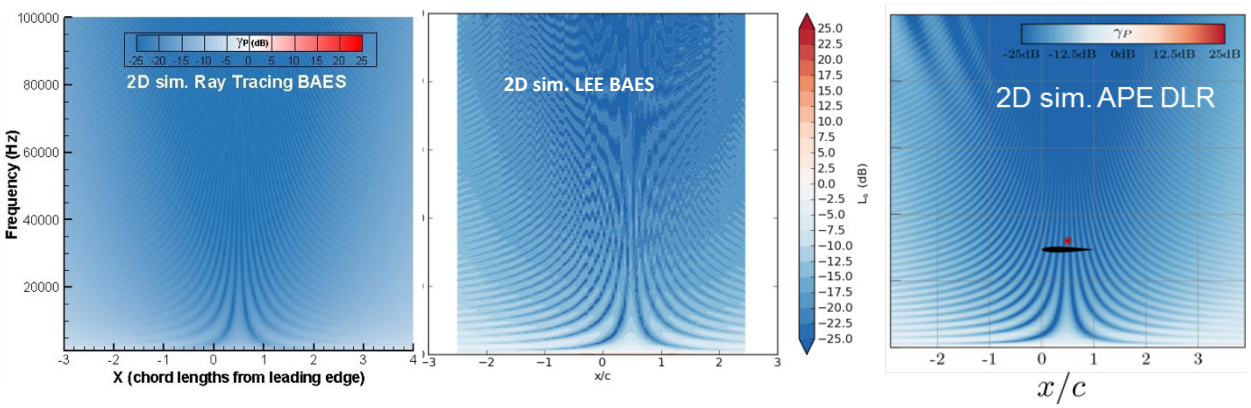

Figure 3-74: Spectrally Resolved Attenuation on NACA0012 for Central Source Position. Left: barrier shielding model, center: BAE Systems LEE solution, right: DLR LEE solution.

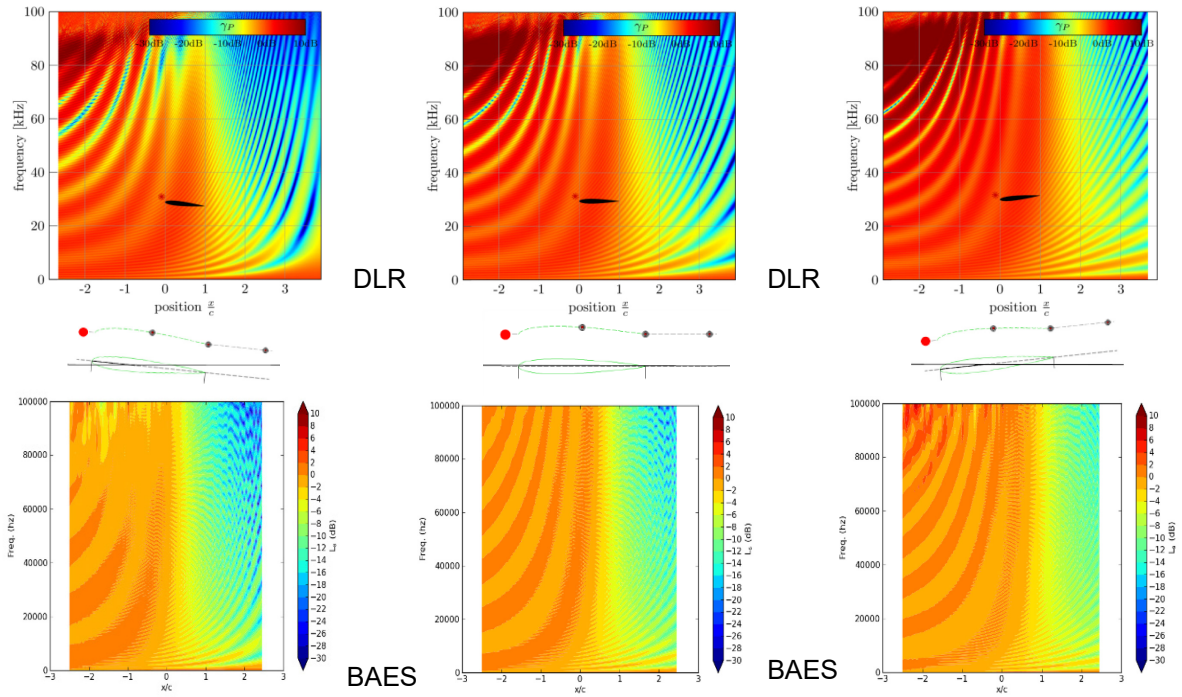

Figure 3-75: Angle of Attack Dependence, Leading Edge Source+10 mm, BAES Altus Versus DLR Code Predictions.

Predictions with BAES Altus code compared with a DLR code for the angle of attack dependence of the spectral overall attenuation for the source above the midchord and the receiver along a line Y = 2 chord lengths below the airfoil are presented in Figure 3-76. With the source located at the midchord, the difference in magnitude of the spectral attenuation is difficult to identify. A change in location of the centroid of the interference fringes can be identified in the predictions from both the BAES and DLR codes for a change in angle of attack. At 0° angle of attack the spectral attenuation is centered on the midchord location at X = 0.5 chord lengths which is predicted by both codes. At +6° angle of attack the centroid of spectral attenuation moves forward centered at approximately X = 0.2 chord lengths with the BAES code and centered at approximately X = 0.0 chord lengths with the DLR code. A change in angle of attack from 0° to +6° results

in a greater shift in the centroid of the spectral attenuation with the DLR code than the BAES code. At -6° angle of attack the centroid of spectral attenuation moves aft and is centered at approximately X = 0.8 chord lengths with the BAES and DLR codes. A change in angle of attack from 0° to -6° results in a similar shift in the centroid of the spectral attenuation with both of the prediction codes.

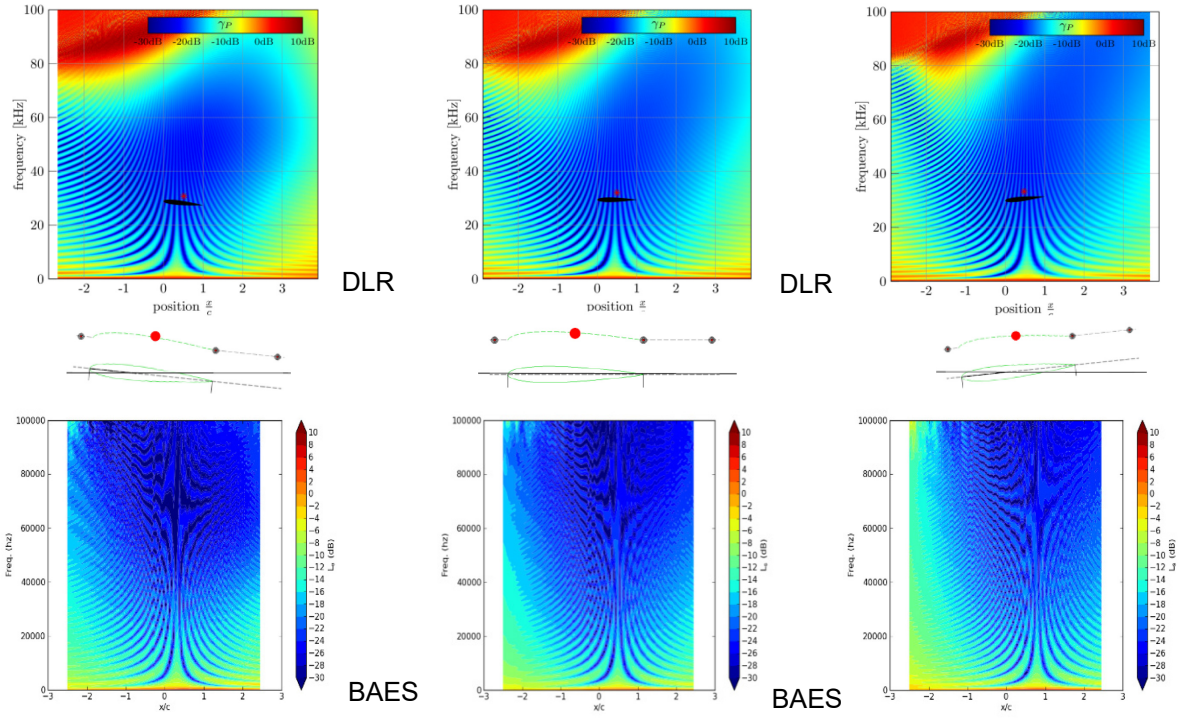

Figure 3-76: Angle of Attack Dependence, Midchord Source, BAES Altus Versus DLR Code Predictions.

Predictions with BAES Altus code compared with a DLR code of the angle of attack dependence of the spectral overall attenuation for the source above the trailing edge and the receiver along a line Y = 2 chord lengths below the airfoil are presented in Figure 3-77. With the source located at the trailing edge, the most noticeable difference with the change in the angle of attack of +6° relative to 0° occurs with the DLR code, where the attenuation increases aft of the trailing edge located at X = 1.0 chord lengths whereas the BAES code predictions show little change. It may also be observed that there is a change in slope of the interference fringes, with the fringes at +6° being at a shallower angle to the x-axis at +6° than 0° angle of attack, this trend being predicted by both codes. This change in the angle of the interference fringes is indicative of a forward shift in the centroid of the spectral attenuation as the angle of attack changes from 0° to +6°.

With the change in the angle of attack of -6° relative to 0°, the DLR code shows an increase in the spectral attenuation aft of the trailing edge, whereas the BAES code predictions show little change. It may also be observed that the centroid of the interference fringes can be observed at X = 2 chord lengths, this trend being predicted by both codes. This observed location of the centroid of the interference fringes is indicative of an aft shift in the centroid of the spectral attenuation as the angle of attack changes from 0° to -6°.

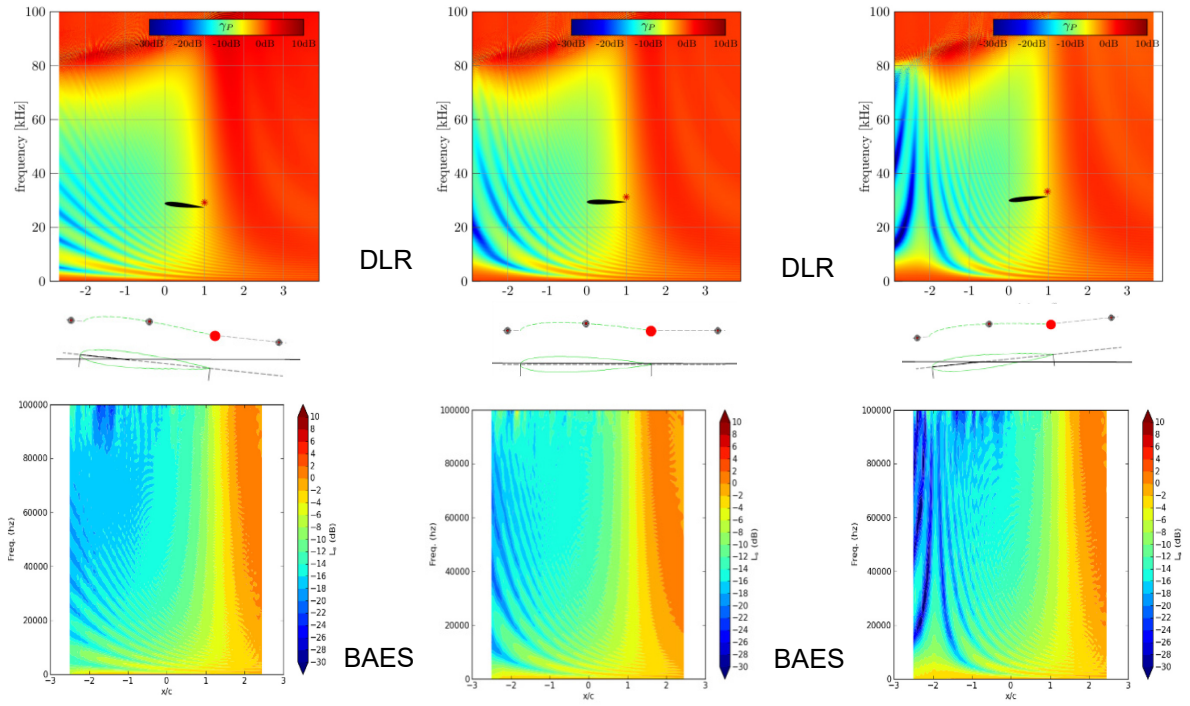

Figure 3-77: Angle of Attack Dependence, Trailing Edge Source, BAES Altus Versus DLR Code Predictions.

Comparisons of the predictions obtained from the BAE Systems codes and the DLR code for the 2D airfoil are very encouraging: the codes predict similar trends for the spectral attenuation. Whilst the spectral attenuation plots are similar, some differences do exist for some geometric configurations. With the source located at the leading or trailing edge, small differences in the attenuation forward of the leading edge or aft of the trailing edge, respectively, were observed. With the source at the midchord location and with +6 ° angle of attack a small difference in the centroid of the interference fringes was observed.

Chapter 4 – ACOUSTIC SHIELDING OF A/C CONFIGURATIONS

Jan W. Delfs, Karl-Stéphane Rossignol and Markus Lummer
DLR – Institute of Aerodynamics and Flow
GERMANY

Russell H. Thomas, Florence Hutcheson, Christopher Bahr and Yueping Guo
Langley Research Center, NASA
UNITED STATES

Dave Patience and Oliver Darbyshire
BAE Systems
UNITED KINGDOM

This chapter deals with the acoustic shielding properties of the SACCON F17E and the HWB N2A aircraft configurations. The objective here is on the one hand to generate a quality experimental data set for the validation of the shielding simulations. On the other hand, the various configurational changes give indications, which geometric elements influence the shielding properties of an aircraft configuration most.

4.1 EXPERIMENTAL TESTS

In AVT-233 the shielding tests at the SACCON F17E and the HWB N2A configurations were carried out by DLR in the DNW-NWB acoustic wind tunnel in Braunschweig, Germany. The laser sound source had to be adapted to the larger dimensions of NWB compared to AWB and required a completely new, large lens system. DLR also built a 1:2 replica of the HWB N2A model NASA investigated in the framework of their Environmentally Responsible Aviation Project. Also, the sting support of the SACCON model had to be adapted.

4.1.1 NWB Test Setup

Two wind tunnel models were selected for the experiments (see Figure 1-1). The first is a scaled-down version of NASA's N2A Hybrid Wing Body configuration (HWB) [4] and the second model is DLR's F17E UCAV, (F17E). All models are mounted vertically on a sting in the open test section of the DNW-NWB (see Figure 4-1).

A total of nine G.R.A.S. 40DP pressure field 1/8'' microphones (3 in-flow, 4 out-of-flow, 2 reference out-of-flow) were used to measure both in-flow and in the far field, i.e., out-of-flow. The far field microphones are attached to a fixed structure 3.4 m away from the tunnel axis, on the opposite side to the sound source (see Figure 4-1). The three in-flow microphones are mounted to an acoustically-lined structure free to move linearly in x. The in-flow microphones are located at $y = 0.7$ m away from the tunnel axis line. This location was chosen to ensure a minimum amount of vibration of the structure through interaction with the tunnel shear layer and the wake of the model. Furthermore, two reference out-of-flow microphones were installed at fixed positions on the source side, upstream of the models. Their purpose is to allow for regular check-up measurements of the laser sound source. For each model, a reference source position was defined at which measurements were done twice a day to document the absolute source levels. This procedure allows ruling out any day-to-day deviation in absolute source reference levels in the later calculation of the shielding factors. As can be seen on the right hand side of Figure 4-1, the laser and lenses, necessary for the realization of the reference sound source are mounted on a three-component displacement system, thus allowing for an easy placement of the source about the models.

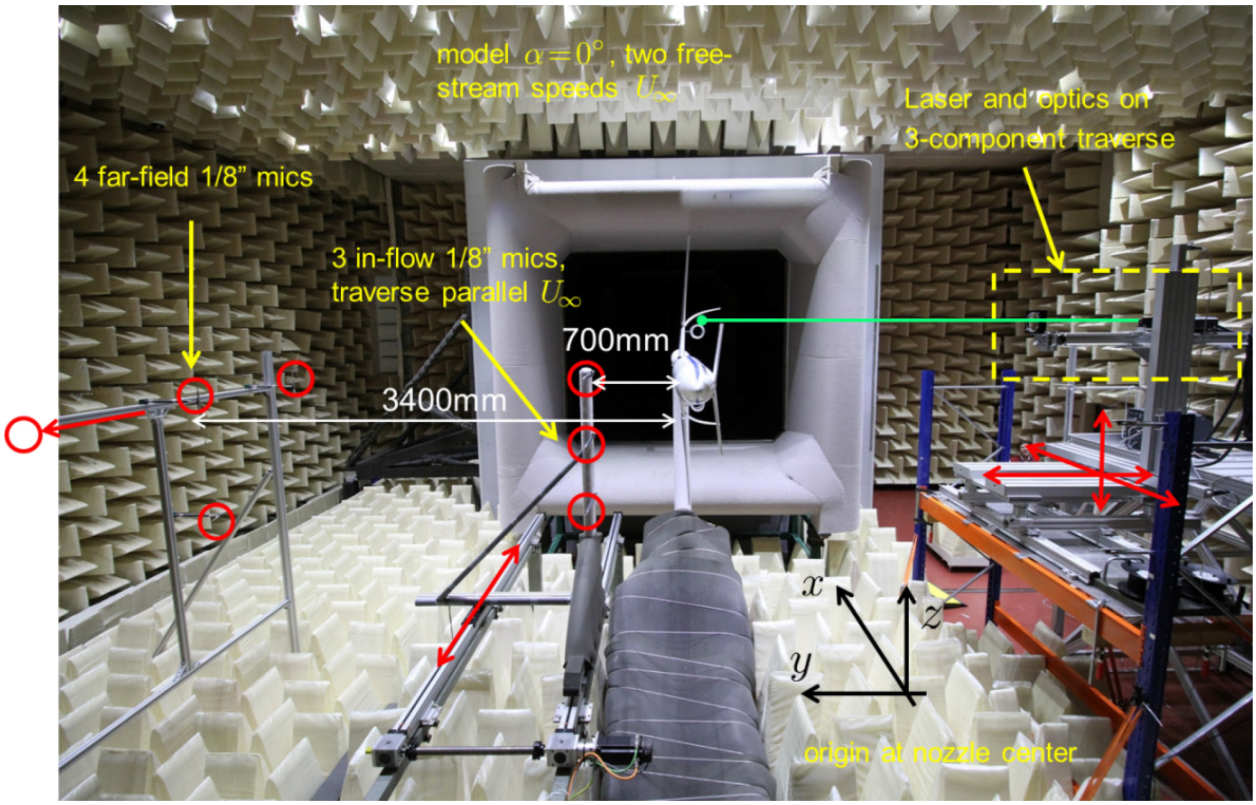

Figure 4-1: Test Setup of an A/C Model in DNW-NWB for Shielding Tests.

In all test cases, the aircraft model was kept at an angle of attack of $\alpha_g = 0°$ and measurements were done for at least two free-stream velocities, U_∞. For each model, different sets of configurations were investigated. For the F17E model only the *"clean"* configuration, i.e., without flow-through nozzles was tested. The HWB model is tested in four different configurations: *"no tailplane, no nacelles(e)"*; *"tailplanes, no nacelles(c)"*; *"tailplanes, two nacelles(a,b)"* and *"no tailplane, two nacelles(d)"*.

Because of the need for a stable in-flow microphone support, the height of support structure had to be kept as short as possible. The highest in-flow microphone therefore only reaches up to the tunnel axis (see Figure 4-1 and Figure 4-2(a)). As one is interested in sampling the widest range of spanwise propagation directions, each set of measurements was repeated with the source placed on either side of the model's symmetry plane. This procedure allows the determination of the radiated noise for a corresponding single source position, i.e., a "single engine" in the following manner. The complete noise field due to a source, on either side of the model symmetry plane, would be obtained by adding the measured contribution to its mirrored version about the symmetry plane, as in Ref. [6]. A sketch of the in-flow microphones setup is given in Figure 4-2, along with the definition of the source emission angles, i.e., θ_{sx} and θ_{sz}, as well as the global coordinate system.

The N2A HWB models had to be protected from the laser beam to prevent burning or the occurrence of small explosions at the model surface. In particular, surface explosions produced secondary spurious noise sources which had to be avoided. Holes had to be drilled into the model to eliminate laser-surface interactions. Inside the model, rough sandpaper was applied to the opposite wall to disperse as much as possible the remaining laser energy.

The F17E model, due its smaller size in comparison to the N2A HWB, could not be tested with the laser beam incidence at 90°, i.e., shooting normal to the model's planform. A laser setup change was necessary to

bring the laser beam parallel to the model surface and therefore eliminate laser-surface interactions. This was achieved using a mirror at 45° to the standard laser output direction. Usage of the mirror prevented, however, the realization of measurements for $U_\infty > 0$ m/s for this configuration.

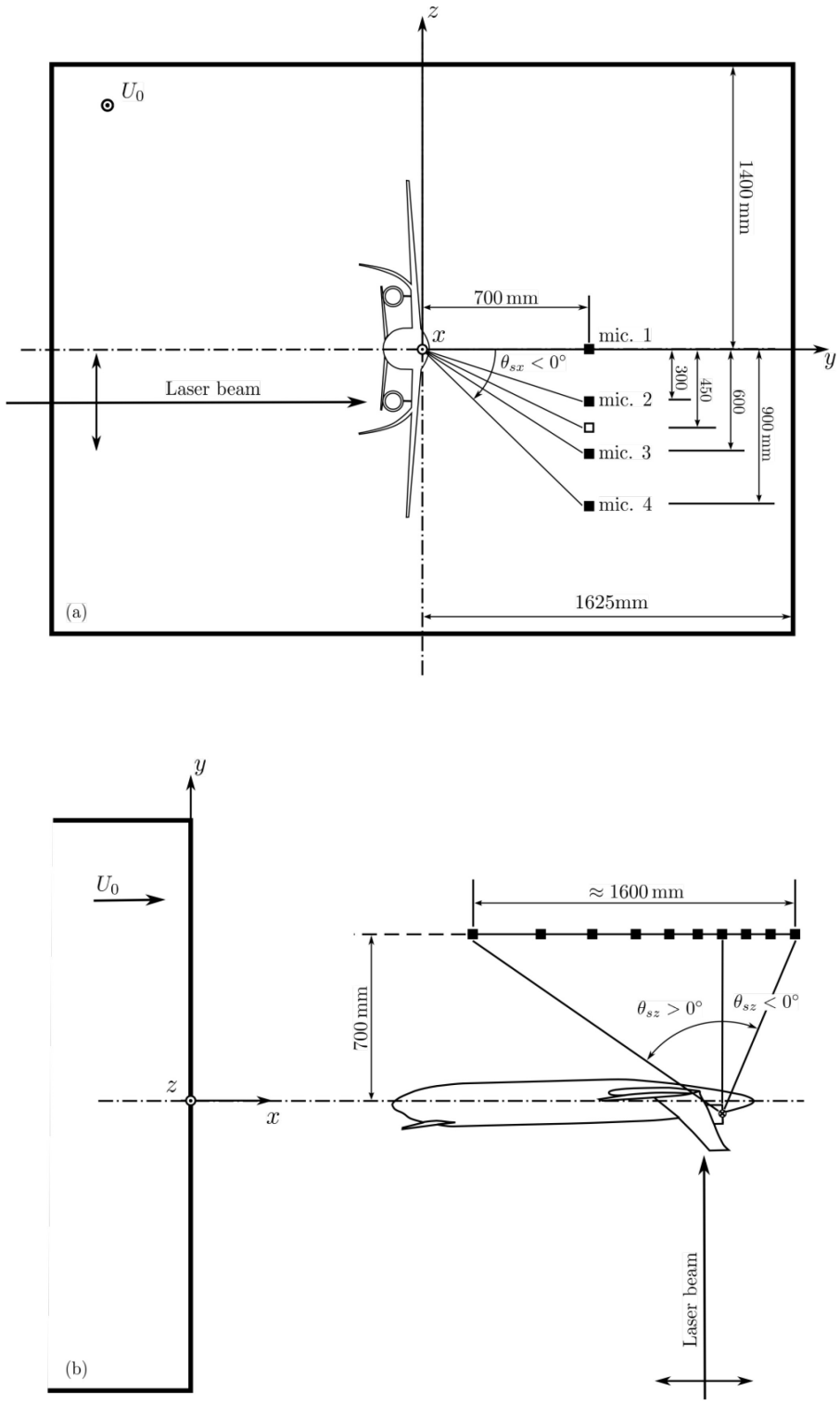

Figure 4-2: Sketch of the Experimental Setup, Coordinate System and Angle Definitions. (a) Upstream view, (b) Top view.

A summary of all the source positions selected for the two models is provided in Figure 4-3. The selection is done with the purpose of investigating the effect on noise shielding of an engine shift about its nominal position. Also, some source positions are picked downstream of the trailing edges, in the prolongation of the engine virtual jet axis, to allow the investigation of the impact of jet noise on noise shielding. For the HWB model, the source was always placed on the virtual engine jet axis (assuming this to be aligned with the free-stream direction, or tunnel axis). This is different for the F17E model, as only the clean configuration was considered. In that case, the source was placed as close as possible to the surface, but never below 10 mm. Downstream of the F17E trailing edge, the source was placed on the virtual engine jet axis.

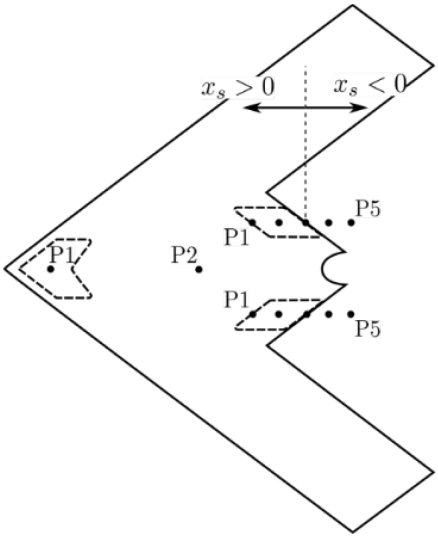

	top/bottom		mid-span	
#	x_s/D	y_s/D	x_s/D	y_s/D
P1	4.62	1.54	22.31	3.15
P2	2.31	1.54	9.38	3.15
P3	0.00	1.54		
P4	-2.00	0.62		
P5	-4.00	0.62		

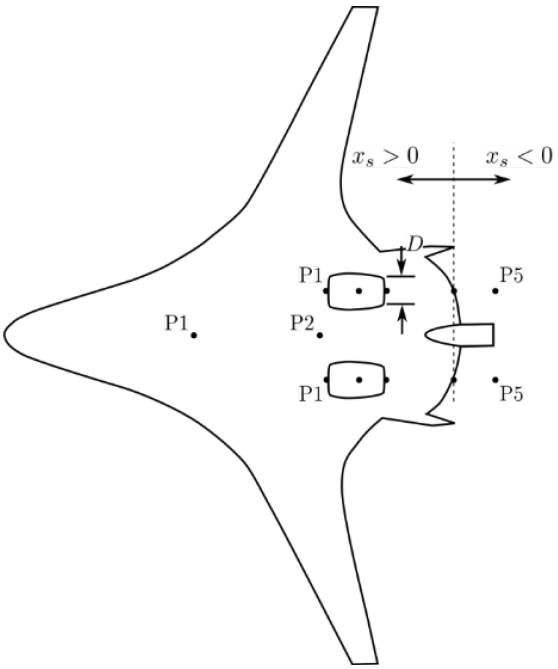

	top/bottom		mid-span	
#	x_s/D	y_s/D	x_s/D	y_s/D
P1	4.49	1.63	9.25	1.68
P2	3.35	1.53	4.76	0.05
P3	2.39	1.45		
P4	0.00	1.15		
P5	-1.49	1.15		

Figure 4-3: Source Positions Definitions. The x_ss coordinate is the source position in x direction relative to the trailing edge and y_s is the distance away from the trailing edge in y direction. Both are referenced to a nozzle dimension D. For the F17E model the nozzle height is taken for D.

4.1.2 Acoustic Shielding Test Results

In this section, an overview of the results for selected test cases is presented. The discussion will concentrate on the general trends revealed by the in-flow measurement data without going into a fine-grained analysis. In the following pages, the data is presented as contour plots of the overall shielding factor, i.e., shielding maps. The shielding factor γ_p is defined as in Equation (3-1), i.e., it represents the overall attenuation over all frequencies contained in the pressure signals measured.

The data presented in Figure 4-4 and Figure 4-5 are calculated for actual measurement positions without back propagation to a 1 m reference distance from the source center. Also, only a single source, i.e., one engine side, is considered. To obtain the complete shielded field for both engines, one could sum up two independent contributions, one for each engine, as is done in Ref. [24]. In Ref. [4], the contribution from each engine is taken to be identical but mirrored about the aircraft plane of symmetry. This is not done here, as we are interested in a most comprehensive description of the shielding characteristics of each aircraft configuration. A more refined analysis of the database will be a matter of much more extended work in the future.

4.1.2.1 Acoustic Shielding at SACCON Configuration

Results for the F17E model are presented in Figure 4-4 for $M_0 = 0$. A sketch of the model equipped with intake and exhaust is added in the contour plots although the measurements were done on the clear F17E.

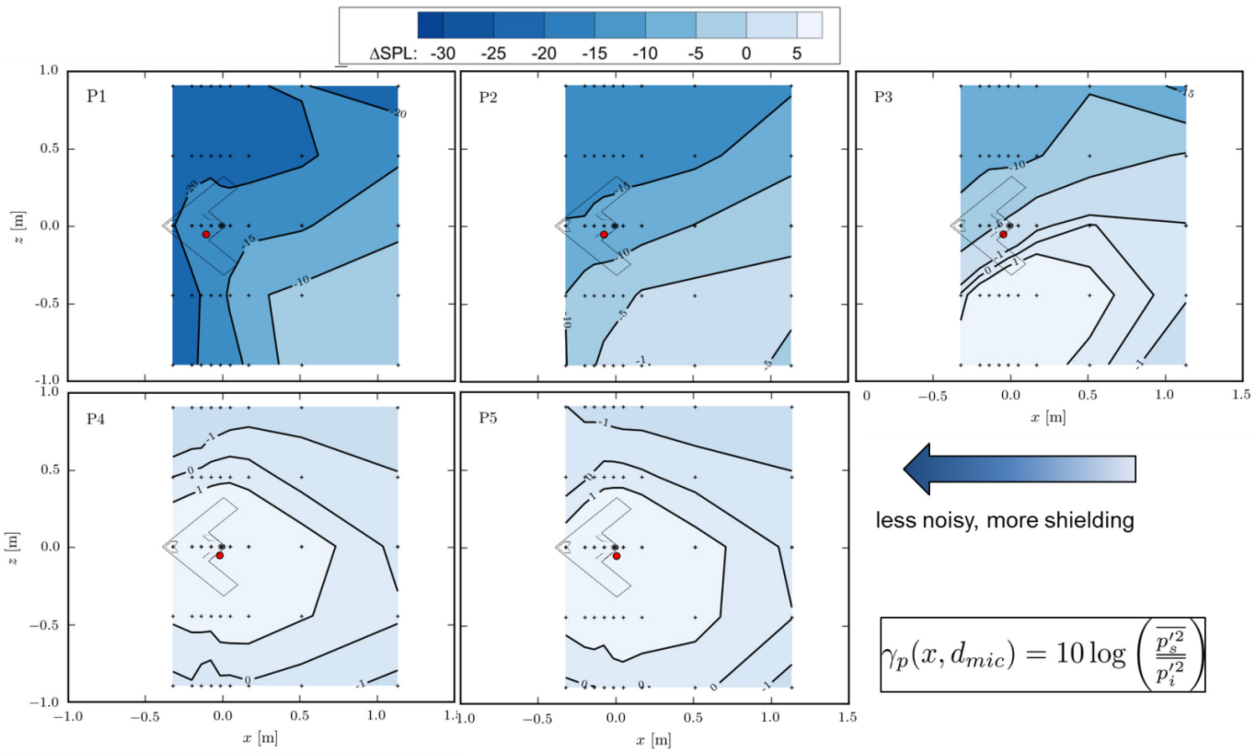

Figure 4-4: Measured Overall (Pulse) Attenuation Below SACCON Geometry in Plane d_{mic} = 0.7 m Below Aircraft. Red dot marks position of source. Crosses indicate microphone positions.

.

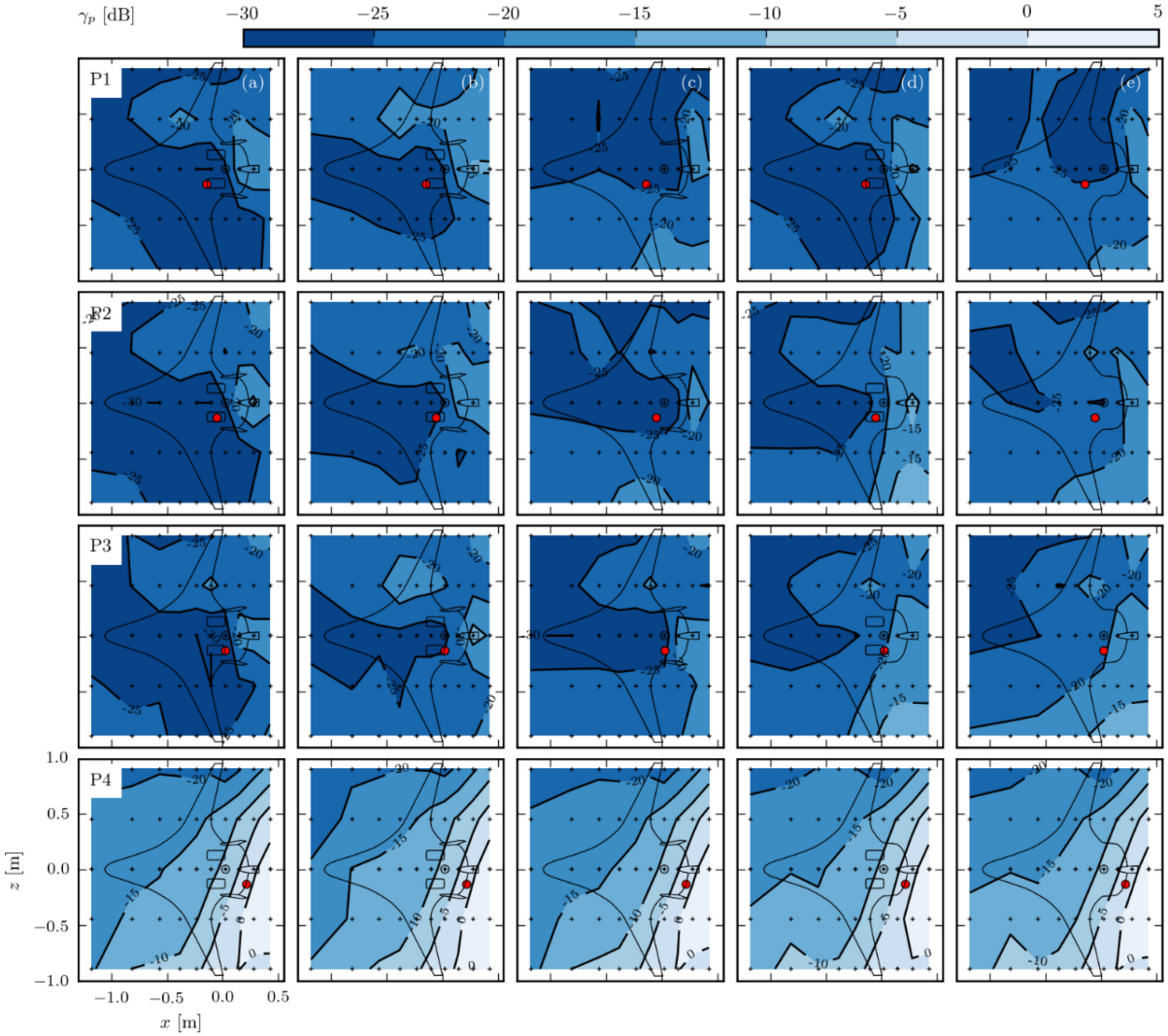

Figure 4-5: Measured Overall (Pulse) Attenuation Below the N2A HWB Geometry in Plane 0.7 m Below Aircraft Including Flow Speed Variation and Geometric Modifications.

As noted previously, the largest sound shielding occurs on the side opposite to the source. For the most upstream source location, levels down by $\gamma_p = -20$ dB are reached, in the most upstream measurement positions. Moving the source further downstream leads to a corresponding increase in γ_p. For source position P3, there appears to be a small zone of sound amplification on the model's port side. The measured data suggest that this effect results from an added contribution due to sound wave reflections on the nearby wing trailing edge; a direct consequence of the model serrated trailing edge design. A relatively important sound shielding is still obtained for the starboard side as the model blocks part of the radiated sound. This is no longer the case when the source is moved downstream to position P4. At this position, the model no longer provides any important sound shielding.

4.1.2.2 Acoustic Shielding of the N2A HWB Configuration

Results for the N2A HWB configuration are presented in Figure 4-5. In the two first columns of Figure 4-5, results for $M_0 = 0$ (column a) and $M_0 = 0.116$ (column b) are presented for the baseline configuration, i.e., vertical tails and nacelles installed. No significant effect of the flow field can be observed in the results, which corresponds to the experimental as well as computational results obtained for the NACA0012. Variations in the contours are related to data uncertainties and the low spatial and level resolution of the contour plots. Removing the nacelle (column c) leads to a lower shielding efficiency to the sideline for P1 and P2, as nothing is blocking sound from propagating between the wing and tail plane. As soon as the source moves to P3 and P4, both configurations deliver very similar results. Removing both the nacelles and the tail planes (column e) leads to a greatly reduced shielding to the sideline for all source positions. Finally, leaving the nacelles installed and unmounting the tail planes (column d), also results in a reduced shielding efficiency for source positions P2 and P3, although not as important as for the previous configuration.

4.2 SIMULATION

The simulation of the 3D aircraft configurations raises severe computational challenges if all the details of the flow field (potential flow gradients, shear layers, boundary layers) are to be taken into account. Although this is principally possible, e.g., by solving the LEE or APE equations numerically as in the study of the 2D NACA0012 shielding problem in Chapter 3, the extreme computational effort requires one to revert to a simplified approach. There are several concepts enabling considerably more efficient computations. Of these, two entirely different approaches may be mentioned here.

One approach would rely on a three-dimensional version of a barrier-shielding approach as demonstrated by BAE Systems in Chapter 3, representing conceptually a ray-tracing concept. There are various ways to account for the diffraction corrections to such ray approaches, one of which is the Maggi-Rubinowicz theory as implemented in DLR's Code SHADOW [41], or the well-known geometrical theory of diffraction of Keller [35].

The other, entirely different concept for a very efficient numerical solution of the shielding problem is to use a boundary element method to solve the Helmholtz Equation. This approach precludes taking into account any flow effects with strong (potential flow) gradients or refraction in shear flows. However, for low Mach number potential flows, Taylor's transformation may be used to include first order flow effects, effectively mapping the convected wave equation back to the Helmholtz equation. In fact, assuming simply the convected wave equation for uniform (low speed) flow may be a very good approximation for slender geometries typical in aeronautics. The essential step to a highly efficient numerical solution to the shielding problem in 3D though is the use of a fast multipole algorithm to solve the boundary integrals in the BEM. In the present case, and as has been shown in Chapter 3, flow effects are practically negligible except for very high frequencies, where boundary layer refraction comes into play.

4.2.1 Computation with Aeroacoustic Prediction Concepts of DLR

At DLR, acoustic shielding effects at full scale aircraft configurations are calculated using the computer code Fast Multipole Code for Acoustic Shielding (FMCAS) [42], which implements a Fast Multipole Boundary Element Method (FM-BEM) solving the Helmholtz equation for the pressure or the acoustic velocity potential. Some information about the theoretical background, as well as the code, will be given.

In case of low Mach number mean flow fields, the shielding of engine noise can be treated as scattering problem governed by the scalar wave equation. Then, the Fourier transformed wave equation (Helmholtz equation) can efficiently be solved by Boundary Element Methods (BEM). Low Mach number potential mean flow fields can be taken into account by a so-called Taylor transformation [43], where the acoustic velocity potential is multiplied by an appropriate flow dependent phase factor. The BEM is obtained by discretization of the Kirchhoff integral solution of the Helmholtz equation. The resulting system of linear equations can be solved using either direct or iterative methods. Direct methods require the storage of the full matrix while for iterative methods, only the calculation of matrix-vector products must be performed. Most efficient are iterative methods, where the calculation of the matrix-vector products is accelerated considerably by so-called Fast Multipole Methods (FMM) [44]. The complexity of the product can be reduced from O(N2) to O(N log N).

FMCAS implements a high frequency formulation of the multi-level FMM basing on a plane wave approximation of the free-field Green's function [45]. The scattering surface is discretized using plane triangles with constant source strength. This requires a minimum resolution of six elements per wavelength. The iterative solvers are taken from the PETSc software library [46]. Acoustic point sources as well as source surfaces with given pressure and velocity values can be used. The code is parallelized using the OpenMP application programming interface.

4.2.1.1 Acoustic Shielding at SACCON Geometry

In a first application of the FMCAS BEM code, the shielding at the SACCON F17E geometry is considered. The geometry in the case of the 28 kHz point source was discretized with a resolution of nine elements per wavelength resulting in about 164000 surface triangles. The iterative solver running on 16 cores converged in about ten steps using about 200 seconds Wall Clock Time. Such a fast convergence is a result of the almost convex shape of the geometry and cannot be achieved for more complex configurations.

In order to get familiar with the shielding properties of this geometry, two prominent source positions are looked at, namely, the central (midspan) position P2, for which maximum shielding may be expected, and P1, right at the position of the exhaust plane (the exhaust geometry cut out was not taken into account, as stated earlier). A frequency of 28 kHz was chosen for this simulation, because (i) it may be considered relevant for the actual aircraft and (ii) because the laser point source provides the highest amplitude in this frequency range, thus allowing for best S/N ratios for comparisons. The right part of Figure 4-6 shows the respective attenuation map for P2 as evaluated in the in-flow measurement plane at a distance of 0.7 m from the aircraft planform plane. Very large shielding factors way beyond 20dB are observed in a square area of 1.5 m x 1.5 m centered about the aircraft. Similarly, large attenuation is found if the source is at the P1 portside position; however, in this case, the location of maximum attenuation plausibly shifts to the front starboard side of SACCON.

A systematic variation of the source position and its consequences on the acoustic attenuation is depicted in Figure 4-7. These results highlight a very strong dependence of the shielding on small variations in the source position in the vicinity of the trailing edge. This is particularly true for the high frequency of 28 kHz, shown in the upper row. At a considerably lower frequency of 7 kHz, the overall shielding is very much reduced due to the stronger diffraction, as expected. The validation of the computation results is discussed in Section 4.3.1.

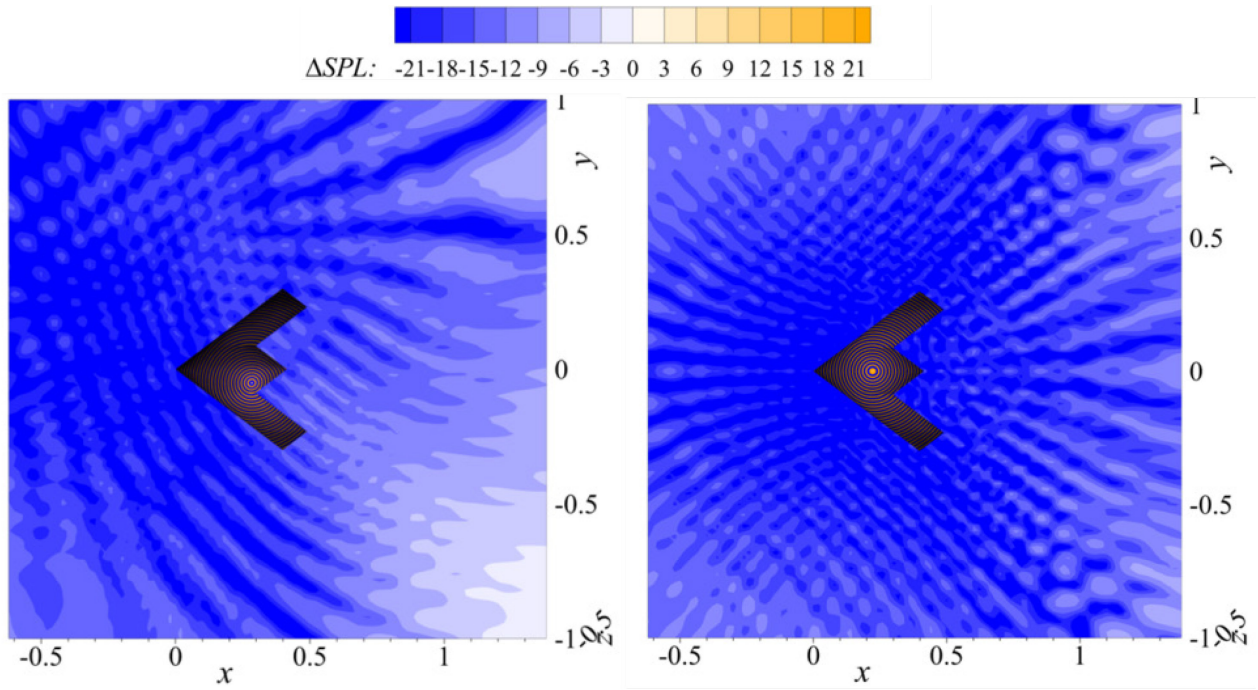

Figure 4-6: Computed Attenuation in Plane 0.7 m Below Aircraft (SACCON Geometry) at f = 28 kHz and M = 0. Left: source position at exhaust outlet plane P1, right: source central position P2.

4.2.1.2 Acoustic Shielding of the N2A HWB Geometry

The N2A HWB geometry in the case of the 28 kHz monopole source was discretized with a resolution of 6 elements per wavelength resulting in about 555000 surface triangles. The iterative solver running on 48 cores converged in about 120 steps requiring about 5200 seconds Wall Clock Time. The SACCON and HWB calculations were executed on different machines, and the performance data shall give only a quick impression of the general efficiency of the FMM code.

The attenuation maps for 28 kHz and 7 kHz are shown in Figure 4-8 for the complete HWB configuration, i.e., containing the nacelles and the verticals. The support sting of the wind tunnel model was included to account for its possible influence on the shielding. Massive shielding on the order of 25 dB is observed for 28 kHz whenever the source is at the intake, inside, or the exhaust of the nacelle. It is noted that the attenuation was evaluated with respect to the isolated point source and not with respect to the field of the isolated nacelle. If the source comes close to the trailing edge of the HWB, the shielding reduces considerably in the rearward domain as expected. Again, as for the SACCON, the attenuation is lower for the 7 kHz source but remains considerably higher than for the SACCON due to the larger size of the HWB.

.

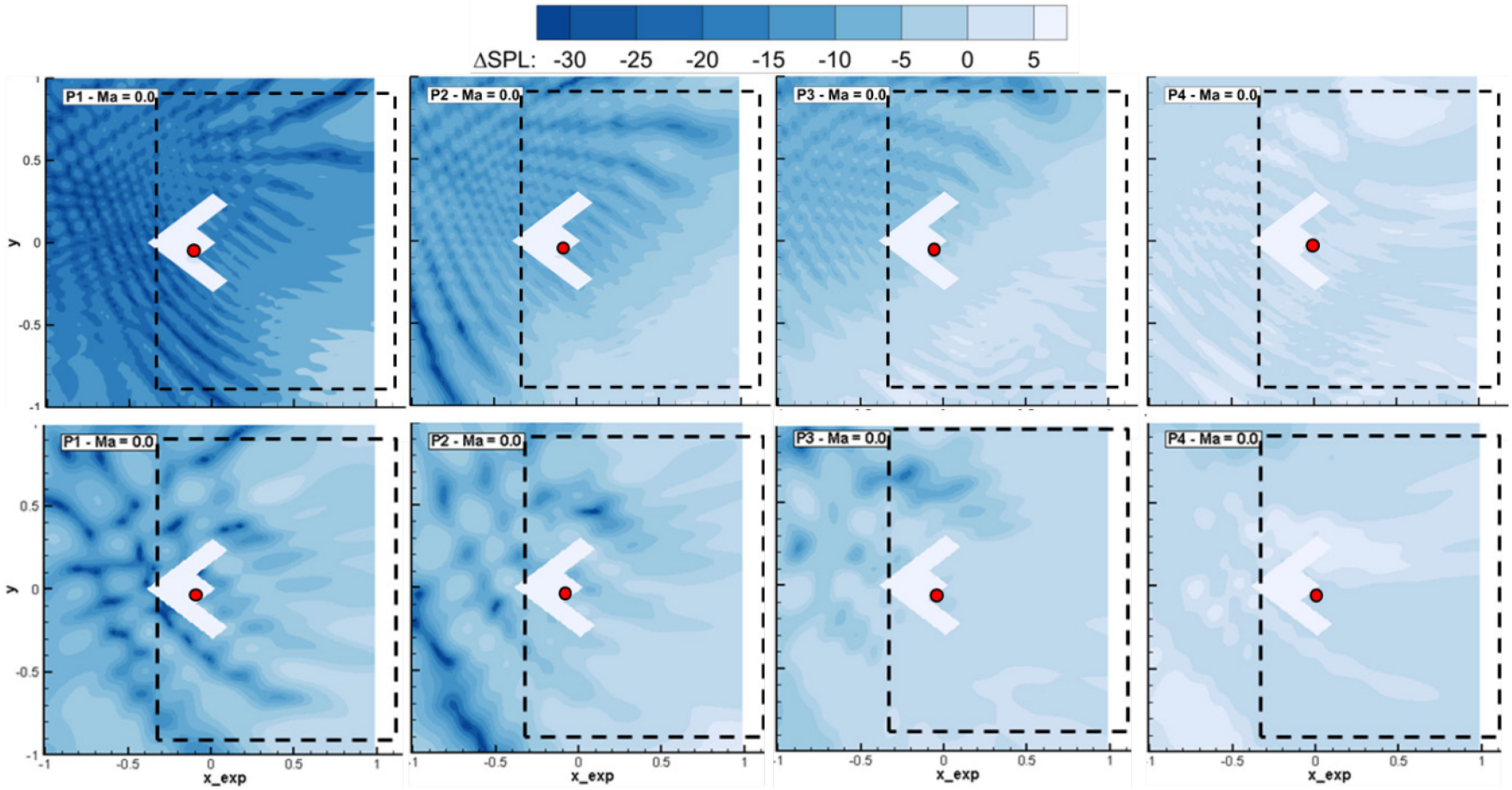

Figure 4-7: Computed Attenuation in Plane 0.7 m Below Aircraft (SACCON Geometry) at M = 0 for Source Position P1, P2, P3, P4. Top row 28 kHz, Bottom row: 7 kHz; dashed boxes indicate area, where validation data were taken in the NWB experiments.

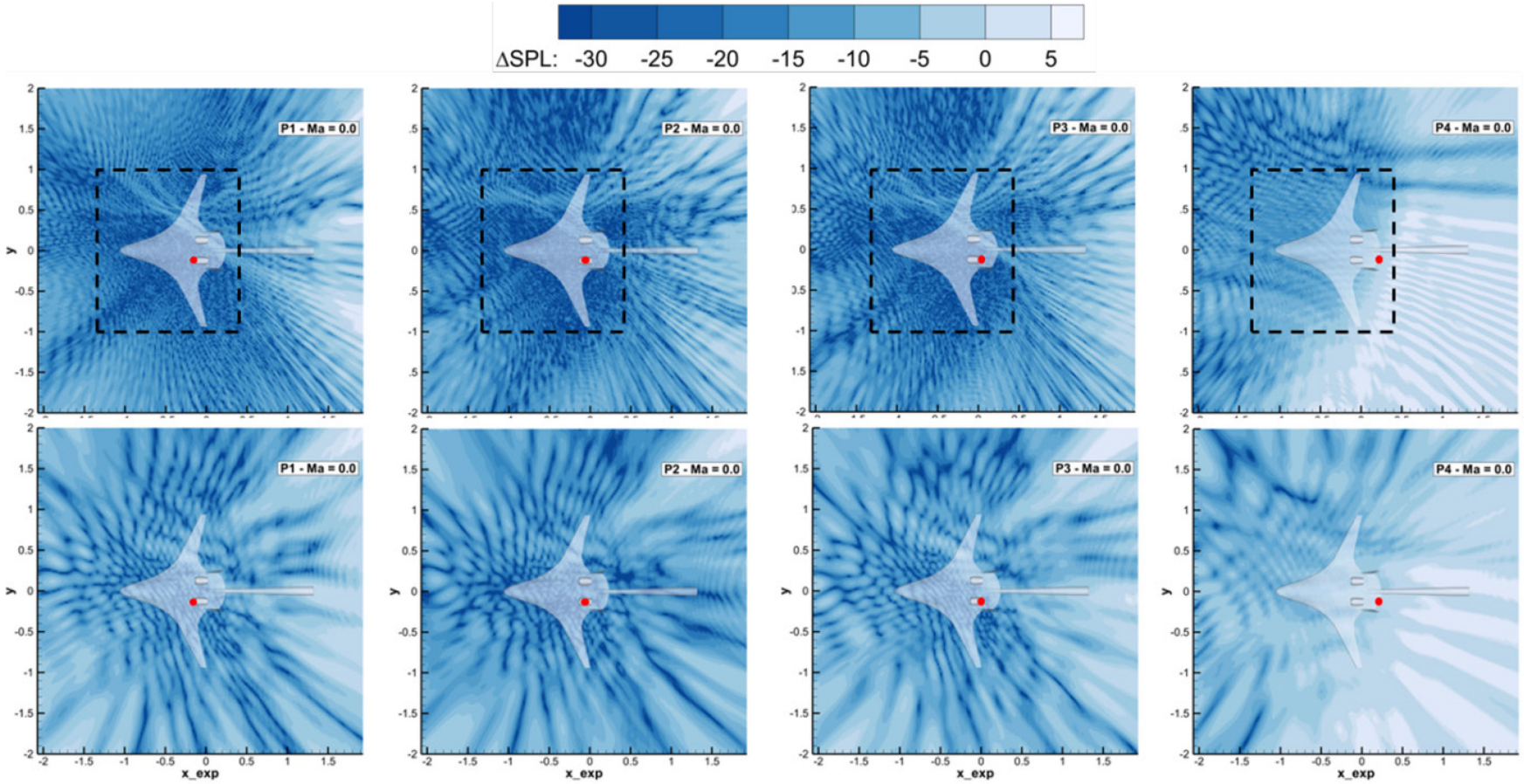

Figure 4-8: Computed Attenuation in Plane 0.7 m Below Aircraft (N2A HWB Geometry) at M = 0 for Source Position P1, P2, P3, P4. Top row 28 kHz, bottom row: 7 kHz; dashed boxes indicate area, where validation data were taken in the NWB experiments.

4.2.1.3 Relevance of Near Field Attenuation in View of Far Field Attenuation

Acoustic shielding experiments need to be done at the complete aircraft geometry. This in turn leads to considerable downscaling of the original dimensions of the aircraft to its model replica, whose size is (strongly) limited by the wind tunnel jet cross section. On the other hand, a large as possible model is preferred in order to realize a representative turbulent flow. Shielding experiments would normally be conducted in an open test section environment of an acoustic wind tunnel in order to avoid any spurious reflections from wind tunnel walls.

The objective of shielding experiments is to determine the far field attenuation of engine sound by the aircraft geometry. Measuring the far field signals in an open test section acoustic wind tunnel almost always will amount to using out-of-flow microphones. This in turn comes with the price of having to deal with refraction and scattering of the sound signals traveling through the wind tunnel shear layers and, thus, some sort of correction. The mentioned small scales of wind tunnel aircraft models and correspondingly up-scaled frequencies of relevance on the one hand, in combination with highly turbulent wind tunnel jet shear layers on the other hand, pose severe difficulties to any such correction.

In order to circumvent these adverse effects, in-flow microphones were used throughout this shielding research. Measuring inside the flow of course has its own challenges. Microphones have to be placed well inside the potential core of the wind tunnel jet, while not approaching the model too closely because the presence of the microphones and their support system could possibly alter the flow field. These compromises will almost always result in measurement positions in the geometric near field of the aircraft, which, unfortunately, is not the objective of shielding tests.

Intuitively, it is not obvious how representative measured geometric near field data from acoustic wind tunnel tests is in view of the desired far field information. The difference of near field to far field information may be analysed on the basis of 3D acoustic computations. Therefore, using DLR's fast multipole boundary element wave solver FMCAS, a respective computational study was conducted for the (relatively) small F17E configuration and the (relatively) large HWB configuration. The relevant measurement (near field = in-flow measurement) distance in the DNW-NWB was 0.7 m. A few far field microphones were also mounted at the wall of the anechoic chamber of NWB at 3.4 m distance.

Computations for the SACCON F17E configuration are shown in Figure 4-9 for various source positions and receiver planes at 0.7 m and 3.4 m below the aircraft for a frequency of 28 kHz. The upper row of contour plots shows the near field plane. For each source position, a dashed square indicates the area, which corresponds to the respective depicted far field area in the lower row. It would appear if the far field area would be geometrically mapped (and shrunk) toward the centerpoint of the aircraft and evaluated at 0.7 m distance. This mapping would correspond to a simple back-propagation by a 1/r rule.

It is quite striking how accurately the corresponding attenuation contours map between far field and near field. As a result of this study, one may conclude that for the SACCON model with a characteristic dimension of about 0.7m, a measurement distance of about one characteristic dimension of the model is sufficient to determine far field information.

The second study is on the N2A HWB model, which has a span of more than 1.8m. One may, therefore, expect that the measurement plane at 0.7 m below the planform of the model definitely is within the geometric near field of the model. This, in turn, suggests that differences should be visible when comparing with the shielding attenuation in the far field. The upper row of Figure 4-10 shows the near field attenuation map at 0.7 m distance, and the lower row depicts the corresponding domain at a distance of 3.4m.

.

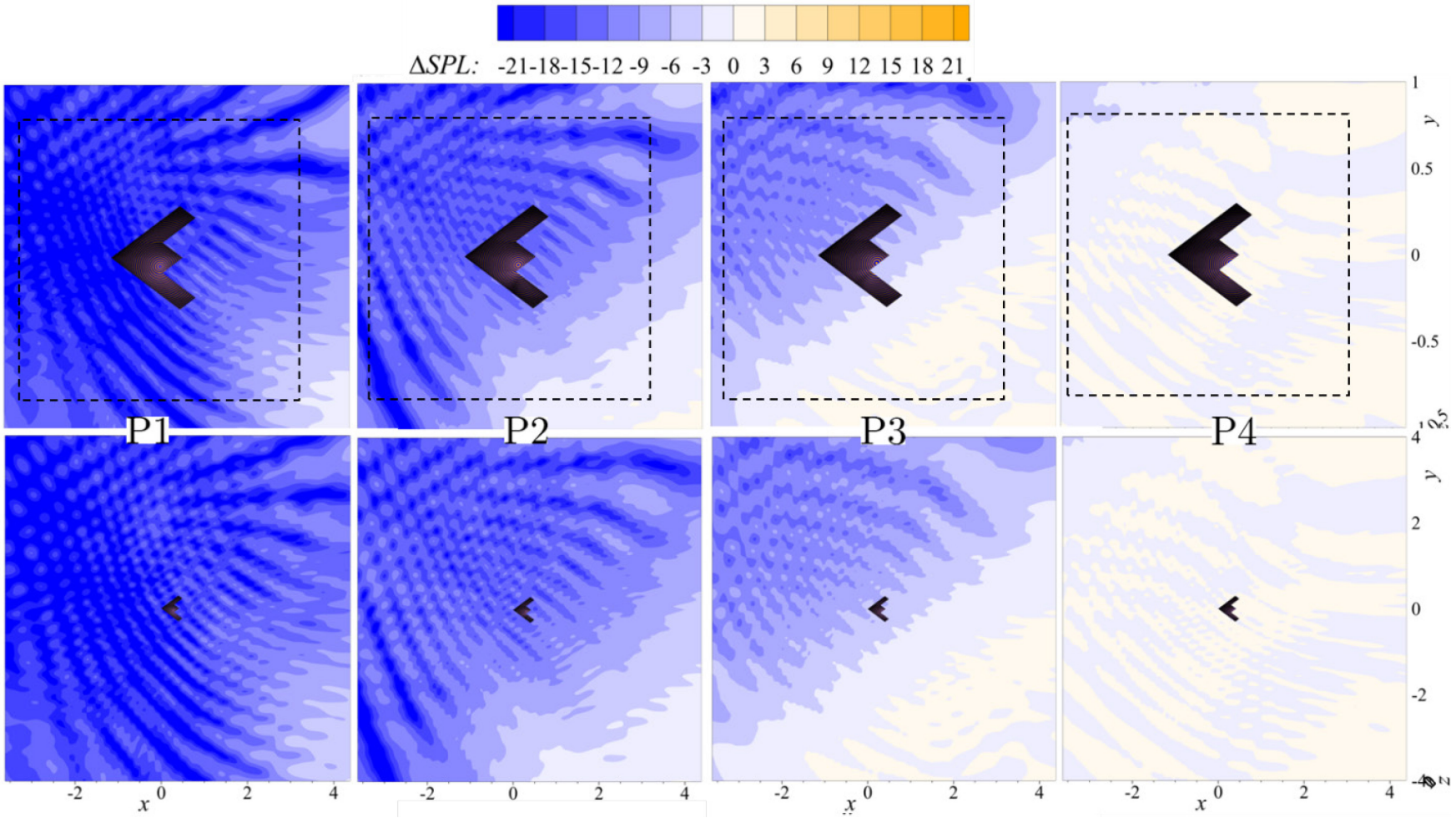

Figure 4-9: Computed Attenuation for SACCON in Plane 0.7 m Below Aircraft (Top Row) in Comparison to Far field Plane 3.4 m Below Aircraft (Bottom Row) for Various Source Positions at f = 28 kHz and M = 0. Dashed square indicates depicted far field area, geometrically mapped (and shrunk) toward the centerpoint of the aircraft at 0.7 m distance.

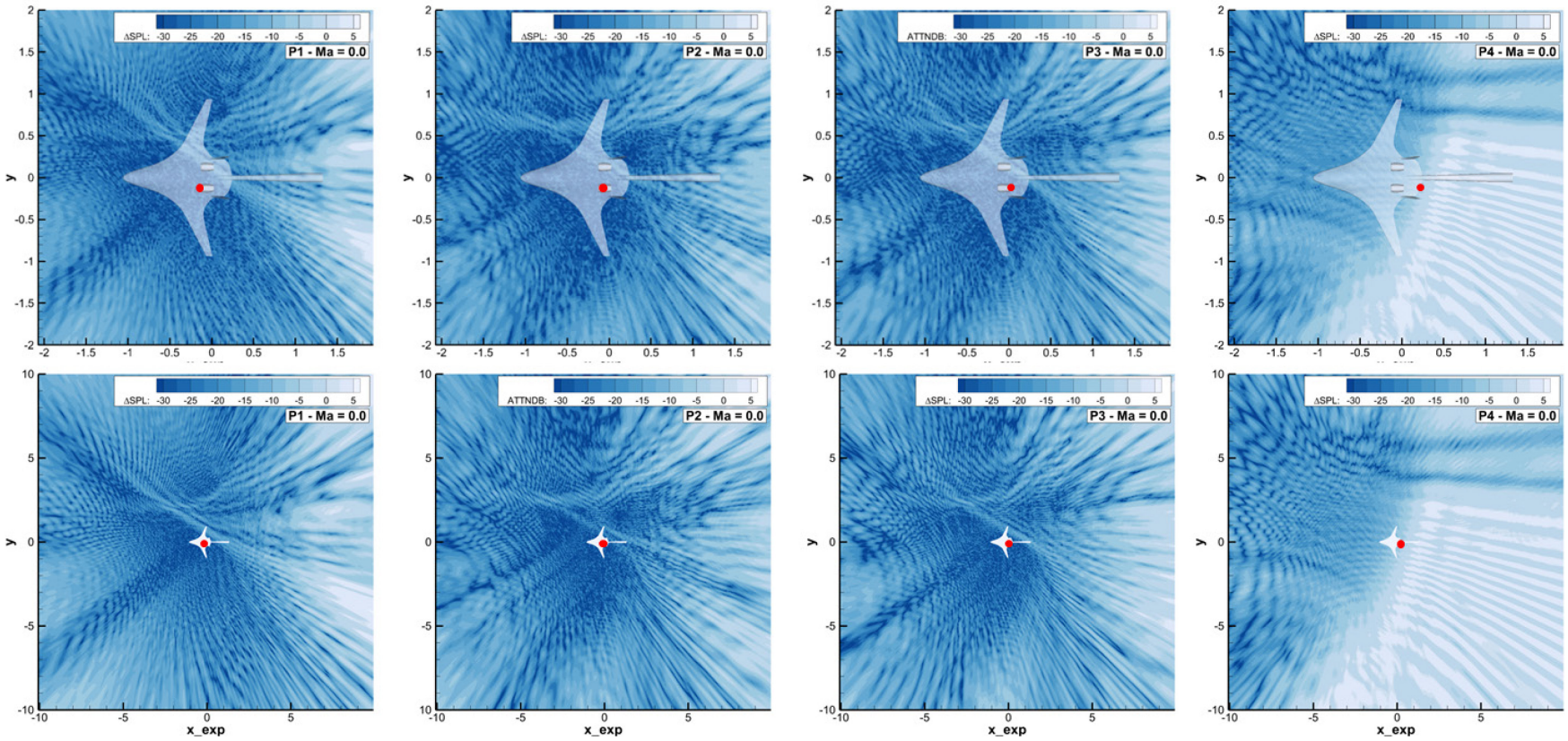

Figure 4-10: Computed Attenuation for the N2A HWB in Plane 0.7 m Below Aircraft (Top Row) in Comparison to Far field Plane 3.4 m Below Aircraft (Bottom Row) for Various Source Positions at f = 28k Hz and M = 0. The depicted domains for 0.7 m and 3.4 m correspond to one another upon assuming geometrically mapping towards the centerpoint of the aircraft.

The similarity of the attenuation maps at the two distances of the aircraft plane is remarkable. Although the 0.7 m plane is definitely in the geometric near field, the patterns are different only by insignificant details to those seen in the 3.4 m plane. This is a relatively surprising result of the study. At the same time, this quite impressively shows that the in-flow measurement at 0.7 m distance to the model is already representative for the far field.

Note that even if the field at 0.7 m distance from the model would not have been representative for the far field, a code validation for a prediction code for shielding could be validated on the basis of near field data, and the same code could then be used to extrapolate the underlying pressure fields to the far field, where the true far field attenuation maps could be produced.

4.2.2 Computation with Aeroacoustic Prediction Concepts of BAE Systems

With the 3D SACCON geometry, predictions with two different techniques were attempted, one based on a ray-tracing method and the second a computational approach based the BAES Altus code. The SACCON geometry used in the predictions is presented in Figure 4-11.

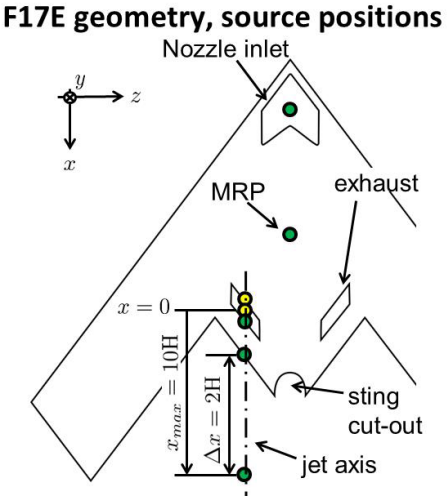

Figure 4-11: SACCON Test Configuration.

4.2.2.1 3D Ray-Tracing Prediction Method

The ray-tracing code used to predict the 2D airfoil was modified to predict the 3D SACCON geometry. This required the inclusion of geometric components in the spanwise direction. A simplified representation of the 3D model was used. As with the 2D airfoil, the 3D aircraft geometry was represented by a planform with no thickness as presented in Figure 4-12. As in the 2D case, the source was located above planform and the receiver was located below the planform. The nose of the aircraft is located at 0.0 in Figure 4-12. Figure 4-12 also shows the two ray paths used in the calculation, one around the leading edge and the other around the trailing edge. Dependent on the source-receiver geometry the trailing edge path may be around any of the trailing edge surfaces.

The effect of flow speed on the predicted effect of shielding is implemented using an effective propagation path as presented in Figure 4-13. For example, for the path from the source to the leading edge shown in orange in Figure 4-13, the effective propagation path is defined as the path such that in the time taken for an acoustic wave to propagate from the source to a point ahead of the leading edge, the flow would propagate the acoustic wave downstream by a distance d. Thus, the distance d is equal to the flow velocity v multiplied by the time t taken for the acoustic wave to propagate from the source to a point ahead of the leading edge.

The path described above is a simplified geometric representation of the actual propagation path from the source to the leading edge, which in the presence of flow has a curved trajectory. Similarly, the paths from the source to the trailing edge and the paths from the leading and trailing edges to the receiver are implemented as effective paths in the presence of flow.

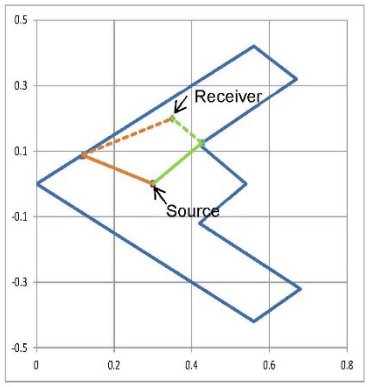

Figure 4-12: 3D Ray-Tracing Modeling of SACCON Configuration.

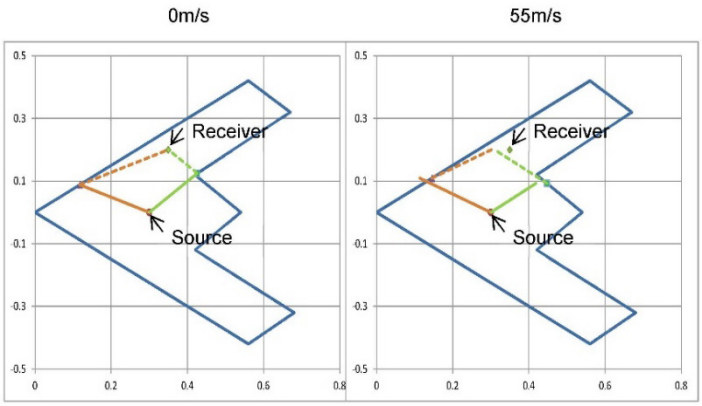

Figure 4-13: Calculate Propagation 3D Paths.

In principle, the adaptation of the 2D ray-tracing code to the simplified 3D SACCON geometry is straightforward. However, in practice, the multiple elements of the trailing edge resulted in significant challenges in calculating the geometry correctly. A fully operational version of the 3D ray-tracing code was not available in the time frame of the task group. Some initial calculations were performed and presented at the task group meetings as an interim status of the progress of the work. The predicted results were clearly incorrect in many regions under the aircraft. Further work is required to correct the code in order to produce presentable attenuation results.

4.2.2.2 BAE Systems Altus Prediction Code

No modifications were required for the Altus code to be used for 3D geometries. Some initial calculations were performed and presented at the task group meetings as an interim status of the predictions. In order to reduce the substantial computational effort, a half model was used in the calculations. The predicted attenuation values were clearly incorrect in a plane under the aircraft. It is thought that issue lies with the implementation of the half model in the calculations that requires further refinement, as the code gives good agreement with other codes for the 2D test cases. Further work is required in order to produce presentable attenuation results.

4.3 COMPARISON OF SIMULATION WITH EXPERIMENTS

This section discusses the validity of the numerical simulation of the acoustic shielding for the SACCON F17E and the N2A HWB configurations, respectively. DLR's fast multipole boundary element code FMCAS was used to simulate the 3D acoustic attenuation of these geometries. NASA's diffraction integral based code KIM was used to simulate the shielding at the N2A HWB trailing edge region. Both (simplifying) approaches appear to be justified because of the findings in Chapter 3, which showed that for low Mach number flows and not too high frequencies, any shear flow effects may be neglected. By using the BEM approach, a potential mean flow may be accounted for at most. In fact, again referring to Chapter 3 one could see that the flow Mach numbers considered in this study are low, i.e., just above 0.1, and thus, only small flow gradients appear. In other words, a uniform flow assumption is well justified for the cases studied. Generally, one may expect flow effects to be practically negligible.

The data acquired in the DNW-NWB measurements are compared with the DLR FMCAS simulations on the basis of acoustic attenuation maps on a plane, 0.7 m below the aircraft (either F17E or HWB). Due to reasons of limited resources, the microphones could not be densely spaced to resolve any detail of the complex interference pattern below the aircraft. In that sense, the measurements mainly served to produce acoustic data, which could be directly compared to simulations, evaluated at exactly these same positions. The same numerical simulation could then be used to produce a densely resolved sensor field to depict the complete shielding map. The predictions of NASA on the HWB configuration were compared with measurements taken on the original larger scale NASA model, see Refs. [4], [47], [48].

4.3.1 DLR Validation of FMCAS Predictions for SACCON F17E

Figure 4-14 shows the comparison of the experimentally vs. the numerically obtained acoustic attenuation for the F17E configuration at 28 kHz for source positions P1 to P4. The upper and center rows, respectively, show the measured and computed attenuation maps as directly generated from the sensor positions depicted in Figure 4-4. The global distribution of the attenuation as simulated corresponds quantitatively well with the measurements. However, local deviations in the distribution may be seen. The reason for these may be inferred from the spatially resolved attenuation map, depicted as a repetition from the computation results section in the bottom row of Figure 4-14. Quite small deviations of the sensor positions from their nominal values may let it pick up a local maximum inside of a narrow interference fringe pattern, while on the desired position there may just be a local minimum.

The same good comparison between measurement and simulation is seen in Figure 4-15 for a much lower frequency of 7 kHz, i.e., a quarter of the frequency considered previously.

4.3.2 DLR Validation of FMCAS Predictions for HWB

Figure 4-16 shows the comparison of the experimentally vs. the numerically obtained acoustic attenuation for the HWB configuration at 28 kHz for source positions P1 to P4. The upper and center rows, respectively, show the measured and computed attenuation maps as directly generated from the sensor positions depicted in Figure 4-5. The global distribution of the attenuation as simulated corresponds quantitatively well with the measurements. However, local deviations in the distribution may be seen. The reason for these may be inferred from the spatially resolved attenuation map, depicted as a repetition from the computation results section in the bottom row of Figure 4-16. Quite small deviations of the sensor positions from their nominal values may let it pick up a local maximum inside of a narrow interference fringe pattern, while on the desired position there may just be a local minimum.

As for the SACCON simulations, the same good comparison between measurement and simulation is seen in Figure 4-17 for a much lower frequency of 7 kHz, i.e., a quarter of the frequency considered previously.

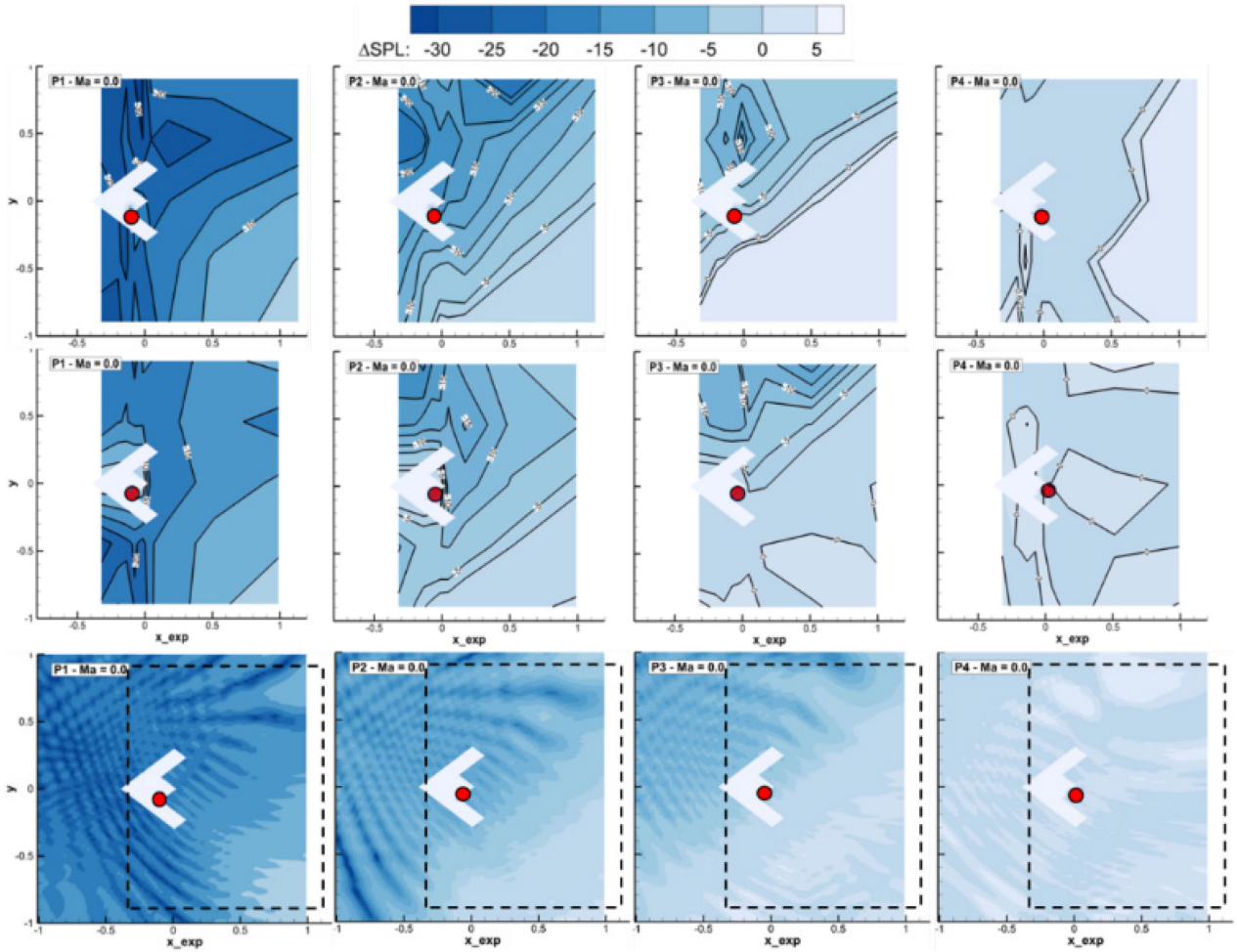

Figure 4-14: Comparison Attenuation in Plane 0.7 m Below Aircraft (SACCON) at 28 kHz, M = 0. Top row: experiment, central row: computation at same sampling points as experiment, bottom row: densely spaced sampling points (repeated from Figure 4-7).

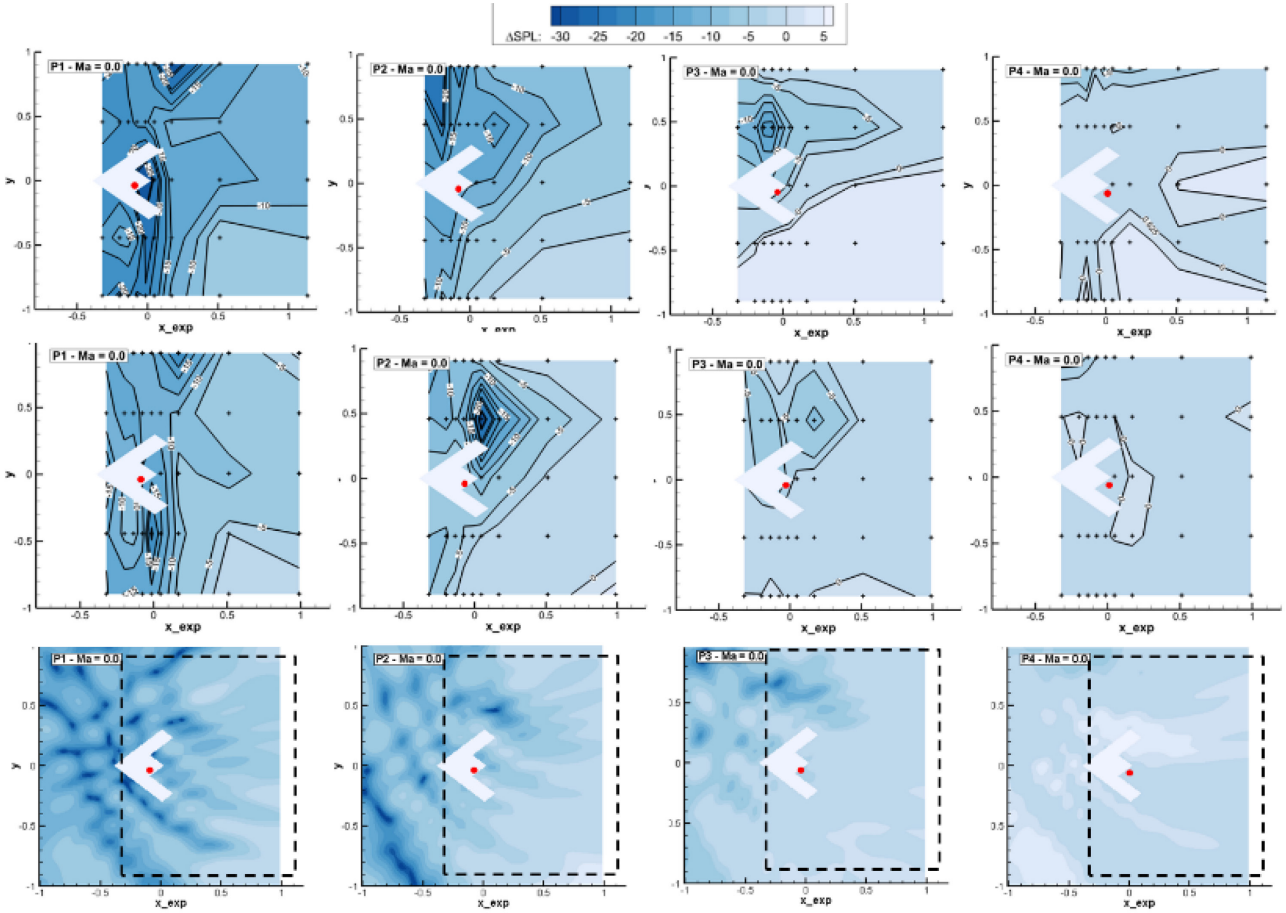

Figure 4-15: Comparison Attenuation in Plane 0.7 m Below Aircraft (SACCON) at 7 kHz, M = 0. Top row: experiment, central row: computation at same sampling points as experiment, bottom row: densely spaced sampling points (repeated from Figure 4-7).

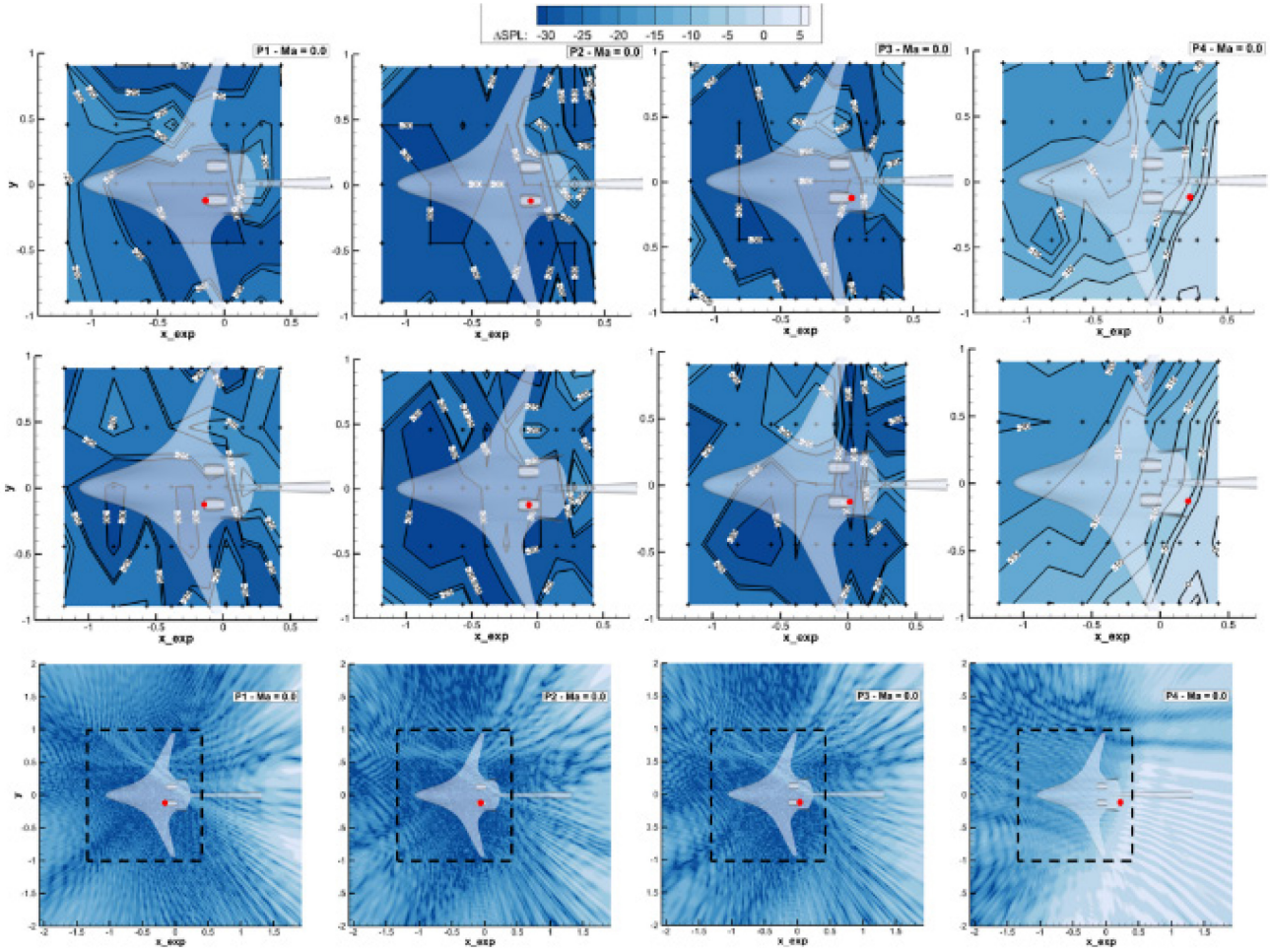

Figure 4-16: Comparison Attenuation in Plane 0.7 m Below Aircraft (HWB) at 28 kHz, M = 0. The top row shows the experiment, the central row: computation at same sampling points as experiment, bottom row: densely spaced sampling points (repeated from Figure 4-8).

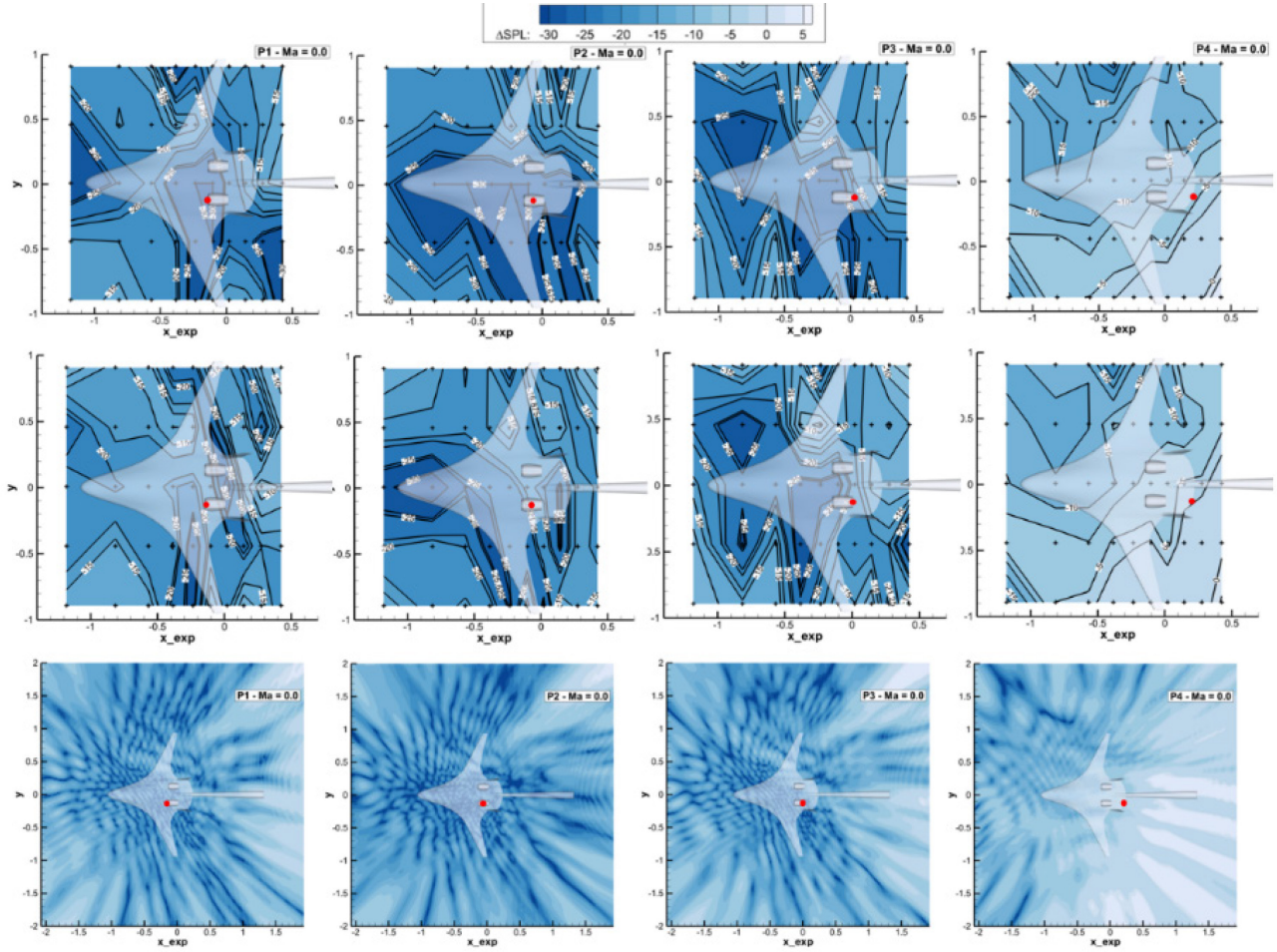

Figure 4-17: Comparison Attenuation in Plane 0.7 m Below Aircraft (HWB) at 28 kHz, M = 0. The top row shows the experiment, the central row: computation at same sampling points as experiment, bottom row: densely spaced sampling points (repeated from Figure 4-8).

4.3.3 NASA KIM Prediction of Shielding of the N2A HWB Wind Tunnel Model

This section discusses validation of the KIM by wind tunnel test data from the N2A HWB aircraft model with a broadband incoherent noise source. This is a very different experiment as compared to the NACA 0012 experiment discussed earlier. In contrast to the spark laser source, the broadband source is generated inside a nacelle and creates a distributed (over the exit plane of the nacelle) noise source. In addition, the N2A is a more complex, complete airframe, in contrast to the 2D NACA 0012 airfoil. The N2A aeroacoustic test has been discussed in detail in Refs. [4], [47], [48], so that only the relevant information is described here to facilitate the discussions. The N2A HWB model is a 5.8% scale version of a full scale aircraft with a similar mission to a Boeing 767 freighter aircraft, and the N2A noise sources, which are broadband and incoherent, are placed inside a nacelle located on the topside of the aircraft in the vicinity of the aircraft trailing edge. The aircraft model is shown in Figure 4-18.

In the KIM prediction of the N2A experimental data, the nacelle itself is not modeled. Instead, the sources are modeled to be at the exit of the nozzle, which is specified by the nozzle diameter D and the distance x between the nacelle exit and the trailing edge of the HWB airframe. Both are indicated in Figure 4-18. The local geometry in the HWB trailing edge region can directly affect the shielding of the noise from the engine. This includes the twin nacelles, the vertical tails and the trailing edge elevons. The elevons are labeled from E1 to E6 in the figure, going from the aircraft centerline to the wing tip. These local geometry features can cause multiple reflections for the acoustic waves, before they reach the edges to be diffracted to the far field. It is intuitive to see that these multiple reflections are likely to affect sideline locations. Since the validations and discussions here are focused on the flyover plane, which is dominated by the diffraction of the waves directly radiated from the source to the aircraft edges, these local geometry features are ignored for now. It is important to point out that they need to be accounted for in more general applications where the measurements include other locations.

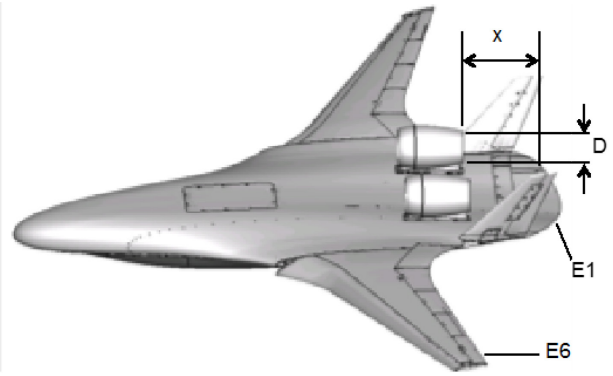

Figure 4-18: N2A HWB Model Used for Broadband Noise Shielding Experiments.

The noise shielding tests were done with variations of the source locations and mean flow Mach numbers, in addition to variations in the aircraft geometry components in the trailing edge region, such as the vertical tails and the elevons. The test conditions are summarized in Table 4-1. The first three columns are self-explanatory, respectively giving the case number, the tunnel mean flow Mach number, and the model Angle Of Attack (AOA) in degrees. The fourth column is the source location as a ratio of the source distance to the trailing edge of the HWB aircraft to the diameter of the nacelle. The fifth column lists the elevon deployment angles in degrees. There is a total of 11 elevons along the trailing edge of the aircraft, symmetrically distributed; E1 is on the centerbody and E2 to E6 are mirrored between the two wings. Because of the symmetry, only half of the set is listed in the table, denoted by E1 to E6, starting from the aircraft centerline and moving outward along the span. A value of 0^o means the element is not deployed. Positive deployment angles represent rotation downward, and negative angles denote rotation upward. The last column indicates the configuration of the vertical tails, either on or off.

Table 4-1: N2A HWB Noise Shielding Test Conditions.

Case Number	*Mach Number*	*AOA (Deg)*	*x/D*	*Elevon Angle (Deg)*	*Vertical Tail*
1	0	13	2.5	0	On
2	0.19	13	2.5	0	On
3	0	13	1.5	0	On
4	0.19	13	1.5	0	On
5	0	13	0	0	On
6	0.19	13	0	0	On
7	0	13	2.5	0	Off
8	0.19	13	2.5	0	Off
9	0.21	15.5	2.5	-10 for E1 to E4, 0 for E5 to E6	On
10	0.23	13.2	2.5	-10 for E1, 0 for E2 to E6	On
11	0	13.2	2.5	-10 for E1, 0 for E2 to E6	On

To illustrate the comparisons between the KIM prediction and the test data, cases #5, #3 and #1 are shown in Figure 4-19, Figure 4-20, and Figure 4-21, respectively, for the source location at the trailing edge, 1.5 fan nozzle diameters upstream of the trailing edge, and 2.5 upstream of the edge, all illustrated in the figures. The noise attenuation due to the shielding is defined as:

$$\Delta SPL = 10\log\left(|p|^2 / |p_I|^2\right) \tag{4-1}$$

where p is the total acoustic pressure and p_I is the incident acoustic pressure. In all three cases, the noise attenuation due to shielding, as defined by Equation (4-1) in decibels, is plotted as a function of the polar angle θ in the flyover plane. The KIM predictions are represented by the solid curves, and the test data are plotted by the dashed curves with symbols indicating the measurements. In addition, the dash-dot curves in the figures represent predictions using the Maekawa formula [49] which is an analytical formula implemented in NASA's Aircraft Noise Prediction Program (ANOPP).

For all cases, results are shown for three frequencies at the small model scale, given in the figures with red color curves for 20000 Hz, green color curves for 40000 Hz, and blue color curves for 63000 Hz. At the scale factor of 5.8%, these model scale test frequencies correspond to 1160 Hz, 2320 Hz and 3654 Hz at full scale, all within the important frequency range for aircraft noise certification. In the test data processing, in order to properly account for the potential effects of the wake flows from the aircraft, the shielding is defined with the baseline given by the case when the source is 0.5 fan nozzle diameters downstream of the aircraft trailing edge [4], [47], [48]. Thus, the quantity p_I in Equation (4-1) is acoustic pressure due to the source with the aircraft model placed upstream of the source. The same definition is used for the predictions so that the comparisons are relevant.

For the case of $x/D = 0$ where the source is located at the trailing edge, shown in Figure 4-19, the shielding is correctly predicted to be zero for all frequencies in the aft quadrant for polar angles larger than 90 degrees. It should be pointed out that the large differences between the solid curves and the dashed curves shown in the figure for the angle of 90 degrees is an artifact of the lack of measurement data at this angle; the dashed

curves are simply the connection of the two symbols at about 85 and 95 degrees and do not represent the correct shielding values at 90 degrees. In fact, if the dashed curves are ignored and the comparisons are made between the solid curves and the symbols, the good agreement between the two becomes clear. It is also apparent from the figure that the Maekawa formula is not applicable for the configuration because the aft quadrant is not a shielded region when the nozzle exit is aligned with the trailing edge of the aircraft.

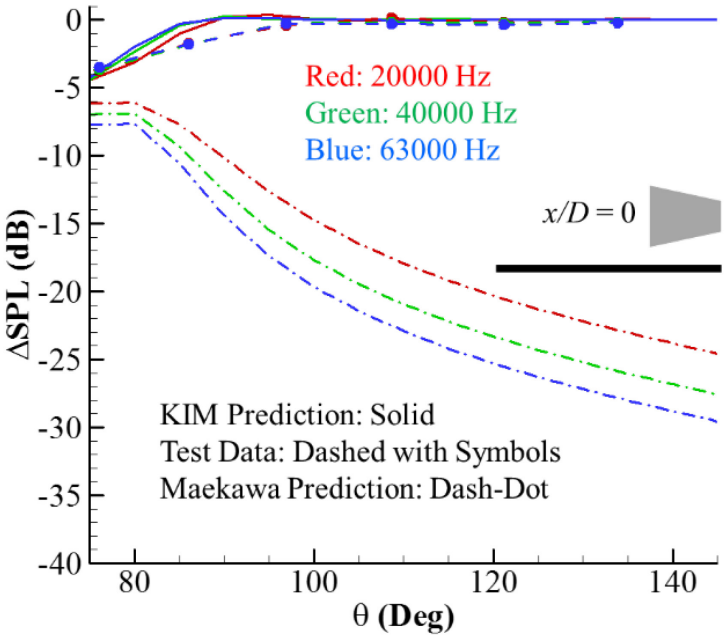

Figure 4-19: Comparison Between Prediction and Data for *x/D* = 0.

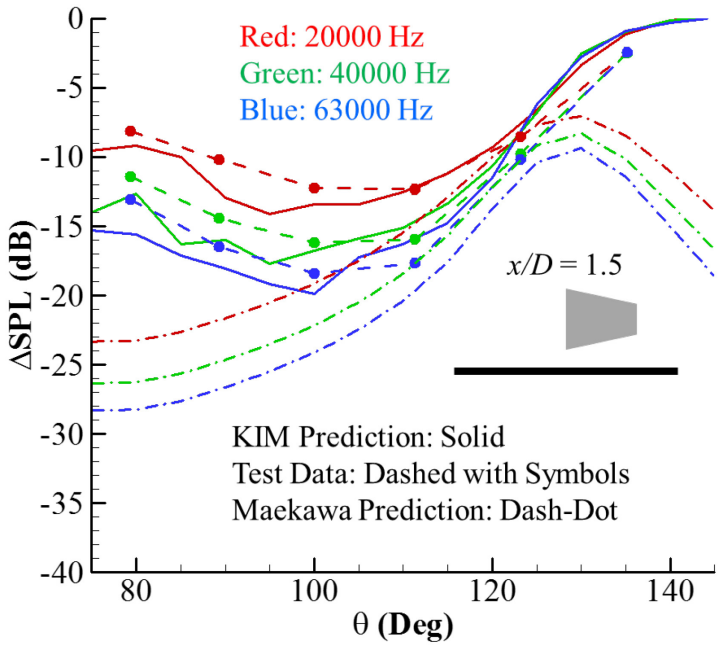

Figure 4-20: Comparison Between Prediction and Data for *x/D* = 1.5.

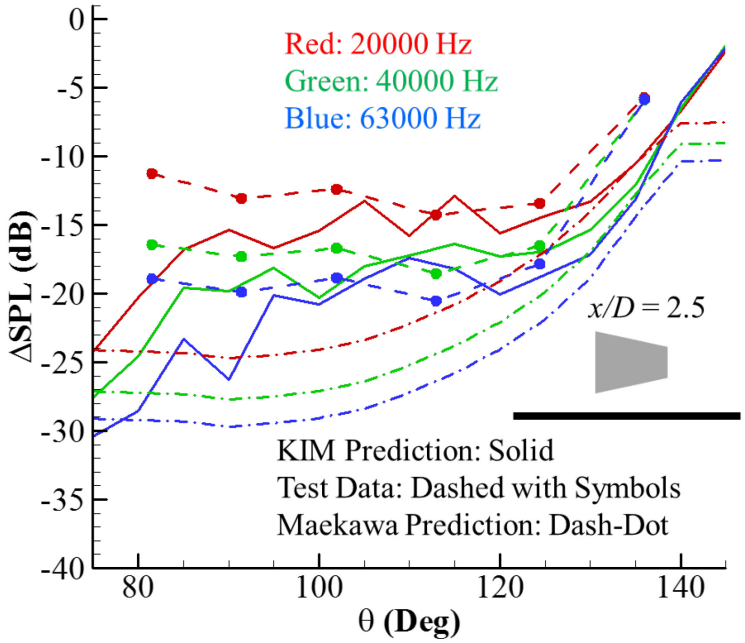

Figure 4-21: Comparison Between Prediction and Data for *x*/*D* = 2.5.

For the case of x/D = 1.5 where the source is located 1.5 diameters upstream of the trailing edge, the comparisons are shown in Figure 4-20. Again, three sets of results are shown in the figure; the solid curves are the KIM predictions, the dashed curves with symbols are the test data, and the dash-dot curves are the Maekawa predictions. The three frequencies are identified by the different colors, as indicated in the figure. The good agreements between the KIM predictions and the test data are evident. In this case, a large angular domain is shielded from the noise radiation, from the forward quadrant to about 135 degrees in the aft quadrant. This is clear from both the predictions and the data. Within the shielded angular domain, the shielding effects increase with frequency. The shielding effect amplitudes, as well as the trends with frequency and with polar angle, are well predicted. For both the KIM predictions and the data, the variations with angle are smooth, which is true for all three cases in Figure 4-19, Figure 4-20, and Figure 4-21. In comparison, the predictions by the Maekawa formula contain significant discrepancies with the test data, more than 10 dB in the deep shadow region where this empirical formula is supposed to work. This is likely due to the idealized configuration of the sources and shielding bodies on which the formula is derived.

When the source is moved further upstream to 2.5 diameters from the trailing edge, the shielded angular domain expands to about 145 degrees in the aft quadrant, and the shielding increases in the shadow region. These results are shown in Figure 4-21 with the same convention for the three sets of results and the same color scheme for the three frequencies as before. Again, the trends in the shielding features are well captured by the KIM predictions. The amplitude comparison also shows good agreement for large polar angles above about 90 degrees; below this angle in the deep shadow region, noticeable differences can be seen, which is likely due to the directivity used in the calculation extracted from the test data with accuracy limited to the aft quadrant. The large differences between the Maekawa predictions and the test data are also clear in this figure.

As discussed earlier in the report, the correct prediction of the shielding effects involves correct modeling of individual features that affect the physical process of noise shielding. The directivity of the sources is one of them. This is especially important for sources of engine fan noise for which the engine nacelle makes the radiation very directional, as shown in Figure 4-22 [4], [47] for three frequencies with the noise levels plotted as a function of the polar and azimuthal angles. This is the baseline case, taken as the unshielded

case, used to compute the shielding effects of the shielded cases. Since the aircraft body is 0.5 diameters upstream of the source, the directivity in the angular domain above about 80 degrees is essentially the same as a truly isolated nacelle. Clearly, there are very significant variations in the noise levels. For example, in the flyover plane, the noise can increase by as much as 15 dB from the location at 80 degrees polar angle to 130 degrees.

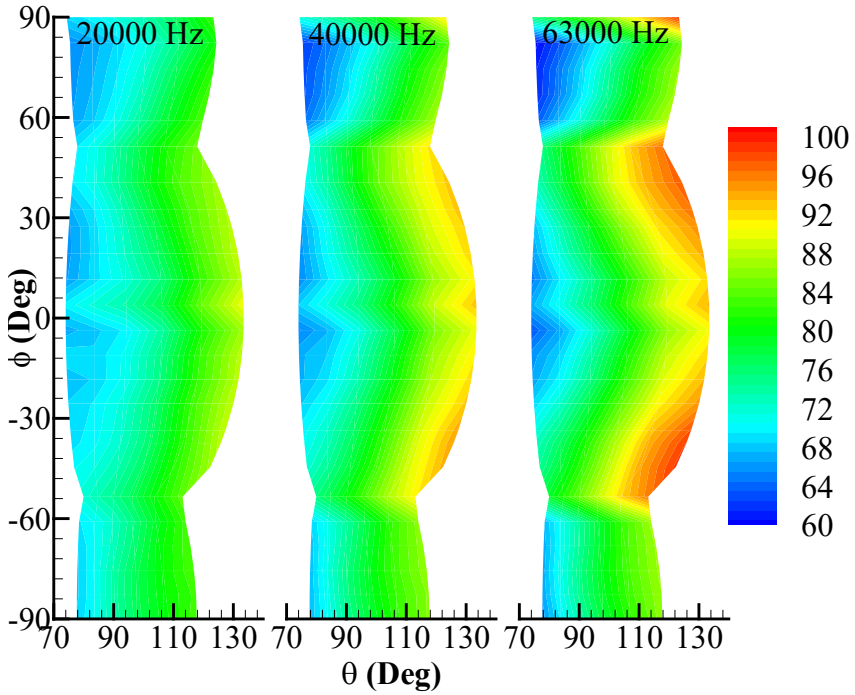

Figure 4-22: Baseline Directivity Pattern, SPL, as a Function of Polar Angle, θ, and Azimuthal Angle, ϕ, of N2A HWB Test.

The correct modeling and implementation of the directivity variations is critical for the prediction of the shielding effects. This has already been shown in Figure 4-20 and Figure 4-21, where the large discrepancies between the Maekawa predictions and the test data are partially due to the assumption of monopole sources in the Maekawa empirical formula. In the comparison between the KIM predictions and test data, the source directivity is extracted from the data shown in Figure 4-22, mostly confined to the aft quadrant, which is likely the reason why the comparisons are good in the aft quadrant. To further emphasize the importance of the source directivity, Figure 4-23 compares the KIM predictions with data for the case of $x/D = 1.5$ with the sources modeled as monopoles with uniform directivity; the predictions are significantly lower than the test data, and the errors are due to the incorrect modeling of the source directivity.

All predictions performed with the KIM method took on the order of seconds with a desktop computer, both for the NACA 0012 airfoil and the far more complex geometry of the N2A. The predicted results show correct trends and noise reduction levels that are very encouraging in comparison to data. However, the comparisons with the N2A have only been made in the plane of symmetry of the model. Predictions at azimuthal angles (wing tip to wing tip) will require improvements to the method. Thus, the tool development in the near future will focus on adding capabilities for the flow effects, coherence modeling, multiple reflections and interactions with turbulent wake flow. Even with all the features modeled and implemented, the computation time is expected to be on an acceptable order of magnitude, consistent with what is required by ANOPP for aircraft system noise studies.

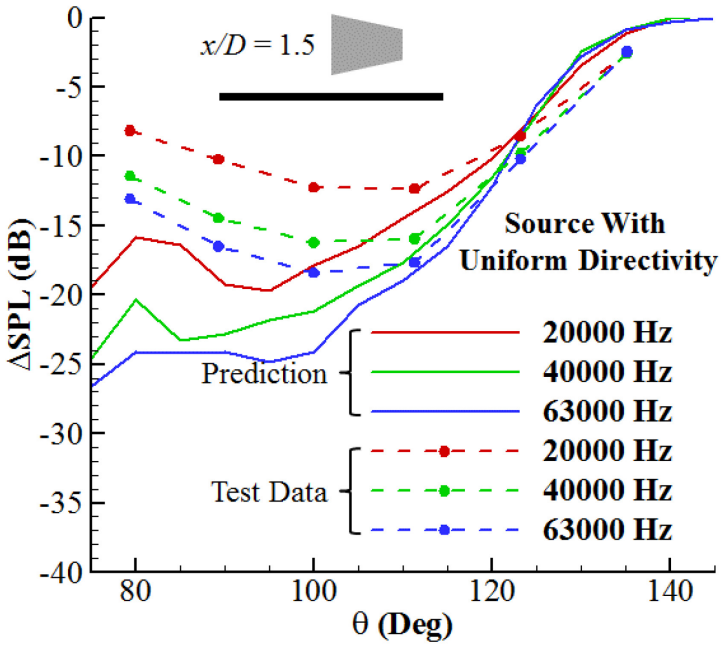

Figure 4-23: Comparison Between Data and KIM Prediction with Uniform Source Directivity.

Chapter 5 – CONCLUSIONS/OUTLOOK

Jan W. Delfs
DLR – Institute of Aerodynamics and Flow
GERMANY

Russell H. Thomas
Langley Research Center, NASA
UNITED STATES

Although not all objectives of AVT-233 could be accomplished in full detail, the group was very successful in achieving the main goals, namely:

- Appropriate test noise sources were developed for the purpose of conducting acoustic shielding tests.
- A model was successfully derived to describe the laser pulse source analytically in time and frequency domain, thus providing simple and relevant sources for prediction codes.
- Highly relevant acoustic shielding test campaigns were conducted in four different wind tunnels.
- Exceptionally good agreement in the shielding results for the NACA0012 was found in three completely different facilities, namely the AWB of DLR as an open section acoustic wind tunnel, the closed section non-acoustic wind tunnel F2 of ONERA and the open section QFF of NASA. Shielding levels along a line below the airfoil differed by at most 1 dB between the measurement results and emphasize the validity of the test in general.
- The systematic computations of the NACA shielding problem ranging from high- to mid-fidelity approaches show that only at very high frequency does low speed flow affect shielding. The 2D analysis provided the basis to justify simplified computation approaches for the 3D diffraction on the aircraft geometries.
- A vast database of 2D acoustic shielding has been established, which has the potential of becoming an open benchmark data set.
- Acoustic shielding data was also measured on the 3D SACCON and N2A HWB geometries.
- The 3D shielding problem was successfully computed using the Fast Multipole BEM on the complete aircraft while shielding from the trailing edge of the N2A HWB could be predicted based on a diffraction integral approach.
- The measurements as well as the prediction results obtained are all consistent.

5.1 LESSONS LEARNED

During the first 1.5 years of AVT-233, the discussion among the membership was intense because of monthly teleconferences. Due to some resource issues, these discussions could not be kept up during the second phase of the activity. This short but regular exchange of ideas and issues should be reestablished in any form of follow-on activity.

The change of leading personnel during the active phase of an AVT group is suboptimal for all sides, especially for the efficiency of the group's work. Planners of any follow-on activity should make sure that the acting members will most probably stay active throughout the entire working group duration.

The above-mentioned change of acting personnel partly affected the coherence in the work schedule across the research groups. The partners need to attempt to align internal work with the AVT schedule and with each other as much as possible.

5.2 ASSESSMENT OF RESULTS

The results are assessed in view of the objectives originally set out for the working group (see Chapter 1). In summary, all the essential objectives of AVT-233 were accomplished. The following section discusses the outcome, objective by objective.

- Demonstration of the availability and reliability of tools capable of predicting the effects of propulsion system installation of generic configurations on received sound as a basis for future acoustic design studies on military aircraft.

  Based on the concept of using the various prediction codes (high- to mid-fidelity) for simple, and later complex geometries, computational approaches could indeed be identified, which are capable of predicting the acoustic installation effects at practically arbitrary aircraft configurations as dedicated validation with experiments was carried out. Depending on the purpose of using such a prediction code, e.g., conceptual design, preliminary or more detailed design, computation times between a few seconds, minutes or an hour seem acceptable for complete aircraft geometries. Some methods indeed showed this capability at the price of neglecting certain physical effects such as refraction, flow gradients and turbulent scattering. Therefore, the objective that computational approaches were identified and validated, which can be used for shielding design studies, was accomplished. This assessment comes with the notice that results must always be critically looked at when nonuniform flow effects may be expected. In this case, it is safe to check for the validity of simplifying approaches by (more time consuming) single high-fidelity simulations. This may possibly be done quite locally at positions of interest, and it may be useful to couple mid- or low-fidelity approaches with high-fidelity codes into versatile mixed fidelity toolsets.

- Prediction of acoustic installation effects with various approaches, codes, and code-to-code comparisons among partners.

  Tools of different fidelity were tested against the challenges of predicting the acoustic shielding of aerodynamic shielding objects of increasing complexity: two extremely fast ray-based approaches were very successful on the NACA0012 problem, as were two volume discretizing methods (Finite differences, Discontinuous Galerkin Finite Elements). A fast multipole boundary element method successfully predicted the complex shielding of the two aircraft shielding geometries. A straight-forward extension/use of one ray-based method to the 3D cases showed some challenges, which could not be overcome entirely within the given time frame. The second ray-based prediction code was successfully tested to describe 3D diffraction at the edges of the HWB configuration.

- Conduct of dedicated aeroacoustic experiments for the purpose of validating the prediction codes for acoustic installation effects.

  An exceptional aeroacoustic database on shielding problems has been established in AVT-233 from various test campaigns in four different wind tunnels. Generic 2D diffraction (NACA0012) as well as diffraction at a convex, sharp edged (SACCON) and a generally shaped, sharp and round edged (HWB) configuration was measured successfully. In preparation for this, two aeroacoustic pulse test sources were developed and successfully used in the shielding experiments, one of which is non-intrusive and, therefore, neither disturbing flow nor sound field. The repeatability of the source events turned out to be very good. The laser-based pulse source was successfully used in all four wind tunnels (open and closed section). A cross validation of the measurements over the AWB, F2 and QFF showed an excellent reproducibility of test results, partially better than expected (deviations less than 1 dB). The various simulation approaches were validated against the measured data; simulation results were also successfully compared mutually from code to code. The use of high-fidelity numerical simulations helped to assess the step by step neglect of physical effects such as shear layer refraction, potential flow gradients and the flow itself. The overall outcome

of these studies showed that for the majority of problems at very low speed, a uniform flow assumption may be acceptable. This study opened the door for justifying the use of some low- to mid-fidelity prediction approaches to the actual aircraft shielding problem.

5.3 OUTLOOK

The results of AVT-233 call for the next logical step in the form of a follow-on AVT TG to now deal with more realistic sources and a realistic, concurrent agile (unmanned) NATO air vehicle design (such as MULDICON). In this way, a new group would naturally integrate the multidisciplinary design work of AVT-251 with the acoustic knowledge and tools provided by AVT-233. This combined expertise could be used not only to numerically analyze the acoustic properties of an aircraft of MULDICON type but will exploit the expertise on acoustic simulation tools gained in AVT-233 to do low noise engine integration design studies. Such simulations should be backed by a large scale complex acoustic wind tunnel test on a wind tunnel model to be built, equipped with pressurized air to simulate a highly integrated jet. This follow-on work should focus on:

- Demonstrating (on a realistic configuration) the qualification and applicability of tools for the prediction of the effects of propulsion system installation on received sound;
- Predicting noise reduction technology as an exercise in aeroacoustic design for agile NATO air vehicles, particularly the MULDICON configuration; and
- The mentioned objectives imply not only code-to-code comparisons among partners, but a dedicated validation dataset from tests in an appropriate (i.e., large enough size) acoustic wind tunnel.

Chapter 6 – REFERENCES

[1] Delfs, J.W. (2014), "Aeroacoustic Tunnel Effect in Noise Shielding Problems" (AIAA 2014-3181), 20th AIAA/CEAS Aeroacoustics Conference, 2014, DOI 10.2514/6.2014-3181.

[2] Rossignol, K-S., Delfs, J.W. (2016), "Analysis of the Noise Shielding Characteristics of a NACA0012 2D Wing" (AIAA 2016-2795), 22nd AIAA/CEAS Aeroacoustics Conference. 22nd AIAA/CEAS Aeroacoustics Conference, DOI 10.2514/6.2016-2795.

[3] Rossignol, K-S., Delfs, J.W. Boden, F. (2015), "On the Relevance of Convection Effects for a Laser-Generated Sound Source" (AIAA 2015-3146), 21st AIAA/CEAS Aeroacoustics Conference, 2015, DOI 10.2514/6.2015-3146.

[4] Hutcheson, F.V., Brooks, T.F., Burley, C.L., Bahr, C.J., and Pope, D.S. (2014), "Shielding of Turbomachinery Broadband Noise from a Hybrid Wing Body Aircraft Configuration," AIAA 2014-2624. 20th AIAA/CEAS Aeroacoustics Conference, DOI 10.2514/6.2014-2624.

[5] Rossignol, K-S., Lummer, M., Delfs, J.W. (2009), "Validation of DLR's Sound Shielding Prediction Tool Using a Novel Sound Source" (AIAA 2009-3329), 15th AIAA/CEAS Aeroacoustics Conference, 2009, DOI 10.2514/6.2009-3329.

[6] Rossignol, K-S., Pott-Pollenske, M., Delfs, J.W. (2017), Silbermann, J., Pereira Gomes, J.M. "Investigating Noise Shielding by Unconventional Aircraft Configurations" (AIAA 2017-3195), 23rd AIAA/CEAS Aeroacoustics Conference, 2017, DOI 10.2514/6.2017-3195.

[7] Boden, F., Delfs, J.W. (2006), "Development of a Laser-Based Sound Source", Inter-Noise. Inter-Noise 2006, 3 – 6 December 2006, Honolulu, Hawaii, USA.

[8] Boden, F. (2007), "Grundlagenuntersuchungen zu einer neuartigen Laserschallquelle", DLR, Braunschweig, Institut für Aerodynamik und Strömungstechnik, IB 124-2007/5.

[9] Yin, J., Rossignol, K.-S., Bulté, J. (2016), "Acoustic Scattering Experiments on Spheres for Studying Helicopter Noise Scattering", Proceedings of the European Rotorcraft Forum.

[10] Yin, J., Rossignol, K.-S., Barbarino M., Bianco, D., Testa, C., Brouwer, H., et al. (2017), "Acoustical Methods and Experiments for Studying Rotorcraft Fuselage Scattering", Proceedings of the European Rotorcraft Forum.

[11] Hosoya, N., Nagata, M., Kajiwara, I. (2013), "Acoustic Testing in a Very Small Space Based on a Point Sound Source Generated by Laser-Induced Breakdown: Stabilization of Plasma Formation", Journal of Sound and Vibration, Vol. 332, no. 19, pp. 4572-4583.

[12] Radziemski, L.J., Cremers, D.A. (1989), "Laser Induced Plasmas and Applications", Marcel Dekker Inc., ISBN-13: 978-0824780784.

[13] Phuoc, T.X, White, C.M. (2010), "Experimental Studies of the Absorption and Emissions from Laser-Induced Spark in Combustible Gases", Optics Communications, Vol. 181, no. 4, pp. 353-359.

[14] Chen, Y-L, Lewis, J.W.L., Parigger, C. (2000), "Spatial and Temporal Profiles of Pulsed Laser-Induced Air Plasma Emissions", Journal of Quantitative Spectroscopy and Radiative Transfer, Vol. 67, no. 2, pp. 91-103.

[15] Ostrovskaya, G.V., Zauidel, A.N. (1974), “Laser Spark in Gases”, Physics-Uspekhi, Vol. 16, no.6, pp. 834-855.

[16] Villagrán-Muniz, M., Sobral, H., Navarro-Gonzàlez, R. (2003), “Shock and Thermal Wave Study of Laser-Induced Plasmas in Air by the Probe Beam Deflection Technique”, Measurement Science and Technology, Vol. 14, no. 5, pp. 614-618.

[17] Phuoc, T.X. “Laser Spark Ignition: Experimental Determination of Laser-Induced Breakdown Thresholds of Combustion Gases” (2000), Optics Communications, Vol. 175, no. 4, pp. 419-423.

[18] Saleh, B.E.A., Teich, M.C. “Fundamental of Photonics” (1991), John Wiley & Sons, New York.

[19] Shannon R.R. “The Art and Science of Optical Design” (1997), Cambridge University Press, Cambridge.

[20] Zemax ®. (2017), “Zemax 13 User’s Manual”. Bernhard Halle Nachfl. GmbH

[21] Mouroulis P., Macdonald J. (1997), “Geometrical Optics and Optical Design”, Oxford University Press, Oxford.

[22] Hecht, E. “Optics 4th Edition” (2002), International edition, Addison-Wesley, San Francisco.

[23] Lebigot, P. (2009). Étude de faisabilité d’une source acoustique impulsionnelle pour l’étalonnage en amplitude et en phase d’un réseau de microphones en soufflerie. Rapport Technique ONERA no 1/22699 DSNA.

[24] Delfs, J.W., Bauer, M., Ewert, R., Grogger, H.A., Lummer, M., Lauke, T. (2008), “Numerical Simulation of Aerodynamic Noise with DLR’s Aeroacoustic Code PIANO”, https://elib.dlr.de/118928/.

[25] Tam, C.K.W., Webb, J.W. (1993), “Dispersion-Relation-Preserving Finite Difference Schemes for Computational Acoustics”, Journal for Computational Physics, p.107.

[26] Engineering Sciences Data Unit (ESDU) (2003), Estimation of Noise Shielding by Barriers, ESDU 79011 Amendment C, June 2003.

[27] Vér, I.L. (2006), Beranek, L.L., Noise and Vibration Control Engineering. John Wiley & Sons, Inc.

[28] Technical Assessment of the Effectiveness of Noise Walls (1999). I-INCE Publication 99-1, September 1999.

[29] Paige, T., (2014), “Outdoor Noise Barriers: Design and Applications,” https://www.enoisecontrol.com/wp-content/uploads/2014/12/outdoor_noise_barrier_wall.pdf.

[30] Government of the Hong Kong (January 2003). Guidelines on the Design of Noise Barriers, Environmental Protection Department, Highways Department, Government of the Hong Kong SAR Second Issue.

[31] Delfs, J.W. (2014). Source Model – DLR Experimental observations, Slide 19, AVT_233_status_Dec14.pptx, 11th December 2014.

[32] Atkins, H., and Shu, C.-W. (1998). “Quadrature-Free Implementation of Discontinuous Galerkin Method for Hyperbolic Equations”, AIAA Journal, pp. 775-782, 1998.

[33] Ewert, R., and Schroder, W. (2003). "Acoustic Perturbation Equations Based on Flow Decomposition via Source Filtering", Journal of Computational Physics, pp. 365-398.

[34] Allan, M.R., and Darbyshire, O.R. (2014). "Comparison of LES and Stochastic Source Generation Methods for Aero- and Hydro- Acoustic Design Guidance", AIAA Aeroacoustics, Atlanta, 2014.

[35] Keller, J.B., (1962), "Geometrical Theory of Diffraction," Journal of the Optical Society of America, Vol. 52, no. 2, pp.116–130.

[36] Sommerfeld, A., (1954), "Lectures on Theoretical Physics: Optics," Volume IV, Academic Press, New York.

[37] Pierce, A.D., (1981), "Acoustics: An Introduction to its Physical Principles and Applications," McGraw-Hill, New York.

[38] Morse, P.M. and Ingard, K.U. (1968), "Theoretical Acoustics," McGraw-Hill, New York.

[39] Guo, Y., Pope, D.S., Burley, C.L., and Thomas, R.H., (2017), "Aircraft System Noise Shielding Prediction with a Kirchoff Integral Method," 23rd AIAA/CEAS Aeroacoustics Conference. DOI 10.2514/6.2017-3196.

[40] Rossignol, K. and Delfs, J., (2016), "Analysis of the Noise Shielding Characteristics of a NACA 0012 2D Wing," AIAA/CEAS Aeroacoustics Conference. DOI 10.2514/6.2016-2795, 201.

[41] Lummer, M. (2008), "Maggi-Rubinowicz Diffraction Correction for Ray Tracing Calculations of Engine Noise Shielding, AIAA Paper 2008-2050, DOI: 10.2514/6.2008-2050.

[42] Lummer, M., Akkermans, R., Richter, Chr., Pröber, C., Delfs, J. (2013), "Validation of a Model for Open Rotor Noise Predictions and Calculation of Shielding Effects using a Fast BEM". AIAA Paper 2013-2096, DOI: 10.2514/6.2003-3109.

[43] Taylor, K. (1978), "A Transformation of the Acoustic Equation with Implications for Wind-Tunnel and Low Speed Flight Tests", Proceedings of the Royal Society London, A 363, pp.271-281.

[44] Coifman, R., Rokhlin, V., Wandzura, S. (1993), "The Fast Multipole Method for the Wave Equation: A Pedestrian Prescription", IEEE Antennas and Propagation Magazine, Vol. 35, no. 3, pp.7-12.

[45] Rahola, J. (1998), "Diagonal Forms of the Translation Operators in the Fast Multipole Algorithm for Scattering Problems", BIT Numerical Mathematics, Vol. 36, no. 2, pp.333-358.

[46] Balay, S., Abhyankar, S., et al. (2017), "PETSc User Manual", Argonne National Laboratory, ANL-95/11 – Revision 3.8.

[47] Hutcheson, F.V. (2014), "Overview of the Hybrid Wing Body Aeroacoustic Test in NASA Langley 14- by 22-Foot Subsonic Tunnel," Oral Presentation, 20th AIAA/CEAS Aeroacoustics Conference, Atlanta, GA, June 16-20, 2014.

[48] Doty, M.J., Brooks, T.F., Burley, C.L., Bahr, C.J., and Pope, D.S., (2014), "Jet Noise Shielding Provided by a Hybrid Wing Body Aircraft," 20th AIAA/CEAS Aeroacoustics Conference. DOI 10.2514/6.2014-2625.

[49] Maekawa, Z., (1968), "Noise Reduction by Screens," Applied Acoustics, Elsevier Publishing Co., Ltd., pp. 157-173.

REPORT DOCUMENTATION PAGE

1. Recipient's Reference	2. Originator's References	3. Further Reference	4. Security Classification of Document
	STO-TR-AVT-233 AC/323(AVT-233)TP/961	ISBN 978-92-837-2282-3	PUBLIC RELEASE

5. Originator

Science and Technology Organization
North Atlantic Treaty Organization
BP 25, F-92201 Neuilly-sur-Seine Cedex, France

6. Title

Aeroacoustics of Engine Installation on Military Air Vehicles

7. Presented at/Sponsored by

This report contains the results of the RTG AVT-233 active in the period 2014 – 2017 and covering the establishment of validated methods to predict fundamental aspects of acoustic installation effects of engine noise for military aircraft.

8. Author(s)/Editor(s)	9. Date
Multiple	October 2021
10. Author's/Editor's Address	**11. Pages**
Multiple	146

12. Distribution Statement

There are no restrictions on the distribution of this document. Information about the availability of this and other STO unclassified publications is given on the back cover.

13. Keywords/Descriptors

Acoustic installation effects; Aeroacoustics; Barrier shielding method; Computational Aeroacoustics (CAA); Edge scattering; Engine integration; Fast multipole boundary element method; Laser pulse source; Ray tracing; Sound diffraction; Sound reflection; Sound refraction; Sound shielding; Spark source

14. Abstract

In the AVT-233 Task Group a comprehensive research program was executed to identify and validate appropriate acoustic prediction methods as a basis for low noise military aircraft design with a focus on acoustic shielding of engine noise. A set of related aeroacoustic shielding tests was carried out in four different wind tunnels for three different geometries of ever-increasing complexity to establish a fundamental aeroacoustic shielding database for the validation of acoustic prediction codes of partners. Generic 2D diffraction (NACA0012), diffraction at a convex, sharp edged (SACCON) and a generally convex-concave shaped, sharp- and round edged (HWB) configuration were all measured successfully. For this purpose, two aeroacoustic pulse test sources were developed successfully. A cross validation of the measurements over three wind tunnels showed excellent reproducibility of test results, even better than expected. The various simulation approaches were validated against measured data. The overall outcome showed that for the majority of problems the use of some fast low- to mid-fidelity prediction approaches to the aircraft shielding problem is justified. Validated tools have been established with which to take the next logical step toward full simulation based low noise design modifications of realistic NATO military air vehicles.

NORTH ATLANTIC TREATY ORGANIZATION

BP 25
F-92201 NEUILLY-SUR-SEINE CEDEX • FRANCE
Télécopie 0(1)55.61.22.99 • E-mail mailbox@cso.nato.int

SCIENCE AND TECHNOLOGY ORGANIZATION

DIFFUSION DES PUBLICATIONS

STO NON CLASSIFIEES

Les publications de l'AGARD, de la RTO et de la STO peuvent parfois être obtenues auprès des centres nationaux de distribution indiqués ci-dessous. Si vous souhaitez recevoir toutes les publications de la STO, ou simplement celles qui concernent certains Panels, vous pouvez demander d'être inclus soit à titre personnel, soit au nom de votre organisation, sur la liste d'envoi.

Les publications de la STO, de la RTO et de l'AGARD sont également en vente auprès des agences de vente indiquées ci-dessous.

Les demandes de documents STO, RTO ou AGARD doivent comporter la dénomination « STO », « RTO » ou « AGARD » selon le cas, suivi du numéro de série. Des informations analogues, telles que le titre est la date de publication sont souhaitables.

Si vous souhaitez recevoir une notification électronique de la disponibilité des rapports de la STO au fur et à mesure de leur publication, vous pouvez consulter notre site Web (http://www.sto.nato.int/) et vous abonner à ce service.

CENTRES DE DIFFUSION NATIONAUX

ALLEMAGNE
Streitkräfteamt / Abteilung III
Fachinformationszentrum der Bundeswehr (FIZBw)
Gorch-Fock-Straße 7, D-53229 Bonn

BELGIQUE
Royal High Institute for Defence – KHID/IRSD/RHID
Management of Scientific & Technological Research
for Defence, National STO Coordinator
Royal Military Academy – Campus Renaissance
Renaissancelaan 30, 1000 Bruxelles

BULGARIE
Ministry of Defence
Defence Institute "Prof. Tsvetan Lazarov"
"Tsvetan Lazarov" bul no.2
1592 Sofia

CANADA
DGSIST 2
Recherche et développement pour la défense Canada
60 Moodie Drive (7N-1-F20)
Ottawa, Ontario K1A 0K2

DANEMARK
Danish Acquisition and Logistics Organization
(DALO)
Lautrupbjerg 1-5
2750 Ballerup

ESPAGNE
Área de Cooperación Internacional en I+D
SDGPLATIN (DGAM), C/ Arturo Soria 289
28033 Madrid

ESTONIE
Estonian National Defence College
Centre for Applied Research
Riia str 12
Tartu 51013

ETATS-UNIS
Defense Technical Information Center
8725 John J. Kingman Road
Fort Belvoir, VA 22060-6218

FRANCE
O.N.E.R.A. (ISP)
29, Avenue de la Division Leclerc
BP 72
92322 Châtillon Cedex

GRECE (Correspondant)
Defence Industry & Research General
Directorate, Research Directorate
Fakinos Base Camp, S.T.G. 1020
Holargos, Athens

HONGRIE
Hungarian Ministry of Defence
Development and Logistics Agency
P.O.B. 25
H-1885 Budapest

ITALIE
Ten Col Renato NARO
Capo servizio Gestione della Conoscenza
F. Baracca Military Airport "Comparto A"
Via di Centocelle, 301
00175, Rome

LUXEMBOURG
Voir Belgique

NORVEGE
Norwegian Defence Research
Establishment
Attn: Biblioteket
P.O. Box 25
NO-2007 Kjeller

PAYS-BAS
Royal Netherlands Military
Academy Library
P.O. Box 90.002
4800 PA Breda

POLOGNE
Centralna Biblioteka Wojskowa
ul. Ostrobramska 109
04-041 Warszawa

PORTUGAL
Estado Maior da Força Aérea
SDFA – Centro de Documentação
Alfragide
P-2720 Amadora

REPUBLIQUE TCHEQUE
Vojenský technický ústav s.p.
CZ Distribution Information Centre
Mladoboleslavská 944
PO Box 18
197 06 Praha 9

ROUMANIE
Romanian National Distribution
Centre
Armaments Department
9-11, Drumul Taberei Street
Sector 6
061353 Bucharest

ROYAUME-UNI
Dstl Records Centre
Rm G02, ISAT F, Building 5
Dstl Porton Down
Salisbury SP4 0JQ

SLOVAQUIE
Akadémia ozbrojených síl gen.
M.R. Štefánika, Distribučné a
informačné stredisko STO
Demänová 393
031 01 Liptovský Mikuláš 1

SLOVENIE
Ministry of Defence
Central Registry for EU & NATO
Vojkova 55
1000 Ljubljana

TURQUIE
Milli Savunma Bakanlığı (MSB)
ARGE ve Teknoloji Dairesi
Başkanlığı
06650 Bakanliklar – Ankara

AGENCES DE VENTE

The British Library Document Supply Centre
Boston Spa, Wetherby
West Yorkshire LS23 7BQ
ROYAUME-UNI

Canada Institute for Scientific and Technical Information (CISTI)
National Research Council Acquisitions
Montreal Road, Building M-55
Ottawa, Ontario K1A 0S2, CANADA

Les demandes de documents STO, RTO ou AGARD doivent comporter la dénomination « STO », « RTO » ou « AGARD » selon le cas, suivie du numéro de série (par exemple AGARD-AG-315). Des informations analogues, telles que le titre et la date de publication sont souhaitables. Des références bibliographiques complètes ainsi que des résumés des publications STO, RTO et AGARD figurent dans le « NTIS Publications Database » (http://www.ntis.gov).

NORTH ATLANTIC TREATY ORGANIZATION

BP 25
F-92201 NEUILLY-SUR-SEINE CEDEX • FRANCE
Télécopie 0(1)55.61.22.99 • E-mail mailbox@cso.nato.int

SCIENCE AND TECHNOLOGY ORGANIZATION

DISTRIBUTION OF UNCLASSIFIED STO PUBLICATIONS

AGARD, RTO & STO publications are sometimes available from the National Distribution Centres listed below. If you wish to receive all STO reports, or just those relating to one or more specific STO Panels, they may be willing to include you (or your Organisation) in their distribution.

STO, RTO and AGARD reports may also be purchased from the Sales Agencies listed below.

Requests for STO, RTO or AGARD documents should include the word 'STO', 'RTO' or 'AGARD', as appropriate, followed by the serial number. Collateral information such as title and publication date is desirable.

If you wish to receive electronic notification of STO reports as they are published, please visit our website (http://www.sto.nato.int/) from where you can register for this service.

NATIONAL DISTRIBUTION CENTRES

BELGIUM
Royal High Institute for Defence – KHID/IRSD/RHID
Management of Scientific & Technological Research for Defence, National STO Coordinator
Royal Military Academy – Campus Renaissance
Renaissancelaan 30
1000 Brussels

BULGARIA
Ministry of Defence
Defence Institute "Prof. Tsvetan Lazarov"
"Tsvetan Lazarov" bul no.2
1592 Sofia

CANADA
DSTKIM 2
Defence Research and Development Canada
60 Moodie Drive (7N-1-F20)
Ottawa, Ontario K1A 0K2

CZECH REPUBLIC
Vojenský technický ústav s.p.
CZ Distribution Information Centre
Mladoboleslavská 944
PO Box 18
197 06 Praha 9

DENMARK
Danish Acquisition and Logistics Organization (DALO)
Lautrupbjerg 1-5
2750 Ballerup

ESTONIA
Estonian National Defence College
Centre for Applied Research
Riia str 12
Tartu 51013

FRANCE
O.N.E.R.A. (ISP)
29, Avenue de la Division Leclerc – BP 72
92322 Châtillon Cedex

GERMANY
Streitkräfteamt / Abteilung III
Fachinformationszentrum der Bundeswehr (FIZBw)
Gorch-Fock-Straße 7
D-53229 Bonn

GREECE (Point of Contact)
Defence Industry & Research General Directorate, Research Directorate
Fakinos Base Camp, S.T.G. 1020
Holargos, Athens

HUNGARY
Hungarian Ministry of Defence
Development and Logistics Agency
P.O.B. 25
H-1885 Budapest

ITALY
Ten Col Renato NARO
Capo servizio Gestione della Conoscenza
F. Baracca Military Airport "Comparto A"
Via di Centocelle, 301
00175, Rome

LUXEMBOURG
See Belgium

NETHERLANDS
Royal Netherlands Military Academy Library
P.O. Box 90.002
4800 PA Breda

NORWAY
Norwegian Defence Research Establishment, Attn: Biblioteket
P.O. Box 25
NO-2007 Kjeller

POLAND
Centralna Biblioteka Wojskowa
ul. Ostrobramska 109
04-041 Warszawa

PORTUGAL
Estado Maior da Força Aérea
SDFA – Centro de Documentação
Alfragide
P-2720 Amadora

ROMANIA
Romanian National Distribution Centre
Armaments Department
9-11, Drumul Taberei Street, Sector 6
061353 Bucharest

SLOVAKIA
Akadémia ozbrojených síl gen. M.R. Štefánika, Distribučné a informačné stredisko STO
Demänová 393
031 01 Liptovský Mikuláš 1

SLOVENIA
Ministry of Defence
Central Registry for EU & NATO
Vojkova 55
1000 Ljubljana

SPAIN
Área de Cooperación Internacional en I+D
SDGPLATIN (DGAM)
C/ Arturo Soria 289
28033 Madrid

TURKEY
Milli Savunma Bakanlığı (MSB)
ARGE ve Teknoloji Dairesi Başkanlığı
06650 Bakanliklar – Ankara

UNITED KINGDOM
Dstl Records Centre
Rm G02, ISAT F, Building 5
Dstl Porton Down, Salisbury SP4 0JQ

UNITED STATES
Defense Technical Information Center
8725 John J. Kingman Road
Fort Belvoir, VA 22060-6218

SALES AGENCIES

The British Library Document Supply Centre
Boston Spa, Wetherby
West Yorkshire LS23 7BQ
UNITED KINGDOM

Canada Institute for Scientific and Technical Information (CISTI)
National Research Council Acquisitions
Montreal Road, Building M-55
Ottawa, Ontario K1A 0S2, CANADA

Requests for STO, RTO or AGARD documents should include the word 'STO', 'RTO' or 'AGARD', as appropriate, followed by the serial number (for example, AGARD-AG-315). Collateral information such as title and publication date is desirable. Full bibliographical references and abstracts of STO, RTO and AGARD publications are given in "NTIS Publications Database" (http://www.ntis.gov).

ISBN 978-92-837-2282-3